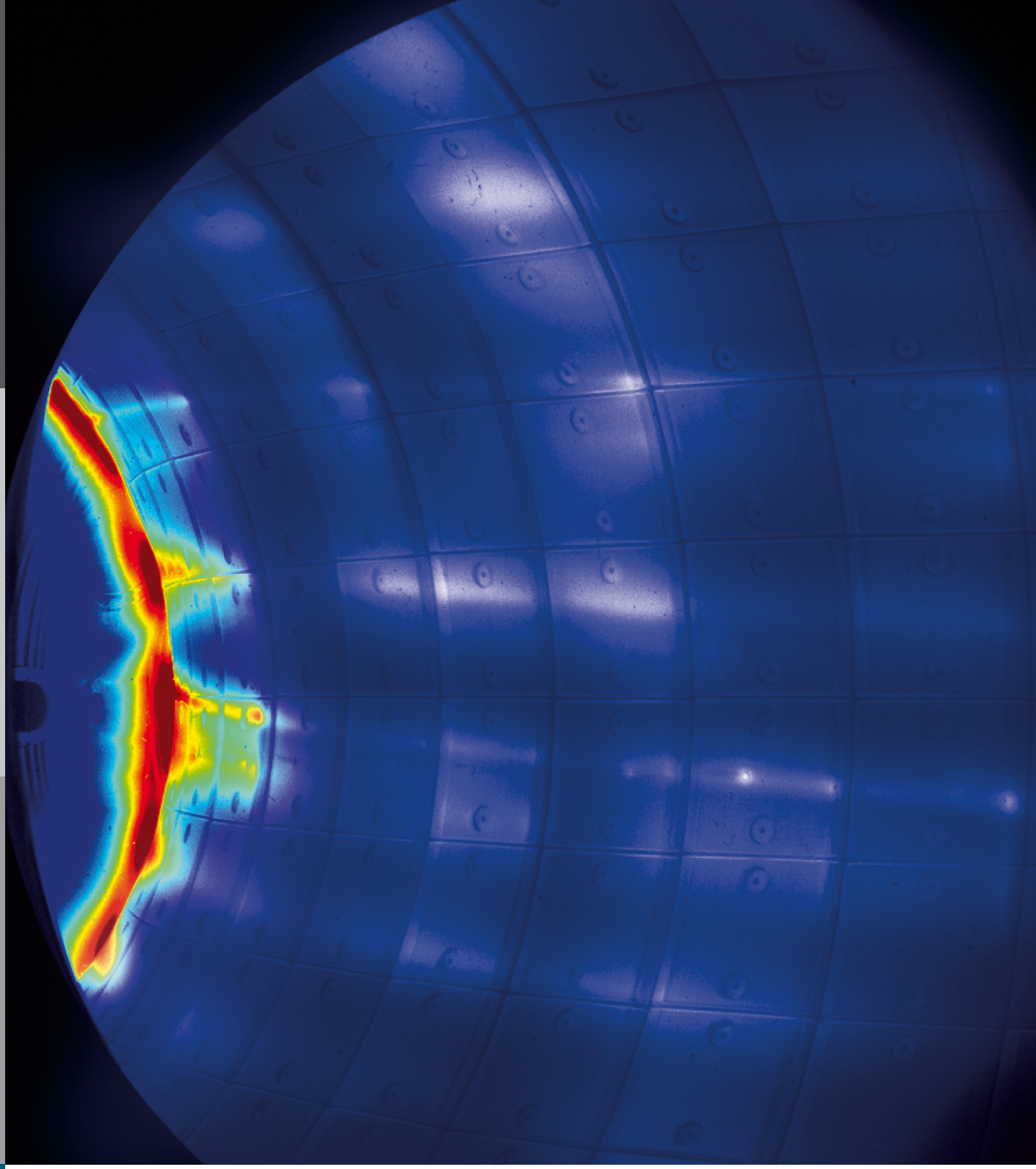

Hydrogen recycling and transport in the helical divertor of TEXTOR

Meike Clever

Mitglied der Helmholtz-Gemeinschaft

JÜLICH
FORSCHUNGSZENTRUM

Schriften des Forschungszentrums Jülich
Reihe Energie & Umwelt / Energy & Environment Band / Volume 87

Forschungszentrum Jülich GmbH
Institute of Energy Research (IEF)
Plasma Physics (IEF-4)

Hydrogen recycling and transport in the helical divertor of TEXTOR

Meike Clever

Schriften des Forschungszentrums Jülich
Reihe Energie & Umwelt / Energy & Environment Band / Volume 87

ISSN 1866-1793 ISBN 978-3-89336-673-6

Bibliographic information published by the Deutsche Nationalbibliothek.
The Deutsche Nationalbibliothek lists this publication in the Deutsche Nationalbibliografie; detailed bibliographic data are available in the Internet at http://dnb.d-nb.de.

Publisher and Distributor:	Forschungszentrum Jülich GmbH Zentralbibliothek 52425 Jülich Phone +49 (0) 24 61 61-53 68 · Fax +49 (0) 24 61 61-61 03 e-mail: zb-publikation@fz-juelich.de Internet: http://www.fz-juelich.de/zb
Cover Design:	Grafische Medien, Forschungszentrum Jülich GmbH
Printer:	Grafische Medien, Forschungszentrum Jülich GmbH
Copyright:	Forschungszentrum Jülich 2010

Schriften des Forschungszentrums Jülich
Reihe Energie & Umwelt / Energy & Environment Band / Volume 87

D 61 (Diss. Düsseldorf, Univ., 2010)

ISSN 1866-1793
ISBN 978-3-89336-673-6

The complete volume ist freely available on the Internet on the Jülicher Open Access Server (JUWEL) at http://www.fz-juelich.de/zb/juwel

Zusammenfassung

Divertoren mit chaotischen Magnetfeldstrukturen sind von großem Interesse in der heutigen Fusionsforschung, nicht nur für Stellaratoren mit ihren inhärenten komplexen Magnetfeldstrukturen, sondern auch für Tokamaks auf Grund der Anwendung resonanter magnetischer Störfelder. Diese Methode wird auch im Limitertokamak TEXTOR angewendet, um eine helikale Divertorstruktur mit einer komplexen, dreidimensionalen Magnetfeldtopologie zu erzeugen. Die Funktionalität solcher Divertoren in Bezug auf die kontrollierte und effiziente Teilchen- und Energieabfuhr wird derzeit untersucht. Das Verständnis in dieser Hinsicht zu erhöhen, war ein Hauptmotiv dieser Arbeit. Der Zugang zu vorteilhaften Divertorregimen mit großem Temperaturgradient zwischen Plasmazentrum und Divertorplatten, hoher Neutralteilchendichte im Divertorvolumen für effizientes Pumpen und starke Strahlung zur Verteilung der Wärmelast (High Recycling Regime) oder zusätzlich mit reduziertem Teilchen- und Wärmefluss (Detachment), wird zu einem großen Teil durch das Wasserstoffrecycling an den Divertorplatten bestimmt. In dieser Arbeit wurde daher das Wasserstoffrecycling an den Divertorplatten des helikalen Divertors in TEXTOR untersucht und damit die Fähigkeit dieser Divertorkonfiguration, solch erwünschte Operationsregimes zu erreichen.

Um die Abhängigkeit des Wasserstoffrecyclings von der Plasmadichte in verschiedenen Dichtebereichen in TEXTOR zu untersuchen, wurden Plasmaentladungen durchgeführt, in denen die Gesamtteilchendichte kontinuierlich bis zum Dichtelimit erhöht wurde. Das Recycling wurde in einer festen helikalen Divertorstruktur untersucht, bei der sich auf den Divertorplatten vier helikale Auftreffpunkte (strike points) mit einer Ausdehnung von $8 - 10\,\mathrm{cm}$ in poloidaler Richtung ausbilden. Die experimentelle Untersuchung des Wasserstoffrecyclings wurde hauptsächlich mit Hilfe spektroskopischer Methoden durchgeführt, unterstützt von Langmuirsonden-, Atomstrahl- und interferometrischen Messungen. Im Rahmen dieser Arbeit wurde ein spektroskopisches Multikamerasystem aufgebaut, welches die gleichzeitige Beobachtung vier verschiedener Spektrallinien ermöglicht, wobei es Bilder der Divertorplatten sowie des Plasmavolumens davor aufnimmt. Das System ermöglicht damit die simultane Messung des poloidalen und toroidalen Abdrucks des Recyclingflusses auf den Divertorplatten, eine sonst häufig dazu notwendige räumliche Verschiebung der Plasmastruktur ist nicht nötig. Die gleichzeitige Beobachtung mehrerer verschiedener Spektrallinien verringert die Unsicherheit bei Auswertungen, die auf mehreren Spektrallinien basieren. Die Unsicherheit in der Reproduzierbarkeit der Plasmaparameter in verschiedenen Entladungen entfällt

und lediglich die Messmethode begrenzt die Messgenauigkeit. Die räumliche Auflösung des Systems in poloidaler und toroidaler Richtung ($\approx 0.8\,\mathrm{mm} \pm 0.01\,\mathrm{mm}$) ist klein im Vergleich zum Abstand der helikalen Auftreffpunkten. Die Fähigkeit der Messmethode, diese Strukturen aufzulösen ist daher durch die Sichtlinienintegration und die Eindringtiefe der lichtemittierenden Spezies begrenzt. Die Messungen haben gezeigt, dass der Recyclingfluss linear mit zunehmender Plasmadichte ansteigt, ein High Recycling Regime (quadratischer Anstieg) wurde nicht beobachtet. Dessen Fehlen kann durch die Anwendung eines erweiterten Zweipunktmodells einschließlich konvektiven Wärmetransports auf diejenige Region erklärt werden, in welcher der parallele Transport dominiert (laminare Zone). Die radiale Eindringtiefe des neutralen Wasserstoffs ($\lambda_\mathrm{n} \approx 3 - 4\,\mathrm{cm}$), bestimmt mit Hilfe der spektroskopischen Messungen, ist vielfach größer als die variierende radiale Ausdehnung der laminaren Zone (wenige mm bis zu 6 cm), was schließlich zu einer Reduktion paralleler Temperaturgradienten auf Grund des verstärkten konvektiven Wärmetransports führt. Eine Vergrößerung der radialen Ausdehnung der laminaren Zone insbesondere vor den Divertorauftreffpunkten könnte in dieser Hinsicht zu einer Verbesserung führen und den Zugang zum High Recycling Regime ermöglichen. Es kann somit erwartet werden, dass sowohl das Schließen der offenen Divertorgeometrie des helikalen Divertors am Stellarator LHD durch den Einbau zusätzlicher Prallplatten, sogenannter *baffles*, der zur Zeit im Gang ist, als auch der größere Inseldurchmesser im Inseldivertor des zukünftigen Stellarators W7-X im Vergleich zu seinem Vorgänger W7-AS dort den Zugang zum High Recycling Regime ermöglichen. Vor der Strahlungsinstabilität, die sich im helikalen Divertor in TEXTOR bei hohen Plasmadichten ausbildet, beobachtet man ein transientes, partielles Ablösen (Detachment) des Plasmas von den Divertorplatten. Die Instabilität führt zur Ausbildung eines poloidal strukturierten und helikal geneigten Strahlungsgürtels, eines helikalen Divertor-MARFE. Während ein MARFE typischerweise zu einer Dichtelimitdisruption der Entladung führt, konnte der helikale Divertor-MARFE mit Hilfe eines Regelungssystems stabilisiert werden und könnte einen Teil der gewünschten Divertorfunktionalität wie niedrige Temperatur an den Auftreffpunkten, erhöhte Neutralteilchendichte und verstärkte Strahlung innerhalb der stochastischen Randschicht bieten. Ein detaillierter Vergleich der experimentellen Beobachtungen mit den Ergebnissen von Modellierungen mit dem dreidimensionalen numerischen Transportcode EMC3-EIRENE zeigte gute Übereinstimmung sowohl im Hochdichteverhalten (insbesondere Fehlen des High Recycling Regimes) als auch in den Absolutwerten der simulierten und gemessenen Teilchenflüsse an den Auftreffpunkten. Simulationen mit zwei verschiedenen senkrechten Transportkoeffizienten haben gezeigt, dass diese Übereinstimmung nur bei einem bestimmten Level senkrechten Transports ($D_\perp = 1\,\mathrm{m^2 s^{-1}}$) beobachtet werden kann. Simulationen, welche zusätzlich Kohlenstoffverunreinigungen enthielten, zeigten außerdem die experimentell beobachteten Reduktion im Recyclingfluss bei hohen Dichten. Diese Ergebnisse stützen die Anwendung des EMC3-EIRENE codes für Vorhersagen für Divertoren mit ähnlichen, stochastischen Magnetfeldstrukturen.

Abstract

Divertors with chaotic magnetic field structures are a field of major interest in todays fusion research not only for stellarators with their inherent complex magnetic field structures but also in tokamaks due to the application of resonant magnetic perturbations. This method is also used in the limiter tokamak TEXTOR for creating a helical divertor structure with a complex, three-dimensional (3D) magnetic field topology. The functionality of such divertors regarding control and efficient exhaust of particles and energy is still under investigation. Increasing the understanding in this respect has been the major motivation for this thesis. The accessibility of favourable divertor regimes with large temperature gradients between plasma core and divertor target, high neutral density in the divertor volume for efficient pumping and strong radiation for heat dissipation (high recycling regime) or additionally with reduced target particle and heat loads (detachment), is largely determined by the recycling of the hydrogen plasma at the divertor target. The aim of this thesis was therefore to investigate the hydrogen recycling at the target plates of the helical divertor in TEXTOR and by this the capability of this divertor configuration to access such favourable operational regimes.

In order to study the different divertor density regimes in TEXTOR, discharges were performed in which the total plasma density was increased continuously up to the density limit. The recycling was investigated in a fixed helical divertor structure where four helical strike points with a poloidal width of about $8 - 10\,\mathrm{cm}$ are created at the divertor target plates. The experimental investigation of the hydrogen recycling was carried out using mainly spectroscopic methods supplemented by Langmuir probe, interferometric and atomic beam measurements. In the framework of this thesis a spectroscopic multi camera system has been built that facilitates the simultaneous observation of four different spectral lines, recording images of the divertor target plates and the plasma volume close to the target. The system facilitates the simultaneous measurement of the poloidal and toroidal pattern of the recycling flux at the divertor target without the need for sweeping the plasma structure. The simultaneous observation of different spectral lines reduces the uncertainty in the analysis based on several lines, as the contribution from uncertainties in the reproducibility of plasma parameters in different discharges are eliminated and only the uncertainty of the measurement method limits the accuracy. The spatial resolution of the system in poloidal and toroidal direction ($0.8\,\mathrm{mm} \pm 0.01\,\mathrm{mm}$) is small compared to the separation of the helical strike points,

the capability of the measurement method to resolve these structures is therefore limited by the line-of-sight integration and the penetration depth of the light emitting species. The measurements showed that the recycling flux increases linearly with increasing plasma density, a high recycling regime is not observed. Its absence can be explained using an extended two point model including heat convection applied to the region dominated by parallel transport (laminar region). The radial penetration depth of the neutral hydrogen particles ($\lambda_n \approx 3 - 4\,\mathrm{cm}$) estimated from spectroscopic measurements was found to be often larger than the varying radial extent of this laminar region (few mm up to 6 cm) which finally leads to convective heat transport reducing parallel temperature gradients. Increasing the radial extent of the laminar region especially in front of the divertor strike points could lead to an improvement in this respect and provide access to a high recycling regime. The closing of the open divertor geometry of the helical divertor at LHD through the installation of baffles (which is currently under way) as well as the larger island size in the island divertor of the stellarator W7-X compared to its predecessor W7-AS is therefore expected to provide access to a high recycling regime there. The radiation instability developing at high plasma densities in the helical divertor in TEXTOR is preceded by a transient partial detachment of the plasma from the divertor target plates and leads to the formation of a poloidally structured and helically inclined radiating belt, a helical divertor MARFE. While typically leading to a density limit disruption, this MARFE has been stabilised using a feedback system and could provide some divertor functionality such as low target temperature, increased neutral density and increased radiation within the stochastic boundary. A detailed comparison of the experimental observations to results from modelling with the 3D numerical transport code EMC3-EIRENE showed agreement in the high density behaviour (in particular absence of a high recycling regime) as well as in the absolute values of the calculated and measured target particle fluxes. Simulations using two different cross-field transport coefficients showed, that this agreement is only found at a certain level of cross-field transport ($D_\perp = 1\,\mathrm{m^2 s^{-1}}$). The inclusion of carbon impurities in the simulations results in the experimentally observed reduction of the recycling flux. These findings support the use of the EMC3-EIRENE code for predictive modelling for other divertors with similar stochastic magnetic field structures.

Contents

1 Introduction

With a growing energy consumption in the world, shortage of energy resources and the climate change demanding electricity generation without greenhouse gas production, the need for alternative energy sources is ever increasing. Controlled thermonuclear fusion, would be capable of replacing present sources for the generation of base load electricity, adding an important part to the envisaged energy mix [Heinloth 2003].

The idea is based on the physical process providing the source of thermal energy in stars: the fusion of atomic nuclei which releases the difference in binding energy in form of kinetic energy. The most feasible process to exploit in a fusion reactor on earth is the fusion of the hydrogen isotopes deuterium and tritium, resulting in the production of an α particle (helium nucleus ${}^4_2\mathrm{He}$), a neutron and the release of 17.6 MeV of kinetic energy distributed amongst the fusion products according to their masses:

$$ {}^2_1\mathrm{D} + {}^3_1\mathrm{T} \rightarrow {}^4_2\mathrm{He}\ (3.5\,\mathrm{MeV}) + {}^1_0\mathrm{n}\ (14.1\,\mathrm{MeV}). $$

This D-T fusion process has the highest reaction rate at the lowest possible temperature compared to all other fusion processes possible, its maximum lies at temperatures of $10 - 30\,\mathrm{keV}$. At such temperatures hydrogen is fully ionized and therefore in the plasma state. Still, coulomb collisions between the charged plasma particles have much larger cross sections than the fusion process leading to particle and power losses. Hence, a good confinement of the hot plasma is necessary to built an efficient fusion reactor.

In a star the confinement of the fusion plasma is naturally given by its own gravitational force, whereas in the laboratory the confinement has to be created artificially by other means. The most promising technique today is the confinement by means of magnetic fields in toroidal devices. Here, in order to confine a thermonuclear plasma the electromagnetic properties of the plasma as an ionized gas are used. The free charged particles in the plasma are confined to a magnetic field by the Lorentz force restricting their movement perpendicular to the magnetic field. For creating a suitable magnetic field configuration, presently two different concepts are investigated: the *tokamak* [Smirnov 2010; Wesson 2004] and the *stellarator* [Spitzer 1958]. The major conceptual difference between these concepts is the method of generating the confining magnetic field: In a stellarator it is created only by external coils whereas in a tokamak part of the confining magnetic field is created by a current induced inside the plasma using a transformer. Both

concepts have certain advantages and disadvantages. A tokamak is a pulsed device as long as the plasma current can only effectively be driven by a transformer, whereas a stellarator is inherently capable of steady state operation. On the other hand the tokamak concept at the moment is technologically more advanced than the stellarator concept. The quality of the plasma confinement reached today in the largest stellarators measured by the size of the triple product $n \cdot T \cdot \tau_E$ is more than one order of magnitude less than in the most advanced tokamaks. The triple product quantifies the condition necessary to gain energy from nuclear fusion, which relies on confining the plasma at sufficiently high density n and temperature T for a sufficiently long time:

$$n \cdot T \cdot \tau_E > 5 \cdot 10^{21}\,\mathrm{m^{-3}\,s\,keV}$$

with the energy confinement time $\tau_E = W/P_H$ where W is the energy content of the plasma and P_H the supplied heating power. The most advanced tokamaks today have reached triple products of $n \cdot T \cdot \tau_E \sim 1.1 \cdot 10^{21}\,\mathrm{m^{-3}\,s\,keV}$ [prepared by C. Gormezano] and energy confinement times of up to $\tau_E \sim 1\,\mathrm{s}$ whereas stellarators have reached $n \cdot T \cdot \tau_E \sim 4.4 \cdot 10^{19}\,\mathrm{m^{-3}\,s\,keV}$ [Ohyabu et al. 2006]. The next step fusion device ITER will also be a tokamak [ITER Physics Basis Editors et al. 1999] and is planned to achieve $\tau_E \sim 4$ with a fusion energy gain factor of $Q = 10$ as the ratio of usable fusion power and supplied heating power.

For a steady state fusion plasma, in order to not only reach this power gain but also to keep the fusion plasma burning, the exhaust of the fusion product helium from the plasma has to be realised as well as an efficient re-fueling with deuterium and tritium [Reiter et al. 1991]. Otherwise a growing dilution of the hydrogen plasma and enhanced radiation losses will finally lead to an extinction of the fusion "flame". Efficient pumping of the helium is possible only by a certain level of plasma-wall contact, making erosion and migration of wall material unavoidable. The control of *particle* as well as *energy* exhaust from the plasma (with the α particles carrying a fifth of the fusion energy) is therefore closely linked to the control of the plasma-wall contact and therefore of the level of negative surface effects such as limited wall material lifetime, fuel retention, dust formation etc. on plasma exposed surfaces. In turn, the contact of the hydrogen plasma with the wall has an important impact on the particle and energy confinement through the production of impurities and the influence of released neutral fuel particles on energy and particle transport. Due to the sink action of material surfaces exposed to plasma, a so-called *recycling* process takes place with fuel ions from the plasma recombining at the wall and subsequently being released as neutral particles. The plasma constantly refuels itself through this process. The recycling has been found to largely influence the possibility of decoupling the plasma-wall interaction zone from the confined plasma and it is therefore a key aspect in the investigation of an exhaust concept for a fusion plasma.

Over the years different exhaust concepts for fusion devices have been developed, in general they can be divided into *limiter* and *divertor* configurations. The basic

principle of these concepts is the creation of a so-called *scrape-off layer* surrounding the confined plasma by creating an intersection of the outermost magnetic field lines with specially designed wall elements called *target plates*. The field lines intersecting a wall element are called *open* field lines in contrast to the closed field lines further inside the plasma. Particles diffusing into the scrape-off layer from the confined plasma quickly flow along the open field lines to the target plates which act as a sink for the plasma. Perpendicular to the magnetic field the particles diffuse with small velocities and the width of the scrape-off layer correspondingly is very small. Particles and energy are deposited on small areas on the target plates leading to high local heat and particle loads. Consequently one of the critical issues of an exhaust concept is the possibility of reducing these steady-state heat and particle loads on the target plates. For tokamaks, the poloidal divertor configuration is the most promising exhaust concept, its main advantages being an improved energy confinement in the so-called *H-mode regime* [Wagner et al. 1982] and improved pumping capabilities for neutral particles and thus a better control of particle exhausts. The limiter configuration poses the disadvantage of the plasma-wall interaction taking place in close vicinity to the confined plasma. Released impurities and recycled neutrals may directly enter the main plasma, the impurity screening and decoupling capabilities are small. In a poloidal divertor in a tokamak, the steady-state particle and heat loads on the target plates and the corresponding damaging effects can be reduced by operating the divertor at high densities [Pitcher and Stangeby 1997]. In the so-called *high recycling regime*, steep temperature gradients between confined plasma and the plasma-wall contact zone are established leading to a reduction of the physical sputtering and an increased radiation in the divertor thereby spreading the power on a larger area. A further increase in the divertor density enables even a detachment of the divertor plasma from the target plates with momentum losses due to ion-neutral friction leading to a reduction in the target ion flux. This regime is correspondingly called *detachment regime*. For the high heat fluxes expected in ITER, the radiation in the divertor has to be increased further by so-called *impurity seeding*, extrinsically introduced light impurities which help to spread the heat load and reduce peak fluxes. Possibilities of reducing the power entering the scrape-off layer by creating a thin radiating belt at the periphery of the confined plasma are also considered.

For optimising the properties of the existing exhaust concepts with respect to heat and particle flux dispersal and a reduction of the impurity content in the core plasma, an alternative concept is investigated, which is based on the concept of *ergodic divertors* [Engelhardt and Feneberg 1978; Feneberg and Wolf 1981]. In this divertor concept, external resonant magnetic perturbations are applied, leading to the formation of an open chaotic magnetic field system at the plasma edge. The basic idea is to enhance cross-field losses at the plasma boundary and hence the plasma exposed surface area. Resonant magnetic perturbations are applied in limiter as well as divertor tokamaks today, such as TEXTOR (with the *dynamic ergodic divertor*), DIII-D and JET and have previously been

studied extensively at Tore Supra [Ghendrih et al. 1996, 2002]. Depending on the level of determination of the plasma exposed area by the chaotic edge layer, the generated configuration is either referred to as an *ergodic divertor* or an *ergodised* poloidal divertor. The latter has shown to extend the field of application of chaotic magnetic edge layers by providing a promising tool for suppressing or mitigating instabilities called ELMs (Edge Localised Modes) [Evans et al. 2006; Liang et al. 2007], an unpleasant side effect of H-mode operation [Huysmans 2005]. Hence, the installation of additional coils for applying resonant magnetic perturbations in ITER is currently considered [Becoulet et al. 2008]. The investigation of chaotic magnetic edge layers is furthermore closely linked to the investigation of exhaust concepts in stellarators, as a chaotic magnetic edge layer is 'naturally' present in the plasma edge of a stellarator owing to the complex structure of the coils. In a tokamak, the resonant magnetic perturbations create a chaotic magnetic edge layer by destroying magnetic surfaces at the plasma edge, thereby breaking the toroidal and poloidal symmetry. Consequently, the plasma transport in such a system is a complex three-dimensional problem which is still not fully understood today and a matter of ongoing research. Uncertainty prevails especially regarding predictions about impurity screening, pumping capabilities and accessibility of the detachment regime in future devices such as Wendelstein7-X [Konig et al. 2004] and also ITER, should it be operated with an ergodised edge layer [Fenstermacher et al. 2007]. The complexity of the system demands for a detailed analysis of experimental observations supported by extensive numerical simulations using appropriate codes.

The functionality of a divertor, i.e. its capabilities regarding impurity screening, pumping and accessibility of the detachment regime is largely determined by the hydrogen recycling, i.e. the recycling of the fuel particles at the divertor target plates. The location of the re-ionisation of the recycled particles for example (which depends on the release process) influences the plasma flow in the scrape-off layer and thereby also the energy transport from the plasma core to the target. This thesis aims at increasing the understanding of recycling and transport of hydrogen in the presence of three-dimensional divertor structures. It addresses the questions if the studied helical divertor configuration in TEXTOR is capable of providing such favourable divertor operating regimes and what could be done to improve its capabilities. Therefore the behaviour of the recycling flux with rising plasma density up to the density limit is investigated experimentally using mainly spectroscopic methods supplemented by Langmuir probe, interferometric and atomic beam measurements. Possible explanations for the observed behaviour are discussed as well as implications for divertors with similar structures such as the island divertors in W7-AS and W7-X or the helical divertor in LHD.

In the divertor configuration studied in this thesis the plasma exposed surface area is determined by the open chaotic magnetic edge layer, the particle and heat fluxes are guided by the magnetic field forming a helical target pattern consisting of several strike points. This is the reason why this divertor configuration is referred

to as a *helical divertor*. The thesis investigates, if it is possible to observe the separate strike points using passive optical emission spectroscopy on hydrogen. This depends on the one hand on the resolution of the respective diagnostic system and on the other hand on the penetration depth of the observed light emitting species. For studying the visible radiation emitted by the hydrogen particles recycling at the graphite target plates and also radiation from weakly ionised carbon impurities, a spectroscopic multi camera system has been designed and built as part of this thesis. It records two dimensional images of the divertor target plates and the plasma volume close to the target. Consisting of four CCD cameras, the system facilitates the simultaneous observation of four different spectral lines for the same line-of-sight. A radiometric calibration of the system for the observation of the Balmer α, β and γ lines was carried out which enabled the determination of particle fluxes and their comparison to target ion flux measurements using a Langmuir probe as well as to calculations using the three-dimensional numerical transport code EMC3-EIRENE. Using this transport code, the same divertor configuration as investigated experimentally in this thesis was studied in [Frerichs 2010a]. The experimental observations are discussed in the framework of the modelling results published in [Frerichs 2010a] and from subsequent additional analysis [Frerichs 2010b] in order to assess if the model, the transport code is based on, includes the relevant physical processes to describe the high density operation in stochastic divertor structures.

The thesis is organised as follows:

Chapter 2 briefly outlines the general aspects of magnetic confinement of fusion plasmas in tokamaks and stellarators and introduces the concepts for particle and energy exhaust. A short introduction into the physics of plasma-wall interaction is given, introducing the processes important in the analysis of the experimental observations followed by a summary of the transport model the EMC3-EIRENE code is based on.

Chapter 3 introduces the experimental setup investigated, namely the tokamak TEXTOR, the coils for generating the resonant magnetic perturbations (the dynamic ergodic divertor, DED) and the helical divertor configuration studied.

Chapter 4 gives an overview of the diagnostic methods used to study the hydrogen recycling and transport at the target plates of the helical divertor.

Chapter 5 gives a detailed insight into the spectroscopic camera diagnostic built in the framework of this thesis, including a radiometric calibration of the diagnostic system, image mapping techniques and a discussion of the measurement uncertainties.

Chapter 6 presents the observations and interpretations of the hydrogen recycling and transport at low plasma core and edge densities.

Chapter 7 presents the observations and interpretations of the variation in the hydrogen recycling and transport for varying core and edge densities.

Chapter 8 constitutes a discussion of the observations and interpretations presented in chapter 6 and 7.

Chapter 9 summarises the thesis addressing the questions raised in the introduction.

2 Divertor concepts in fusion devices

Divertor concepts have proven to be the most promising candidate to provide a controlled interaction zone between plasma and wall components in magnetic confinement fusion devices. Achieving a limitation of a fusion plasma while maintaining a sufficient fusion triple product imposes certain requirements on the plasma boundary making this quite a challenging task: The plasma exposed surfaces have to be protected from overheating and material erosion, impurities created in the plasma surface interaction processes have to be kept from reaching the plasma core and effectively exhausted from the plasma together with the helium ash, preventing dilution and radiation cooling. At the same time some way of refuelling has to be realised and the core plasma has to be kept at fusion relevant conditions. While much experience and physical understanding has been gained in tokamak divertors with the so-called *poloidal divertor configuration*, the physical mechanisms governing divertor configurations in confinement devices with inherent three-dimensional structures like stellarators are much less understood.

In tokamaks such a three-dimensional divertor structure can also be realised by applying resonant magnetic perturbations using additional magnetic field coils. In the tokamak TEXTOR this is done using the *dynamic ergodic divertor* (DED). Earlier studies showed, that the perturbation field of the DED creates a helical divertor structure, i.e. that the plasma exposed surface area is completely determined by the helical pattern of the magnetic field structure [Schmitz 2006]. In this thesis the similarities and differences of the hydrogen recycling in this divertor configuration compared to other exhaust concepts are examined, in particular with respect to operation at different plasma densities. Hence, the presented work is connected and relevant to both confinement concepts.

In this chapter an introduction is therefore given into the magnetic field configuration of tokamaks and stellarators, including their advantages and disadvantages (section 2.1). In section 2.2, the different concepts of plasma edge control and their realisations in tokamak and stellarator devices are described followed by a summary of the physics of plasma surface interaction and edge transport in section 2.3 introducing the different divertor regimes *low recycling*, *high recycling* and *detachment*.

2.1 Magnetic confinement concepts

Both magnetic confinement concepts, the tokamak and the stellarator, are based on the confinement of the fusion plasma in a toroidal device. In such a device the magnetic field lines have to be helically twisted in order to prevent polarisation of the plasma by drifting particles and thus to provide confinement. The confining magnetic field therefore consists of two components: a toroidal magnetic field B_t and a poloidal field B_p. In tokamaks this required twist of the magnetic field lines is created by an induced net toroidal plasma current whereas in stellarators it is generated only by external coils.

The helical winding of a field line is described by the rotational transform ι or the safety factor q. Historically, when describing tokamaks the latter is used, whereas for stellarators the rotational transform is common. The safety factor q is defined by

$$q \equiv \frac{\Delta\phi}{2\pi}$$

where $\Delta\phi$ is the toroidal angle after which the field line has described one complete poloidal turn (2π). The rotational transform is the angle of rotation of the field line after one toroidal turn. It is related to the safety factor by $\iota = 2\pi/q$. If a field line joins up on itself after m toroidal and n poloidal rotations, it has the rational q value $q = m/n$. Most magnetic field lines do not close on themselves but map out an entire toroid, a so-called magnetic flux surface. Surfaces pertaining to different field lines form a set of nested surfaces around the torus axis (see figure 2.2). The safety factor is in general different from surface to surface: the configuration is said to possess magnetic shear.

2.1.1 Tokamak

The principal setup of a tokamak [Wesson 2004] is shown schematically in figure 2.1. Tokamaks are characterised by a strong toroidal magnetic field B_t which is created by toroidal field coils surrounding the torus shaped vacuum vessel. The required rotational transform of the magnetic field lines is generated by an additional poloidal field created by a large toroidal plasma current I_p. This current is primarily created inductively with the current through a coil around the core of the torus (primary winding) generating a magnetic flux change in a transformer yoke and the plasma acting as the secondary winding. The poloidal field does not have to be as large as the toroidal field and in a typical tokamak is considerably smaller, by a factor which scales with the aspect ratio (ratio of major to minor radius) of the device. Furthermore in a tokamak an external vertical field B_v has to be added to prevent the plasma as a whole from increasing its major radius.

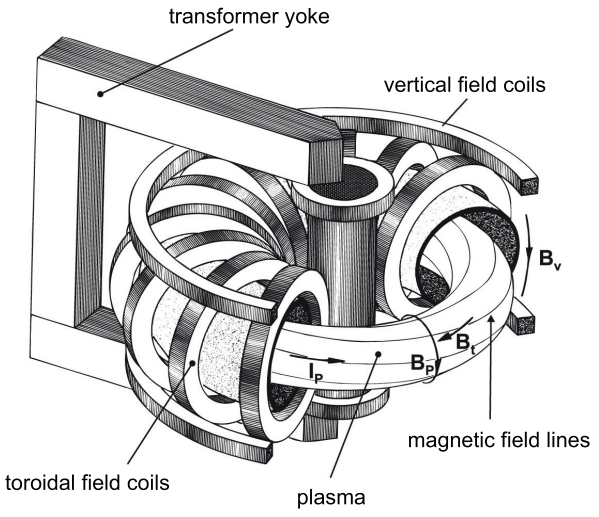

Figure 2.1
Principal setup of a tokamak demonstrated on the basis of a device with circular cross section such as TEXTOR.

An example of the magnetic flux surfaces created by the helically wound field lines can be seen in figure 2.2. On each flux surface the plasma pressure and the current density is constant. In a tokamak of circular cross section such as TEXTOR the magnetic flux surfaces are toroids, but other shapes are possible and even more advantageous like the D-like shape on the tokamak JET and the future tokamak ITER. The inboard side of the tokamak, close to the vertical axis, where the toroidal field is the highest, is commonly called the *high field side* (HFS), the outboard side is correspondingly called the *low field side* (LFS).

In a tokamak the field lines can always be separated into *open* field lines intersecting material surfaces such as the vessel wall or some other limiting object (see section 2.2) and *closed* field lines not intersecting a material surface. The flux surface spanned by the outermost closed field line (with respect to the plasma centre) is called the *last closed flux surface* (LCFS). For a tokamak of circular cross section such as TEXTOR the large plasma radius R is therefore defined as the distance between the vertical axis at the centre of the torus and the centre of the LCFS and the small plasma radius $r = a$ as the radius of the LFCS. The centres of the flux surfaces in a tokamak are shifted with respect to the centre of the last closed flux surface, the shift $\Delta(r)$ (so-called Shafranov shift) varying from surface to surface.

The helical winding of a field line on a magnetic flux surface described by the safety factor q has a large impact on the stability of the plasma. To avoid the formation of instabilities such as kink instabilities for example [Wesson 1978] the safety factor at the plasma edge should be larger than two. For a tokamak of large

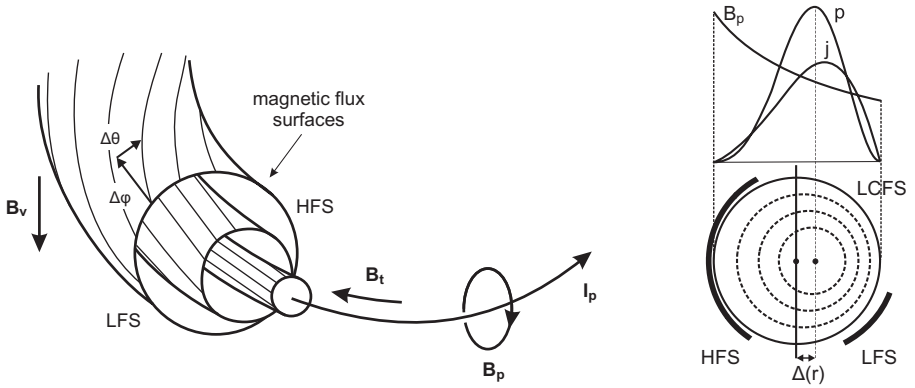

(a) Magnetic flux surfaces in a tokamak. **(b)** Shafranov shift.

Figure 2.2 Magnetic equilibrium in a tokamak of circular cross section: Magnetic flux surfaces and their shift $\Delta(r)$ versus the centre of the last closed flux surface (Shafranov shift).

aspect ratio the radial dependence of q can be described as

$$q(r) = \frac{2\pi r^2 B_\mathrm{t}}{\mu_0 I(r) R} \quad ,$$

with the radial current profile $I(r)$. At the edge of the plasma we have $r = a$ and $I(a) = I_\mathrm{p}$ is the complete plasma current. For a given toroidal magnetic field B_t therefore the plasma current I_p determines the q profile and the size of the safety factor at the plasma edge.

As long as ignition is not reached in a fusion machine, the plasma has to be heated by means other than the heating by alpha particles. In addition to contributing to the plasma confinement and stability, the plasma current heats the plasma by ohmic dissipation. This type of heating is efficient up to plasma temperatures of the order of 1 keV. At higher temperatures the plasma resistivity quickly drops and the efficacy of this heating method decreases. Moreover, the current density is limited by magnetohydrodynamic stability requirements. On many devices, auxiliary, external heating is applied, such as neutral beam injection (NBI) [Koch 2008a] and the injection of electromagnetic radiation like Electron Cyclotron Resonance Heating (ECRH) [Westerhof 2008], Lower Hybrid Heating (LHH) and Ion Cyclotron Resonance Heating (ICRH) [Koch 2008b].

The important advantage of the tokamak is the inherent stability provided by both the strong toroidal field and the large plasma current. One of the major drawbacks of the tokamak scheme might be the pulsed nature of the induced plasma current which implies a non stationary operation. Nevertheless, in view of continuous

reactor operation, methods are being studied to sustain plasma current via other means such as injected radiofrequency waves or the so-called bootstrap current [Faulconer 2008; Murakami et al. 2006; Voitsekhovitch et al. 2009].

2.1.2 Stellarator

There exists a multitude of possibilities of using external coils to generate a toroidal, helical magnetic field [Hartmann 2008]. In this thesis the term "stellarator" is used in a generic sense for helical confinement systems without a net toroidal plasma current encompassing classical and advanced stellarators, torsatrons (or heliotrons) and heliacs. Generally this confinement scheme has two advantages: in principle steady-state plasma operation is possible and it does not have to brace itself against disruptions of a toroidal plasma current. On the other hand, the abandonment of the toroidal plasma current requires some of the external coils to helically revolve around the plasma and means giving up toroidal symmetry. Plasma and magnetic field coils in stellarators have a complex three-dimensional structure (see fig. 2.3). Due to this complexity, stellarator devices are still one generation behind, achieving energy confinement times and ion temperatures one order of magnitude smaller and electron temperatures a factor of two smaller compared to those achieved in high performance tokamak devices.

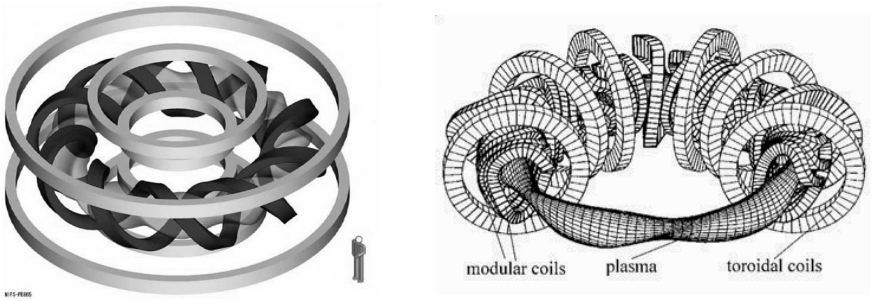

(a) Large helical device (LHD) [Iiyoshi et al. 1999]

(b) Wendelstein 7-AS (W7-AS) [Hirsch et al. 2008]

Figure 2.3 Two examples of stellarator coil configurations.

Stellarators can be divided into two groups: In the first group the magnetic field is generated by an assembly of field coils of simple geometric forms, e.g. planar or helical. These devices require at least one coil to encircle the torus toroidally. Examples of such devices are the classical stellarator Wendelstein 7-A [Grieger et al. 1985; Hirsch et al. 2008], the torsatron/heliotron LHD (see fig. 2.3(a)) and the heliac TJ-II [Alejaldre et al. 1990]. The second group are devices where

the magnetic field is generated by modular field coils of complicated geometric shape that encircle the torus only poloidally. The first stellarator that used such a modular coil system was Wendelstein 7-AS (see fig. 2.3(b)) whose additional planar toroidal coils were only used to increase the experimental variability. The successor of W7-AS is the stellarator Wendelstein 7-X (W7-X) which is currently under construction in Greifswald, Germany [Renner et al. 2002].

An example of the complex three-dimensional structure of the magnetic field in a stellarator is shown in fig. 2.4. Three different regions can be identified here: An inner region where the field lines form closed nested flux surfaces. This region can be perturbed by magnetic islands that are caused by magnetic field errors. It is surrounded by a second region of additional islands that are caused by the toroidicity of the field and which are referred to as "natural islands". Outside of the islands the field lines become stochastic with short connection lengths to the torus walls. Even though the flux surfaces have a complicated three-dimensional structure fast equilibrium processes along the field lines assure that they are also surfaces of constant plasma pressure. Typically the radial variation of the rotational transform, expressed by the magnetic shear $S = \mathrm{d}\iota/\mathrm{d}r$, behaves differently in tokamaks and stellarators: they have opposite sign. The different stellarator types also have different shear, W7-AS is an example of a device with low shear whereas LHD (as all torsatrons/heliotrons) is an experiment with strong shear.

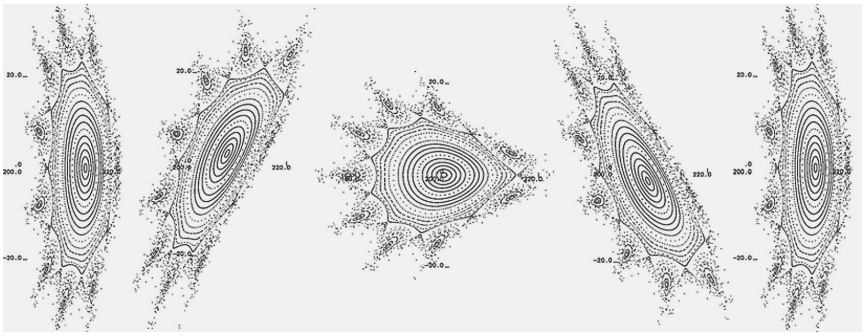

Figure 2.4 Five poloidal cross sections of the vacuum magnetic field configuration in W7-AS. One of the five magnetic field periods is shown. The edge is bounded by large magnetic islands, which are utilised for the island divertor [Grigull et al. 2001].

2.2 Plasma edge control

In this section the different concepts are introduced which are used in tokamak and stellarator devices to control the interaction of the plasma with the wall and

by that the exhaust of power and particles from the plasma. The crucial tasks of these concepts can be divided into three main areas [Pitcher and Stangeby 1997]:

Target lifetime: the wide dispersal of plasma power exhausted from the main plasma and the reduction of target sputtering

Pumping and density control: the production of sufficiently high gas pressures in the vicinity of pump ducts to enable the removal of fuel and helium ash

Impurity content: the reduction of impurity production and screening of impurities (intrinsic and extrinsic) from the plasma core

All this has to be realised while maintaining a good core confinement, a sufficiently high plasma core density and temperature. The different capabilities of the exhaust concepts regarding these tasks will be summarised.

In section 2.2.1 the *limiter configuration* is introduced which is the most simple plasma edge control concept. It is commonly used in tokamaks as well as stellarator devices especially also during the start-up phase in divertor machines. A limiter configuration in TEXTOR, described in more detail in chapter 3, serves as a reference configuration for the investigations of the hydrogen recycling in the helical divertor configuration in TEXTOR based on the concept of *ergodic divertors*. Thus, the general concept of ergodic divertors is shortly described in section 2.2.3 while a more detailed description of the configuration discussed in this thesis follows in chapter 3. The behaviour of the hydrogen recycling in TEXTOR is also compared to the current knowledge about the hydrogen recycling in *poloidal divertor configurations*, which are specific to the tokamak concept and are installed e.g. in the tokamaks JET, ASDEX Upgrade and DIII-D, and in *island and helical divertor configurations* used in the stellarators W7-AS and LHD. These concepts are therefore introduced in section 2.2.2 and 2.2.4, respectively.

2.2.1 Limiter

In this configuration a limiting object is mounted in the plasma chamber which intersects the closed magnetic flux surfaces (see fig. 2.5(a)) and thereby defines the last closed flux surface (dashed line). It separates the plasma volume into two regions: an inner, confined region with closed magnetic flux surfaces (dark grey area) and the scrape-off layer (SOL, light grey area) with short open field lines ending on the limiter surface. The transport of particles and heat in these two regions is fundamentally different: From the plasma core only cross-field transport carries particles and heat across the LCFS into the SOL. Inside the SOL parallel transport along the open field lines dominates and quickly guides particles and heat onto the limiting surfaces. This way, the plasma-surface interaction is concentrated on relatively small surfaces which need to be able to resist very localised, intense

thermal fluxes. The sputtering of the surface material by impinging plasma particles furthermore causes pollution of the plasma by the plasma facing material. This has lead to the choice of a light element such as carbon in many devices as it is able to withstand high heat loads and does not melt. The typical distance parallel to the magnetic field that a particle has to travel from the stagnation point to the limiter surface is $L_c/2 \approx \pi\, R\, q$. To avoid too large power flux densities on the limiter the plasma wetted area should be as large as possible, this can be guaranteed by appropriate shaping of the limiter. Often toroidal limiters are used which run around the circumference of the torus. Effective pumping meeting the requirements regarding helium ash removal for a fusion reactor can be achieved in limiter configurations by using so-called pump limiters. They also allow for a better control of the plasma density.

Due to the geometry in limiter configurations, released impurities and recycled neutrals (recombined ions and electrons at the wall) may directly enter the main plasma and the impurity screening capabilities of the limiter configuration are small. It is therefore advantageous to remove the plasma-wall interaction zone as far as possible from the confined volume which is the basic idea of the divertor configuration [Spitzer 1958].

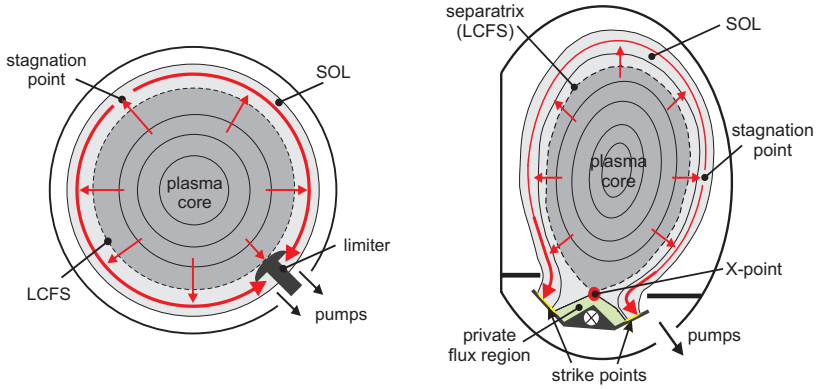

(a) Limiter configuration **(b)** Divertor configuration

Figure 2.5 Schematic view of a poloidal cross section of a tokamak demonstrating limiter and poloidal divertor configuration.

2.2.2 Poloidal divertor

A divertor configuration in a tokamak is produced by placing additional coils inside the vacuum vessel in order to divert the outermost magnetic field lines out of the main plasma chamber into a separate chamber where they intersect a material

divertor target (see fig. 2.5(b)). A poloidal divertor is formed by toroidal coils carrying current in the same direction as the plasma current to form a null in the net poloidal magnetic field (the *X-point*). The magnetic field lines passing through the X-point create the last closed flux surface known as the *separatrix* (dashed line). All field lines interior to the separatrix remain within the confinement volume and particles on them are confined. Particles that cross the separatrix however are swept along the field lines in the SOL to the divertor target plates. The area at the target plates struck by these particles is called the *divertor strike point* and the area below the X-point between the so-called inner and outer divertor leg is called the *private flux region*. This region has no common border with the core plasma and is shielded from it by the adjacent SOL plasma which quickly drags away any particle flowing from the core towards the private flux region. Mainly neutral particles which come from the divertor target plates and are not bound to the magnetic field populate this area, the plasma density is low. Depending on the fraction of neutrals which has the possibility of penetrating into the central plasma, the geometry of the poloidal divertor can be more or less open or closed, when the neutrals are stopped by mechanical baffles near the X-point.

The plasma wetted area in poloidal divertors is relatively small, which results in high localised particle and heat fluxes. The radial width of the scrape-off layer is approximately proportional to the square root of half of the target-to-target connection length of the magnetic field lines in the divertor SOL: $\lambda_{\mathrm{SOL}} \sim \sqrt{L_{\mathrm{c}}/2}$. For divertors with rather short divertor legs, the target-to-target connection length is $L_{\mathrm{c}} \approx 2\pi\, R\, q$, the same as in the limiter configuration. JET for example has $L_{\mathrm{c}} \approx 80\,\mathrm{m}$ and a scrape-off layer width of a few centimeter. The parallel power fluxes flowing in the SOL for present experiments (at highest power levvels) are approximately $300\,\mathrm{MW\,m^{-2}}$ and are expected to be $2000\,\mathrm{MW\,m^{-2}}$ in ITER. This power must be dispersed to the point that fluxes hitting surfaces are brought down to acceptable levels, i.e. preferably less than $10\,\mathrm{MW\,m^{-2}}$.

The poloidal divertor configuration has shown to be capable of handling the tasks set, though at the moment it is not clear if or how all four of these tasks can be accomplished simultaneously [Pitcher and Stangeby 1997]. Furthermore there are still numerous uncertainties in the extrapolation of experimental results from todays devices to the next step device ITER. The advantages of the poloidal divertor configuration over the limiter configuration are mainly an improved energy confinement and the creation of high neutral densities in the divertor region for better pumping. The *H-mode* (high confinement mode) [Wagner et al. 1982; Keilhacker 1987; Groebner 1993], with energy confinement times about two times higher than those obtained in the standard regime termed L-mode from 'low' confinement. The H-mode is triggered by a certain threshold of the heating power and can also be obtained on limiter tokamaks, but the threshold is much higher for the limiter than for the divertor configuration. This difference in the heating power threshold is strongly related to the behaviour of recycling neutrals and their influence on the balance between convective and conductive contributions

to the heat losses at the edge. Strong convective heat losses at the plasma edge prohibit the L-H transition [Kalupin et al. 2006]. On the other hand, the H-mode operation also brings with it a disadvantage: the so-called *Edge Localised Modes* (ELMs) [Huysmans 2005], instabilities, which periodically deposit a large fraction of the heat and particle content of the plasma on the wall. In ITER this could lead to a significant reduction of the wall lifetime [Federici et al. 2003]. A possible solution to this problem is the creation of an ergodised edge layer by resonant magnetic perturbation which has shown to be capable of suppressing ELMs in the DIII-D tokamak [Evans et al. 2004, 2006] or mitigating them in JET [Liang et al. 2007] and DIII-D without degrading the improved core confinement. These findings have led to the discussion about the installation of additional coils for the application of resonant magnetic perturbations in ITER [Becoulet et al. 2008; Schaffer et al. 2008].

The divertor configuration allows the access to steep temperature gradients between the confined plasma and the plasma-wall contact zone [Pitcher and Stangeby 1997]. At high core and divertor densities ($n_e = 10^{19} - 10^{20}\,m^{-3}$), the plasma in the divertor volume exhibits low temperatures (down to 5 eV) and becomes sufficiently opaque for recycling neutrals. This *high recycling regime* leads to an improved impurity screening, increased radiation in the divertor volume and a reduction of the physical sputtering. The ultimate stage of this evolution is the *detachment regime*, during which ion-neutral friction processes become sufficiently effective to introduce a momentum and power loss and extinguish the thermal flux to the divertor plates when the plasma temperature in the divertor drops below $\sim 5\,eV$ [Loarte et al. 1998]. The ion flux to the divertor target plates then decreases by a factor of three to $\Gamma_{D^+} \approx 10^{22}\,m^{-2}\,s^{-1}$ [Brezinsek et al. 2009] compared to the high recycling regime. The radiation level in the divertor can be enhanced further by intentionally introducing impurities into the divertor volume.

2.2.3 Ergodic divertor

The ergodic divertor poses an alternative technique for the control of particle and energy exhaust from a tokamak fusion plasma [Engelhardt and Feneberg 1978; Feneberg and Wolf 1981]. It involves the application of resonant magnetic perturbations leading to a stochastisation of the magnetic field at the plasma edge and consequently to three-dimensional magnetic field structures without simple poloidal or toroidal symmetries. The creation of such open chaotic edge layers is also used to supplement other configurations for optimising their properties with respect to heat and particle flux dispersal and a reduction of the impurity content in the plasma. Theoretical as well as experimental aspects of the ergodic divertor concept have been described in detail in literature [Ghendrih et al. 1996; Finken et al. 2005], therefore only a short summary shall be given here. The influence of this stochastisation on the hydrogen recycling and thus on the high

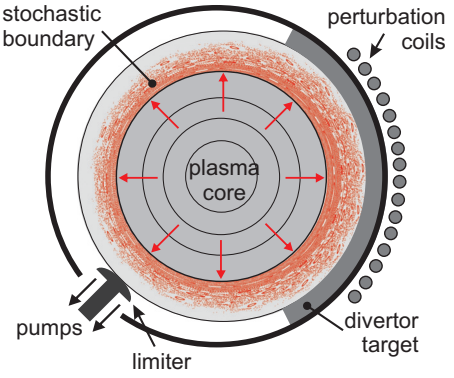

Figure 2.6
An example of a stochastic boundary in the tokamak TEXTOR showing the geometric setup superimposed by a magnetic field line plot (Poincaré plot, see section 3.3.2).

density divertor operation in such structures, though, is still the subject of ongoing research [Fenstermacher et al. 2007] and the increase of its understanding is one of the major goals of this thesis.

The principal concept of ergodic divertors is to achieve the transition between the confined plasma and the wall in a layer where the flux lines have been ergodised (see figure 2.6), i.e. where the field lines are not longer restricted to a single flux surface but can completely fill a certain radially extending volume. The layer is produced due to the superposition of the magnetic field from external coils and the closed magnetic flux surfaces of the equilibrium field of the tokamak. The magnetic perturbations are resonant to the helicity of particular flux surfaces with rational safety factor $q = m/n$. As q varies with the minor radius in a tokamak the resonances can be selected to be strongest at the plasma boundary and decay rapidly towards the plasma core aiming at avoiding the deterioration of the confinement in the core. On these so-called *rational flux surfaces* magnetic island chains are formed. When the islands on adjacent rational flux surfaces start to overlap, the magnetic surfaces are destroyed and the field lines explore a volume which also extends in the radial direction. The statistical properties of the resulting radial random walk of the perturbed field lines can be described by a radial diffusion coefficient of the field lines. This diffusive radial transport ends with the field line connecting to the wall. As a consequence, no well defined separatrix exists anymore between the magnetic field lines touching the wall and the closed field lines further inside the plasma.

A characteristic parameter to measure the stochasticity is the Chirikov-parameter σ_{Chir} which relates the distance between two neighbouring resonant magnetic surfaces to the respective island widths [Chirikov 1960; Ghendrih et al. 1992]. The necessary condition for island overlap is $\sigma_{\mathrm{Chir}} > 1$ which is therefore also a condition for stochasticity. Ergodicity of field lines is only given when the field lines have the possibility to sufficiently diverge from each other. The correlation of neighbouring field lines, i.e. the length that characterises this divergence, is

quantified by the Kolmogorov length L_{K}. It is a statistical measure of the e-folding length of the separation of neighbouring trajectories and can be determined either numerically [Finken et al. 2005] or approximated by using an analytical formula derived from quasi-linear theory [Ghendrih et al. 1992]

$$L_{\mathrm{K}} = \pi\, q\, R_0 \left(\frac{\pi\sigma_{\mathrm{Chir}}}{2}\right)^{-4/3}$$

This analytical estimation however tends to deviate considerably from the numerically derived correlation length which is probably due to the fact that the quasi-linear theory is valid only for highly developed stochastic layers.

The chaotic magnetic edge layer or stochastic boundary is often separated into different regions in order to e.g. discriminate different transport domains, apply simplified 0D or 1D models and gain an understanding of the influence of the stochastisation on the energy and particle exhaust. Some of these definitions used in literature are ambiguous as was already pointed out in [Runov et al. 2001; Kobayashi et al. 2004] and can easily lead to confusion. This confusion partly stems from the fact, that the magnetic field topology of stochastic edge layers deviates strongly from the topology in limiter and poloidal divertor configurations. In these configurations only two different 'regions' are known which can be discriminated by the dominant transport process leading to transport of particles to the wall as well as by the type of the field lines mapping out these regions: open field lines in the scrape-off layer (and in the private flux region) and closed field lines in the confined region. The open field lines in the scrape-off layer have a well defined target-to-target connection length of exactly one poloidal turn (plus the length of the two divertor legs). In chaotic magnetic edge layers a zoo of open field lines exists with target-to-target connection length of less than one poloidal turn (private flux region) up to more than ten poloidal turns (infinity?). In such a system two different kinds of transport regimes can be identified [Ghendrih et al. 2002]:

An **ergodic regime** with decorrelation of trajectories and thus diffusive like transport, i.e. a random walk process with a balance between parallel and transverse transport.

A **laminar regime** where exponential separation of neighbouring trajectories prevails and where transport is mainly parallel, i.e. 'scrape-off layer like'.

Thus, when following a field line, one experiences first a region of laminar transport before going into the ergodic transport. The corresponding regions of laminar or diffusive transport have correspondingly been termed *laminar* and *ergodic region* with the terminology of the laminar region narrowed down to the region extending from the plasma facing components into the plasma. These two regions surround the region of unperturbed, closed flux surfaces. Accordingly, the two transport regimes cannot be attributed to specific regions of field lines corresponding to their target-to-target connection length L_{c}. The important parameter is the

characteristic parallel scale length for laminar transport of energy and particles L_{transp} which is closely related to the correlation lengths of the field lines given by the Kolmogorov length. To decide, whether a point in the stochastic boundary belongs to the ergodic or laminar region, its shortest distance from the target along the magnetic field line $L_{\mathrm{c,short}}$ (so-called *shortest connection length*) has to be determined and compared to L_{transp}. The field lines in the laminar region show a different excursion towards the confined plasma with the penetration depth correlated to the target-to-target connection length L_{c} of the field line. Correspondingly, the laminar region is further split up into those field lines with $L_{\mathrm{c}} \leq L_{\mathrm{K}}$ (which were found to be starved of power) and those with $L_{\mathrm{c}} > L_{\mathrm{K}}$ which connect the region of power efflux to the wall.

Previous extensive investigations of stochastic boundary structures in Tore Supra [Ghendrih et al. 2002] and TEXT [McCool et al. 1990] have shown, that the control of particles and energy removal is possible using stochastic edge layers. For the ergodic divertor in Tore Supra the same density regimes were found in ohmically heated discharges [Meslin et al. 1999], which are also reported for poloidal divertors (see section 2.3.2). The linear regime is found at very low density, followed by the high-recycling regime until the particle flux rollover in the detached regime when the edge temperature drops below 10 eV. MARFE (multifacetted asymmetric radiation from the edge) behaviour, namely toroidally symmetric radiation instability were not observed. At the plasma exposed surfaces a redistribution of the particle and heat flux was observed, the resulting strike points were correlated to the magnetic topology created. In the ergodic zone the radial pressure gradient induces a flux of particles along the field lines corresponding to an outward radial particle flux due to the radial field line diffusion. This results in flat temperature profiles which were measured in the ergodic zone. In the laminar zone the interaction with the wall is particularly intense and it is to some degree equivalent to the scrape-off layer in a conventional divertor tokamak. The plasma structure in the laminar zone strongly depends on the relation between radial penetration depth of the field lines and the parallel scale lengths of heat and particle transport which also determines the heat and particle fluxes at the target plates [Ghendrih et al. 1996; Nguyen et al. 1997].

A more detailed description of the ergodic divertor setup at TEXTOR, an overview of previous results regarding particle recycling and transport with the ergodic divertor at TEXTOR and a description of the helical divertor configuration studied in this thesis is given in chapter 3.

2.2.4 Island and helical divertor

Generally, divertor configurations in stellarators follow the same principle as the poloidal divertor in a tokamak (section 2.2.2): the magnetic field lines outside the

last closed flux surface are diverted to target plates. Depending on the type of stellarator, this is realised in different ways [Konig et al. 2002]:

- In moderate to high-shear heliotrons like LHD one can make use of intrinsic helical diverting field lines to create a *helical divertor* (HD). By employing additional field perturbation coils this machine benefits also from the flexibility to create externally imposed n/m = 1/1 islands, which allow the installation of a so-called *local island divertor* (LID).
- In low to moderate-shear advanced stellarators like W7-AS and W7-X one makes use of the intrinsic natural islands in 'high ι' configurations to create an *island divertor*. Additional resonant perturbations created by control coils are often applied to modify the island geometry, thereby giving control over key parameters for the creation of an effective divertor plasma, like island size, connection lengths and X-point height above the target.

In the following the magnetic field structure and geometry of these divertor configurations will be described in more detail, taking the examples of the helical divertor in LHD and the island divertor in W7-AS.

The Helical Divertor in LHD

In toroidal helical systems the edge magnetic structure is more complicated than the scrape off layer in (axisymmetric) poloidal divertor tokamaks. The edge magnetic structure in LHD is illustrated in figure 2.7(a), its features show many similarities to the magnetic structure in ergodic divertors. There is no clear separatrix and two types of open field line layers exist between the LCFS and the residual X-points due to the toroidicity [Masuzaki et al. 2002]:

Stochastic layer created by the overlap of the natural island layers in the peripheral region of the core. It is about 10 cm thick and the connection lengths of magnetic field lines in this layer (several km $\approx$ 100 toroidal circulations) are much longer than that in the SOL in an axisymmetric divertor in tokamaks.

Edge surface layers a structure of multiple layers with field lines of long connection length (several hundred meters). They are generated due to the radial movement of the X-point and the high local rotational transform and shear. The field lines in the region surrounded by these edge surface layers (labelled A in figure 2.7) are connected to the divertor plates with relatively short connection lengths but do not connect to the stochastic layer. The field lines in the edge surface layers finally reach the divertor plates through the residual X-point. The connection lengths of field lines from the residual X-point to the divertor plates are very short (several metres, $\sim$ 2 m on average). The field direction is almost in the poloidal direction.

The helical divertor in LHD consists of four divertor legs which rotate helically around the torus. The traces of these legs are covered by water-cooled isotropic graphite tiles. There are no baffles installed to keep recycled neutrals from leaving the divertor region, the setup is currently an open divertor configuration. The divertor traces (calculated using magnetic field line tracing) and the particle deposition profiles (measured by Langmuir probes) at the divertor plates show a strong non-uniformity also in the helical direction [Masuzaki et al. 2002].

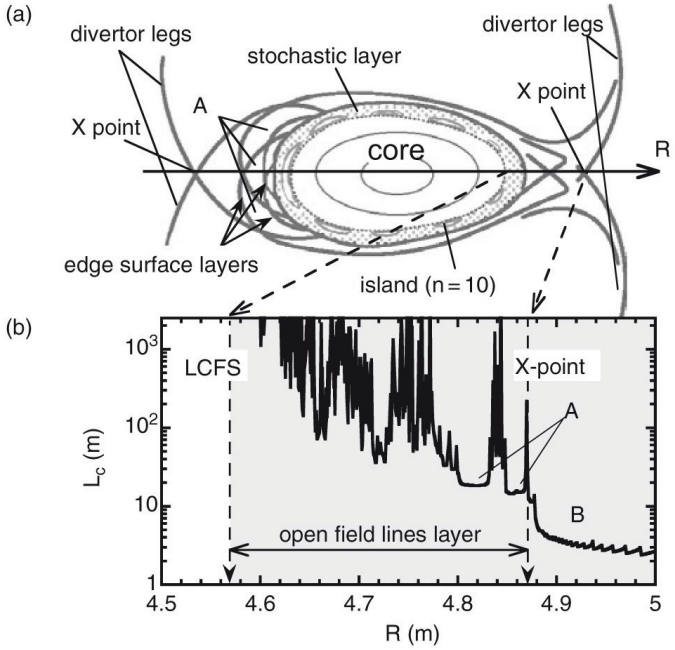

Figure 2.7 (a) Scheme of the LHD magnetic configuration (in the horizontally elongated cross-section). (b) Profile of the connection lengths of the magnetic field lines ($R_{ax} = 3.75\,\mathrm{m}$). The LCFS was defined as the flux surface which was kept after 40 toroidal circulations ($\sim 1\,\mathrm{km}$) of field line tracing. Taken from [Masuzaki et al. 2002].

In recent years extensive investigations were undertaken at LHD regarding the functionality of this helical divertor structure [Miyazawa et al. 2006a; Feng et al. 2009]. Experimental results showed no evidence of high recycling, i.e. particle flux enhancement, with increasing plasma density which can be explained by viscous transport between counter streaming flow channels in neighbouring island chains. They cause significant momentum losses and thereby break the pressure conservation along the flux tubes. Both, simulations and experiments show a linear increase in the divertor flux with increasing plasma density up to a rollover point

just before the onset of detachment. Different kinds of detachment phenomena, transient and stable, have been observed, characterised by a more or less strong decrease in the target ion flux and strongly increased radiation. In case of the so-called *serpens mode* [Miyazawa et al. 2006b] a rotating radiation belt can be detected inside the LCFS in conjunction with a shrinking of the confinement region and a strong reduction in the energy content. The strong reduction in the recycling flux is also attributed to the momentum loss from counter streaming flows, enhanced by the observed inward shift of the ionisation front [Feng et al. 2008]. Furthermore, strongly reduced core radiation at high densities were observed supporting the prediction by simulations of reduced impurity release and efficient impurity screening at high densities in the scrape-off layer [Feng et al. 2009].

The Island Divertor in W7-AS

In the standard W7-AS island divertor configuration nine macroscopic magnetic islands are formed at the edge and are opened by intersecting target plates (see figure 2.8(b)). The islands originate from the non-axisymmetry of the configuration and are formed when sideband Fourier harmonics of the radial magnetic field spectrum are resonant with local values of the rotational transform [Sardei et al. 1997]. The open field lines inside the islands guide the power and particles entering the islands across the inner separatrix towards the targets located at the rear of the islands. The islands form an intermediate SOL between the confinement core and the plasma-surface interaction region, preventing the core plasma from a direct exposure to the recycling neutrals and the sputtered impurities. Hence, the radial position, the radial width and the internal field line pitch of the islands (determining the connection lengths L_c between the upstream stagnation plane and the target) have a crucial impact on the divertor performance. The larger connection lengths ($L_c \sim 100\,\mathrm{m}$ in W7-AS) and shorter target-to-core distances ($\sim 4\,\mathrm{cm}$) of the island divertor enhance the perpendicular-to-parallel transport ratio compared to the poloidal divertor in tokamaks.

The divertor consists of ten identical modules, two per field period, placed at the top and bottom of the elliptical cross sections (see figure 2.8(b)) where the islands experience the largest radial extent. Each module is composed of an inertially cooled target made of CFC and baffles made of graphite to prevent the recycling neutrals from escaping from the divertor region towards the midplane. The baffling though is weak and the configuration is therefore called an open island divertor. The targets are shaped in order to achieve nearly homogeneous thermal load distributions in the helical direction. Each target plate toroidally extends over 18° and poloidally cuts two islands in order to increase the deposition area.

The island divertor in W7-AS significantly improves the plasma density control and gave the discovery of a new confinement regime, the *high density H-mode* (HDH-mode) [McCormick et al. 2002], which is characterised by high density, good

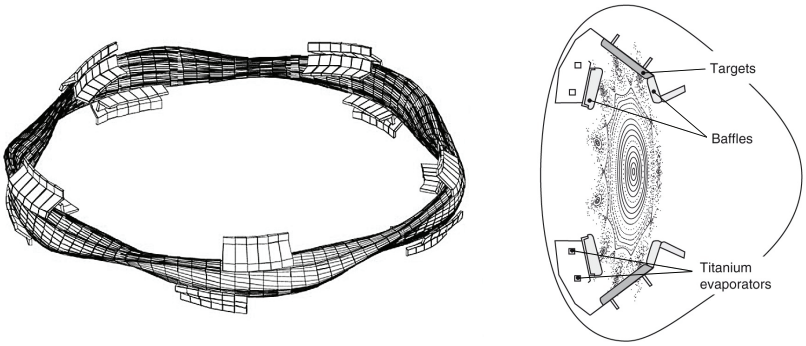

(a) [Feng et al. 2006] **(b)** [Grigull et al. 2001]

Figure 2.8 Standard W7-AS island divertor configuration: nine islands are formed at the edge. Ten up/down symmetric divertor plates and baffles are installed on the elliptical cross sections where the islands have the largest radial size.

energy and low impurity confinement. It has been demonstrated experimentally that more than 90 % of the SOL power can be removed by impurity line radiation and the radiation layer can be stabilised outside the confinement region without a remarkable degradation of the global energy confinement. Detachment is achieved by increasing the density beyond the density threshold for the HDH-mode. No evidence of a particle flux enhancement (high recycling) could be observed which was reproduced by three-dimensional modelling with the EMC3-EIRENE code. Like for the helical divertor in LHD, the reason for the absence of a high recycling regime is the friction of counter streaming plasma flows on neighbouring island fans [Feng et al. 2009]. For a further increase of the density the plasma evolves from a stable partial detachment to a deeply detached state followed by the formation of a toroidal belt of strong radiation from recombining hydrogen which was identified as a MARFE [Miyazawa et al. 2006a].

2.3 Plasma surface interaction and plasma edge transport

The functionality of the edge control concepts described in the previous section is largely dominated by the interaction of the plasma with the material surfaces of the limiter or divertor as well as by the transport processes at the plasma edge. Moreover, also global confinement properties can be affected by edge processes. An important part of the edge plasma in limiter as well as divertor configurations

is the scrape-off layer, the region where parallel transport along the magnetic field lines dominates the transport to the wall elements. This section gives an overview on the physics of plasma surface interaction in a fusion device, particle transport and physical processes in the scrape-off layer and the different operational regimes of scrape-off layers known today.

2.3.1 Hydrogen recycling

The plasma in a tokamak or stellarator represents an open system with the wall being a perfect plasma sink. The confinement times of particles and energy τ_P and τ_E are finite and therefore the plasma has to be renewed continuously. The energy content is sustained by heating while the number of particles in the plasma is sustained by a permanent flow of hydrogen gas from the wall elements (hydrogen being a synonym here for all the hydrogen isotopes present in a fusion plasma): When charged plasma particles strike a solid surface they stick to it long enough to recombine forming neutral atoms or molecules. Then they are released from the surface by different mechanisms back into the plasma where they are dissociated and/or ionised again. In a hydrogen fusion plasma this cycle of the fuel particles is called *hydrogen recycling* and has a very short timescale compared to the duration of a plasma discharge.

Initially the solid surface also acts as a mass sink, all but the promptly back-scattered hydrogen particles are retained in or on the solid. Such retention saturates at some level and thereafter a steady-state situation results. Then the rate at which hydrogen particles are lost to the surface is the same as the rate of re-emission of neutrals and the plasma refuels itself. Theoretically, in this case no external sources of hydrogen particles are needed and the plasma density stays constant. In reality, particles lost from the system by active pumping at the limiter or divertor and by implantation into lower lying layers of the solid wall have to be replaced via external sources. In a fusion power plant fuel has to be replenished as well at the rate that it is lost in the fusion processes.
The ratio of the particle loss rate and the reemission rate of neutral particles is equivalent to the ratio of the two corresponding particle flux densities Γ_{H^+} and Γ_{tot}. It is defined as the recycling coefficient $R = \Gamma_{\mathrm{tot}}/\Gamma_{\mathrm{H}^+}$ which is equal to one when the surface is saturated with hydrogen particles. Typically, a graphite surface is saturated with hydrogen after approximately 1 ms and therefore complete recycling ($R = 1$) can be assumed for these surfaces.

Release mechanisms

Owing to the different release mechanisms, different particle velocities can be observed which has an important impact on the edge plasma. Hydrogen may be

released from a graphite surface as an atom, a hydrogen or hydrocarbon molecule. The probability for the different release mechanisms is connected to the surface temperature which determines the residence time of the particle in the surface.

Atomic release (Γ_{H})
: The particle is directly reflected, staying only long enough for recombination to take place. The residence time is very short and the energies of the reflected particles are quite high ($\sim kT_i$) leading to large penetration depths into the plasma. Furthermore atoms are released by physical sputtering and atom- or ion-induced desorption, leading to particle energies of a few eV.

Molecular release ($\Gamma_{\mathrm{H_2}}$)
: The particle is adsorbed, subsequently combines with a second atom and thermally desorbes as a molecule after a medium residence time.

Release of hydrocarbons
: Chemical erosion and sputtering of carbon-based materials due to hydrogen leads to the formation and erosion of hydrocarbon molecules $\mathrm{C_xH_y}$. It is most important at low incoming fluxes as the yield of chemical erosion/sputtering decreases significantly at high incoming fluxes and large surface temperatures. In contrast to physical sputtering no threshold energy exists.

No release
: The atom or ion is implanted in the bulk material and remains trapped in the solid for some extended period of time.

The first two categories therefore contribute to the re-fueling of the plasma whereas the last category describes the loss of particles from the system already mentioned above. The third category plays a role in impurity production as well as re-fueling of the plasma. When the loss of particles, the release of particles as ions from the surface and chemical processes are neglected, the total flux density of re-emitted hydrogen atoms Γ_{tot} consists of a flux of re-emitted atoms and a flux of re-emitted molecules, with each molecule contributing two hydrogen atoms, and is equal to the the incoming ion flux density $\Gamma_{\mathrm{H^+}}$:

$$\Gamma_{\mathrm{tot}} = \Gamma_{\mathrm{H}} + 2\Gamma_{\mathrm{H_2}} = \Gamma_{\mathrm{H^+}}$$

It has been found that in the recycling process at low surface temperatures mainly molecules are desorbed while above about 1200 K the majority of particles is released as atoms.

Neutral particle processes

After their release from the surface the neutral particles are subsequently dissociated and ionised. Various ionisation and dissociation channels compete, the most

important ones in a fusion edge plasma are by electron impact, with their cross sections depending on the electron energy. Figure 2.9 shows the rate coefficients for the most important processes:

$$\mathrm{e} + \mathrm{H}_2 \rightarrow 2\mathrm{H}^0 + \mathrm{e} \qquad \text{(Franck-Condon dissociation)} \tag{2.1}$$
$$\mathrm{e} + \mathrm{H}_2 \rightarrow \mathrm{H}^0 + \mathrm{H}^+ + 2\mathrm{e} \tag{2.2}$$
$$\mathrm{e} + \mathrm{H}_2 \rightarrow \mathrm{H}_2^+ + 2\mathrm{e} \tag{2.3}$$
$$\mathrm{e} + \mathrm{H}^0 \rightarrow \mathrm{H}^+ + 2\mathrm{e} \qquad \text{(Electron impact ionisation)} \tag{2.4}$$
$$\mathrm{e} + \mathrm{H}_2^+ \rightarrow \mathrm{H}^0 + \mathrm{H}^+ + \mathrm{e} \tag{2.5}$$
$$\mathrm{e} + \mathrm{H}_2^+ \rightarrow 2\mathrm{H}^0 \qquad \text{(Dissociative recombinaion)} \tag{2.6}$$

Reaction (2.1) is only dominant at or below $T_\mathrm{e} = 10\,\mathrm{eV}$, whereas at higher T_e the molecule is first ionised (2.3) and then dissociated (2.5). Reaction (2.5) resembles two similar reactions noted **a** and **b** in fig. 2.9, both involving the creation of an excited molecular ion. The atoms resulting from the dissociation of molecules in ground state gain energies in the range of 2.2 eV. A further important reaction without electron impact which leads to the creation of fast atoms due to collisions with fast ions, is the charge exchange reaction:

$$\mathrm{H}^0_{\mathrm{slow}} + \mathrm{H}^+_{\mathrm{fast}} \rightarrow \mathrm{H}^+_{\mathrm{slow}} + \mathrm{H}^0_{\mathrm{fast}} \qquad \text{(Charge exchange)} \tag{2.7}$$

Its rate coefficient, which is also depicted in fig. 2.9, is similar to the rate coefficient for ionisation.

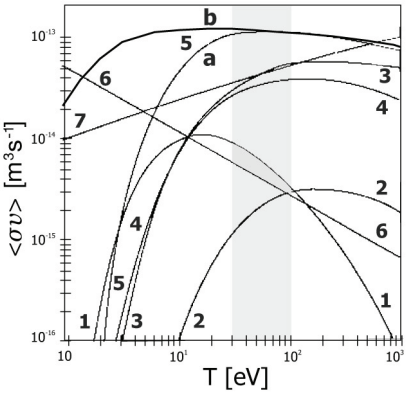

Figure 2.9
Rate coefficients of important reactions calculated by integrating the cross section of the respective process over the velocity distribution of the electrons (taken to be Maxwellian). The shaded area shows the energy range of a high temperature edge plasma.

Recombination reactions in the plasma only play a role at temperatures below 10 eV and at high electron densities like in a detached divertor plasma.

2.3.2 The scrape-off layer

The scrape-off layer in limiter and poloidal divertor tokamaks is toroidally symmetric, hence its main features can be discussed by reducing the transport inside the SOL to a two-dimensional problem: flow along the field lines and diffusion in radial direction. For simplicity the SOL can furthermore be straightened out (fig. 2.10), thereby neglecting toroidal effects which is possible in first order due to the low collisionality at the plasma edge and the small radial extent of the SOL.

The SOL begins at the last closed flux surface and is limited at both ends by the limiter or divertor target. At this target a thin sheath (the *Debye sheath*) forms that shields the electrostatic potential of the surface, which is charged up negatively by electrons on a time scale of µsafter the initiation of the discharge. The shielding is not perfect, however, due to the thermal motion of the particles, and gives rise to a small electric field in the plasma (the pre-sheath) which accelerates the ions towards the target. The electrons feel a corresponding retarding field. The plasma fluid as a whole is quasi-neutral, no net electric force acts on it. The symmetric plasma flow towards both ends of the SOL is driven by the pressure gradient which develops due to the plasma sink action of the solid surfaces. At the stagnation point the parallel flow velocity and the parallel flux are zero. At both ends the parallel flow velocity reaches sound speed $v_{\|} = c_s = \sqrt{k(T_\mathrm{e} + T_\mathrm{i})/m_\mathrm{i}}$ (following from the *Bohm criterion*).

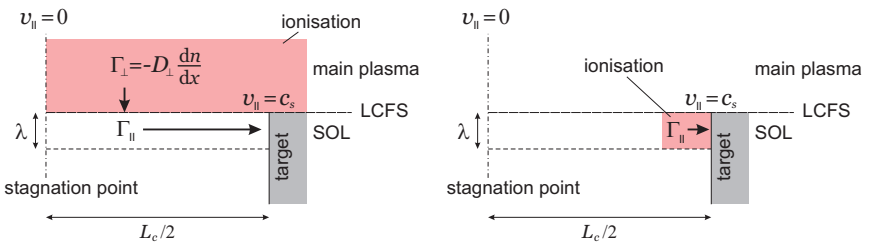

(a) The simple SOL **(b)** The complex SOL

Figure 2.10 Two-dimensional models of the scrape-off layer. Only half of the SOL is shown as it is symmetric to the plane of the stagnation point when drift effects are neglected.

Due to the different dominating plasma transport mechanisms *into* the SOL and *inside* the SOL (cross-field diffusion vs parallel transport), the fact how the neutral particles are released into the plasma and where they get ionized strongly influences the whole recycling process. Two different situations can be distinguished with respect to the particle sources in the SOL: the *simple* and the *complex* SOL (fig. 2.10 and table 2.1). While the first situation is usually realised in limiter tokamaks

and in divertor tokamaks with low plasma densities, the second situation can only be realized in divertor tokamaks at high plasma densities.

	Simple SOL	Complex SOL
Plasma sources	only diffusive cross-field transport from confined plasma ($\Gamma_\perp = -D_\perp \partial n/\partial x$), no ionisation of neutrals inside the SOL.	mainly ionisation of neutrals inside SOL. No perpendicular particle flux from confined plasma.
Plasma sinks	only the target surface.	volumetric sinks (volume recombination) can be important.
Parallel plasma flow	throughout whole SOL.	only in the ionisation region close to the target.
Heat sources	in the core of the confined plasma.	in the core of the confined plasma.
Heat sinks	no volumetric heat sinks inside the SOL.	volumetric energy sinks (line radiation) may be important
Heat transport	dominantly convective, fluid flow is isothermal, $\nabla T_{e,i} \approx 0$.	dominantly conductive. Temperature gradient must develop, $\nabla T_{e,i} \neq 0$.
Momentum sources and sinks	only the target surface.	volumetric sinks (friction) can be important.

Table 2.1 The principal distinctions between the simple SOL and the complex SOL

2.3.3 Attached conditions

Regarding plasma parameters in the scrape-off layer, the most desirable case is one where the SOL is hot at the stagnation point adjacent to the confined plasma and cold near the targets, reducing sputtering. To establish significant temperature gradients along the SOL, a necessary condition is the fact that parallel heat convection does not play a large role in carrying the power along the SOL from the main plasma to the targets. It is not a sufficient condition, however, as temperature gradients may still be negligible even if heat transport is dominated by conduction.

The situation of significant temperature gradients along the length of the SOL is called the *conduction-limited regime* and can only be reached with a complex SOL due to the necessity of the localisation of the ionisation of neutrals close to the target. The isothermal case is called the *sheath-limited regime*. In both regimes the plasma is in an *attached* state, characterised by the following three assumptions:

1. Friction processes (ion-neutral friction due to charge exchange processes and elastic scattering) can still be neglected in comparison to ionisation processes due to sufficiently high SOL temperatures ($T_{\mathrm{target}} > 10\,\mathrm{eV}$). The total plasma pressure (static plus dynamic pressure) is therefore constant along the field lines and the static pressure drops from the stagnation point to the target to half of its value

$$p_{\mathrm{target}} \cong p(0)/2$$

2. Volumetric plasma sink processes (volume recombination) inside the SOL can also still be neglected at these SOL temperatures. Hence, the ion flux to the target can be described as the parallel ion flux density at the sheath entrance with the velocity given by the Bohm criterion and the density at the sheath entrance:

$$\Gamma_{\mathrm{target}} \cong n_{\mathrm{se}}\, c_{\mathrm{s}}$$

3. Volumetric energy loss processes (line radiation from fuel and impurities) can be neglected compared to the kinetic power of the particles. All the power that enters the SOL reaches the target via particle collisions.

Sheath-limited regime

This regime is characterised by a weak temperature difference between the stagnation point ($z = 0$) and the target plate:

$$T_{\mathrm{target}} \cong T(0)$$

Furthermore, since the total plasma pressure is assumed to be constant, the density along the SOL $n(z)$ drops from the stagnation point to the target to half of its value:

$$n_{\mathrm{target}} \cong n(0)/2$$

This is the reason why this regime is also called *linear* regime: the target density rises linearly with the discharge density.

The ion flux density to the target is therefore approximately given by

$$\Gamma_{\mathrm{target}} = \frac{1}{2}\, n(0)\, c_{\mathrm{s}}$$

The power flux density from the plasma onto the surface can be related to the particle flux leaving the plasma with the help of the so-called sheath transmission coefficient γ which has typically a value of ≈ 8.

$$q_{\text{target}} = \gamma \, \Gamma_{\text{target}} \, k \, T_{\text{target}}$$

The temperature at the stagnation and point and therefore the temperature at the target is related to the power flux density by

$$T_{\text{target}} \cong (2m)^{1/3} \left(\frac{q(0)}{\gamma \, n(0)} \right)^{2/3} \tag{2.8}$$

The power flux density and the plasma density at the stagnation point can be considered to be specified externally to some extent, $q(0)$ is related to the input power of the discharge and $n(0)$ is related to the average density of the discharge, generally controlled by feedback to gas valves. In the sheath-limited regime the temperature at the target surface remains high, unless the density inside the confined volume is very high (stability problem) or the power flux into the SOL is reduced by power loss mechanisms inside the confined volume.

Conduction-limited regime

This regime is only accessible in a complex SOL. The effects in such an SOL can be quantified using a simple analytic model called the *two point model*. It is based on the concept of the magnetic flux tubes which connect the stagnation point to the target. The stagnation point is located where, in the simplified model, all the energy from the main plasma enters the SOL and is called the *upstream* position. The two-point model relates the upstream parameters, which are only determined by the main plasma, to the plasma parameters at the target, the *downstream* position. In the upper part of the SOL, the so-called *conduction region*, heat transport is dominated by parallel heat conduction along the magnetic field lines. This region constitutes the major part of the SOL and is free of sources and sinks. The area close to the target, the *recycle region*, is characterised by strong plasma sources due to ionisation and possibly sinks of energy (line radiation from fuel and impurity particles), momentum (ion-neutral friction) and particles (recombination).

In the conduction-limited regime, the temperature in the recycle region is constant due to strong parallel convection and comparably small volumetric energy losses. The plasma temperature at the target plate T_t strongly depends on the upstream density

$$T_\mathrm{t} \sim \frac{1}{n_\mathrm{u}^2}$$

Thus the goal of achieving low temperatures adjacent to the target plates to reduce physical sputtering can be attained simply by increasing the plasma density. The density at the target is an even stronger function of the upstream density

$$n_\mathrm{t} \sim n_\mathrm{u}^3$$

reflecting the particle flux amplification, the reason why this regime is also called *high-recycling regime*.

2.3.4 Detached conditions

When the plasma temperature at the target is sufficiently low, e.g. at high plasma density or when radiation losses are large, the rate of neutral ionisation is reduced to a level where it becomes small compared to the rate of ion-neutral friction processes. In such a situation the total plasma pressure throughout the recycling region does not remain constant, since ion momentum is lost through collisions with neutrals. With these friction losses introduced by the factor $f_\mathrm{fric} < 1$, the pressure balance reads

$$n_\mathrm{t}\, T_\mathrm{t} = f_\mathrm{fric}\, n_\mathrm{u}\, T_\mathrm{u}/2$$

Momentum losses due to charge exchange processes between ions and neutrals play a major role in high density poloidal divertors in tokamaks. Furthermore, in the helical divertor of LHD and the island divertor of W7-AS, detachment processes at higher temperatures have been observed which have been related to friction losses caused by counter streaming plasma flows in neighbouring flux tubes in the complicated three-dimensional geometry [Feng et al. 2009].

In the case of friction losses due to charge exchange, the friction factor is linked to the rate coefficients for ionisation and charge exchange. An expression for f_fric has been derived in [Pitcher and Stangeby 1997] following a one-dimensional analytical solution for the momentum balance in [Self and Ewald 1966]:

$$f_\mathrm{fric} = 2\left(\frac{\alpha}{\alpha+1}\right)^{(\alpha+1)/2} \qquad \text{with} \quad \alpha \equiv \frac{\langle\sigma v\rangle_\mathrm{i}}{\langle\sigma v\rangle_\mathrm{cx} + \langle\sigma v\rangle_\mathrm{i}}.$$

In the detached divertor state, particle and power flux to the divertor plate are strongly reduced, it is therefore the envisaged divertor regime for coming fusion devices like ITER and W7-X.

2.4 Plasma edge transport modelling

In order to help in the interpretation of present fusion experiments and to aid in the design activities for future devices such as ITER and W7-X, much effort is put

into realistic computer simulations of the plasma edge, quantifying plasma flows and resulting plasma structures. Such computer simulations are based on models that describe the physics of partly ionised, magnetised plasmas near surfaces of the vacuum chamber, including not only hydrogen plasma transport but also the production and transport of neutral particles due to plasma surface interaction processes and even plasma impurities.

The different exhaust concepts described in section 2.2 pose different requirements on such models. Symmetric configurations such as the axisymmetric toroidal limiter and poloidal divertor configuration are commonly simulated using two-dimensional models, thereby reducing complexity and required computer power. In the absence of any common symmetries for plasma and neutral gas dynamics, on the other hand, which is the case for stellarators and tokamaks with a stochastic boundary due to the very complex three-dimensional magnetic field structure, three-dimensional modelling is required. Such codes can then be used to quantify the impact of the complex magnetic field structures on plasma transport and structure in these devices, but also - more generally - to investigate any three-dimensional effects on edge transport in limiter and poloidal divertor tokamaks, e.g. due to coil misalignments. The experimental observations made in the framework of this thesis provide valuable input for the simulations of three-dimensional stochastic divertor structures while in turn modelling results also help in the interpretation of the experimental data.

In the framework of [Frerichs 2010a] transport modelling for the helical divertor configuration in TEXTOR was carried out and analysed using the three-dimensional transport code EMC3-EIRENE [Feng et al. 2004; Reiter et al. 2005], a coupling of the two Monte Carlo codes EMC3 and EIRENE. EMC3 is a three-dimensional fluid code that contains a fluid treatment of particle, parallel momentum and energy transport for the plasma. EIRENE is a kinetic neutral particle transport code that calculates the particle, energy and momentum sources and sinks in front of and on the wall. The iterative coupling of the two codes provides a self-consistent description of the plasma edge.

The EMC3 code is based on a steady state model for a plasma in a given magnetic field structure, i.e. the magnetic field is externally prescribed and kept fixed during the entire calculation. The magnetic field calculation is hereby based on the *vacuum approach*, taking an axisymmetric MHD equilibrium and superimposing the three-dimensional vacuum field of the perturbation coils. The code then solves a set of steady state fluid equations in this prescribed magnetic field structure: the balance equations for the macroscopic plasma quantities density, momentum and energy for electrons and ions. For the inclusion of impurities in the model, the so-called trace impurity approximation is used assuming a small impurity concentration in a hydrogen plasma. This allows to treat impurity transport in a separate approach from the main hydrogen plasma or to neglect it as it was done for part of the simulations in [Frerichs 2010a]. The only effect of impurities

on the main plasma in this approximation is an additional energy sink due to inelastic collisions between electrons and impurity ions. The main plasma is described as a two component plasma of electrons and hydrogen ions with the resulting six balance equations reduced to four equations under the assumption of quasi-neutrality and locally ambipolar flow. These balance equations are derived from the well-known Braginskii equations [Braginskii 1965] which describe the strongly anisotropic plasma transport in a magnetised, collisional plasma, known as the so-called *classical transport theory*. These equations contain transport coefficients, which - in case of the classical transport theory - account for Coulomb collisions but neglect the influence of micro turbulence. As cross-field transport processes were found to be much larger than predicted by the classical theory and also by the neo-classical theory which accounts for drifts in inhomogeneous magnetic fields, this 'anomalous' cross-field transport is taken into account by free model parameters. Because of the strong anisotropy, a precise knowledge of the magnetic field is required to separate parallel and cross-field transport effects. In the EMC3 code, the fast parallel transport is decoupled from the slower cross-field transport by introducing a field aligned coordinate system. Interactions with neutral particles are taken into account by sources of particles, momentum and energy calculated by the EIRENE code. The calculations with the EIRENE code include a number of atomic processes: electron impact ionisation and excitation of atomic and molecular hydrogen, charge exchange between hydrogen atoms and ions, electron impact dissociation of molecular hydrogen and molecular hydrogen ions. Recombination processes are not included in the version of the code used. The interaction with material surfaces is taken into account based on surface reflection data from the TRIM code database [EIRENE 2010], with non-reflected hydrogen ions released back into the plasma as hydrogen molecules.

For solving the partial differential equations of the transport model, boundary conditions have to be applied. At the inner simulation boundary of the EMC3 part of the code, which is located in the vicinity of the last closed flux surface, the total fluxes across the surface of the simulation boundary and the plasma density are prescribed. The latter is realised iteratively by scaling the total target particle flux accordingly while the total power influx has to be prescribed as a fixed boundary condition. The particle influx is obtained from EIRENE, the simulation domain of which is extended further inside to the core plasma to calculate the ionisation of neutrals in the core which then contributes to the particle influx in steady state. No cross-field transport of parallel momentum is assumed at the inner simulation boundary and the energy influx is estimated from earlier experimental observations of the total heating power less the radiated power in the core plasma. For the investigation of the different density regimes using the three-dimensional transport code, a density scan was performed, i.e. a sequence of simulations starting from $n_{\mathrm{in}} = 0.7 \cdot 10^{19}\,\mathrm{m}^{-3}$ to $n_{\mathrm{in}} = 4.8 \cdot 10^{19}\,\mathrm{m}^{-3}$ while $P_{\mathrm{in}} = 600\,\mathrm{kW}$ is kept fixed. At the outer simulation boundary of the EMC3 code (in the far SOL) an exponential decay of the plasma parameters is expected. The outer simulation boundary of

EIRENE extends further outside up to the vessel wall because neutral particles are not bound to the magnetic field. At the target surfaces of the divertor complete recycling is assumed. Here, the Bohm condition provides the boundary condition for parallel momentum flux and the heat flux is related to the target particle flux by sheath transmission coefficients. In addition to the boundary conditions, the coefficients for anomalous cross-field transport of particles and energy have to be specified. Most of the simulations analysed in [Frerichs 2010a] were performed using $D_\perp = 1.0\,\mathrm{m^2 s^{-1}}$ as the cross-field particle transport coefficient and $\chi_\perp = 3D_\perp$ as the cross-field energy transport coefficient. This level of cross-field transport proved to be in good agreement with the experimental observations made within this thesis while additional simulations using $D_\perp = 0.2\,\mathrm{m^2 s^{-1}}$ did not agree with the experimental findings.

3 The experimental setup

3.1 The tokamak TEXTOR

The tokamak TEXTOR (**T**orus **Ex**periment for **T**echnology **O**riented **R**esearch) went into operation in 1981 and was constructed especially for the investigation of the plasma edge and plasma surface interaction in a toroidal, magnetically confined high temperature plasma. A detailed description of the current status of the setup can be found in [Neubauer et al. 2005] and a schematic view of TEXTOR is shown in figure 3.1. TEXTOR is operated at the *Institute for Energy Research - Plasma Physics* of the Forschungszentrum Jülich in the framework of the Trilateral Euregio Cluster (TEC).

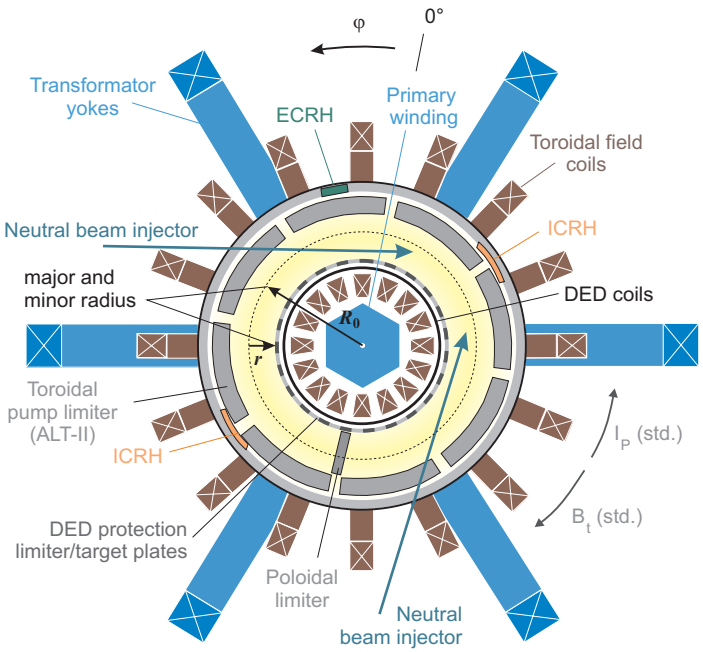

Figure 3.1 Top view of an equatorial cut of the tokamak TEXTOR. The location of the different heating systems, limiters and the DED coils are shown.

TEXTOR is a medium sized limiter tokamak with circular cross section and a major radius of $R_0 = 1.75\,\mathrm{m}$. This is the distance between the centre of the central solenoid to the centre of the so-called liner. The liner is a toroidally shaped metallic wall made of inconel with a minor radius of 0.55 m which serves as the first wall inside the vacuum vessel and can be heated to 300 °C to improve vacuum conditions in TEXTOR. The minor radius of the plasma is determined by the position of the plasma column in relation to the various limiters inside the vessel (see section 3.2), i.e. the last closed flux surface. The confined plasma volume is approximately $7.3\,\mathrm{m}^3$ and the whole surface of the first wall is about $31\,\mathrm{m}^2$. The toroidal coordinates (major radius R_0, minor radius r, poloidal angle θ, toroidal angle φ) used throughout this thesis are shown in figures 3.1 and 3.3(a).

The vacuum vessel is surrounded by 16 toroidal field coils which are symmetrically distributed around the torus and create a toroidal magnetic field B_t of up to 2.8 T on the plasma axis. A plasma current of up to 800 kA can be induced in the plasma by the varying magnetic flux in the central solenoid of the transformer. To generate plasma discharges with a constant plasma current lasting several seconds, discharges with a lower plasma current are usually performed. In the discharges analysed in this thesis plasma currents of 350 kA to 400 kA were used. The maximum duration of a TEXTOR discharge is 10 s, the typical duration is about 6 s.

Additional to the ohmic heating due to the plasma current and finite resistivity of the plasma (about $0,5\,\mathrm{MW}$), auxiliary heating systems with a maximum total heating power of 9 MW are available: TEXTOR is equipped with two neutral beam injectors [Uhlemann and Ongena 1999], two Ion Cyclotron Resonance Heating (ICRH) antennae pairs [Koch et al. 2005] and an Electron Cyclotron Resonace Heating (ECRH) [Westerhof et al. 2005]. For the experiments presented in this thesis only neutral beam heating was used injecting in the direction of the plasma current (co-injection).

3.2 The limiter configuration

For the spatial limitation of the plasma in TEXTOR several limiters are available (see figure 3.3(a)), all of them made of graphite:

ALT-II
: The **A**dvanced **L**imiter **T**est-II is a toroidal belt limiter consisting of eight segments mounted below the equatorial plane at the low field side of the tokamak. The segments are made of graphite and each cover a toroidal angle of $\Delta\varphi = 42.5°$ and a poloidal angle of $\Delta\theta = 45°$. Its radial position can be varied between 0.46 m and 0.48 m, during the experiments presented here it was located at a geometrical minor radius of $r = 0.47\,\mathrm{m}$. ALT-II

is a pump limiter, i.e. beneath each segment a pump duct facilitates the removal of neutral fuel, ash and impurity particles (i.e. hydrogen and its isotopes, helium, hydrocarbons, etc.). The surface of the pump limiter is $3.6\,\mathrm{m}^2$ [Goebel et al. 1989].

Poloidal limiters

Two graphite limiters made up of five exchangeable elements are located at one poloidal location at the top and bottom of the vessel. They are mounted on one of the transformer yokes thereby decoupled from the liner. Their radial position can be varied, during the experiments presented here they were located at $r = 0.47\,\mathrm{m}$.

DED protection limiter

The coils of the dynamic ergodic divertor at the high field side (see section 3.3) are protected by graphite tiles forming the DED protection limiter at a geometrical minor radius of $r_{\mathrm{DED}} = 0.477 \pm 0.03\,\mathrm{m}$. The uncertainty in the radial position is due to the difficulty in the exact alignment of the tiles. They cover a poloidal angle of $\pm 62^\circ$ around the equatorial plane which is equivalent to ~ 0.34 of the total poloidal circumference. In the helical divertor configuration these tiles form the divertor target plates.

In the framework of this thesis, a limiter configuration was used as a reference configuration for comparisons to the hydrogen recycling in the helical divertor configuration. The parameters of the studied discharges presented in this thesis are summarised in table 3.1the limiter discharge corresponds to a discharge with $I_{\mathrm{DED}} = 0\,\mathrm{kA}$. In order to ensure the plasma to be limited by the divertor target (the DED protection limiter), the plasma center was moved towards the HFS in relation to the geometric center by 2.4 cm. The plasma center is hereby defined as the center of the last closed flux surface in the limiter configuration. The LCFS touches the DED protection limiter in the equatorial plane (see figure 3.3(a)) and the poloidal limiters and the ALT-II limiter lie outside the LCFS in the scrape-off layer. A rough estimation of the distribution of the recycling flux on the different limiters was done by analysing the Balmer α-emission observed by a filtered CCD camera viewing a complete poloidal cross section (figure 3.2). This image shows the two poloidal limiters, part of the DED protection limiter and almost a whole ALT-II blade. For this estimation, the assumption is made that the relation between the grey value measured by the camera and the recycling flux is the same for all the limiters. Furthermore the assumption is made based on geometric considerations, that the fraction of photons observed by the camera in front of the DED protection limiter (which corresponds to the recycling flux at this surface) is about 6 % of the total photon emission from the whole DED protection limiter. In this case, at a line averaged plasma density of $\bar{n}_{\mathrm{e,c}} = 3.5 \cdot 10^{19}\,\mathrm{m}^{-3}$ in the limiter discharge investigated, the major fraction of the recycling takes place at the DED protection limiter ($\sim 92\,\%$), while $\sim 4\,\%$ takes place at the two poloidal limiters and the ALT-II limiter, respectively. At higher plasma densities, still a major

fraction of the recycling takes place at the DED protection limiter ($\sim 82\,\%$ at $\bar{n}_{e,c} = 5.2 \cdot 10^{19}\,m^{-3}$), though the recycling at the ALT-II limiter increases, the fraction growing to $\sim 12\,\%$ while the fraction of the recycling at the poloidal limiters is still roughly the same. In conclusion, throughout the density ramps investigated in this thesis (discharges with a controlled, steady increase in plasma density), the DED protection limiter constitutes the main limiting object.

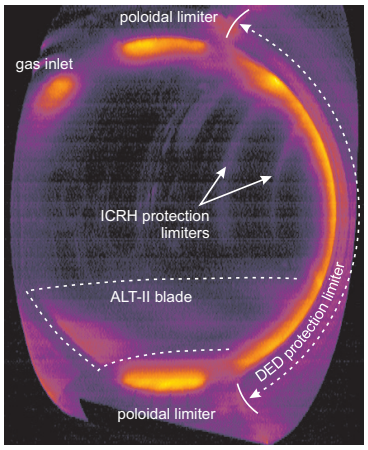

Figure 3.2
Poloidal cross section of TEXTOR in the light of Balmer α-emission (pseudo- colored) using a filtered CCD camera.

3.3 The helical divertor configuration

Since 2002 the dynamic ergodic divertor (DED) is operated at TEXTOR as a flexible experimental tool for creating a resonant magnetic perturbation of the equilibrium tokamak field [Finken et al. 1999]. Earlier studies showed, that the perturbation field of the DED creates a helical divertor structure [Schmitz 2006], i.e. the plasma exposed surface area is completely determined by the helical pattern of the magnetic field structure. Since its conceptual design, different methods have been developed to describe the induced magnetic field topology and the behaviour of the plasma in it [Abdullaev et al. 2003; Finken et al. 2005]. The experimental results presented in this thesis are compared to these topological calculations and modelling results from the three-dimensional modelling code EMC3-EIRENE. In this section, at first the technical setup of the DED is described followed by a description of the induced magnetic topology.

3.3.1 The technical setup of the dynamic ergodic divertor

The dynamic ergodic divertor consists of 16 perturbation and 2 compensation coils installed at the high field side (HFS) of the vacuum vessel. Each coil helically

revolves once around the torus and is inclined parallel to the magnetic field lines on the $q = 3$-flux surface. Hence the main resonance of the perturbation field lies on this surface which typically is located at the plasma edge (at $r \approx 0.43\,\mathrm{m}$). The coils are installed at a geometrical minor radius of $r = 0.532\,\mathrm{m}$ and the envelope of all tiles covers a poloidal angle of $\Delta\theta = 72°$.

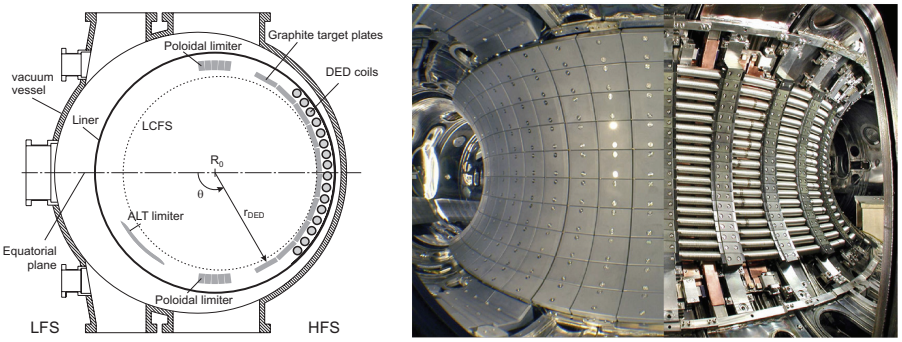

(a) Schematic drawing of a poloidal cross section.

(b) The DED coils before (right) and after installation of the graphite target tiles.

Figure 3.3 Illustration of the dynamic ergodic divertor, the graphite divertor target plates and the location of the other main limiters in TEXTOR.

The wiring of the coils is variable and determines the mode spectrum of the created magnetic perturbation field. This way, perturbation fields with different multipole order can be generated [Finken et al. 2005]. The nomenclature of the base mode configurations refers to the main resonances of the respective perturbation field given in poloidal m and toroidal n mode numbers. Three base mode configurations with different multipole order and therefore different penetration depth of the perturbation field are possible: The $m/n = 3/1$ base mode creates a perturbation field with the lowest multipole order and therefore largest penetration depth. The perturbation field in the $m/n = 12/4$ base mode has a large multipole order, the field radially decreases very quickly and is restricted to the plasma edge. The base mode configuration mainly studied in the course of this work is the $m/n = 6/2$ base mode which resides between the former two regarding multipole order and penetration depth.

The DED can be operated at direct (DC) and alternating (AC) current, this way a rotating electromagnetic perturbation field with a rotation frequency of up to 10 kHz can be generated. However, in the course of this thesis only static operation was studied. For technical reasons, the maximum possible current in the coils depends on the base mode configuration and the rotation frequency. For DC operation, it is $I_{\mathrm{DED}} = 15\,\mathrm{kA}$ in the 3/1 base mode, 7.5 kA in the 6/2 base mode and 3.75 kA in the 12/4 base mode. The perturbation fields created by these

currents have magnetic field strengths of $B_{\mathrm{DED}} \lesssim 0.02\,\mathrm{T}$ which is about 1/10 of the poloidal magnetic field [Finken et al. 2005].

Apart from the DC and AC operation it is also possible to vary the phases of the coil currents in such a way, that the perturbation field does not rotate but the current maximum is "slowly" shifted from one coil to the next. This so-called *sweep-mode* is often used to scan the perturbation field and thereby the plasma modulation across the observation point or observation line of diagnostic systems with restricted spatial resolution such as the Langmuir probes or atomic beams (see section 4).

3.3.2 The magnetic topology of the helical divertor

The DED creates a helical perturbation field that destroys the axial symmetry of the equilibrium tokamak field. A three-dimensional magnetic field topology is formed. As the charged plasma particles are largely influenced by the magnetic field and are confined to it in first approximation, the analysis of the measurements needs a detailed knowledge of the complex magnetic field topology.

Prior to and during the operation of the DED at TEXTOR two different methods were developed and used to calculate the magnetic field topology: numerical field line integration and simplectic mapping. Both methods are based on magnetic field calculations without plasma response, the so-called vacuum approximation. In this approach the vacuum perturbation field is superimposed to an (axisymmetric) equilibrium field, while the modification of the magnetic perturbation field due to a plasma response is neglected. The validity of this approach is still the subject of ongoing research [Kobayashi et al. 2000; Reiser and Chandra 2009] and is related to the issue of the penetration of resonant magnetic perturbations into a plasma. At TEXTOR though, a good agreement between calculated magnetic field structures employing this vacuum approximation and experimentally observed plasma edge structures has been found [Jakubowski et al. 2006; Lehnen et al. 2008].

The calculations made in the course of this work and mainly presented here were performed using the ATLAS code [Jakubowski 2004] which incorporates simplectic mapping methods based on a model developed by [Abdullaev 2004]. The magnetic field for the three-dimensional plasma modelling with the EMC3-EIRENE code was calculated using the GOURDON code, a field line tracing code that numerically integrates the ordinary differential equation describing the magnetic field lines [Frerichs 2010a]. The resulting complex magnetic field structure at the plasma edge can be visualised by different methods involving two-dimensional representations of the magnetic field on representative surfaces. Typically these planes are either poloidal cross sections (φ = const.) or the surface of the DED target plates ($r = 0.477\,\mathrm{m}$).

Poincaré plots
This has become a wide-spread method in studies of nonlinear systems and chaos. The plots show intersections of magnetic field lines with a chosen poloidal reference plane (red dots in figure 2.6 and black dots in figure 3.4). Due to the short field line connection lengths at the very edge of the plasma, only few 'dots' can be found there, thus, for the visualisation of the magnetic field structures in this region Poincaré plots are not well suited.

Connection Length plots
This visualisation method is based on the wall-to-wall connection length L_c of the magnetic field lines. For a poloidal cross section the field lines are traced from a number of selected starting points in both directions until they intersect the wall or until some cut-off length $L_{c,max}$ is reached. This yields the connection length in positive and negative direction L_c^+ and L_c^- , respectively, which is combined to the total wall-to-wall connection length $L_c = L_c^+ + L_c^- \leq 2L_{c,max}$. Examples can be found in figures 3.4 and 3.5(a). Similarly, for the surface of the DED target plates, field lines are traced from the target until they intersect the wall or until reaching some cut-off length. This yields the so-called *magnetic footprints* giving a first indication of how the plasma surface interaction area is influenced by the resonant magnetic perturbations (see figures 3.6 and 3.7(a)).

Shortest Connection Length plots
This plot is similar to the Connection length plot for poloidal cross sections. Instead of the total wall-to-wall connection length, the shorter of the positive and negative connection length $L_{c,short} = \min(L_c^+, L_c^-)$ is plotted (figure 3.5(b)).

Penetration Depth plots
This is a different version of a magnetic footprint. It shows the maximum radial penetration of the magnetic field lines from the DED target plates (figure 3.7(b)).

DED base mode m/n	6/2
DED current I_{DED}	3.75 kA
Edge safety factor q_a	3.7
Plasma current I_p	353 kA
Plasma position R_0	1.726 m
Toroidal magnetic field B_t	1.9 T
Poloidal beta β_p	~ 0.5

Table 3.1 Parameters of the plasma discharges characterising the magnetic field topology studied in this thesis.

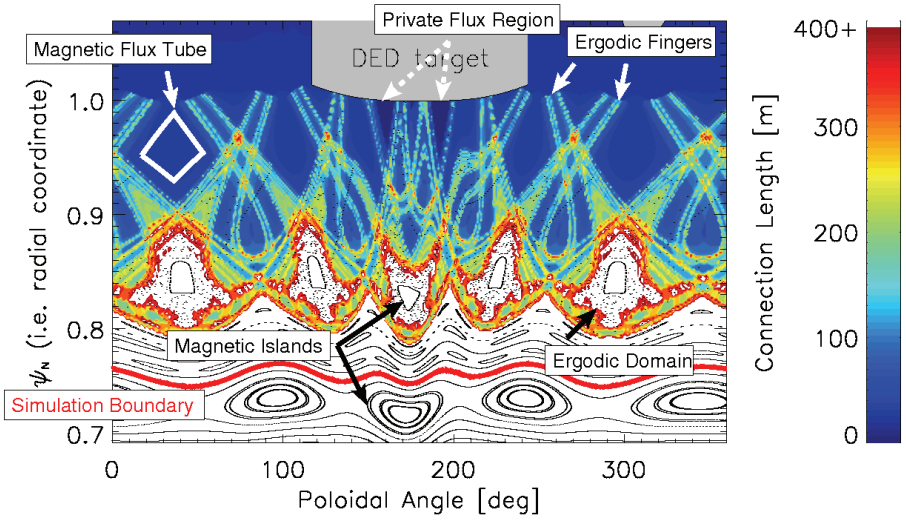

Figure 3.4 Magnetic field structure of the TEXTOR helical divertor scenario extracted from [Frerichs 2010a]. Combined Poincaré and Connection Length plot at the toroidal position $\varphi = 90°$. White contours indicate the shape of a short magnetic flux tube.

The helical divertor configuration studied experimentally in this thesis is characterised by the parameters summarised in table 3.1. This configuration is comparable to the configuration studied in [Frerichs 2010a] using the three-dimensional modelling code EMC3-EIRENE as it is based on the same magnetic equilibrium. Figure 3.4 shows the visualisation of the magnetic field topology at a poloidal cross section calculated by the GOURDON code. The figure shows the full poloidal range with the divertor target at the HFS located in the middle and the LFS located at either end. The resonant magnetic perturbation leads to a complex structure with intact and partially ergodised magnetic islands and a region with field lines in a wide range of connection lengths. A feature of this helical divertor configuration is the formation of two short magnetic flux tubes with strongly correlated field lines which connect within one poloidal turn from one strike point to the other. The shape of one of these flux tubes is indicated in white in figure 3.4 by its contour in the poloidal cross section and in figure 3.6 by its footprints on the divertor target. The flux tubes are embedded into a region with field lines of long connection length, sometimes called *ergodic fingers*, although parts of some of these long field lines belong to the laminar region defined in section 2.2.3.

Figure 3.4 shows that the magnetic topology is compressed in the region in front of the divertor target. As this is the main region of interest in this thesis with the hydrogen recycling taking place mainly at the divertor target plates, an enlarged view of this poloidal range is shown in figure 3.5 (calculated using the ATLAS

code). The connection lengths in this plot are given in the number of poloidal turns $N_{\text{p.t.}}$ enabling a direct translation into the number of times the field line passes the high field side, where it is either pushed inwards or pulled outwards towards the target plates. Two grey areas can be identified in figure 6.5(a), they are regions of field lines with very short connection lengths of less than half a poloidal turn and are similar to the private flux region (PFR) known from poloidal divertors. In the following the region between 150° and 160° will be called the lower private flux region and the region between 183° and 194° will be called the upper private flux region. Besides the private flux regions the short magnetic flux tubes can be identified (blue areas) and furthermore regions with wall-to-wall connection lengths of two poloidal turns (cyan areas) mixed with areas of longer field lines with up to ten or more poloidal turns. From $N_{\text{p.t.}}$, the target-to-target connection length in metre can be estimated by $L_{\text{c}} \approx N_{\text{p.t.}} \cdot 2\pi\, q\, R_0$ neglecting the variation due to the field line diffusion.

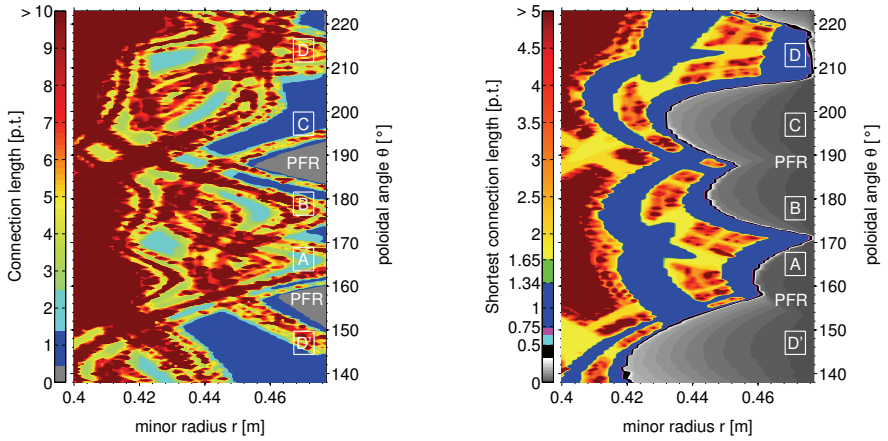

(a) Connection length plot with field line lengths given in poloidal turns.

(b) Shortest Connection Length plot with field line lengths given in poloidal turns.

Figure 3.5 Magnetic field topology in front of the divertor target plates at a toroidal angle of $\varphi = 154.7°$. The field line tracing was stopped for $L_{\text{c}} > 20\,\text{p.t.}$.

For the identification of the different regions introduced in section 2.2.3 (ergodic and laminar region), the distance of each point in the poloidal cross section $(r, \theta, \varphi = \text{const})$ from the wall along the magnetic field line at this location, i.e. the shortest connection length $L_{\text{c,short}}$, has to be calculated. The result is shown in figure 3.5(b). Note that possible intersections of other limiter structures (such as the ALT-II and the poloidal limiters) are not included in these magnetic field calculations. The number of these field lines is however small for the plasmas

considered here as the plasma was moved towards the perturbation coils at the high field side leading to a major part of the "open" field lines intersecting the divertor target plates. Hence, it is possible to separate the field lines into several groups according to the number of times they pass the low field side before intersecting the target. Field lines with a shortest connection length of less than $124°/360° \approx 0.34$ poloidal turns (grey shaded area) do not pass the low field side on their way to the wall but directly connect to the target within up to $\Delta\theta \approx 124°$ (at maximum from the bottom of the target to the top or vice versa). Field lines with a shortest connection length of more than 0.65 and less than 1.34 poloidal turns (magenta and blue area) pass the low field side once more before intersecting the wall and field lines with more than 1.65 poloidal turns pass the low field side at least twice.

To define now a laminar region, the shortest connection length can be compared to the Kolmogorov length as a first approximation. With this definition, the laminar region is defined by the parallel scale over which the field lines do not exhibit diffusive behaviour [Ghendrih et al. 1996], i.e. the parallel length over which neighbouring field lines remain coherent. In this area, the transport of the plasma particles parallel to the magnetic field lines is the dominant feature and governs the particle and energy deposition on the divertor target. When analysing transport effects, the cross-field transport actually increases this coherence length by introducing an averaging process. This increased characteristic length of parallel transport is discussed in section 3.3.3. The Kolmogorov length was derived in [Schmitz et al. 2008b] with the ATLAS code for a similar magnetic topology as investigated here giving $L_{\mathrm{K}} \approx 16 - 20\,\mathrm{m}$ up to a radius of $r = 0.4\,\mathrm{m}$ (local value derived not from quasi-linear theory but by a statistical evaluation of the field line behaviour). The laminar zone therefore corresponds to the region in figure 3.5(b) with shortest connection lengths $L_{\mathrm{c,short}} \leq 0.5\,\mathrm{p.t.} \approx 20\,\mathrm{m}$ (grey shaded and black area in figure 3.5(b)). The radial width of the laminar region strongly varies in the poloidal direction between a few mm and about 6 cm. This is expected to have a strong impact on the recycling. If a major fraction of the neutrals coming from the target are ionised outside the laminar region, i.e. outside the scrape-off layer of the helical divertor, strong plasma flows towards the target will establish and lead to convective heat transport dominating over conduction parallel to the magnetic field. Eventually, this will prevent large temperature gradients between core and target.

At the divertor target the chaotic magnetic field structure described above results in the formation of a helical strike point pattern, which is visualised in figure 3.6 by a magnetic footprint showing target-to-target connection lengths L_{c}. Particle and heat fluxes are guided by the magnetic field lines to this helical target pattern and the configuration is therefore called a helical divertor. This footprint plot shows only half of the divertor target in toroidal direction as the magnetic topology repeats itself after half a toroidal turn in the 6/2-base mode configuration. Four strike points - or strike lines - are formed on the target, two of them located between the labelled private flux regions and the other two above the upper

private flux region. The additional patterns below the lower private flux region and above the topmost strike point actually belong to these four strike points (this can be seen when imagining placing two of these plots next to each other and connecting the other ends to complete the toroidal circumference). According to the calculated particle and heat fluxes, the four strike points were labelled A, B, C and D in [Frerichs 2010a], for convenience the same labelling will also be used throughout this thesis (see figures 3.5(a) and 3.7). The two short magnetic flux tubes each intersect the target in two different strike points. The ends of one of the flux tubes is located at strike point B and at strike point C. Parts of the footprints of the second short magnetic flux tube are visible at the left side of the plot. The footprints of the second short magnetic flux tube are therefore identical to those of the first one but they are located mainly in the toroidal section not shown in figure 3.6. One end of the second flux tube is therefore located at strike point A and the other end is located at strike point D.

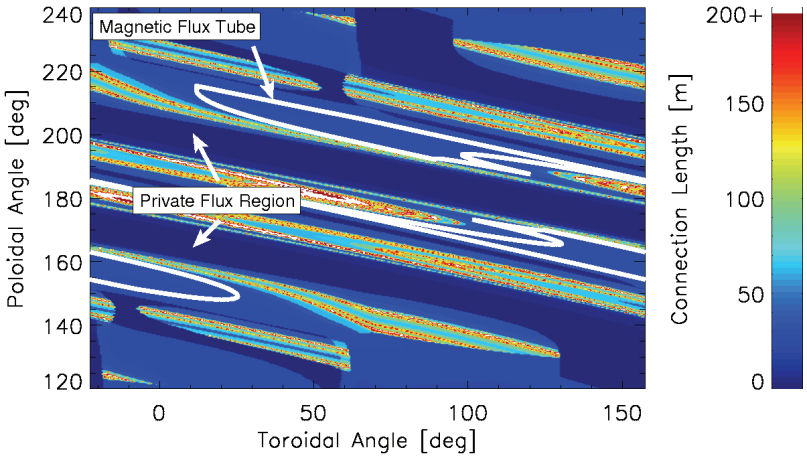

Figure 3.6 Magnetic footprint on the DED target of the TEXTOR helical divertor with the toroidal axis shifted by 90° (extracted from [Frerichs 2010a]). White contours indicate the shape of a short magnetic flux tube.

An enlarged view of the magnetic footprint at the divertor target showing the poloidal and toroidal range covered by the observation system described in section 5 is shown in figure 3.7 (as well calculated using the ATLAS code). As pointed out above and e.g. in [Ghendrih et al. 1996; Nguyen et al. 1997], the particle and heat loads at the target are not determined by this total wall-to-wall connection length of the field lines intersecting the target (which can merely serve as an indication of the field line penetration). It is rather the radial penetration of the field lines over the corresponding characteristic transport length (see section 3.3.3) which determines the fluxes. As these characteristic lengths differ, figure 3.7(b) shows

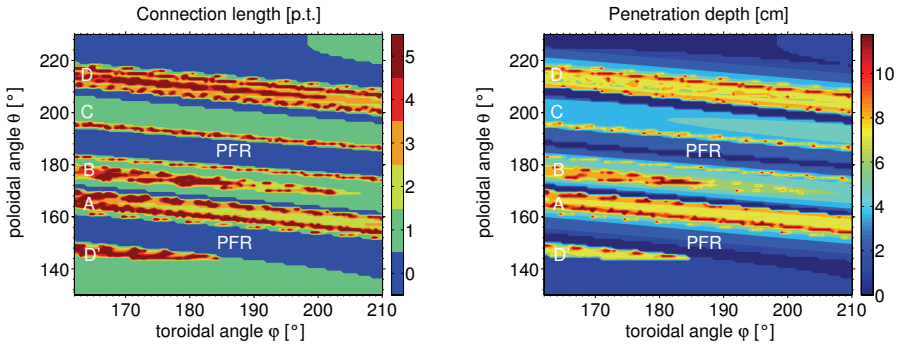

(a) Target-to-target connection lengths of field lines intersecting the divertor target given in poloidal turns.

(b) Deepest radial penetration of the field lines over the whole connection length.

Figure 3.7 Helical strike point pattern on the divertor target visualised by magnetic footprints calculated using the ATLAS code.

the deepest penetration depth of the field lines intersecting the target over their whole connection length. A correlation between this deepest penetration depth and the wall-to-wall connection length shown in figure 3.7(a) is clearly visible, short field lines penetrate less deep into the plasma than longer filed lines.

3.3.3 Particle recycling and transport in the helical divertor

In this section, the characteristic scale length for energy transport is introduced as an extension of the definition of the laminar region in the previous section followed by a summary of the knowledge gained prior to this thesis about particle recycling and transport in the helical divertor of TEXTOR.

As already pointed out in the previous section, when analysing transport effects, the cross-field transport increases the coherence length of neighbouring field lines by introducing an averaging process. This effect governs the logarithmic correction to the parallel transport scale length L_{transp} according to [Rechester and Rosenbluth 1978] yielding $L_{\mathrm{transp}} \sim 1/2\, L_{\mathrm{K}} \ln(\alpha_{\mathrm{transp}})$, where α_{transp} is the ratio of the radial transport induced by the field line diffusion divided by the anomalous transverse transport. This relation is only valid, if $\alpha_{\mathrm{transp}} \gg 1$ which is the case for typical divertor discharges in TEXTOR [Jakubowski et al. 2007]. At Tore Supra it was found, that the power deposition on the plasma facing components is determined by the maximum radial penetration of the field lines over the characteristic parallel

length of energy transport [Nguyen et al. 1997]

$$L_{\mathrm{T}} \approx \frac{1}{2} L_{\mathrm{K}} \ln\left(\frac{\chi_{\parallel} D_{\mathrm{FL}}}{\chi_{\perp} L_{\mathrm{K}}}\right).$$

For the configuration investigated here, with $L_{\mathrm{K}} \approx 20\,\mathrm{m}$, $\chi_{\parallel} \approx 2.1 \cdot 10^{8}\,\mathrm{m^2 s^{-1}}$, $D_{\mathrm{FL}} \approx 6 \cdot 10^{-6}\,\mathrm{m^2/m}$ [Schmitz et al. 2008b] and $\chi_{\perp} \approx 3\,\mathrm{m^2 s^{-1}}$ [Frerichs 2010a] we get a parallel scale length of

$$L_{\mathrm{T}} \approx 30\,\mathrm{m} \approx 0.75\,\mathrm{p.t.} \tag{3.1}$$

In the region with $L_{\mathrm{c,short}} \leq L_{\mathrm{T}}$ energy transport is expected to be dominantly parallel to the magnetic field (see figure 3.5(b)) and hence this area is seen to correspond to the scrape-off layer in poloidal divertors. The maximum radial penetration of the field lines over the length L_{T} can be inferred partly from the target-to-target connection length shown in figure 3.5(a). Short field lines in the helical divertor SOL exhibit shorter penetration depths while longer field lines even connect to the ergodic region. The long flux tubes therefore provide a major loss channel of the plasma to the edge, with the energy flux being partially cascaded down to the shorter ones until deposition onto the divertor [Kobayashi et al. 2004].

Since the beginning of its operation a number of experiments has been carried out investigating the influence of the resonant magnetic perturbations of the DED on the plasma structure in the plasma edge, the change in heat and particle load on the plasma facing components compared to the limiter configuration and on the divertor functionality regarding high density operation and impurity screening. At the same time and already during the design phase of the DED, theoretical models and codes were developed, adapted and used to study and explain these phenomena. The large flexibility of the DED setup regarding the applied perturbation field with the different base mode configurations and the position of the resonant surfaces is a blessing and a curse. On the one hand it gives the opportunity to study a large variety of stochastic boundary layers, with different radial extent, consisting of more or less developed laminar and ergodic regions. On the other hand this flexibility creates a very large parameter space.

Common to all the investigated scenarios in different base mode configurations and with different positions of the resonant surfaces is the observation of helical strike points (2, 4 or 8 in $m/n = 3/1$, $6/2$ and $12/4$, respectively) at the divertor target plates. At these strike points most of the power and particles are deposited and target temperature and density are highest, separated by areas of almost no flux and lower plasma parameters [Lehnen et al. 2005b,a, 2008; Jakubowski et al. 2007]. In front of these strike points a concentration of the emission from ionised carbon (C^{2+}) is observed. The width of the strike points in poloidal direction is a few cm up to 20 cm depending on the base mode. A comparison to the calculated magnetic field structures shows, that these strike points correspond to bundles

consisting of an intermixture of long and short field lines intersecting the target. These *divertor legs* are similar to the divertor legs of the helical divertor in the stellarator LHD (see section 2.2.4) with the difference of being broader, shorter with respect to the distance between target and residual 'X-point' (on top of the private flux region) but comprising field lines of longer connection length along the field line to the residual 'X-point'. For the helical divertor in TEXTOR, a correlation was found between peak heat fluxes at the divertor target and the radial penetration of the field lines in the divertor legs within a characteristic parallel length along the field lines [Jakubowski et al. 2007; Lehnen et al. 2008]. In a magnetic field configuration very similar to the configuration investigated in this thesis ($q_a = 3.6$, $I_{DED} = 3.75\,kA$, $\beta_p \approx 0.45$, $P_H = 1.1MW$, horizontal shift towards the HFS by 2-5 cm) a factor of 60 between the ion flux in the private flux region and in one of the strike points was measured [Lehnen et al. 2008]. The target ion flux was measured with an array of Langmuir probes embedded in the divertor target plates at one poloidal location (see section 4.2) applying strike point sweeping, thereby sweeping the magnetic structure $\pm 22.5°$ in the toroidal direction. Furthermore this measurement lead to the conclusion, that a major fraction of the particle and heat flux, namely 65%, is transported to the target via flux tubes with target-to-target connection lengths of 1-2 poloidal turns. As this measurement stems from a single toroidal cut at $\theta = \text{const} = 173°$ it is highly questionable, if this measurement is representative of the particle and heat flux distribution across the whole divertor target.

Inside the short magnetic flux tubes with a target-to-target connection length of one poloidal turn, the electron density has been found to decrease exponentially in the poloidal direction and electron temperature, target ion and heat flux exponentially decrease in the toroidal direction. Investigations of the plasma structure in the plasma edge revealed, that a correlation exists between magnetic field topology and measured plasma density and temperature. On the low field side, in regions with short target-to-target connection lengths, lower plasma density and temperature compared to the unperturbed case have been observed. In regions of long connection lengths the measured plasma density and temperature were higher than in the short connection length regions [Schmitz et al. 2008a]. The radial profiles of electron density and temperature at the edge are shifted inwards compared to the unperturbed case [Jakubowski et al. 2006].

In [Lehnen et al. 2007] the impurity screening capabilities as well as the possibilities of creating significant temperature gradients between the last closed flux surface and the target were estimated based on the magnetic topology. Therefore, the stochastic boundary was separated into the so-called *downstream* and *upstream area* based on the shortest connection length of the field lines to the divertor target plates $L_{c,short}$. The downstream area was defined as the area comprising all field lines with $L_{c,short} < 1$p.t. and the upstream area correspondingly that with $L_{c,short} \geq 1$p.t.. For the configuration discussed in this thesis, this definition is very similar to the discrimination of laminar and ergodic region adopted here from

[Ghendrih et al. 1996, 2002] (see section 2.2.3). The downstream area was found to show a strong variation in poloidal and radial direction with a radial extent of up to 7 cm in the 6/2 base mode configuration studied. The fraction of ionisation in the downstream area compared to the total ionisation in front of the divertor target was estimated by taking the Balmer α-radiation from neutral hydrogen as a measure of the ionisation source. This fraction is thought to give an estimation of the convective energy transport to the target (the higher the fraction, the lower the convective heat flux) and hence an indication of the possibility of establishing a significant temperature gradient between LCFS and target according to the high recycling regime in poloidal divertors. The fraction of the ionisation sources was shown to vary slightly with the edge safety factor with the highest fraction observed in the 6/2 configuration at $q_a \approx 3.6$ ($\approx 50\%$). This is one of the reasons for choosing a very similar magnetic field configuration for the investigations of high density operation in the framework of this thesis. However, cold and dense divertor plasma operation so far could only be achieved in the 3/1 base mode configuration [Lehnen et al. 2005b], where a high recycling regime was observed with the downstream density and ion flux growing more than linearly with the upstream density followed by a rollover of the target ion flux (detached regime) at target electron temperatures of $T_e \approx 10\,\mathrm{eV}$. Hereby, the upstream density as well as the temperature was measured in the plasma edge at the low field side in order to distinguish between core and edge transport. Indications for an increase in volume recombination in the vicinity of the divertor target, as known from deeply detached states in poloidal divertors, were not been observed. The detachment always occurred at plasma core densities close to the density limit. It used to be followed by a radiation instability creating a radiating belt at the high field side known as a MARFE (multifacetted asymmetric radiation from the edge) leading to a density limit disruption. In discharges with auxiliary neutral beam heating, the density for the onset of a MARFE was increased compared to the limiter configuration whereas the density limit was seen to be reduced in discharges with pure ohmic heating. Studies of high density regimes in the 12/4 base mode configuration using the target Langmuir probes [Van Rompuy 2009] revealed, that changes to β_p during density ramps in TEXTOR have a significant influence on the magnetic topology which cannot be neglected in this configuration. Hence, it is not surprising that the standard two-point model does not provide a satisfactory description of the measured scalings of the target ion flux and the electron temperature with the volume averaged electron density. The 6/2 configuration investigated in this thesis is more robust towards such changes of the poloidal beta with increasing density and furthermore develops broader strike points, thus reducing the effect of topology changes on the very localised Langmuir probe measurements.

Different capabilities of the scenarios were found regarding impurity screening. In the 6/2 and 12/4 base mode no reduction of the impurity content in the plasma core was seen, sometimes even an increase could be observed [Lehnen et al. 2007].

In the 3/1 base mode, a significant reduction of the carbon concentration in the plasma core by 30% was observed which is however still much less than the reduction seen with the ergodic divertor in Tore Supra.

All this previous work on particle recycling and transport in the helical divertor of TEXTOR shows that the investigation of high density divertor regimes is a complex three-dimensional problem. Radiation and recycling zones are unequally distributed along the magnetic flux tubes with distributions which depend on the precise path of the connecting field line. Due to the intimate contact between the different flux tubes and their different penetration depth on parallel transport scale lengths, cross-field transport is expected to play a role, leading to cascading effects for power and particles from the deeper penetrating flux tubes to the short ones and to friction between counter streaming flows as observed also in the helical divertor in LHD and the island divertor in W7-AS.

4 Diagnostic methods to characterise the plasma edge

The measurement of the hydrogen recycling and transport in the plasma edge is done using passive optical emission spectroscopy. In contrast to active diagnostic methods which can perturb the plasma by e.g. probes, particles or radiation, passive emission spectroscopy uses the radiation from the plasma particles themselves without disturbing the plasma. Hence, the method has the advantage that it does not involve possible changes of the quantities which are measured. For hydrogen a substantial fraction of the emitted radiation lies in the visible spectral range and can easily be recorded spectroscopically. The interpretation of this spectroscopic data can be very complex depending on the geometries and plasma parameters involved. For the understanding of plasma processes in detail a combination of this method with other active and passive diagnostic methods has to be used and complemented by plasma modelling.

In this chapter the background for the interpretation of spectroscopically measured photon emission is introduced, followed by a short description of complementing diagnostic methods used in the thesis such as probe measurements with Langmuir probes and beam emission spectroscopy with atomic beams.

4.1 Passive optical emission spectroscopy

In the plasmas investigated in this thesis predominantly collisions with electrons in the plasma are responsible for the population of excitation and ionisation stages of the emitting particles - neutral and not fully ionised atoms and molecules. Passive optical emission spectroscopy therefore provides information not only on the particles emitting the radiation but also on the plasma electrons (and possibly other species involved in the process).

The type of the emitting species can be determined from the wavelength of the emitted spectral line. For the determination of the number or number density of atoms and molecules, population models are needed that describe the population and depopulation processes of excited states and ionization stages in the plasma (see section 4.1.1). Such models calculate population densities depending on the plasma parameters. The number of photons emitted by the plasma (section 4.1.2) can then

be related to the number of particles in the ground state of the corresponding species (section 4.1.4) provided there is sufficient knowledge of the plasma parameters. Depending on the dominating line broadening mechanism (identified with the help of the line profile), the line shape of the spectral line can give insight into e.g. the electron density in case of the Stark effect or the energy and thereby the thermal velocity of the particles in case of the Doppler effect. The velocity in conjunction with the local electron density and temperature determines the penetration depth of the particles (section 4.1.3). The penetration depth of an atomic or molecular species in the plasma is the characteristic length describing the reduction of the particle density of this species due to ionisation or dissociation processes. It can therefore be estimated from the change of the particle density along the attenuation length. The velocity and therefore the penetration depth can give insight into the origin of the particles such as the release mechanism from the target surface or collision processes in the plasma. Electron density and temperature can also be determined from the ratio of the line radiation from different electronic transitions of the same species such as the Balmer lines for atomic hydrogen. For this, the ratio of three spectral lines is needed and these ratios, i.e. the ratios of the rate coefficients, must have a sufficient dependence on the two parameters. The relation of these spectral lines can also give insight into the dominating creation process of the emitting species such as electron impact excitation or recombination into excited states.

4.1.1 Equilibrium and population models

The densities of atomic, molecular and ionic species in a volume of plasma change as a result of competition between transport in and out of the volume, radiative transitions and state-changing collisions within the volume. The plasma is hereby thought of as providing an environment, usually defined by the plasma electron temperature and density, and atoms, molecules and ions move within this environment. Two types of species can be discriminated: those that come to collisional and radiative equilibrium with the plasma environment in times short compared to typical transport time scales and those, whose collisional and radiative time scales are of the same order or longer than the transport time scales. Transport calculations only need to be done for the slowly varying species and their densities can be considered as quasi-constant for the calculation of the equilibrium populations of the fast varying species or states (QSS: quasi-steady-state assumption for the 'fast' component). If transport processes for all states can be neglected compared to time scales in the population kinetics model, then all population ratios are fixed by the collision/radiation kinetics, they depend on the balance of the different processes dominant for reaching this so-called *collisional-radiative equilibrium*:

For **very high electron densities** ($n_e \gtrsim 10^{24}\,m^{-3}$ in hydrogen plasmas), the

population of excitation states and ionisation stages can be described by the local thermodynamic equilibrium (LTE) and the following three equilibrium distributions are valid:

- *Saha equation* relating the number densities of atoms, ions and electrons
- *Boltzmann distribution* of population among excited states
- *Maxwell distribution* of particle velocities

If the radiation energy is furthermore described by the *Planck blackbody function*, each collision and radiation process is in equilibrium with its inverse process and the plasma is in thermodynamic equilibrium.

For **very low electron densities** ($n_e \lesssim 10^{17}\,m^{-3}$ in hydrogen plasmas) the equilibrium populations can be described by the *corona model*. In this model it is assumed that upward transitions are due to electron collisions from the ground state only while downward transitions occur by radiative decay. The balance equations concerning population of excited states of atoms are:

$$a + e \rightarrow a^* + e \qquad \text{electron impact excitation}$$
$$a + h\nu \leftarrow a^* \qquad \text{spontaneous emission}$$

and the balance equations for the population of ionisation stages are:

$$a + e \rightarrow a^+ + e + e \qquad \text{electron impact ionization}$$
$$a + h\nu \leftarrow a^+ + e \qquad \text{radiative recombination}$$

where a and a^+ denote the atom and ion in its ground state, e is an electron, a^* is an electronically excited atom and $h\nu$ describes the radiation. At these low electron densities the population of the upper excited states is so low that further excitation into higher states or even ionization can be neglected and the ground state density represents the atomic density.

For **intermediate electron densities** the important population and depopulation processes for all excitation states and ionisation stages have to be balanced by the population model. Here, cascading from higher excited states, excitation out of metastable states or different dissociation processes of molecules can significantly influence the population densities. Such models are called collisional radiative models (CR models). For high and low densities collisional radiative models reduce to the LTE and corona equilibrium, respectively. For hydrogen different collisional radiative models have been developed, but models including hydrogen molecules are scarce as the vibrational and rotational excitation levels in molecules lead to further complexity. For *atomic* hydrogen the most prominent CR model is included in the ADAS package [Summers 2004]. The database provides rate coefficients for ionisation, recombination and charge exchange as well as photon

emission coefficients resulting from electron impact excitation and recombination into excited states depending on electron density and temperature.

Collisional-radiative equilibria (for all states) often hold in astrophysical plasmas, whereas in fusion plasmas typically some kind of transport equilibrium can be found. Usually only the transport of the ground state of neutral particles and ions and sometimes also of metastable states has to be considered while the time scales of the excitation and de-excitation processes ($\sim 10^{-7} - 10^{-8}$ s) are short compared to typical transport time scales ($\sim 10^{-1} - 10^{-5}$ s). The equilibrium (QSS-)populations of the excited states (fast varying species) relative to those of the slow species are then determined by collisional/radiative kinetics and can be determined by applying one of the above equilibria with respect to the excited states. Depending on the electron temperature, plasmas are often either of the ionising (> 10 eV) or recombining (< 1 eV) type, which means that the population densities of excited states are determined mainly by electron impact excitation from atomic hydrogen or recombination from the hydrogen ion (H^+), respectively (see figure 4.1). Edge plasmas in high temperature fusion devices typically have electron densities in the order of $n_e \approx 10^{18}\,m^{-3}$ and above and electron temperatures of several 10 eV and below. Therefore fusion edge plasmas mostly belong to the ionising plasmas and photon emission due to recombination can be neglected. However, when a divertor plasma passes into the high recycling regime or detached state the electron temperature drops between 1 eV and 10 eV and the plasma is neither dominantly ionising nor recombining. In this intermediate parameter range the average energy of the plasma particles is either below or close to the threshold energy of some of the excitation processes and the population densities are very sensitive to small changes in the plasma parameters. Furthermore, the simple relation between ionisation and photon emission rate does not hold anymore.

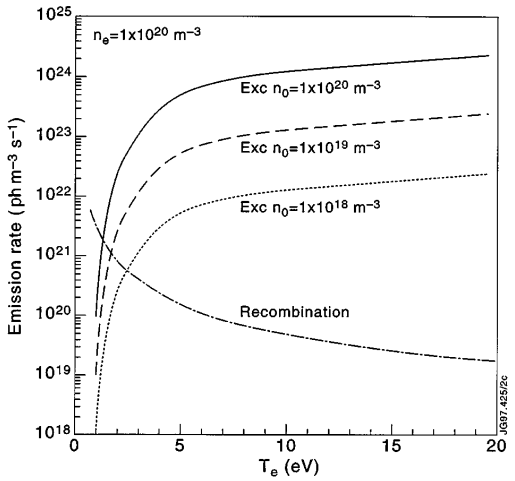

Figure 4.1
H_α emission rates due to excitation and recombination for an electron density $n_e = 10^{20}\,m^{-3}$ from the ADAS database [Summers 2004; McCracken et al. 1998]. The excitation rates are calculated for three different neutral densities.

The application of the ADAS CR model is not justified for the edge plasma conditions discussed in this thesis and either modifications or replacement of the CR model is necessary. The recycling at graphite plasma facing components in fusion devices has been found to involve a large fraction of hydrogen molecules thermally released from the surfaces [Brezinsek 2001]. Hence, population processes from additional neutral particles (H_2) or ions (H_2^+) can influence the population of excited states. In this case modifications to the inverse photon efficiencies calculated by the atomic CR model are often used in the interpretation of spectroscopic data (see section 4.1.4). The neutral transport code EIRENE [Reiter et al. 2005; EIRENE 2010], which was used to model the hydrogen recycling and transport in the helical divertor configuration in TEXTOR (by coupling it to the three-dimensional fluid code EMC3 in [Frerichs 2010a]), includes CR models also for hydrogen molecules. In EIRENE, the population of electronically excited states of atoms and molecules as well as the vibrationally excited states of the hydrogen molecules are calculated by these CR models relative to the transport dominated densities of electrons and the ground states of neutral and ionised hydrogen atoms and molecules.

4.1.2 Emission of spectral lines

The emission of a spectral line, i.e. the number of photons emitted per unit solid angle, time and volume of a transition between two electronic states $p > q$, from some point $\vec{r}$ in the plasma volume is given by the local emission coefficient $\epsilon_{p,q}(\vec{r})$:

$$\epsilon_{p,q}(\vec{r}) = \frac{1}{4\pi} n_p(\vec{r}) A_{p,q},$$

where $n_p(\vec{r})$ is the local particle density in the excited state p of the emitting species (atom, molecule or ion) at point $\vec{r}$ and $A_{p,q}$ the transition probability given by the Einstein coefficient of spontaneous emission. Hence emission spectroscopy yields the population density in the upper state p of the measured transition. A collisional radiative model now relates the population density in the upper state to the density in the ground state depending on the plasma parameters at the location of the emission.

In the simplest approximation the population density can be calculated by the corona equilibrium: The relation of the population of the excited state $n_p(\vec{r})$ to the density of atoms or ions in the ground state $n_1(\vec{r})$ is governed by the balance between electron impact excitation from the ground state and the spontaneous emission into all the lower excited states $q < p$:

$$\overbrace{n_1(\vec{r})\ n_\mathrm{e}(\vec{r})\ \langle \sigma_{exc}\ v_\mathrm{e} \rangle}^{\text{electron impact excitation}} = \overbrace{n_p(\vec{r})\ \sum_{q<p} A_{p,q}}^{\text{spontaneous emission}} \tag{4.1}$$

with local electron density $n_e(\vec{r})$ and the rate coefficient of electron impact excitation from the ground state $\langle \sigma_{exc}\ v_e \rangle$. The dependence of $n_p(\vec{r})$ on the local electron temperature $T_e(\vec{r})$ is implicitly given in the rate coefficient by the velocity of the electrons v_e: the rate coefficient is obtained from the convolution of the excitation cross section σ_{exc} with the electron energy distribution function. With this simple approximation, the local photon emission at point $\vec{r}$ per unit solid angle, time and volume is given by

$$\epsilon_{p,q}(\vec{r}) = \frac{B}{4\pi}\ n_1(\vec{r})\ n_e(\vec{r})\ \langle \sigma_{exc}\ v_e \rangle \tag{4.2}$$

with the branching ratio

$$B = \frac{A_{p,q}}{\sum_{q<p} A_{p,q}}.$$

Emission spectroscopy hence provides a measurement of the density of the ground state n_1 by measuring $\epsilon_{p,q}$, if the local electron density and temperature are known (actually emission spectroscopy typically provides a measurement of the line integrated emission). With knowledge of n_1, any other quantity determined by n_1 and an atomic rate coefficient can be inferred such as the ionisation rate according to equation 4.3.

If the corona equation for excitation has to be extended by other processes, e.g. excitation out of metastable states, or if a full collisional radiative model has to be applied, then still collisional and radiative balance relations (like 4.1) provide reduced population coefficients n_p/n_1 between the fast species n_p and the slow species n_1, so that emission spectroscopy also measures n_1.

The emission spectrum of atoms and molecules is determined by their atomic structure. For atomic hydrogen the radiative transitions into the excited state $p = 2$ (Balmer lines) lie in the visible spectral range and are commonly observed and analysed in fusion plasmas. In molecular hydrogen, due to the additional degrees of freedom in comparison to an atom, vibrational and rotational energy levels exist in the ground state and in many electronically excited states of the molecule. The molecular spectrum in the visible range corresponds usually to an electronic transition coupled to a vibrational transition. These vibrational bands consist of individual rotational lines originating from different rotational branches. An example of such a vibrational band is the so-called *Fulcher band* ($d^3\Pi_u - a^3\Sigma_g^+$ transition) corresponding to a $3 \rightarrow 2$ transition in the triplet system. In a molecule, the sum of all the vibrational and rotational populations yields the population in the electronically excited state.

4.1.3 Penetration depths

Consider the idealised situation of a planar, infinite plasma facing component made of graphite exposed to a homogenous plasma (see figure 4.2). Due to the impinging

ions, neutral particles will be partly reflected from the surface and released in random directions (with cosine characteristic) with the velocity of the individual particles $\vec{v}$ determined by the release process (as discussed in section 2.3.1). The individual particle velocities are given by the velocity distribution function $f(\vec{v})$. The ensemble of neutral particles moves away from the surface with fluid velocity

$$\vec{v}_\mathrm{f} \equiv \frac{1}{n} \int \vec{v}\, f(\vec{v})\, \mathrm{d}\vec{v}.$$

The local particle flux density $\vec{\Gamma}(r)$ in particles per unit area and time in front of the surface is defined as the product of the local particle density and the fluid velocity

$$\vec{\Gamma}(r) = n_1(r) \cdot \vec{v}_\mathrm{f}.$$

For the case considered here, the fluid velocity and therefore also the particle flux density always points in the direction of the surface normal (the radial direction r). Furthermore, the neutral particle density and therefore also the particle flux density only depends on the radial coordinate.

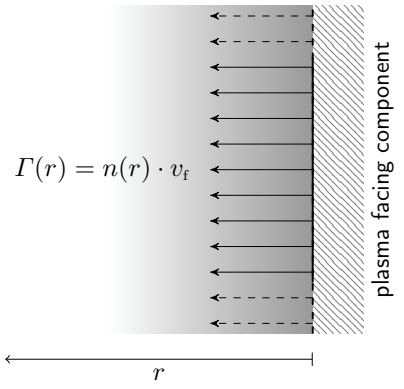

Figure 4.2
Local particle flux density $\Gamma(r)$ [particles $\mathrm{m}^{-2}\,\mathrm{s}^{-1}$] in front of a planar, infinite graphite surface. The grey gradient shows the radially decreasing neutral density $n(r)$.

The penetration of the neutral particles is limited by the ionisation and recombination events taking place in the plasma, i.e. by the population and depopulation processes of ionisation stages. From the point of view of the neutral particle density the particle source at the target surface defined as the total number of particles released per unit time $\partial N_\mathrm{e}/\partial t$ is equal to the volume integral of the sum of the local source strengths in the plasma over the attenuation volume V_att, such as volume recombination and ionisation. At low electron densities, the dominating population process is electron impact ionisation from the ground state described by the ion source distribution:

$$S_I(\vec{r}) = n_1(\vec{r})\; n_\mathrm{e}(\vec{r})\; \langle \sigma_I\; v_\mathrm{e} \rangle \tag{4.3}$$

with $\langle \sigma_I\; v_\mathrm{e} \rangle$ being the rate coefficient of electron impact ionisation from the ground state dependent on the electron temperature and therefore also on the

radial coordinate. Volume recombination is negligible, so that every atom coming from the surface is ionised exactly once on its way into the plasma. Hence, the number of ionisation events is equal to the number of atoms coming from the surface, i.e. the volume integral of the ionisation source strength is equal to the particle flux density through the surface of the attenuation volume A_{att}. According to Gauss's theorem this is equal to the volume integral over the divergence of the local particle flux density:

$$\frac{\partial N_{\mathrm{n}}}{\partial t} = \int\limits_{V_{\mathrm{att}}} S_I(\vec{r})\,\mathrm{d}V = -\int\limits_{A_{\mathrm{att}}} \vec{\Gamma}(\vec{r})\cdot\hat{n}\,\mathrm{d}S = -\int\limits_{V_{\mathrm{att}}} \mathrm{div}\,\vec{\Gamma}(\vec{r})\,\mathrm{d}V \tag{4.4}$$

For the case considered here the rate of change of the local particle flux density with r is therefore equal to the ion source distribution:

$$\frac{\partial \Gamma(r)}{\partial r} = -n_1(r)\; n_{\mathrm{e}}(r)\; \langle \sigma_I\; v_{\mathrm{e}} \rangle \tag{4.5}$$

and in case of a radially constant fluid velocity yields a formula for the radial change of the neutral particle density by integrating equation 4.5 from the target surface $r = 0$ to the radial position r:

$$n_1(r) = n_1(0)\cdot \exp\left(-\frac{1}{v_{\mathrm{f}}}\int_0^r n_{\mathrm{e}}(r')\; \langle \sigma_I\; v_{\mathrm{e}} \rangle\; \mathrm{d}r'\right)$$

When electron density and temperature are taken to be radially constant this equation can be simplified to:

$$n_1(r) = n_1(0)\cdot \exp\left(-\frac{r}{\lambda_{\mathrm{i}}}\right) \quad \text{with} \quad \lambda_{\mathrm{i}} = \frac{v_{\mathrm{f}}}{n_{\mathrm{e}}\; \langle \sigma_I\; v_{\mathrm{e}} \rangle} \tag{4.6}$$

The quantity λ_{i} is the ionisation length it can be regarded as a "mean free path" of the neutral particles before ionisation. It is a first estimate of the penetration depth of particles into the plasma and can be used to characterise the radial extent of the ion source distribution. In a more detailed estimation of the penetration depth of particles released from the surface, the type of the species plays an important role:

In case of molecules, the decay occurs either by ionisation or by dissociation. For hydrogen molecules at the electron temperatures relevant here, ionisation is the most probable process. The threshold energy for this molecular ionisation is much lower than the threshold energy for the ionisation of atoms. Therefore the penetration depth of molecules is much smaller than the penetration depth of atoms which are directly released from the target surface.

In case of hydrogen atoms, the rate coefficients for electron impact ionisation and resonant charge exchange are very similar at the plasma parameters typical of fusion edge plasmas. Resonant charge exchange processes can

significantly increase the velocity of the individual atom and lead to an increased penetration depth. In this case, the penetration depth is given by the geometric mean of the ionisation length λ_i as given above and the mean free path for the charge exchange process using for both the thermal ion velocity $v_\mathrm{i,th} = \sqrt{kT_\mathrm{i}/m_\mathrm{i}}$:

$$\lambda_\mathrm{pen} = \frac{v_\mathrm{i,th}}{n_\mathrm{e}\ \sqrt{\langle \sigma_I\ v_\mathrm{e}\rangle \langle \sigma_{CX}\ v_\mathrm{e}\rangle}}$$

Experimentally, the penetration depth can be estimated from the observation of the radial change of the local photon emission. Equations 4.2 and 4.6 provide the relation

$$\epsilon_{p,q}(r) = \epsilon_{p,q}(0) \cdot \exp\left(-\frac{r}{\lambda_\mathrm{i}}\right)$$

For the simplified assumption of constant electron density and temperature in the radial direction, the e-folding length of the local photon emission coefficient is an estimate of the penetration depth of the neutral particles.
The measurement of the local photon emission coefficient from atomic or molecular hydrogen recycling at a plasma facing component in a hydrogen fusion plasma is however not possible as every observation system integrates along the line of sight through the plasma. For the analysis of this integrated photon emission, the assumption has to be made, that the photon emission is very localised, decreasing the uncertainty in the determination of the local photon emission.

4.1.4 Deduction of particle fluxes

Measurements of spectral lines can be used to determine particle fluxes from limiter or divertor target plate surfaces. The *total* neutral particle flux density $\mathit{\Gamma}_\mathrm{n}$ released from a plasma facing component with area A_S in particles per unit surface area and time is given by (see 4.4)

$$\mathit{\Gamma}_\mathrm{n} = \frac{1}{A_\mathrm{S}}\frac{\partial N_\mathrm{n}}{\partial t} = \frac{1}{A_\mathrm{S}} \int\limits_{V_\mathrm{att}} n_1(\vec{r})\ n_\mathrm{e}(\vec{r})\ \langle \sigma_I\ v_\mathrm{e}\rangle \,\mathrm{d}V \tag{4.7}$$

A collisional radiative model relates the number of particles in the ground state in a certain volume (slow species) to the number of emitted photons from this volume by considering the different population and depopulation processes of the upper state of the radiative transition (fast species, see section 4.1.2). The number of photons $\partial N_\mathrm{p}/\partial t$ emitted per unit time from the attenuation volume is calculated by the volume integral of the emission coefficient of the respective spectral line over the attenuation volume multiplied by 4π, assuming a homogenous emission

in every direction. In the simple low density case, when the corona model can be applied, this gives:

$$\frac{\partial N_\mathrm{p}}{\partial t} = 4\pi \int\limits_{V_\mathrm{att}} \epsilon_{p,q}(\vec{r})\ \mathrm{d}V = B \int\limits_{V_\mathrm{att}} n_1(\vec{r}) n_\mathrm{e}(\vec{r}) \langle \sigma_{exc}\ v_\mathrm{e} \rangle\ \mathrm{d}V \tag{4.8}$$

Taking the ratio of equation 4.7 and 4.8 yields a relation between the total particle flux density and the measurable photon emission integrated over the attenuation volume of the neutral particles in the plasma:

$$\Gamma_n = \frac{\partial N_\mathrm{p}/\partial t}{A_\mathrm{s} \cdot B} \cdot \frac{\int n_1(\vec{r})\ n_\mathrm{e}(\vec{r})\ \langle \sigma_I\ v_\mathrm{e} \rangle(\vec{r})\ \mathrm{d}V}{\int n_1(\vec{r})\ n_\mathrm{e}(\vec{r})\ \langle \sigma_{exc}\ v_\mathrm{e} \rangle(\vec{r})\ \mathrm{d}V} \tag{4.9}$$

A general solution of this equation is only possible if the particle densities and rate coefficients are precisely known in the attenuation volume. Since the latter is mostly not fulfilled, a simpler version of equation 4.9 can be derived provided the ratio $\langle \sigma_I\ v_\mathrm{e} \rangle / \langle \sigma_{exc}\ v_\mathrm{e} \rangle$ has only a weak spatial (i.e. temperature) dependence in the region of interest:

$$\Gamma_n = \frac{\partial N_\mathrm{p}/\partial t}{A_\mathrm{s} \cdot B}\ \frac{\langle \sigma_I\ v_\mathrm{e} \rangle}{\langle \sigma_{exc}\ v_\mathrm{e} \rangle} = \frac{\partial N_\mathrm{p}/\partial t}{A_\mathrm{s} \cdot B} \cdot \frac{S}{X} \tag{4.10}$$

Thus, with knowledge of the inverse photon efficiency S/XB (see figure 4.3 for an example), photon fluxes can be converted into particle fluxes. In general terms, the excitation rate $X = \langle \sigma_{exc}\ v_\mathrm{e} \rangle$ can be replaced by a population rate provided by a collisional radiative model, which treats the excitation and deexcitation from all possible levels into the emitting one. The same holds for all possible ionisation processes. In the case of molecules the ionisation rate S is replaced by a decay rate D, as not only ionisation but also dissociation plays a significant role in the decay of the molecule.

In the determination of total particle flux densities from limiter or divertor target plate surfaces, special care has to be taken regarding the geometry of the particle releasing area and the observation volume. The photon emission measured by a light sensitive device is integrated over a volume ΔV, which is determined by the optical setup and the smallest unit of the sensor such as a single pixel on a CCD chip. The quantity measured is the volume integrated number of emitted photons $\partial N_\mathrm{p}/\partial t$ [photons s^{-1}] detected in a single pixel (see section 5.2). A line integrated photon flux density can be calculated from $\partial N_\mathrm{p}/\partial t$ by approximating the volume by a rectangular box spanned by the line of sight and the area ΔA imaged onto a single pixel.

For the case considered before and depicted in figure 4.2, the local particle flux density depends only on the radial coordinate. The total neutral particle flux density Γ_n released from the plasma facing component per unit time and area can therefore be determined by choosing the line of sight $r_2 - r_1$ in the direction of the

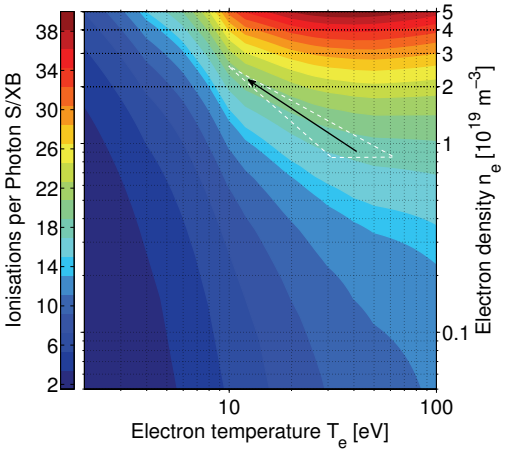

Figure 4.3
Ionisations per D_α photon $(S/XB)_{D_\alpha}$ from the ADAS database [Summers 2004]. The density and temperature range measured at the divertor target are indicated by the dashed triangle with the arrow marking the direction of the density increase.

surface normal. Any area on the particle releasing surface is equally representative for the determination of the total particle flux density, the area A_s can therefore be chosen e.g. equal to the area ΔA imaged onto a single pixel. The photon flux density is then determined by

$$\Phi = \frac{\partial N_p/\partial t}{\Delta A} = \frac{\partial N_p/\partial t}{A_s}$$

and equation 4.9 reads

$$\Gamma_n = \Phi \cdot \frac{S}{XB}$$

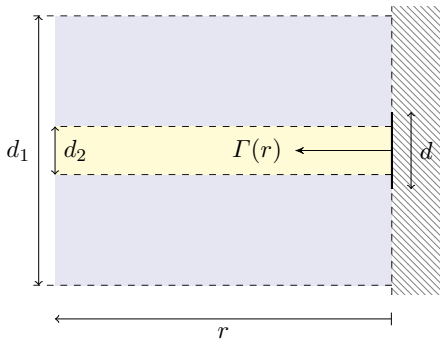

Figure 4.4
Neutral particle flux density from an area of width d on a plasma facing component. The extent of the surface and the particle source is assumed to be infinite in the direction perpendicular to the drawing plane.

The situation is different, if the spatial extent of the particle source is restricted in at least one direction, e.g. to the width d of a limiter or of a strike point on a divertor target (see figure 4.4). In the second direction along the surface often toroidal symmetry can be assumed, consequently the extent of the surface is

infinite in this direction and the particle flux density is assumed to be homogenous. In this situation, the local particle flux density of the neutral fluid $\Gamma(r)$ is not anymore directed radially from the whole particle source although the particle release is still assumed to be homogeneous across the whole source. In the previous example shown in figure 4.2 the local particle flux density was always directed radially because of the homogeneity and infinite extent of the particle source.

Depending on the relation between the extent of the particle source d and the penetration depths of the particles released from it λ_{pen}, two possibilities exist to determine the total particle flux density:

$d < 2\lambda_{\text{pen}}$: The volume of integration of the photon emission has to be chosen that large, that all the particles released from the surface are ionised inside it (with respect to the direction of the finite extent, width d_1 in figure 4.4). This way, the number of particles emitted per unit length (perpendicular to the drawing plane) and time is determined and has to be divided by the width d of the particle source to determine the flux density (i.e. the flux per area).

$d > 2\lambda_{\text{pen}}$: The above method for the infinite source can be applied to the area, the edges of which are at least λ_{pen} away from the edges of the whole particle source (width d_2 in figure 4.4). This holds true, of course, only if the spatial resolution is small enough. The method for $d < 2\lambda_{\text{pen}}$ can also be applied alternatively.

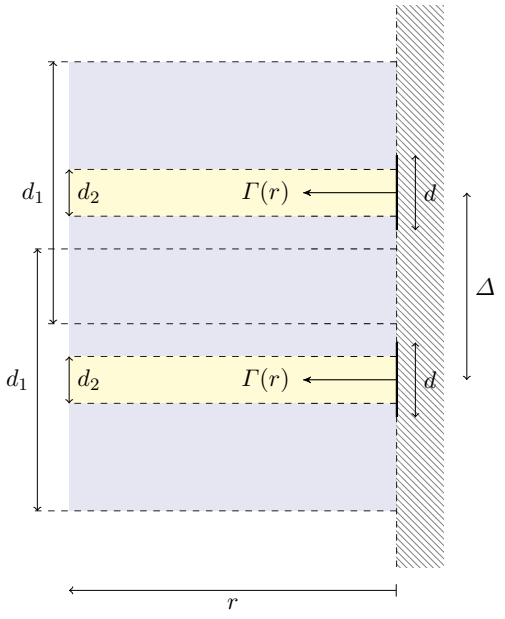

Figure 4.5
Neutral particle flux density from two adjacent areas of width d and distance Δ on a plasma facing component. The extent of the surface and the particle sources is assumed to be infinite in the direction perpendicular to the drawing plane.

The situation gets even more complicated, if several sources like the one shown in figure 4.4 are located next to each other (see fig. 4.5). In this case not only the width of the particle sources but also their distance Δ is decisive for the applicability of the method:

$\Delta > 2\lambda_{\mathrm{pen}}$: The sources can be separated, the methods of particle flux density determination can be applied depending on the above condition regarding d and λ_{pen}. For the first method, d_1 has to be chosen carefully in order not to include particles from the adjacent sources.

$\Delta < 2\lambda_{\mathrm{pen}}$: The sources cannot be separated, particle mixing from adjacent sources takes place. Still, the method for $d > 2\lambda_{\mathrm{pen}}$ discussed above can be applied if $\Delta > d - \lambda_{\mathrm{pen}}$. If $d < 2\lambda_{\mathrm{pen}}$, the particle flux density from the individual sources cannot be determined from photon emission measurements.

4.2 Langmuir probes

Langmuir probes are polarised conductors of small dimension widely used in diagnosing fusion edge plasmas due to their simplicity of operation. The probe collects charged particles from the plasma, resulting in a current which is a function of the polarisation potential (I-V characteristic) and from which different plasma parameters can be deduced.

For measuring local plasma parameters at the divertor target plates in TEXTOR an array of Langmuir probes is embedded in the target tiles. The probes are dome shaped with a radius of $r_{\mathrm{LP}} = 2\,\mathrm{mm}$ and are made of carbon fibre composite (CFC). They stick out from the graphite target tile which replaces the housing by 2 mm (see figure 4.6).

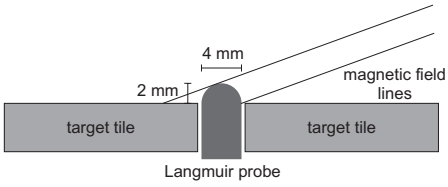

Figure 4.6
Sketch of Langmuir probe built into a target tile.

During the discharges analysed in this thesis unfortunately only one of these Langmuir probes delivered reliable data. This probe is located at a toroidal angle of $\varphi = 176.5°$ just below the equatorial plane at a poloidal angle of $\theta = 173.8°$ (see figure 4.7), which is the location of one of the helical strike points in the divertor configuration. The probe is located within the oblique line of sight of the spectroscopic camera diagnostic (see section 5) enabling a direct comparison

to the measured spectroscopic data when using the corresponding line of sight (profile P1).

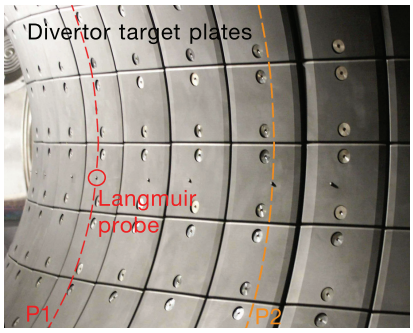

Figure 4.7
Target Langmuir probes and locations of profiles P1 and P2 for analysis of spectroscopic data (see figures (a)and 5.8).

The measurement principle of a Langmuir probe is describe in detail in literature, see e.g. [Hutchinson 1988; Stangeby 2001] and references therein. Therefore only a short summary will be given here. The probes at TEXTOR are biased in single probe mode with respect to machine ground and provide an I-V characteristic with a time resolution of 2.5 ms. By exponentially fitting the measured I-V characteristics, the ion saturation current I_{sat}, electron temperature T_{e} and floating potential V_{f} can be obtained using the function

$$I = I_{\mathrm{sat}} \left(1 - \exp\left(\frac{e(V - V_{\mathrm{f}})}{kT_{\mathrm{e}}}\right)\right).$$

In order to obtain the local ion flux density at the target $\Gamma_{\parallel}$ (parallel to the magnetic field) from the ion saturation current, the perpendicularly projected probe area has to be known. This area depends (weakly) on the incidence angle of the magnetic field lines α and can be calculated by $A = \frac{1}{2}\pi r_{\mathrm{LP}}^2(1 + \sin\alpha)$. Based on the parallel ion flux density, the electron density n_{e} at the probe sheath edge can be estimated assuming the ion flow velocity to be equal to the ion sound speed and the ion temperature to be equal to the electron temperature $T_{\mathrm{e}} = T_{\mathrm{i}}$.

Furthermore the parallel heat flux to the target $q_{\parallel}$ can be calculated from the parallel ion flux density and electron temperature measurement, according to

$$q_{\parallel} = \gamma\, k_{\mathrm{B}}\, T_{\mathrm{e}}\, \Gamma_{\parallel} \tag{4.11}$$

with the sheath transmission coefficient γ for the transfer of heat through the electrostatic sheath in front of the wall (usually $\gamma \approx 8$) and based also on the assumption that $T_{\mathrm{e}} = T_{\mathrm{i}}$.

4.3 Atomic beams

The application of material probes as those described in the previous section is restricted to the cold plasma edge, mostly to the scrape-off layer of the fusion

plasma. Passive optical emission spectroscopy due to the line of sight integration is rather limited regarding the delivery of spatially resolved information on plasma parameters. Active emission spectroscopy with the help of locally injected atomic beams facilitates the measurement of radial profiles of plasma parameters. Here the observation volume is defined by the intersection of the atomic beam and the line of sight of the observation system.

At TEXTOR different systems based on helium exist, one of them, the supersonic helium beam (SHE, [Kruezi 2007]), was available for measuring radial profiles in the discharges studied in this thesis. The helium beam is able to penetrate deep into the edge plasma and facilitates the simultaneous measurement of electron density and temperature also inside the last closed flux surface up to several $10^{19}\,\mathrm{m}^{-3}$ and about 200 eV. The diagnostic method is based on the measurement of three selected lines in the visible spectral range (667.8 nm, 728.1 nm and 706.5 nm). With the help of a collisional radiative model, electron density and temperature can be deduced from the ratio of these three lines. The supersonic helium beam is characterised by a particularly low divergence of the helium beam while still providing a high atomic density in the beam and therefore a good signal-to-noise ratio.

The SHE beam is located at a toroidal angle of $\varphi = 315°$ (see figure 5.2) at the top of the vessel shifted by 7.5 cm towards the low field side with respect to the centre of the geometrical minor radius at $R = 1.75\,\mathrm{m}$. For the magnetic configurations investigated in this thesis with the plasma column shifted towards the high field side, the beam therefore enabled the measurement of density and temperature profile about one centimetre inside the last closed flux surface in the limiter configuration. In the divertor configuration the observation volume correspondingly lies completely in the stochastic edge layer.

5 Spectroscopic camera observation system

The diagnostic mainly used in the course of this work is the SPectroscopic observation system for Emissions at the TEXTOR Wall (SPEW) - a camera observation system that monitors the inner wall at the high field side of TEXTOR covered by graphite target plates (see fig. 5.1(a)). During a plasma discharge, incident hydrogen ions impinging on the DED target plates, recycle and emit line radiation as neutrals (re-)entering the plasma again. Furthermore carbon and hydrocarbon particles are eroded (e.g. by physical and chemical sputtering) at the target surface which leads to the presence of line radiation also from those species (see fig. 5.1(b)). This optical emission is detected by the observation system introduced here, which spectrally selects the light coming from the plasma using narrowband interference filters and records it using a CCD (charge coupled device) camera as detector.

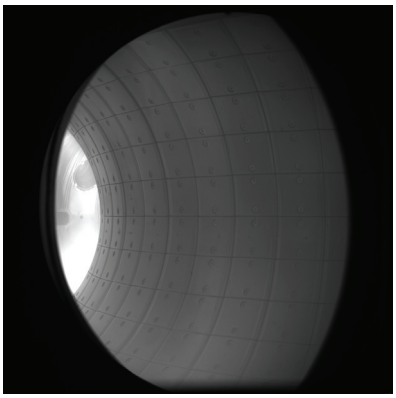

(a) Spectrally unfiltered image with homogeneous illumination of the target tiles during the breakdown of the discharge.

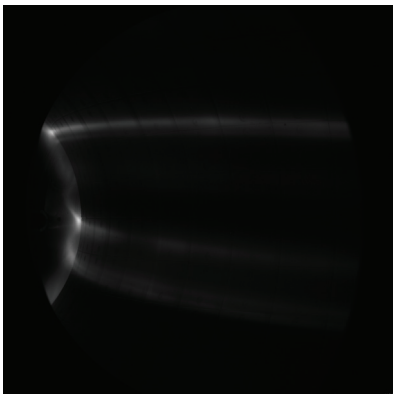

(b) C II (514 nm) emission during divertor operation (#106585).

Figure 5.1 Two images taken with the first setup stage of the observation system which consisted of only one CCD camera.

The final version of the system consists of two CCD cameras and two intensified CCD cameras and is therefore able to simultaneously record four images of different

line radiation representing up to four species in the plasma with the same line of sight. In this chapter the diagnostic setup is described, including the line-of-sight and the radiometric calibration of the observation system followed by a discussion of the spatial resolution and the uncertainties of the measurement.

5.1 Diagnostic setup

The diagnostic setup of the observation system (see green circle in figure 5.2) consists of an optical setup described in section 5.1.2 and the detection system comprising the four CCD cameras and image intensifiers described in section 5.1.3. The description of the diagnostic setup starts with specifying the observation angle of the system in section 5.1.1.

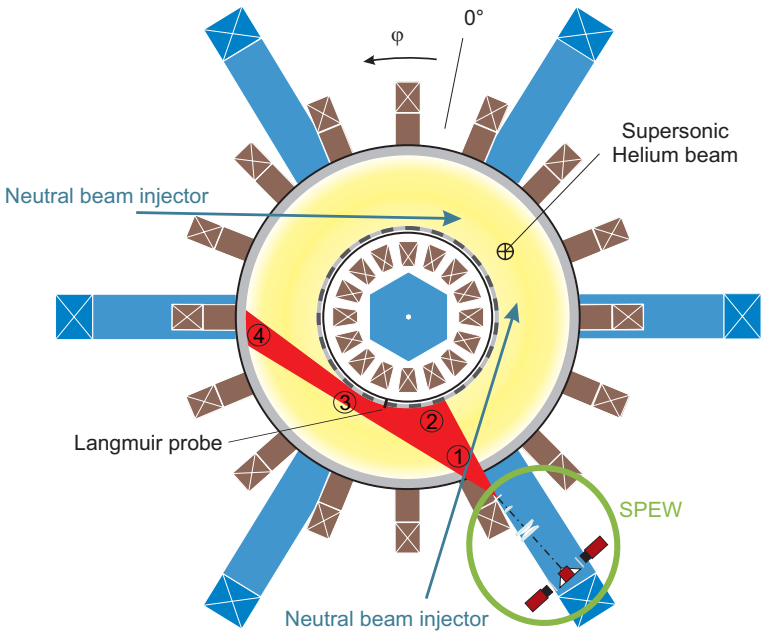

Figure 5.2 Schematic view of an equatorial cut of TEXTOR showing the location of SPEW (green circle). Outside the vacuum vessel several lenses image the light onto a reflective pyramid which splits up the light onto the four CCD cameras (see fig. 5.4). The locations of several other edge diagnostics used in this work are also depicted. The encircled numbers label the different regions of photon emission discussed in section 5.1.1.

5.1.1 Line-of-sight and observation angle

The observation system is located between two toroidal field coils and one of the TEXTOR transformer yokes, looking through a diagnostic port in the equatorial plane at the low field side of TEXTOR. The design of the system was made in such a way as to be able to view not only the target plates (region 2 in figure 5.2), but also lines of sight tangential to the target surface (region 3) providing information about the penetration depths of the neutral particles and the structure of the magnetic field of the helical divertor. The line integrated photon flux density from region 2 gives insight into the flux of neutral particles from the target surface as discussed in section 4.1.

The complete view of the observation system is depicted in figure 5.1 with figure 5.1(b) showing the same view as (a) but in the light of line radiation from singly ionised carbon (CII multiplet at 514 nm) during a plasma discharge with divertor operation. It illustrates the strike line pattern observed at the target plates created by the resonant magnetic perturbations. As can be seen from the images, the system mainly observes the inner wall directly; the toroidal angle covered spans from $\varphi = 160°$ to 210° and the poloidal angle from $\theta = 130°$ to 230° (the poloidal angle defined as shown in figure 3.3(a)). The line of sight is mostly not perpendicular to the target but under an oblique angle. At the right hand side of the image (at $\varphi \approx 205°$) the line of sight is almost identical to the target normal. Towards the left hand side of the image the angle between target normal and line of sight increases until it reaches 90° when the observation view passes the target tangentially. The toroidal position of this cross section was estimated to $\varphi = 154.7°$. The integration path length increases with increase of the incidence angle, leading to a rise of the integrated photon emission. Photon emission from particles recycling at the wall at the low field side in regions 1 and 4 can also contribute to the recorded integrated photon flux densities. However, the fluxes from these regions are expected to be considerably smaller than the photon fluxes from the particles recycling at the high field side. In the discharges discussed here, the main plasma wall interaction took place at the DED target plates because the plasma was moved towards the high field side by 2.4 cm leading to a large plasma wall clearance at the low field side. Only at low plasma core densities molecular photon fluxes almost comparable to the fluxes from the target plates are observed in region 4. Increasing the core density however raises the target photon fluxes much more than the fluxes from the low field side. Besides that, region 1 lies outside the depth of field of the optical system, the light emitted there is not focused on the sensor of the camera but only raises the background level in the whole image.

5.1.2 Optical setup

The optical setup of SPEW can be separated into several parts, one part being used also by an infrared camera. Hence, the window and collimating lens (L1) in this part of the setup are made of CaF_2, a material of sufficient transmittance not only in the visible but also in the infrared range of the electromagnetic spectrum. The light is then split up spectrally by a dichroic mirror (D) transmitting the visible and reflecting the infrared radiation optimised for an incidence angle of 45°. After its transmission through the beamsplitter the light passes through a set of collimating lenses (L2) creating the appropriate field of view (⌀ 10 cm), before falling onto the reflective pyramid. The pyramid geometrically splits the light into four equivalent arms of the diagnostic, each consisting of a set of filter wheels for neutral density and interference filters, a focusing lens (L3) and a CCD camera. Details about the optical and geometrical properties are given in table 5.1.

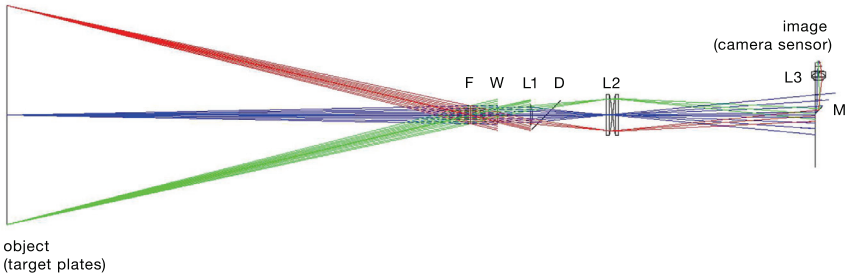

(a) The complete optical setup for the camera without MCP. TEXTOR is located on the left, the distance to the port window (W) is ≈ 1.7 m and the distance from W to the top of the pyramid is ≈ 1.14 m.

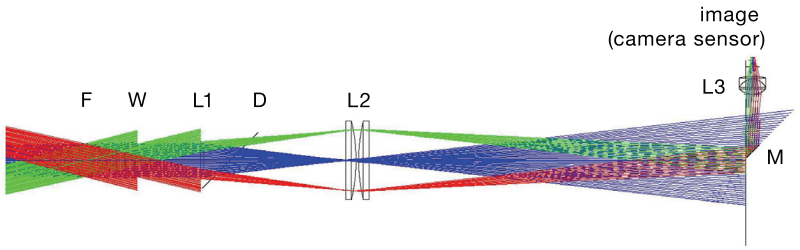

(b) Closer look at the optical setup still showing all of the imaging elements.

Figure 5.3 Drawing of the optical setup of SPEW created using the optical design software ZEMAX. Only one camera without image intensifier is shown exemplarily. At each light transmitting or reflecting element some of the rays are vignetted by the limited aperture of the element. The optical elements are summarised in table 5.1.

Symb.	Optical element	Material/Optical properties	Size [mm^2]	Focal length [mm]
D	dichroic mirror (45°)	400-800 nm : $T = 75\%$ 3-5 µm : $R > 60\%$	100×150	n/a
F	aperture (flange)	n/a	⌀ 63 mm	n/a
L1	plano-convex lens	CaF_2	⌀ 76.2 mm	253.7
L2	pair of identical plano-convex lenses	BK7	⌀ 150 mm	620
L3	achromat			
	for camera	N-SSK5 and SF6	⌀ 50 mm	50
	for MCP-camera	450-700 nm : $T > 99\%$	⌀ 50 mm	100
M	mirror on pyramid	Al coated crown glass	$\approx 65 \times 42$	n/a
W	window	CaF_2	⌀ 82 mm	n/a

Table 5.1 Optical elements and their properties.

Wavelength [nm]	Spectral line	Transition	FWHM [nm]
434.0	D_γ	D(5)→D(2)	1.5
465.0	C III		3.0
486.0	D_β	D(4)→D(2)	1.5
514.0	C II		1.5
601.5	D_2	Fulcher band ($d^3\Pi_u - a^3\Sigma_g^+$)	1.5
656.0	D_α	D(3)→D(2)	3.0

Table 5.2 Interference filters with central wavelengths and spectral widths. All filters are blocked for IR radiation.

In order to select only the desired spectral line from the complete light emission of the plasma, narrowband interference filters with a FWHM of 1 to 3 nm were placed in front of each camera. Filters were used to observe e.g. the Balmer series of deuterium (D_α, D_β, D_γ), wavelengths spans of the Fulcher band of molecular deuterium and atomic carbon lines (CI, CII, CIII). The filters used and their properties are summarised in table 5.2. The standard filter setting applied to study the hydrogen recycling consisted of the three Balmer line filters and the Fulcher band filter covering the first main diagonal transition of molecular deuterium.

The filter characteristic, i.e. the transmission as a function of the wavelength, of the Balmer line interference filters $\tau(\lambda)$ has been measured using an integrating sphere as a light source and a high resolution spectrometer for detecting the transmission spectrum. In the radiometric calibration of the observation system described in section 5.2 the filter characteristic is needed to calculate the so-called

effective bandwidth $\Delta\lambda_{\text{eff}}$ defined by

$$\Delta\lambda_{\text{eff}} \equiv \frac{\int \tau(\lambda) d\lambda}{\tau(\lambda_0)} \tag{5.1}$$

where λ_0 is the wavelength of the observed spectral line. In case λ_0 exactly matches the central wavelength of the narrowband interference filter, the effective bandwidth can be approximated by the peak transmission of the filter and its FWHM.

To control the amount of light detected by the camera sensors and especially to protect the image intensifiers from damaging over-saturation, neutral density filters were installed in a second filter wheel. The approximate optical densities and transmissions of these neutral density filters at a wavelength range of 400 nm to 700 nm are given in table 5.3. The transmission characteristic $\tau(\lambda)$ of each of these filters was measured using a commercially available system for spectral transmission and reflection measurements. The internal setup is identical to the setup used to measure the interference filters.

Optical density	Transmission
0.5	0.32
1.0	0.10
1.5	0.03
2.0	0.01
2.5	0.003

Table 5.3 Neutral density filters installed in one of the filter wheels in each arm of the diagnostic. The approximate optical density and transmission is given for a wavelength range of 400 to 700 nm.

5.1.3 Detection system

Digital, monochrome CCD cameras (AVT Pike F-100B fiber) are used to record the spectrally filtered light emission from the plasma. According to the spectral lines that should be observed, the camera type was chosen to be sensitive in the visible spectral range. Furthermore, a camera model had to be chosen that is capable of undisturbed data recording and transfer in spite of the harsh environment at the location of the diagnostic due to electromagnetic fields. The camera was proven to withstand magnetic field strengths of 90 mT measured during TEXTOR operation about 50 cm closer to the TEXTOR vessel than the location of the cameras in the final version of SPEW. One reason for the good performance of this camera type in this environment is its data connection via optical fibers (FireWire).

The cameras are equipped with a Kodak image sensor (KAI-1020) with a maximum resolution of 1000×1000 pixels and a pixel size of $7.4\,\mu\text{m} \times 7.4\,\mu\text{m}$. The dynamic range of the sensor is 10 bit, i.e. the contrast ratio that can be captured is about 1000:1, and the camera has an ADC of 14 bit, allowing the full dynamic range

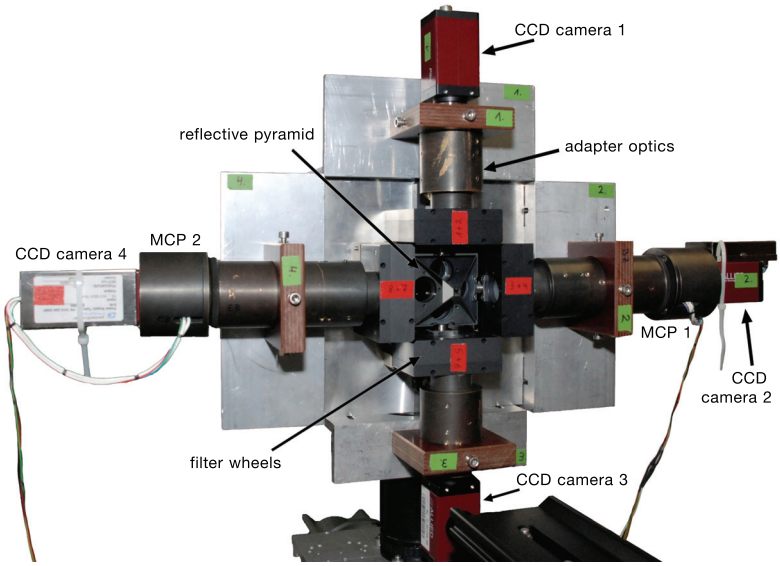

Figure 5.4 SPEW set up in the laboratory. The centre of the diagnostic is a reflective pyramid which splits up the light coming onto the plane from the TEXTOR window to the four arms of the diagnostic.

to be stored in an image. The sensor is an interline transfer CCD, i.e. it has a light sensitive area interleaved with a separate storage area, and is equipped with microlenses to effectively increase the light sensitive area. The electronic shutter allows exposure times between 43 µs and ≈ 67 s and the cameras can operate at a full frame rate of 32.8 Hz (or 59.9 Hz with reduced dynamic range).

An image acquisition software has been written as part of this thesis to be able to integrate the cameras into the triggering scheme used at TEXTOR in order to define an appropriate timeline. This acquisition software is capable of storing images in RAW or PNG file format (16 bit mode) and additionally in BMP format in 8 bit mode. The cameras can be either operated in so-called single-shot mode, with each frame triggered separately, or in multi-shot mode, where a preset number of frames is recorded after an initial start trigger. The start of exposure for the first frame jitters by ±1.65 µs and the readout time is 8.2 µs. Typically the cameras were operated at maximum frame rate and at exposure times of 1 to 30 ms. The acquisition software selectively stores the recorded images under the appropriate TEXTOR shot number and uploads the recorded images into the central storage facility directly after each discharge making it available for subsequent data analysis.

Image intensifiers

Two of the four cameras have been equipped with single MCP image intensifiers (MCP-PROXIFIER, see [Proxitronic 2010]) to be able to also record spectral lines of low intensity such as the D_γ line or the emission from molecular deuterium and CD molecules. Hence, two different types of image intensifiers were chosen: MCP 1 in figure 5.4 is optimised for detecting radiation around 400 nm (BV 2562 BZ), MCP 2 is optimised for the range of 500 to 600 nm (BV 2562 EZ).

A single MCP image intensifier consists of a photocathode, one microchannel plate and a phosphor screen. The input diameter of the photocathode is 25 mm. The image intensifiers were coupled to the camera sensor by a fibre taper which was glued directly onto the CCD chip after removing the protection glass. The choice of the photocathode mainly determines the spectral sensitivity of the image intensifier, whereas the choice of the phosphor screen determines the response time of the intensified camera and its emission spectrum has to fit the sensitivity of the CCD chip coupled to it. The phosphor screen is made of Gd_2O_2S:Tb which has its maximum emission close to the maximum sensitivity of the CCD at 545 nm and a slow decay time of 1 ms (from 90% to 10%).

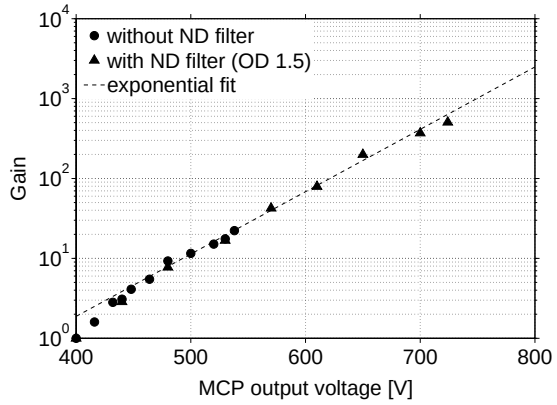

Figure 5.5
Measured gain of the intensified camera comprising image intensifier BV 2562 BZ with the D_γ filter installed in front of the photocathode. The dashed line shows an exponential fit of the data points above 450 V.

The gain of the image intensifier is externally controlled by a control voltage of 0 to 5 V which is translated into an MCP output voltage of 400 to 800 V. The dependence of the gain of the intensified camera on the output voltage has been measured for both image intensifiers using an integrating sphere as a stable light source. Fig. 5.5 shows the result for image intensifier BV 2562 BZ with the D_γ filter installed in front of the photocathode. The dots show results from measurements using no neutral density filter to attenuate the light from the integrating sphere. The triangles show results from measurements with a neutral density filter installed transmitting only 3 % of the available light. For output voltage values of more than 450 V the gain grows exponentially with increasing output voltage. Below it

decreases stronger than the exponential fit predicts. The measurements shown in fig. 5.5 were done using the same setup as in the calibration of the CCD cameras (see section 5.2). Therefore from this data the calibration factor for each control voltage setting could be calculated in order to translate the measured grey value into a flux of photons from the plasma. The comparison of the measurement with and without neutral density filter shows that in this intensity range, the gain of the intensified camera is also independent of the incident amount of light.

5.2 Radiometric calibration of the observation system

The observation system integrates the photon emission from the plasma over

time: determined by the exposure time t_{exp} set

spectral region: determined by the wavelength range transmitted by the system (especially the interference filter)

spatial region: the observation volume ΔV imaged onto each pixel determined on the one hand by the emission volume (determined by the penetration depth of the emitting species) and on the other hand by the optical setup, partly characterised by the solid angle of the observation system $\Delta\Omega$

In order to be able to deduce the number of photons N_{p} emitted by the plasma for a certain spectral line of wavelength λ_0 from the images taken by SPEW, the spectral response of the complete diagnostic system has to be measured. For such an absolute or radiometric calibration a light source of known spectral radiance is needed, such as a spectrally calibrated integrating sphere (so-called Ulbricht sphere).

Optical and digital imaging deals with different spaces and consequently different coordinate systems. In the following discussion, these spaces are called the object space (the tokamak with the plasma as the source of light) $V_{\mathrm{r}} \subset \mathbb{R}^3$, the sensor space (the plane of the CCD image sensor) $V_{\mathrm{s}} \subset \mathbb{R}^2$ and the image space $V_{\mathrm{i}} \subset \mathbb{Z}^2$ with discrete grid coordinates described by the grid vectors

$$\vec{r}_{\mathrm{i}} = (m\,\Delta x, n\,\Delta y) \quad \text{with} \quad m, n \in \mathbb{Z}. \tag{5.2}$$

The recorded image, expressed by the grey value $GV(\vec{r}_{\mathrm{i}})$ in each pixel measured in counts, is a scalar field on the image space V_{I}. A calibration relates this grey value to the integral of $\epsilon(\vec{r}_{\mathrm{r}})$, which is a scalar field on the object space. The grey value in each pixel is proportional to the integral of the photon flux density $i(\lambda, t, \vec{r}_{\mathrm{s}})$ incident on the sensor over the pixel area $\Delta x\,\Delta y$ and the exposure time t_{exp}. The spectral response of the sensor $s_{\mathrm{CCD}}(\lambda)$ at a certain wavelength in counts per photon

is taken to be constant across the image sensor, variations in the uniformity are assumed to be negligible compared to other measurement uncertainties. In this case, the grey value can be expressed as:

$$GV(\lambda, \vec{r}_\mathrm{i}) = s_\mathrm{CCD}(\lambda) \cdot t_\mathrm{exp} \cdot \Delta x \cdot \Delta y \cdot \langle i \rangle(\lambda, \vec{r}_\mathrm{i})$$

with

$$\langle i \rangle(\lambda, \vec{r}_\mathrm{i}) = \frac{1}{t_\mathrm{exp}\, \Delta x\, \Delta y} \int_0^{t_\mathrm{exp}} \int_{(m-1/2)\Delta x}^{(m+1/2)\Delta x} \int_{(n-1/2)\Delta y}^{(n+1/2)\Delta y} i(\lambda, t, \vec{r}_\mathrm{s})\, \mathrm{d}t\, \mathrm{d}x\, \mathrm{d}y$$

being the incident photon flux density averaged over exposure time and pixel area. The incident photon flux density $i(\lambda, t, \vec{r}_\mathrm{s})$ is determined by

- the photons *emitted* by the plasma or the integrating sphere given either in photons $\cdot\, \mathrm{m}^{-3} \cdot \mathrm{s}^{-1} \cdot \mathrm{sr}^{-1}$ or in photons $\cdot\, \mathrm{m}^{-2} \cdot \mathrm{s}^{-1} \cdot \mathrm{sr}^{-1}$
- the observation volume $\Delta V(\vec{r}_\mathrm{i})$ or observation area $\Delta A(\vec{r}_\mathrm{i})$ imaged onto a single pixel on the sensor with grid vector $\vec{r}_\mathrm{i}$ determined by the optical setup
- the emission solid angle $\Delta\Omega$ determined by the optical setup
- the spectral transmission properties of the interference filter given by its filter characteristic $\tau(\lambda)$
- the transmission of the neutral density filter T_ND
- the transmission of the optical setup T_Sys without filters

The detailed determination of the photon flux density incident on the sensor from the plasma and from the integrating sphere is discussed in the following.

Photon flux from the plasma

The number of photons per unit time *incident* on the pixel with grid vector $\vec{r}_\mathrm{i}$ for a specific spectral line λ_0 is proportional to the number of photons N_p *emitted* by the plasma per unit time from the volume $\Delta V(\vec{r}_\mathrm{i})$:

$$\langle i_\mathrm{Pla} \rangle(\lambda_0, \vec{r}_\mathrm{i}) \cdot \Delta x\, \Delta y = \tau(\lambda_0)\; T_\mathrm{Sys}(\lambda_0)\; T_\mathrm{ND}(\lambda_0) \cdot \frac{\partial N_\mathrm{p}(\Delta V(\vec{r}_\mathrm{i}))}{\partial t}$$

The photon emission from the plasma can be calculated from the local emission coefficient $\epsilon_\mathrm{p,q}(\vec{r}_\mathrm{r}, t)$ by integrating over the plasma exposure time t_Pla, the volume $\Delta V(\vec{r}_\mathrm{i})$ and the solid angle of the observation system $\Delta\Omega$. As the emission coefficient is constant over the solid angle, this integral can be executed:

$$\frac{\partial N_\mathrm{p}(\Delta V(\vec{r}_\mathrm{i}))}{\partial t} \cdot t_\mathrm{Pla} = \Delta\Omega \int_{t_\mathrm{P}} \int_{\Delta V(\vec{r}_\mathrm{i})} \epsilon_\mathrm{p,q}(\vec{r}_\mathrm{r}, t)\; \mathrm{d}t\; \mathrm{d}V$$

The grey value is therefore given as:

$$GV_{\mathrm{Pla}}(\lambda_0, \vec{r}_{\mathrm{i}}) = s(\lambda_0) \int_{t_{\mathrm{Pla}}} \int_{\Delta V(\vec{r}_{\mathrm{i}})} \epsilon_{\mathrm{p,q}}(\vec{r}_{\mathrm{r}}, t)\ \mathrm{d}t\ \mathrm{d}V \tag{5.3}$$

with the spectral response of the observation system at the observed spectral line λ_0 consequently defined as:

$$s(\lambda_0) = s_{\mathrm{CCD}}(\lambda_0) \cdot T_{\mathrm{Sys}}(\lambda_0) \cdot T_{\mathrm{ND}}(\lambda_0) \cdot \tau(\lambda_0) \cdot \Delta\Omega$$

This spectral response can now be determined by the measurement with a light source of known spectral radiance.

Photon flux from the integrating sphere

An integrating sphere (also called Ulbricht sphere) is a hollow sphere with a diffusely reflecting internal surface and typically two or more small openings (ports) for introducing light sources or attaching a photodetector. In this calibration setup the sphere is used to create a light source with known intensity uniform over all positions within its circular aperture and independent of direction except for the cosine function inherent to ideally diffuse radiating surfaces (Lambertian surfaces). The emission of the sphere is given by its spectral radiance for a range of wavelengths (see fig. 5.6):

$$L_\lambda = \frac{\partial^3 \phi}{\cos\theta\ \partial A\ \partial\Omega\ \partial\lambda} \qquad \text{with} \qquad [L_\lambda] = \frac{\mathrm{mW}}{\mathrm{cm}^2 \cdot \mathrm{sr} \cdot \mu\mathrm{m}} \quad ,$$

where ϕ is the radiant flux (or radiant power) in Watts, $\cos\theta\ \partial A$ the projected source area and $\partial\Omega$ the unit solid angle of emission. From this, the photon flux density emitted by the sphere is calculated using the energy of a single photon according to $E(\lambda) = h \cdot \nu = h \cdot c \cdot \lambda^{-1}$.

The number of photons incident on a pixel per unit time from the integrating sphere is therefore given by:

$$\langle i_{\mathrm{Cal}} \rangle(\lambda_0, \vec{r}_{\mathrm{i}}) \cdot \Delta x\, \Delta y = \int \frac{L_\lambda(\lambda)}{E(\lambda)}\ T_{\mathrm{Cal}}(\lambda)\ T_{\mathrm{ND,Cal}}(\lambda)\ \tau(\lambda)\ \mathrm{d}\lambda\ \mathrm{d}A\ \mathrm{d}\Omega$$

with T_{Cal} denoting the transmission of the setup (without filters) used in the calibration measurement. This transmission differs from the transmission T_{Sys}, because the calibration measurement was executed in the laboratory with the same optical setup except for the TEXTOR window. The transmission of this window is taken into account using a constant transmission of $T_{\mathrm{W}} \approx 0.96^2$. This value is reasonable for a freshly installed window, depositions during the operation of TEXTOR, though, will lower the transmission and change the wavelength

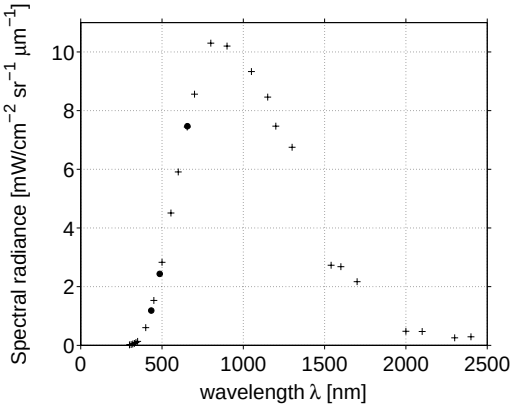

Figure 5.6
The spectral radiance L_λ of the sphere used in the calibration measurement. The crosses mark the known values, the dots were interpolated from these values for the central wavelengths λ_0 of the Balmer line interference filters used in the measurements.

characteristic. However, exemplary measurements prior to and after an earlier measurement campaign showed, that the transmission in the wavelength range of 420 to 700 nm stayed only weakly dependent on the wavelength. In the calibration measurements, also different neutral density filters were used, due to the different spectral radiance of the integrating sphere compared to the plasma. Exposure time and neutral density filter had to be adjusted for each interference filter in order to avoid saturation of the images.

The spectral radiance, photon energy and transmissions T_{Cal} and $T_{\mathrm{ND,Cal}}$ are taken to be constant across the narrow filter width and can hence be approximated by their values at the wavelength of the observed spectral line λ_0. The opening of the integrating sphere was oriented perpendicular to the optical axis. Executing the integration over observation area and emission angle leads to a formula giving the grey value in the calibration measurement of:

$$GV_{\mathrm{Cal}}(\lambda_0, \vec{r}_{\mathrm{i}}) = t_{\mathrm{Cal}} \cdot s_{\mathrm{CCD}}(\lambda_0) \cdot T_{\mathrm{Cal}}(\lambda_0) \cdot T_{\mathrm{ND,Cal}}(\lambda_0) \cdot \Delta\Omega \cdot \Delta A(\vec{r}_{\mathrm{i}}) \cdot \frac{L_\lambda(\lambda_0)}{E(\lambda_0)} \int \tau(\lambda) \mathrm{d}\lambda$$

As the calibration measurements were done using the same setup of the observation system as used for the plasma measurements (except for the TEXTOR window), the spectral response of this setup $s(\lambda_0)$ with the neutral density filter of transmission $T_{\mathrm{ND}}(\lambda_0)$ can be calculated by:

$$s(\lambda_0) = \frac{GV_{\mathrm{Cal}}(\lambda_0, \vec{r}_{\mathrm{i}})}{t_{\mathrm{Cal}}} \cdot \frac{E(\lambda_0)}{L_\lambda(\lambda_0) \cdot \Delta\lambda_{\mathrm{eff}} \cdot \Delta A(\vec{r}_{\mathrm{i}})} \cdot \frac{T_{\mathrm{W}}(\lambda_0) \cdot T_{\mathrm{ND}}(\lambda_0)}{T_{\mathrm{ND,Cal}}(\lambda_0)} \tag{5.4}$$

with the effective bandwidth $\Delta\lambda_{\mathrm{eff}}$ defined according to equation 5.1. The spectral response that was determined for the standard setting of the Balmer line filters in CCD camera 1-3 (see figure 5.4) without neutral density filter is exemplarily given in figure 5.7.

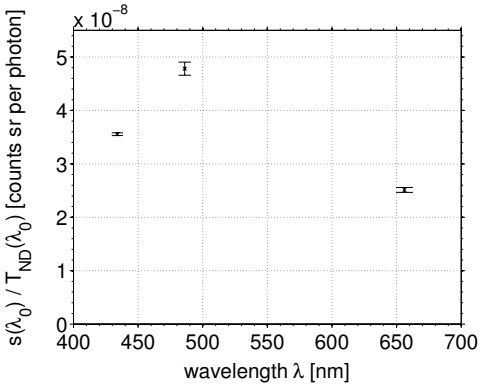

Figure 5.7
Spectral response for the D_β (camera 1), D_γ (camera 2, MCP output voltage 440 V) and D_α (camera 3) interference filter without neutral density filter.

With the spectral response calculated above using equation 5.4, the number of photons $N_\mathrm{p}(t_\mathrm{P}, \Delta V, \vec{r}_\mathrm{i})$ can be calculated that is emitted by the plasma from the observation volume ΔV imaged onto a single pixel during the exposure time t_P in every direction 4π sr assuming an isotropic photon emission:

$$N_\mathrm{p}(t_\mathrm{P}, \Delta V, \vec{r}_\mathrm{i}) = 4\pi \int_{t_\mathrm{P}} \int_{\Delta V(\vec{r}_\mathrm{i})} \epsilon_\mathrm{p,q}(\vec{r}_\mathrm{r}, t)\ \mathrm{d}t\ \mathrm{d}V = 4\pi \cdot \frac{G V_\mathrm{P}(\lambda_0, \vec{r}_\mathrm{i})}{s(\lambda_0)} \tag{5.5}$$

The photon flux in photons per unit time from the volume $\Delta V(\vec{r}_\mathrm{i})$ averaged over the exposure time can be calculated from $N_\mathrm{p}(t_\mathrm{P}, \Delta V, \vec{r}_\mathrm{i})$ by dividing by t_P.

5.3 Transformation between image and object space

The grey values recorded by the cameras in counts per pixel are transferred to a photon flux in photons per unit time by the calibration introduced in the previous section. Up to now this photon flux is still only defined on the image space coordinates $\vec{r}_\mathrm{i}$. These have to be mapped onto the coordinates in object space in order to estimate the object distance which is relevant for calculating the line integrated photon flux density. The line integrated photon flux density $\Phi(\vec{r}_\mathrm{p})$ in photons per unit time and area can be calculated from the calibrated signal when the observation volume $\Delta V(\vec{r}_\mathrm{i})$ is approximated by a rectangular box spanned by the intersection of the line of sight with the emission volume and the area $\Delta A_\mathrm{P}(\vec{r}_\mathrm{i})$ at the location of the photon emission imaged onto a single pixel. Thus, the photon flux density is defined on a plane in the object space, denoted by coordinates $\vec{r}_\mathrm{p}$. The area $\Delta A_\mathrm{P}(\vec{r}_\mathrm{i})$ is not constant throughout the image as the distance between object and principal plane changes especially for the oblique lines of sight. Hence, the area is a function of the coordinates in object space $\Delta A_\mathrm{P}(\vec{r}_\mathrm{i}) = f(\vec{r}_\mathrm{r})$. The

mapping onto object space coordinates is furthermore necessary to be able to compare the photon flux densities to measurements with other diagnostics, to magnetic field structure calculations using the ATLAS code and to results from three-dimensional modelling with the EMC3-EIRENE code.

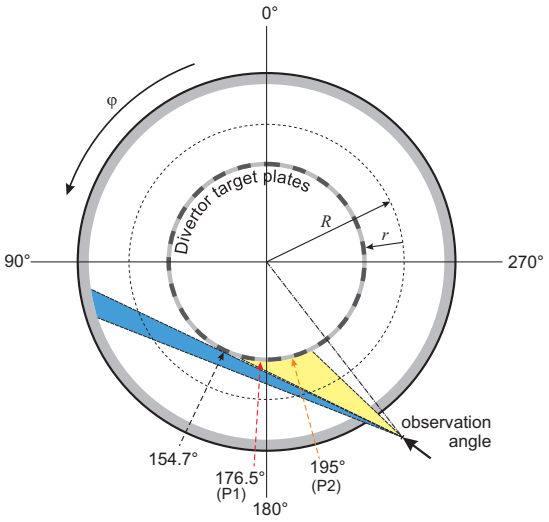

Figure 5.8
Equatorial cut of TEXTOR showing the definition of toroidal angle φ, major radius R and minor radius r of the toroidal coordinate system. The observation angle of SPEW is split into the tangential (cyan) and the "oblique" part (yellow).

For the transformation between image and object space, the recorded images are separated into two separately treated parts (see figures 5.8 and 5.9(a)): the line of sight *tangential* to the target surface (cyan) and the observation angle *obliquely* incident on the target surface (yellow). Furthermore the figures show the toroidal locations of two profiles (P1 and P2) which were chosen exemplarily from the oblique observation angle for the analysis in chapter 6 and 7. The dot-dashed line shows the line of sight perpendicular to the target surface, which lies just outside the observation angle. Due to the location and size of the TEXTOR window used, it was not possible to include both the tangential line of sight and the perpendicular in the observation angle.

5.3.1 Tangential line of sight

The tangential line of sight shows part of a poloidal cross section of the torus at a toroidal angle of $\varphi = 154.7°$ (dashed black arrow in fig. 5.8). The image space coordinates $\vec{r}_\mathrm{i}$ can be mapped onto object space coordinates $\vec{r}_\mathrm{p}$ in the plane of this poloidal cross section by fixing two points and linearly interpolating between them. These two points are the geometric center of the cross section at major radius $R = 1.75\,\mathrm{m}$ and the surface of the DED target tiles at minor radius $r = 0.477\,\mathrm{m}$. For convenience, the center of the object space coordinates is placed at the geometric center of the cross section.

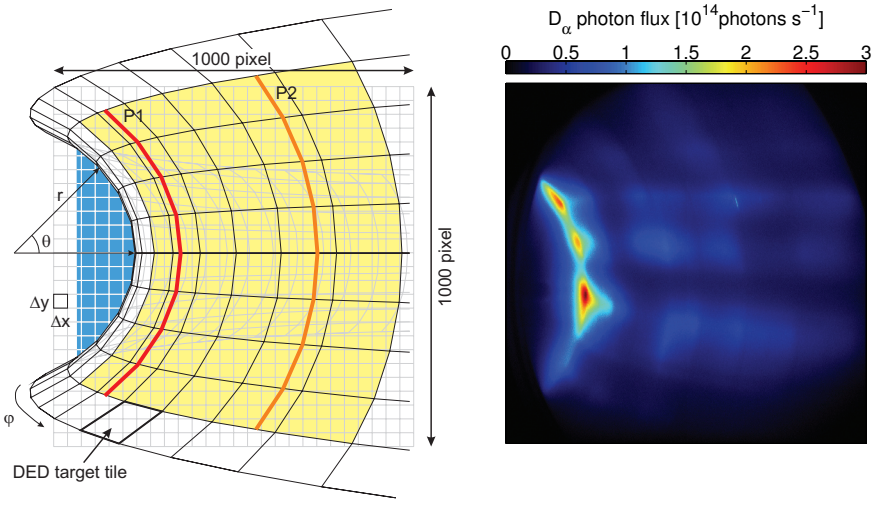

(a) Sketch of the pixel lattice in the image space together with the grid from the image mapping code LEOPOLD showing the DED target tiles.

(b) Calibrated image showing the photon flux in photons per second at and in front of the divertor target plates.

Figure 5.9 Illustration of the coordinate systems for the description of the measured photon fluxes.

The transformation includes several steps: a translation, a possible rotation by some angle θ_{off} and a scaling of the coordinates. Under the assumption that the (x,y)-grid in image and object space is equidistant: $\Delta x = \Delta y$ and $\Delta x_{\text{p}} = \Delta y_{\text{p}}$, according to equation 5.2 the coordinates in the image space can be described by

$$\vec{r_{\text{i}}} = \Delta x(m, n) \quad \text{with} \quad m, n \in \mathbb{Z}$$

and accordingly, the object space coordinates in the plane of the cross section can be described by:

$$\vec{r_{\text{p}}} = \Delta x_{\text{p}}(m_{\text{p}}, n_{\text{p}}) \quad \text{with} \quad m_{\text{p}}, n_{\text{p}} \in \mathbb{Z}.$$

The mapping between these coordinates can be described by the mapping function $\text{M} : V_{\text{i}} \mapsto V_{\text{p}} \subset V_{\text{r}}$ with

$$\vec{r_{\text{p}}} \equiv \text{M}(\vec{r_{\text{i}}}) = s \cdot \Delta x \cdot D \cdot (m - m_0, n - n_0)^T$$

with scaling factor s, rotation matrix

$$D = \begin{pmatrix} \cos\theta_{\text{off}} & -\sin\theta_{\text{off}} \\ \sin\theta_{\text{off}} & \cos\theta_{\text{off}} \end{pmatrix}$$

and (m_0, n_0) mapped onto the origin of the object space coordinates:

$$\text{M}(\Delta x(m_0, n_0)) = (0.0\,\text{m}, 0.0\,\text{m}).$$

The scaling factor s can be calculated from

$$\mathrm{M}(\Delta x(m_\mathrm{t}, n_\mathrm{t})) = (0.477\,\mathrm{m}, 0.0\,\mathrm{m})$$

with $(m_\mathrm{t}, n_\mathrm{t})$ being the pixel coordinates at the target surface in the equatorial plane. It is given by

$$s = \frac{0.477\,\mathrm{m}}{\Delta x((m_\mathrm{t} - m_0)\cos\theta_\mathrm{off} - (n_\mathrm{t} - n_0)\sin\theta_\mathrm{off})}$$

and the distance of the grid points in the object space is therefore

$$\Delta x_\mathrm{p} = s \cdot \Delta x(\cos\theta_\mathrm{off} - \sin\theta_\mathrm{off}).$$

As an example, figure 5.10 shows the tangential part of image 5.9(b) in image space coordinates (a) and in object space coordinates (b). The photon flux in photons per second was already normalised using the area ΔA_P that is imaged onto a single pixel to determine a line integrated photon flux density in photons per unit time and area.

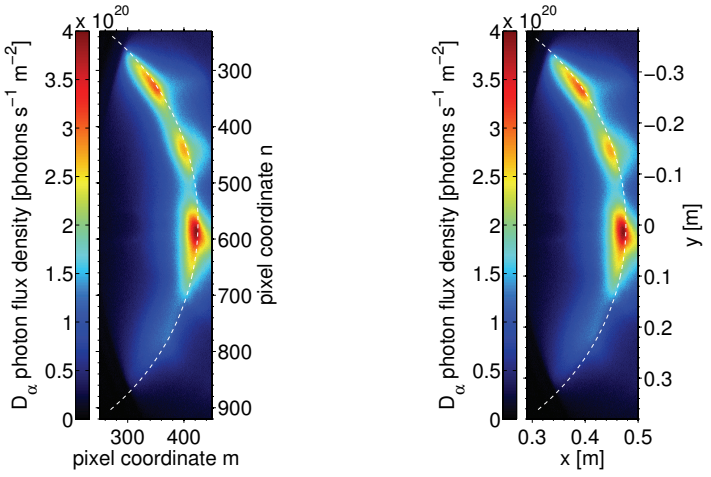

(a) Image space coordinates $\vec{r}_\mathrm{i}(m, n)$. **(b)** Object space coordinates $\vec{r}_\mathrm{p} = \mathrm{M}(\vec{r}_\mathrm{i})$

Figure 5.10 Part of image 5.9(b) showing the line integrated D_α photon flux density at a cross section of the torus at $\varphi = 154.7°$.

The distance of the grid points in the poloidal cross section Δx_p differs slightly from the length of the area imaged onto a single pixel because the plane of the cross section is not quite perpendicular to the optical axis but slightly turned by 11.4°. The distance between the object plane and the principal plane of the optical

setup increases with the x-coordinate defined above and the target surface (which is a perfect sector of a circle in object space) is perspectively projected onto the image plane as an ellipsis. The size of the area ΔA_P imaged onto a single pixel consequently decreases with x. Due to the small angle and large object distance however, it is possible to fit a circle to the target surface with good agreement and the variation in the area size lies within the uncertainty of its determination: $\Delta A_\mathrm{P} = (0.75 \pm 0.02)\,\mathrm{mm}^2$. This area is needed to calculate the line integrated photon flux density $\Phi(\vec{r}_\mathrm{p})$ from the photon flux according to (see equation 5.5):

$$\Phi(\lambda_0, \vec{r}_\mathrm{p}) = \frac{N_\mathrm{p}(t_\mathrm{P}, \Delta V(\vec{r}_\mathrm{i}), \mathrm{M}(\vec{r}_\mathrm{i}))}{t_\mathrm{P} \cdot \Delta A_\mathrm{P}} = 4\pi \, \frac{G V_\mathrm{P}(\lambda_0, \mathrm{M}(\vec{r}_\mathrm{i}))}{t_\mathrm{P} \cdot s(\lambda_0) \cdot \Delta A_\mathrm{P}} \tag{5.6}$$

For the comparison of the photon flux densities determined this way to modelling results and magnetic field calculations, it is convenient to map the data from the cartesian coordinate system to polar (r, θ)-coordinates in the plane of the poloidal cross section with

$$r = \sqrt{x^2 + y^2}$$
$$\theta = \arctan \frac{y}{x}$$

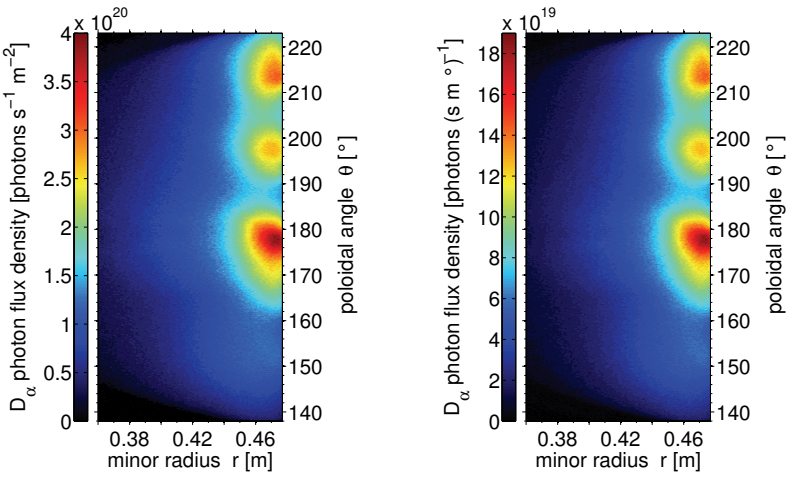

(a) $\Phi(r, \theta)$ **(b)** $\tilde{\Phi}(r, \theta) \equiv \Phi(r, \theta) \cdot r$

Figure 5.11 Part of image 5.10(a) left of the dashed circle mapped onto polar (r,θ)-coordinates showing the line integrated D_α photon flux density.

The polar angle is defined counter clockwise and $\theta = 180°$ is located in the equatorial plane at the high field side. For the mapping, a new grid in polar

coordinates was defined with distances between the grid points of $\Delta r = 0.86\,\mathrm{mm}$ and $\Delta\theta = 0.1°$. These distances were chosen according to the spatial resolution of the (x, y)-grid. At each point of the new grid, the photon flux density $\Phi(r, \theta)$ in photons per unit time and area is determined by nearest neighbour interpolation via

$$\Phi(r,\theta) = \Phi((m - m_0)\,\Delta x_\mathrm{p}, (n - n_0)\,\Delta x_\mathrm{p}) \quad \text{with} \quad \begin{aligned} m &= \lfloor r \cdot \cos\theta \rceil \\ n &= \lfloor r \cdot \sin\theta \rceil \end{aligned}$$

with

$$\lfloor z \rceil = \max\{k \in \mathbb{Z}\,|(k - m_0)\,\Delta x_\mathrm{p} \leq z + 0.5\}.$$

The photon flux N [photons s^{-1}] can be calculated from $\Phi(\vec{r})$ by integrating over a specific area A in the object plane:

$$N = \int_A \Phi(x,y)\ \mathrm{d}x\,\mathrm{d}y = \int_A \Phi(r,\theta)\ r\ \mathrm{d}r\,\mathrm{d}\theta = \int_A \tilde{\Phi}(r,\theta)\ \mathrm{d}r\,\mathrm{d}\theta$$

with

$$\tilde{\Phi}(r,\theta) \equiv \Phi(r,\theta) \cdot r$$

denoting a line integrated photon flux density in photons per unit time, length and angle. Figure 5.11 shows an example of the photon flux density mapped onto (r, θ)-coordinates (a) and the photon flux density $\tilde{\Phi}(r, \theta)$ is shown in (b).

5.3.2 Oblique line of sight

The oblique line of sight was mapped onto the poloidal and toroidal plane using an image mapping code used before for deforming images taken by the infrared camera described in chapter 4 [Jakubowski 2004]. In the framework of this thesis the code was adapted to be used also with the visible spectroscopy setup.

The code (called "LEOPOLD") incorporates a detailed grid of the DED target tiles, part of this grid is shown in figure 5.9(a). This grid has to be adjusted to the camera images with the help of several control parameters. The spatial resolution of the (φ, θ)-grid used here for the mapping is $\Delta\varphi = 0.1°$ and $\Delta\theta = 0.12°$. This corresponds to a spatial resolution along the target tiles of 2.2 mm in toroidal direction and 1 mm in poloidal direction. Figure 5.12 shows part of image 5.9(b) processed with the LEOPOLD code.

The area ΔA_P used to determine the line integrated photon flux density varies across the target as the object distance decreases from left to right and towards top and bottom of the image as can be seen from figures 5.9(a) and 5.8. The area was calculated in dependence of the toroidal and the poloidal angle and used in equation 5.6 to calculate the photon flux density per unit area and time for the oblique line of sight. The area size ranges from $\Delta A_\mathrm{P} = (0.63 \pm 0.02)\,\mathrm{mm}^2$ at the smallest object distance to $(0.76 \pm 0.02)\,\mathrm{mm}^2$ at the largest object distance.

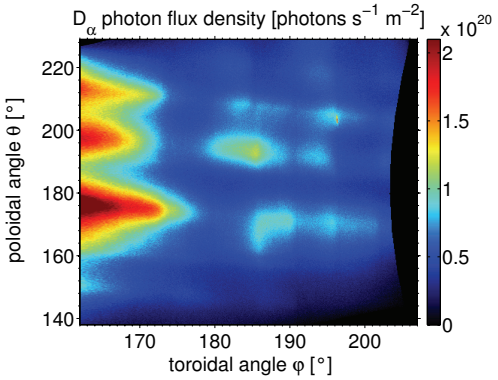

Figure 5.12
Line integrated D_α photon flux density at the oblique line of sight of the divertor target mapped onto the (φ, θ)-plane at $r = 0.477\,\mathrm{m}$.

5.4 Measurement uncertainties

The observation system initially suffered from a systematic error due to stray light. Because of a small slit between interference filter and filter wheel it was possible that a small fraction of the light entering the optical system was imaged onto the camera sensor without passing through the interference filter. The size of this slit depends on the positioning of the filter wheel. It was possible that the slit was completely covered and no stray light reached the sensor. In an upgraded version of the observation system, additional rings were installed inside the filter wheels to keep stray light from reaching the detector. The measurements presented in this thesis, however, were done mostly in the status with the potential systematic error.

Measurements have been carried out to determine the uncertainty introduced by this systematic error. Two situations have to be distinguished here: plasma measurements and calibration measurements using the integrating sphere. In the calibration measurements the continuum emission from the integrating sphere provides a large amount of possible stray light whereas the plasma emits a line spectrum which is dominated by the Balmer α line. Therefore, as an approximation the error estimation for the plasma measurements can be done taking only the D_α line into account.

In order to estimate the amount of stray light in the images taken during plasma discharges, a D_α filter has been installed in front of the integrating sphere. This way the amount of D_α light that passes the D_β and D_γ interference filter could be measured directly. For the D_α filter a measurement with a covered slit has been subtracted from a measurement of the maximum stray light with an uncovered slit. This measurement of the D_α stray light has to be scaled by a factor of 450 to take into account the fact that the D_α emission from the plasma is larger than the D_α emission from the integrating sphere. Comparing this D_α stray light (see open magenta circles in fig. 5.13) to the amount of measured D_α, D_β or D_γ light resp.

(see magenta solid circles in fig. 5.13) leads to the approximation of the relative systematic error in table 5.4. In the calibration measurements the situation is different. Here the stray light (see open blue squares in fig. 5.13) is in the same order of magnitude as the light passing through the interference filter (see solid blue squares in fig. 5.13). Therefore one has to make sure that the slit is covered when calibrating the system using the integrating sphere.

Spectral line	Wavelength [nm]	Systematic error
D_α	656.1	2 %
D_β	486.0	7 %
D_γ	433.9	0.1 %

Table 5.4 Relative measurement uncertainties due to the systematic error introduced by the stray light for the three Balmer line filters.

The uncertainty in the measured grey value is furthermore determined by those image noise types that cannot be removed using dark frame subtraction. For CCD sensors this is typically dominated by the signal dependent photon noise which is governed by Poisson statistics. The measurement uncertainty is then given by the standard deviation of the number of incident photons $\sqrt{s_{\mathrm{CCD}} \cdot GV}$. At the light levels recorded here the noise is negligible compared to other measurement uncertainties which stem from the uncertainty in the determination of the sensitivity of the observation system (i.e. the calibration factor) and, for the determination of the photon flux density, from the determination of the area imaged onto a single pixel ΔA_{P}. The uncertainty in the calibration factor is dominated by the uncertainty in the determination of the transmission of the TEXTOR window of approximately 10 %, while the area can be determined with an uncertainty of about 3 %.

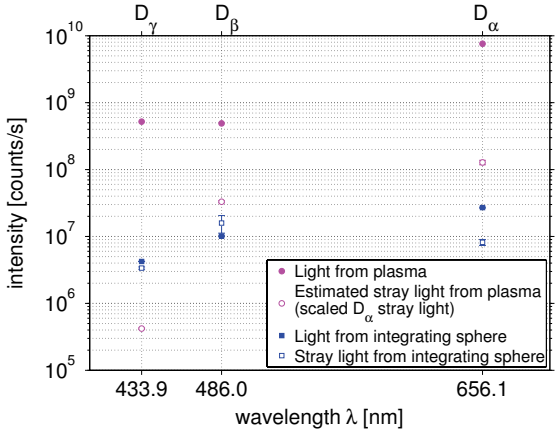

Figure 5.13 Estimation of the stray light for the three Balmer line filters (D_α, D_β and D_γ).

Measurements of plasma discharges are furthermore subject to the uncertainty in the reproducibility of the plasma parameters. One of the benefits of the observation

system described in this section is therefore the reduction of this uncertainty due to the reproducibility by enabling the acquisition of all the important information in a single discharge. Only when comparing different magnetic configurations, such as the limiter and the divertor configuration, reproducibility is needed. Reproducible in that sense means that the discharges would exhibit the same parameters, if the perturbation field was not operated. For the discharges analysed within this thesis, the reproducibility especially at high plasma densities was increased by operating glow discharges (typically lasting five minutes) in the TEXTOR vessel in between the regular TEXTOR discharges. This reduces the hydrogen inventory in the vessel wall and thereby creates similar boundary conditions for the consecutive discharges.

6 The hydrogen recycling in the low density regime

In this chapter the influence of the resonant magnetic perturbation on the hydrogen recycling characterised by the Balmer photon emission, electron density and temperature and the ion and heat flux is shown. For this purpose these quantities are compared in a discharge with divertor operation to a reference discharge without divertor operation (limiter discharge). This is done here for low plasma core and edge densities, when the plasma parameters are in a range, where radiation from volume recombination processes at the plasma edge is negligible.

In order to study the low density regime as well as the high density regime in the helical divertor in TEXTOR, discharges were performed in which the line averaged density at the plasma center was increased continuously while the current in the divertor coils was kept constant (so-called *density ramps*). The points in time of the compared discharges correspond to the same line averaged electron density at the plasma centre: $\bar{n}_{\mathrm{e,c}} = 3.5 \cdot 10^{19}\,\mathrm{m}^{-3}$ as well as approximately the same total electron content in the plasma. In both cases - limiter and divertor operation - the plasma column was moved towards the high field side by 2.4 cm with respect to the center of the vessel at major radius $R = 1.75\,\mathrm{m}$, so that in the discharge without divertor operation the DED target plates at the high field side served as the main limiter. Thus, the main plasma wall interaction takes place at these graphite limiter/divertor target plates covering the DED coils. Other recycling areas are the top and bottom poloidal limiters and the toroidal belt limiter ALT-II, they contribute only a minor fraction to the total recycling flux in the configuration studied here. External pumping of the neutral particles however takes place only at the toroidal belt limiter, as no pumps are installed at the target plates of the helical divertor.

6.1 Plasma parameters at the edge

For the interpretation of the photon fluxes observed at the target plates (see section 6.2), knowledge about the local plasma parameters, namely the distribution of electron density and temperature, in front of the target plates is important. They have been measured locally by a Langmuir probe (see section 4.2) embedded

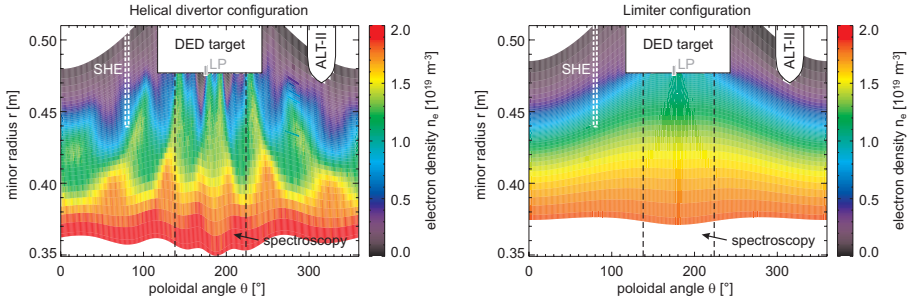

(a) Electron density.

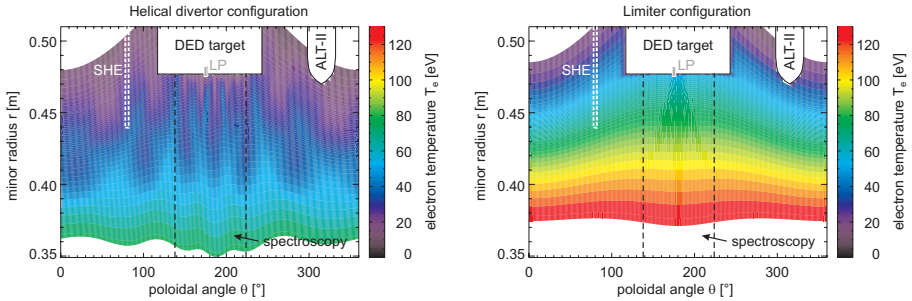

(b) Electron temperature.

Figure 6.1 Two-dimensional graphs of plasma parameters modelled with the EMC3-EIRENE code [Frerichs 2010a] for the divertor and the limiter configuration at the tangential line of sight of the diagnostic SPEW (see fig. 5.8).

in a target tile and by the supersonic helium beam (see section 4.3) at the top of the vessel at a remote toroidal location from the Langmuir probe and the spectroscopic measurements at the divertor target. Both diagnostics measure the plasma parameters very localised at a fixed toroidal and poloidal position, a radial profile in the case of the helium beam. For a thorough analysis of the spectroscopic data, especially with the three dimensional divertor structure, at least a two dimensional pattern of electron density and temperature is needed. This can only be provided by three-dimensional modelling using e.g. the EMC3-EIRENE code, cross checked for consistency with the local measurements.

Two-dimensional cuts at one toroidal location of the calculated electron temperature and density at the plasma edge are shown in fig. 6.1 for the limiter and the helical divertor configuration at a separatrix density of $\bar{n}_{\mathrm{e,sep}} \approx 2 \cdot 10^{19}\,\mathrm{m}^{-3}$ (input parameter). This density corresponds to a line averaged electron density at the plasma center of approximately $\bar{n}_{\mathrm{e,c}} = 4.1 \cdot 10^{19}\,\mathrm{m}^{-3}$. The alteration of electron temperature and density at the plasma edge due to the magnetic field

structure of the helical divertor is clearly visible. It has to be noted, that the plasma parameters not only vary in the poloidal but also in the toroidal direction. In the limiter configuration the plasma is toroidally symmetric and the plasma parameters in front of the target plates also vary little in the poloidal direction. For the divertor discharge at the line averaged electron density of $\bar{n}_{e,c} = 3.5 \cdot 10^{19}\,m^{-3}$ studied in this chapter (corresponding to $\bar{n}_{e,sep} \approx 1.8 \cdot 10^{19}\,m^{-3}$) the calculations predict a target electron temperature of $T_{e,t} \approx 25\,eV$ and an electron density of $\bar{n}_{e,t} = 8 \cdot 10^{18}\,m^{-3}$ at the location of the Langmuir probe. These calculations will be compared to the local measurements by the Langmuir probe and the supersonic helium beam and used in the following sections for the interpretations of the observed Balmer photon emissions. The poloidal locations of the Langmuir probe (LP), the supersonic helium beam (SHE) and the view of the spectroscopic measurements are indicated in figure 6.1, the first two however are located at a different toroidal location than the plane shown in the graphs.

Electron density and temperature measured by the Langmuir probe at the target plates at $\theta = 173.8°$ and $\varphi = 176.5°$ are shown in table 6.1 for a limiter and a divertor discharge at $\bar{n}_{e,c} = 3.5 \cdot 10^{19}\,m^{-3}$. The parameters measured by the Langmuir probe in the limiter discharge are lower than in the divertor discharge due to small inaccuracies in the alignment of the target plate tiles. The recycling at the tile that the probe sits in, is generally lower than at other toroidal locations, pointing towards a shadowing of the tile by the surrounding tiles. In the discharge with divertor operation, the shadowing of the tile is less effective due to the magnetic perturbation field drawing the field lines and with them the plasma onto the divertor target plates. Within the measurement uncertainties, the measured electron density corresponds well to that calculated by the EMC3-EIRENE code while the measured electron temperature is about twice as high. However, no significant difference in the type of the dominating atomic processes can be expected in this temperature range. Only when the temperature drops below 15 eV, the principal break-up channel for molecular hydrogen changes from ionisation to dissociation.

Configuration	Electron density	Electron temperature
Limiter	$7.4 \cdot 10^{18}\,m^{-3}$	15 eV
Divertor	$8.6 \cdot 10^{18}\,m^{-3}$	53 eV

Table 6.1 Plasma parameters measured by a Langmuir probe embedded in the target plates at poloidal angle $\theta = 173.8°$ and toroidal angle $\varphi = 176.5°$.

Figure 6.2 shows the electron density and temperature profiles at the plasma edge measured by the supersonic helium beam at a line averaged central density of $\bar{n}_{e,c} \approx 4 \cdot 10^{19}\,m^{-3}$. The temperature profiles at this toroidal and poloidal location are very similar in the two configurations while the density profile is considerably flattened inside the last closed flux surface (LCFS) in the divertor configuration.

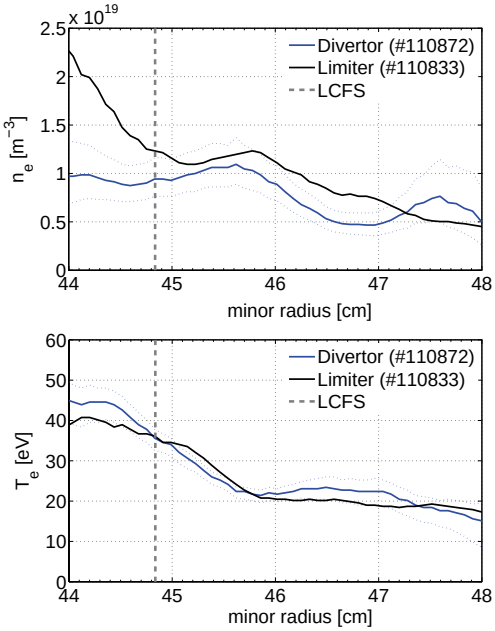

Figure 6.2
Plasma parameter profiles measured by the supersonic helium beam during the limiter and divertor discharges at similar line averaged densities in the plasma center ($\bar{n}_{e,c} \approx 3.8 \cdot 10^{19}\,m^{-3}$ and $4 \cdot 10^{19}\,m^{-3}$, resp.). The measurement uncertainty is given for the divertor discharge by the dotted blue lines. The position of the LCFS is determined by the divertor target and was calculated for a plasma equilibrium without magnetic perturbation field.

The helium beam diagnostic is located at the top of the vessel (see figure 6.1) and a remote toroidal location ($\varphi \approx 304°$) from the Langmuir probe and the spectroscopic measurements at the divertor target. Due to the complex SOL geometry, a direct transfer of these parameters is not possible but can be used for a consistency check of the modelled parameters. In the limiter case, the temperature at the LCFS of $T_e \approx 35\,eV$ can be taken as a lower limit for the target temperature, further hinting towards the assumption that the Langmuir probe was shaded in the limiter case. This rough estimate is not applicable in the divertor discharge due to the modulation of the edge plasma by the resonant magnetic perturbations and the formation of the helical divertor.

6.2 Photon emission at the target plates

The hydrogen particles recycling at the graphite limiter/divertor target plates emit Balmer line radiation in front of the target as can be seen exemplarily in figure 6.3. The distribution and amount of this photon emission is determined by

- the number (flux) of incident particles
- the number of particles released from the target
- the velocity distribution of these particles

- the plasma parameters met by the particles in front of the target (see previous section 6.1)

The number of particles coming from the target is closely linked to the incoming ion flux. The ratio of the two fluxes is denoted by the recycling coefficient R which is close to one in case of a saturated graphite surface: $R \approx 1$. Hence, strong ion flux *onto* the target typically leads to strong neutral particle flux *from* the target. The velocity of the neutral particles depends on the release mechanism and possible processes in front of the target such as charge exchange processes with incoming ions. The velocity and the plasma parameters determine the penetration depths of the particles, which is analysed in more detail in the next section (6.3).

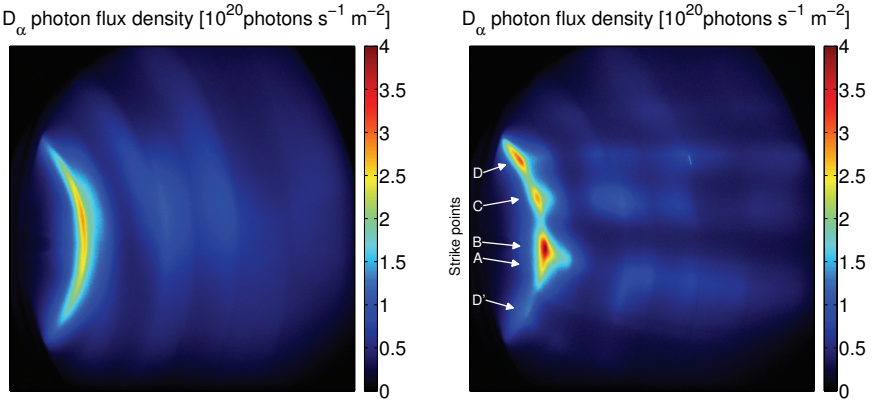

(a) Without divertor operation (#110833). **(b)** With divertor operation (#110872).

Figure 6.3 D_α photon flux density at the divertor target plates with and without divertor operation at the same line averaged electron density in the plasma center. The flux density was calculated using a constant area of $\Delta A = 0.75\,\mathrm{mm}^2$ (see equation 5.6).

A comparison of figures 6.3(a) and (b) shows, that the photon flux is strongly modulated in the toroidal as well as in the poloidal direction by the application of the magnetic perturbation field and formation of the helical divertor. In the limiter discharge the emission is largest in the equatorial plane and spreads across the target in the poloidal direction decreasing in absolute value. With divertor operation the emission is concentrated poloidally at several locations, the divertor strike points or strike lines. These strike lines run around the torus with a helical inclination following the inclination of the divertor coils behind the target tiles. In analogy with [Frerichs 2010a], in the following discussions the strike points will be labeled A, B, C and D (see section 3.3). As can be seen from figure 6.3b, the brightest strike point is made up of the unresolved strike points A and B,

strike point C is the first and strike point D the second above the equatorial plane. Below strike points A/B another part of strike point D is dimly visible.

6.2.1 Poloidal and radial distribution

The poloidal and radial distribution of the D_α photon flux density in front of the divertor target from figures 6.3(a) and (b) is shown in more detail in figure 6.4. The toroidal angle of this cross section is $\varphi = 154.7°$. This tangential line of sight allows conclusions on the radial penetration depths of the particles (6.3) and also visualises the modulation of the recycling flux from the target in the poloidal direction (6.6). When interpreting this photon flux distribution, however, it has to be taken into account, that the distribution does not show an exact cut at the respective toroidal location but that the photon emission is integrated along the line of sight of the observation system. As the strike lines *helically* run around the torus, the integration leads to smearing compared to the cross sectional photon emission.

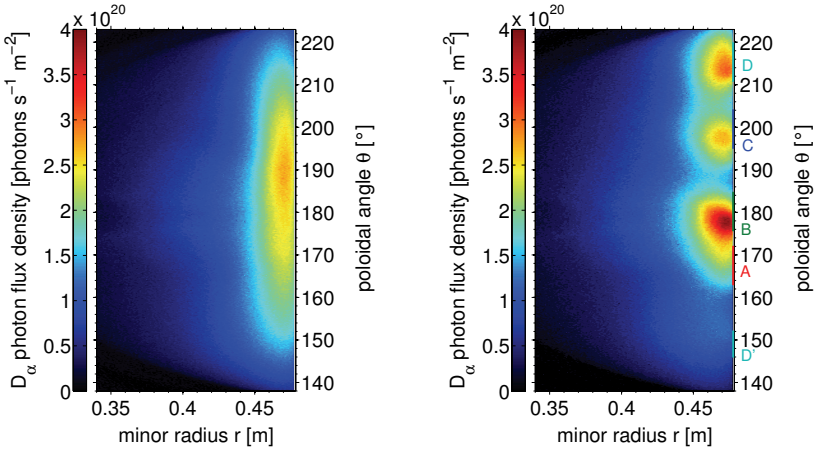

(a) Without divertor operation (discharge #110833).

(b) With divertor operation (#110872). The strike points are labelled by A,B,C and D.

Figure 6.4 Radial and poloidal distribution of the D_α emission in a discharge with and without divertor operation at $\varphi = 154.7°$ at the same line averaged electron density in the plasma center.

As could already be seen in figure 6.3, in the reference discharge the emission is evenly spread in the poloidal direction decreasing towards top and bottom while during divertor operation the emission is concentrated at several poloidal locations,

the strike points of the divertor. In the reference discharge the peak emission is located at a poloidal angle of $\theta = 180°$ to 190°. For a more detailed discussion of the photon fluxes during divertor operation a look at the magnetic structure at the location of the cross section is needed. This structure can be characterised partly by the connection lengths of the field lines from target to target (figure 6.5(a)) as discussed in section 3.3.2.

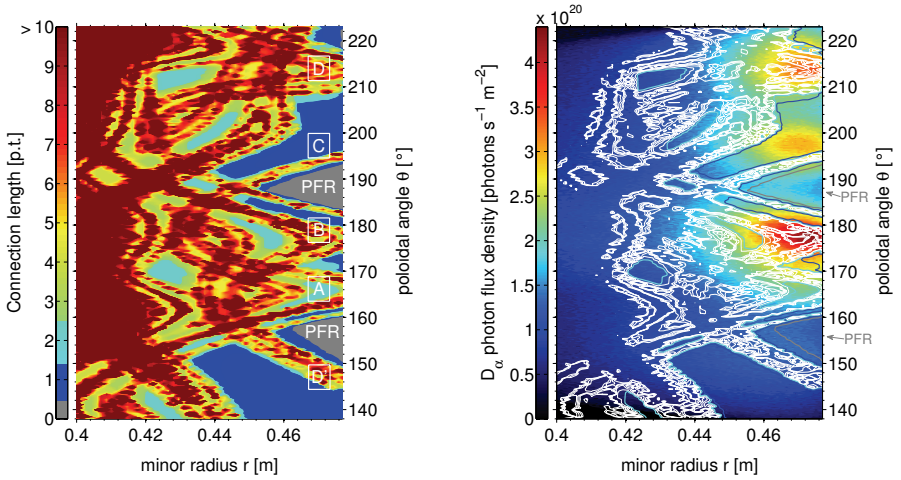

(a) Lengths of magnetic field lines L_c from target to target given in poloidal turns. The field line tracing is stopped for $L_c >$ 20 p.t.

(b) D_α photon flux density (fig. 6.4(b)) overlaid with contour lines showing areas of different field line connection lengths (taken from (a)).

Figure 6.5 Comparison between magnetic field topology and D_α photon emission at the poloidal cross section at $\varphi = 154.7°$.

Figures 6.5(a) and (b) show that large photon emission corresponds to long field lines hitting the target. The peak emission with divertor operation is located at $\theta = 170°$ to 180° (corresponding to strike points A and B) with a local photon flux of $\sim 3.6 \cdot 10^{20}\,\mathrm{s^{-1}m^{-2}}$. This is about 2.6 times more than at the target in the upper private flux region $10° \mathrel{\widehat{=}} 8\,\mathrm{cm}$ next to the strike point. At $\theta \approx 210°$ (Strike point D) considerably less emission is seen in the reference discharge, which demonstrates the strong impact of the magnetic field structure imposed by the resonant magnetic perturbations on the local particle transport. Little photon emission is also seen at locations where field lines with connection lengths of one poloidal turn and less hit the target. As discussed in section 3.3.2, these short field lines carry less particles and heat to the target than the long field lines because they do not penetrate deep into the plasma but stay at large minor radii while they travel around the torus where the plasma is less dense and hot. These areas are filled by diffusion from the adjacent areas of longer field lines.

The so-called *short magnetic flux tube* which exists in this configuration (field lines of one poloidal turn showing a strong correlation) connects strike points B and C, in the cross section shown in figure 6.5(a) one end of the flux tube hits the target in the blue area between approximately $\theta = 196°$ and $205°$ while the other end hits the target in a very thin stripe at $\theta \approx 172°$ (see also figure 3.4). It can be seen in figure 6.5(b) that in the "upper" flux tube end the photon emission is not as low as in the two private flux regions (grey areas in fig. 6.5(a)) where the field line connection lengths are extremely short.

6.2.2 Poloidal and toroidal distribution

Besides the tangential line of sight, part of the divertor target is viewed by looking directly onto the target plates, thereby radially integrating the photon emission in front of the plates. These lines of sight give insight into the poloidal *and* toroidal structure of the photon emission and by that the distribution of the neutral particle sources (6.5) and the recycling flux (6.6). The poloidal and toroidal distribution of the D_α photon flux is shown in figure 6.6 mapped versus the poloidal and toroidal angle. The comparison of the two images clearly shows the strike line structure at the divertor target introduced by the resonant magnetic perturbations. The strike lines are inclined relative to the horizontal plane, following the helical setup of the DED coils. The photon flux is redistributed due to the divertor operation with some regions emitting less and some regions emitting more photons than in the reference case.

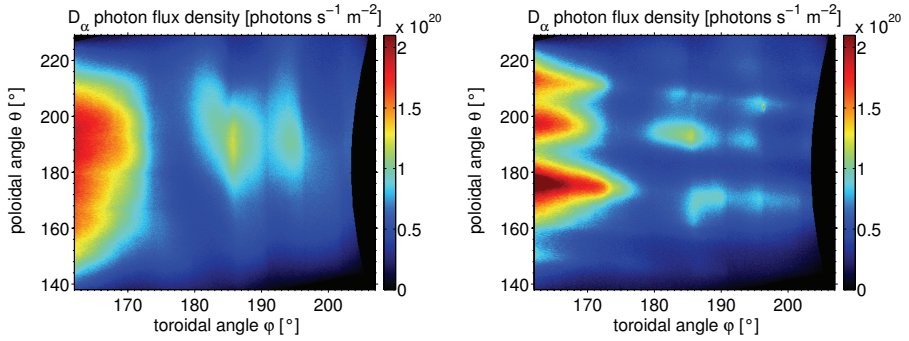

(a) Without divertor operation (#110833). **(b)** With divertor operation (#110872).

Figure 6.6 Comparison between radially integrated D_α photon emission with and without divertor operation at the same line averaged electron density in the plasma center.

Due to the geometrical setup of the observation system, the photon integration is mostly not radial but under some oblique incidence angle. At $\varphi \approx 207°$ the line of

sight is identical to the target normal and towards smaller toroidal angles (the left hand side of the image) the angle between target normal and line of sight increases until it reaches 90° at $\varphi = 154.7°$. The larger the incidence angle gets, the longer the integration path is, leading to an increased integrated photon emission. This becomes clear from the image of the limiter discharge in figure 6.6(a). Due to the toroidal symmetry of the limiter configuration, a homogeneous emission across the target can be assumed here. Furthermore, an additional inhomogeneity of the flux across the whole target exists due to small inaccuracies in the alignment of the DED target tiles which cause leading edges and shadowed areas with different recycling fluxes.

Figure 6.7 shows a comparison between the measured target pattern of the recycling flux and the topology of the magnetic field lines intersecting the divertor target. The white contour lines are derived from a magnetic footprint plot, areas with high line density correspond to areas where long field lines intersect the target which also penetrate deep into the plasma. A more detailed comparison between the line integrated photon flux density and the connection length and penetration depth of field lines is done in section 6.5.

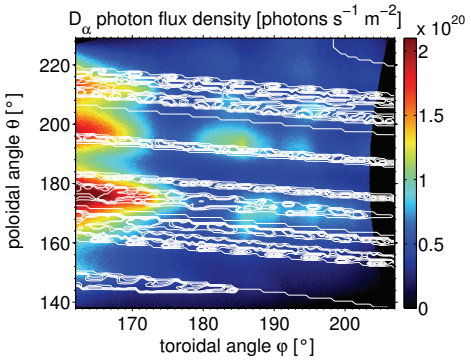

Figure 6.7
Radially integrated D_α photon emission with divertor operation overlaid with contour lines of a magnetic footprint plot (see figure 3.7).

6.3 Penetration depths of atomic and molecular hydrogen

In this section a closer look will be taken at the penetration depths of the neutral atomic and molecular hydrogen particles coming from the target. The difference in the penetration depth between limiter and divertor operation will be discussed as well as the variations in the poloidal direction in case of the divertor operation. The estimation of the penetration depth is important for the analysis of the photon emission in front of the target regarding the neutral source distribution as discussed in section 4.1.4.

6.3.1 Simple estimations

The radial penetration depths of atomic and molecular hydrogen can be compared to simple approximations of the ionisation lengths valid for constant plasma parameters (see equation 4.6). The plasma parameters used for these approximations are taken from the EMC3-EIRENE modelling results shown in figure 6.1. Two poloidal locations are chosen exemplarily: strike point B at $\theta = 175°$ and the upper private flux region $\approx 8\,\mathrm{cm}$ above this location along the target. Figure 6.8 shows radial profiles of the calculated electron density and temperature at these two locations up to 1 cm in front of the target surface. At the target surface the plasma parameters at the strike point are considerably higher than in the PFR, radially in front of the target however they rise to similar values within one centimetre. The gradients are therefore quite different, especially the electron temperature in front of the strike point shows a flattening between $r = 0.47\,\mathrm{m}$ and $0.43\,\mathrm{m}$.

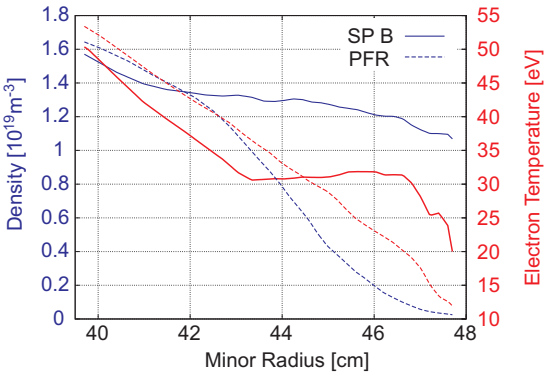

Figure 6.8
Radial profiles of electron density and temperature calculated by three-dimensional modelling with EMC3-EIRENE at strike point B (solid lines) and in the upper PFR (dashed lines) at $\varphi = 143.4°$ [Frerichs 2010b].

As discussed in section 2.3.1, the velocities of the neutral hydrogen particles initially depend on the release mechanism and then on the subsequent processes such as dissociation and charge exchange. For graphite surfaces at surface temperatures below 1000 K, 90% of the hydrogen is released as molecules while 10% is attributed to reflected or charge exchange atoms [Brezinsek 2001]. The molecules are thermally released from the surface, their velocity therefore corresponds to the temperature of the solid surface. The penetration of the neutral molecules is limited either by ionisation or dissociation. At the electron temperatures stated above, the reaction with the highest rate coefficient is electron impact ionisation creating a molecular ion (reaction 2.3 in section 2.3.1) with a rate coefficient of about $3 \cdot 10^{-14}\,\mathrm{m^3 s^{-1}}$ at an electron temperature of 30 eV. For a particle velocity of $1.6 \cdot 10^3\,\mathrm{ms^{-1}}$ and an electron density of $1 \cdot 10^{19}\,\mathrm{m^{-3}}$ the corresponding ionisation length is about 5 mm. The molecular ion produced this way is then dissociated by electron impact into a hydrogen atom and an ion.

The dissociation products of the recycled molecules were experimentally found to be composed of different energy components. In the boundary plasma of

TEXTOR [Hey et al. 2000] a large population of atoms with very low energies ($< 0.5\,\mathrm{eV}$) were found, together with a temperature component of 2 eV to 5 eV. Direct electron impact dissociation of the neutral molecule leads to characteristic atomic energies of 2.2 eV, while reflected atoms have large energies of several tens of electronvolts just as the atoms undergoing charge exchange reactions. At a constant electron density of $1 \cdot 10^{19}\,\mathrm{m}^{-3}$ and electron temperature of 30 eV the rate coefficient for electron impact ionisation of a hydrogen atom is $\approx 3 \cdot 10^{-14}\,\mathrm{m}^3\mathrm{s}^{-1}$ leading to a penetration depth for atomic hydrogen of 3 cm. At lower density and temperature such as in the private flux region (assuming $0.5 \cdot 10^{19}\,\mathrm{m}^{-3}$ and 15 eV) the penetration depth increases to 13 cm. A fast atom after a charge exchange process has a theoretical penetration depth of ≈ 20 cm and ≈ 90 cm for the assumption of constant plasma parameters. In a real edge plasma these penetration depth will be shorter due to the existence of density and temperature gradients.

6.3.2 Molecular hydrogen

The penetration depth of molecular hydrogen is expected to be much smaller than the penetration depths of atomic hydrogen as outlined above. The photon emission from molecular hydrogen consists of numerous lines in so-called molecular bands of which mostly only parts are observed (in this case part of the Fulcher band, see section 4.1.2). The population of the upper level of the Fulcher band is low, the decay rate per photon emission rate ($D/XB \sim 2000$) being considerably lower than the inverse photon efficiency of the Balmer $\alpha line$. Therefore the observed photon fluxes are considerably smaller than the D_α photon flux. In the low density regime considered here, the recorded intensity and therefore the signal to noise ratio was particularly low because the settings of the diagnostic were chosen in order not to saturate the images at higher recycling fluxes at high plasma densities later in the discharge.

Figure 6.9 shows the photon emission from molecular deuterium in the limiter and the divertor discharge at the tangential line of sight, i.e. corresponding to figure 6.4 which showed the D_α emission from atomic deuterium at this location. The comparably strong signal at the center of the images in figure 6.9 is attributed to a molecular source at the low field side visible past the divertor target. This additional contribution has to be taken into account particularly when analysing radial profiles of the photon emission as done below. The molecular photon fluxes at the low field side are observed to be almost comparable to the molecular fluxes from the target plates only in the low density regime discussed in this chapter. Increasing the core density raises the target photon fluxes much more than the fluxes from the low field side. Figure 6.9b shows, that the observation of the Fulcher band emission facilitates the observation of the separate strike points, in

particular strike points A and B can be discriminated in spite of the line-of-sight integration and the particle mixing.

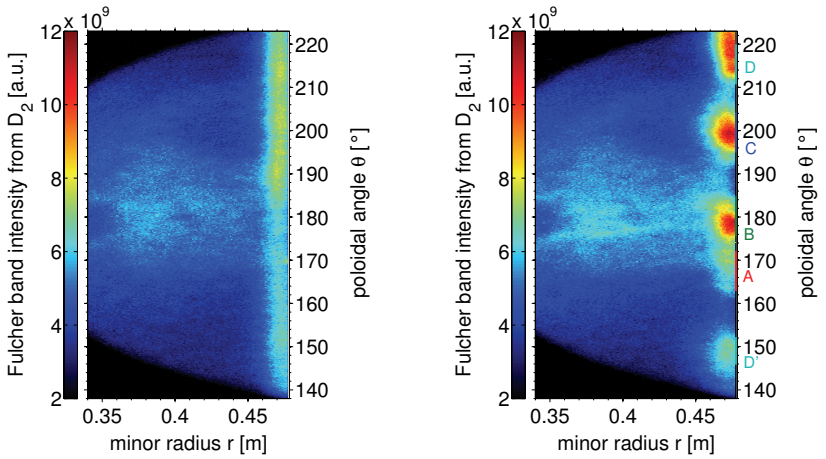

(a) Without divertor operation (#110833).

(b) With divertor operation (#110872).

Figure 6.9 Radial and poloidal distribution of the Fulcher band emission from molecular deuterium (central wavelength of the filter: 601.5 nm) at $\varphi = 154.7°$ at the same line averaged electron density in the plasma center.

Radial profiles of the Fulcher band intensity are shown in figure 6.10 at the two poloidal locations already considered above (strike point B and upper private flux region). To estimate the part of the signal which can be attributed to the molecules recycling at the DED target plates, in each profile the signal from the recycling molecules at the LFS has been estimated by averaging between $r = 0.41\,\mathrm{m}$ and $r = 0.43\,\mathrm{m}$ and subtracted from the whole profile. The result is shown in figure 6.10(b) together with smoothed profiles using a Savitzky-Golay filter.

In the divertor discharge, the position of the peak emission at the strike point (solid green line) is very close to the target ($\approx 2\,\mathrm{mm}$) and the profile quickly falls off towards the plasma centre. In the private flux region the profile is much flatter, the peak emission is 7 times lower and located about 1 cm further away from the target.

In the limiter discharge (dashed lines) the peak emission is unexpectedly different at the two poloidal locations (which were chosen according to the divertor magnetic field structure). This could already be seen in figure 6.9(a), showing a larger molecular emission above the equatorial plane. Possible reasons for this are a

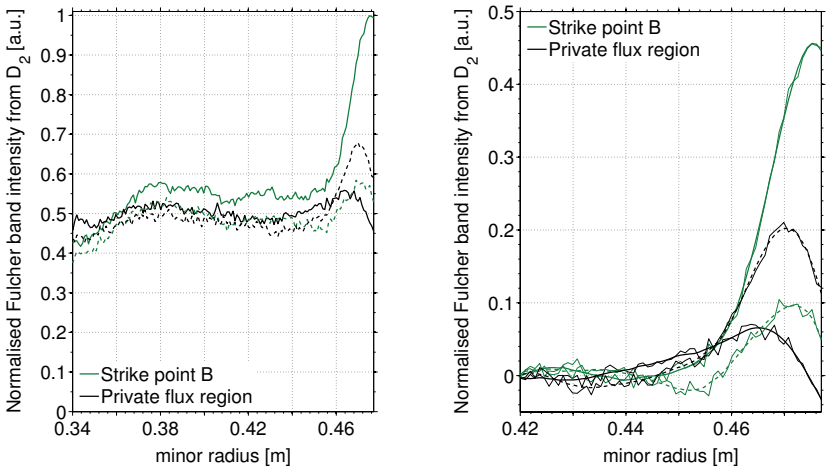

(a) Fulcher band signal from recycling molecules at the LFS (plateau) and at the divertor target (peak).

(b) Molecular emission from LFS subtracted as constant background signal. The thin solid line shows the unsmoothed signal of each profile.

Figure 6.10 Radial profiles of the Fulcher band emission of D_2 at the tangential line of sight in the limiter (dashed lines) and the divertor discharge (solid lines). The intensity was averaged over a poloidal range of $\Delta\theta = 1°$.

small vertical shift of the whole plasma column towards the top of the vessel or the alignment of the DED target tiles. Due to its better signal to noise ratio, the dashed black profile is therefore used as the reference location in the limiter discharge. Here, the peak emission is located slightly further away from the target than in the divertor discharge (about 7 mm from the target surface) but the e-folding length of the emission is the same as at the strike point in the divertor discharge (about 1 cm). The e-folding length is the distance between the radial position of the peak emission in front of the target ($r_{\mathrm{DED}} = 0.477\,\mathrm{m}$) and the radial position at which the photon emission has dropped to 1/e of its peak value. It is a measure of the radial penetration depth of the corresponding neutral particles. At this position, most of the molecules have already been ionised or dissociated and only few are left to contribute to the photon emission of the highly excited Fulcher band. Generally short mean free paths of a few mm are expected for molecular deuterium because its particle velocities are small reflecting the temperature of the target plates and electron temperature and density are typically sufficient for ionisation and dissociation to be effective close to the target.

At the private flux region in the divertor discharge, the radial e-folding length is

difficult to interpret as it does not take into account the different source strengths at the target. Adjacent stronger sources contribute to the neutral particle flux and therefore the photon emission radially in front of the PFR. The e-folding length reflects this mixture of neutral particles, leading to the observed shift in the peak emission away from the target. A further influence on the radial profiles is also expected from the line-of-sight integration, its effect is discussed in the analysis of the D_α emission in the following section with the help of the calculated Balmer α emission using the EMC3-EIRENE code.

6.3.3 Atomic hydrogen

Radial profiles of the D_α line emission in front of the target at the two poloidal locations discussed above are shown in figure 6.11(a). In the limiter discharge, the radial position of the peak emission is about 47 cm at both poloidal locations. In the divertor discharge the peak emission at the strike point is also located at about 47 cm, whereas in the private flux region it is 1 cm further away from the target and the profile is very flat.

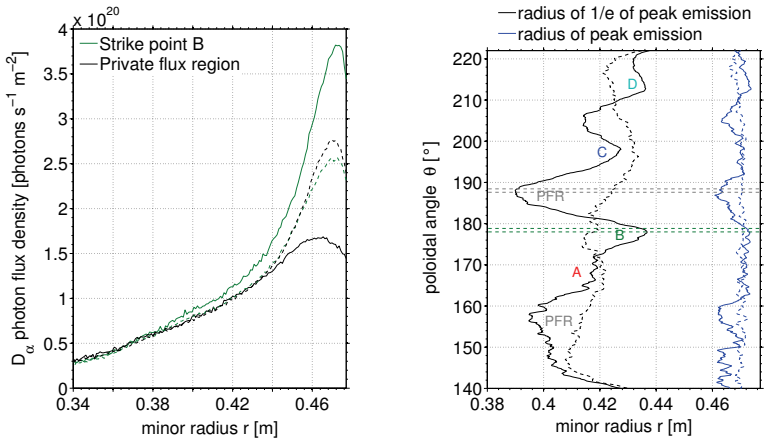

(a) Radial profiles of photon flux averaged over a poloidal range of $\Delta\theta = 1°$.

(b) Radial position of maximum emission and e-folding radius.

Figure 6.11 Radial profiles and e-folding length of the D_α photon flux at the tangential line of sight in the limiter (dashed lines) and the divertor discharge (solid lines).

For an estimation of the radial penetration depths of the neutral particles, the radial position in front of the target was determined at which the D_α emission has dropped to 1/e of its peak value. At this position, most of the neutrals have

already been ionised and only few are left to contribute to the Balmer photon emission. Figure 6.11(b) shows this e-folding length of the D_α photon emission along the target versus the poloidal angle. According to this estimation, at strike point B the radial ionisation length is about 4 cm. As expected from the flat profile at the private flux region, the e-folding length here is larger lying at a radial position of about 38 cm. Generally from a comparison to image 6.3(b), we see that the e-folding length is short at poloidal angles of strong emission, whereas the profiles are very flat and hence the e-folding lengths are large at locations of weak emission. As already discussed above, at these locations adjacent stronger sources contribute to the photon emission radially in front of the weak sources and mix up the contributions. Furthermore, line-of-sight integration can lead to deviations of the measured radial profiles from the local photon emission. Deconvolution is needed and obtained by three-dimensional modelling of the processes at and in front of the target. The modelled photon emissivities can then be compared to the measured photon distribution and help to explain the observations.

Figure 6.12 shows the calculated H_α emissivity and illustrates the effect of the line of sight integration on the poloidal and radial photon distribution. In the poloidal cut in figure 6.12(a) the modulation of the photon emission is more pronounced, the emission from both private flux regions is negligible. In the simulated camera picture strike points A and B are less separated and the emission from the private flux regions is only about five times lower than at strike point B. At strike point D, the line-of-sight integration has even led to a relative increase in intensity while strike points C and D are still distinguishable. Furthermore, the location of the emission at strike points C and D has moved down by about 1° to 2°.

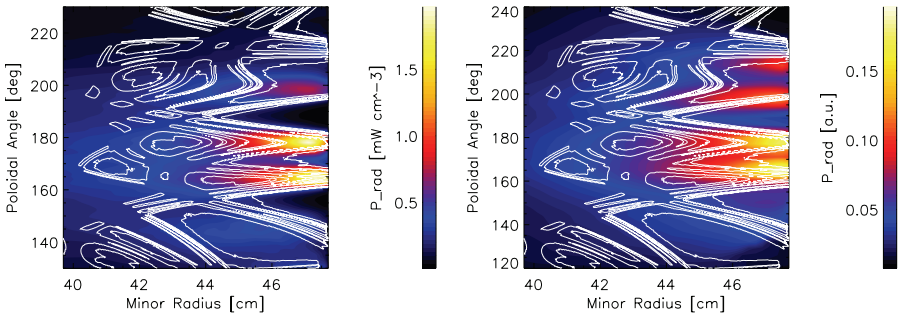

(a) Poloidal cut of modelled H_α emission. **(b)** Simulated camera image.

Figure 6.12 Local and line integrated H_α emission calculated by 3D modelling with the EMC3-EIRENE code at $\varphi = 157.5°$ from [Frerichs 2010a]. The images are overlaid by white contour lines of a connection lengths plot similar to figure 6.5(b).

Radial profiles of the local and line integrated photon emission have been extracted from figures 6.12(a) and (b) at strike point B and at the private flux region (fig. 6.13). The comparison of the profiles shows that the line-of-sight integration leads to a movement of the location of the peak emission towards the target surface and a flattening of the profile in front of the strike point. For the line integrated signal the emission drops off to about 75% of the peak value up to a minor radius of $r = 0.42\,\mathrm{m}$ while the local signal drops off to 75% at $r \approx 0.43\,\mathrm{m}$. The integration therefore leads to an overestimation of the neutral penetration depth by roughly 1 cm. The poloidal modulation in the photon emission characterised by the comparison of the emission at the two chosen poloidal locations also differs between the local and the line integrated signal. Locally, the peak emission in the private flux region is about 86% smaller than the peak emission at the strike point while the difference between the line integrated signals is about 75%.

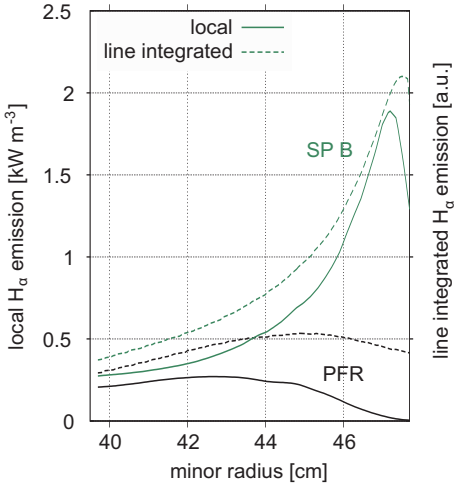

Figure 6.13
Radial profiles of the calculated H_α emission comparing the local emission (solid lines) to the line-of-sight integrated signals (dashed lines) [Frerichs 2010b]. The target surface is located at $r = 0.477\,\mathrm{m}$.

The modelled line-integrated profile at the strike point is similar to the experimentally observed profile shown in figure 6.11(a). The calculated peak emission is located a bit closer to the target surface by about 1 mm while the experimentally observed photon emission has dropped off by about 70% at $r = 0.42\,\mathrm{m}$ at the strike point. The difference between modelled and measured profile at the private flux region is more pronounced. The calculated emisson profile at the location of the private flux region is very flat and peaks at a minor radius of $r \approx 0.44\,\mathrm{m}$ which is larger by about 2 cm compared to the experimentally observed profile. Furthermore, the measured peak emission in the private flux region is only about 55% smaller than the peak emission at the strike point. The probable reason for this discrepancy is the additional light from the low field side (as already discussed above) which imposes an offset on the measured emission profiles. This offset is not constant but changes according to the recycling taking place at the low field side and therefore has a different effect at the different poloidal locations (strike

point and private flux region). Assuming a constant offset along the radial profile in front of the strike point, the comparison to the calculated profile leads to an approximation for the offset of about 7% of the peak emission.

6.4 Plasma source distribution

The penetration depths of neutral particles released from the divertor target, i.e. the location of their ionisation, determines the plasma source distribution. In the previous section the radial penetration depth at the strike points of the helical divertor was estimated to be about $3 - 4\,\mathrm{cm}$ in the low density regime. The relation of this plasma source distribution to the magnetic field structure in front of the target determines the plasma flow back to the target. If the major part of the neutrals reaches the confined plasma and is ionised there (as typical of limiter configurations), plasma flow throughout the whole scrape-off layer results, energy is mainly transported by convection and the SOL is in the sheath-limited regime (see section 2.3.3). If the ionisation is restricted to the scrape-off layer, the plasma flow within the SOL can be stagnant if the location and extent of the ionisation can be restricted to a small volume in front of the target. In this case a significant temperature gradient can develop between LCFS and target which is a prerequisite for high recycling, i.e. flux amplification to occur in the divertor. This is readily achieved in poloidal divertors when the penetration depth of the neutral hydrogen particles coming from the target gets smaller than the distance between X-point and divertor target.

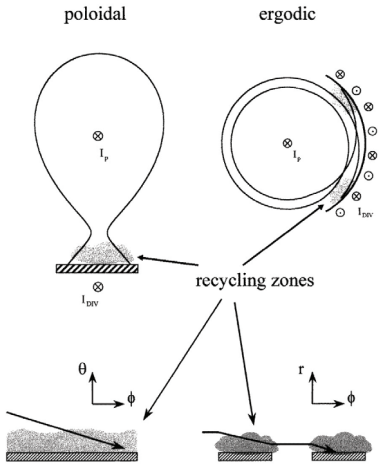

Figure 6.14
Schematic view of the relation between recycling zone and divertor geometry in poloidal and ergodic divertors from [Gunn et al. 1999].

Due to the more complex three-dimensional topology of the magnetic field in the helical divertor in TEXTOR the determination of the scrape-off layer and

especially of the distribution of energy, particle and momentum sources in this scrape-off layer is not straightforward. The distribution of the ionisation source term along a field line may have several maxima. Field lines of more than one poloidal turn can pass the recycling zone in the vicinity of the target plates without directly connecting to the wall thereby creating an upstream plasma source in close vicinity to the target. Figure 6.14 illustrates how particles recycling from the target in an ergodic divertor structure can constitute such upstream plasma sources on a field line with two poloidal turns. The distribution of upstream particle sources along magnetic field lines of short and long target-to-target connection length was analysed and discussed in [Frerichs 2010a] using three-dimensional modelling. Several locations of particle sources along a field line with four poloidal turns were identified exhibiting a strong effect on electron density, temperature and plasma flow quantified by the mach number along the field line at separatrix densities above $3 \cdot 10^{19}\,\mathrm{m}^{-3}$. This is the reason why the scrape-off layer of this helical divertor, defined as the volume governed by parallel energy flow to the target (see sections 3.3.2 and 3.3.3) shows a strong poloidal and radial variation with a radial extent between a few mm and up to 6 cm. Comparing this to the penetration depth of the neutral hydrogen particles estimated in the previous section shows, that a considerable part of the neutral particles released from the divertor target plates can be expected to be ionised outside the scrape-off-layer.

That part of the scrape-off layer in a poloidal divertor where recycling neutrals from the target plates are mainly ionised is sometimes referred to as the *downstream area*. This area is governed by strong plasma flow to the target and consequently convective dominates over conductive energy transport. The extent of this downstream area with respect to the connection length to the upstream location is usually small, especially in the high recycling regime. In the helical divertor in TEXTOR correspondingly a downstream area can be defined as that part of the scrape-off layer in front of the divertor target plates where the major part of the recycling takes place. In this area also high flow velocities towards the target are expected [Lehnen et al. 2007; Frerichs 2010a]. The detailed distribution of the sources amongst the different flux tubes connecting to the target, however, cannot be determined with this simple picture. For the configuration studied in this thesis, the downstream area is the region in front of the divertor target plates at the HFS which covers a poloidal angle of $\Delta\theta = 124°$ (see section 3.2) corresponding to about 0.3 of the total poloidal circumference of the torus. The downstream area correspondingly roughly comprises the region with shortest connection lengths to the target of less than 0.3 poloidal turns (see figure 6.15(a)). This is the maximum value for all the different flux tubes intersecting the target. Due to the complex three-dimensional structure, some flux tubes can have shorter downstream areas depending on the individual field line path. The strongly correlated short magnetic flux tubes for example have shorter recycling regions, according to the magnetic topology at maximum of about 0.1 poloidal turns.

Experimentally, the plasma source distribution is approximated as the integral

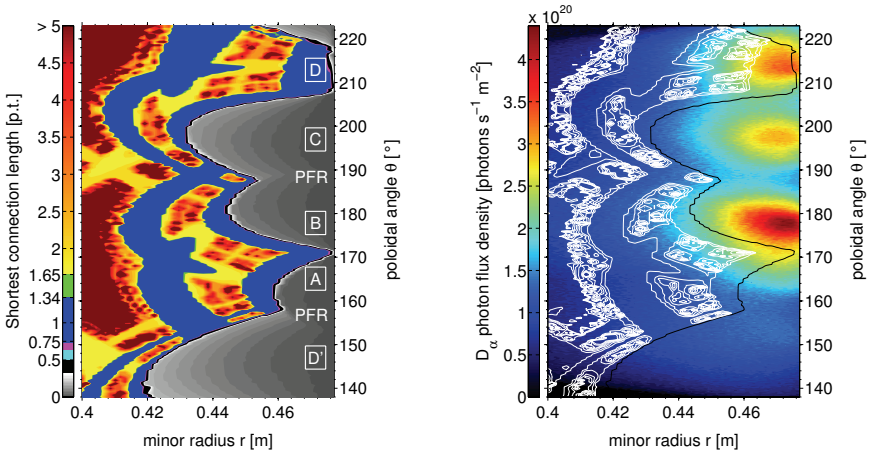

(a) Shortest distance along the field lines from the poloidal plane shown to the target plates in poloidal turns.

(b) Fig. 6.4(b) overlaid with contour lines taken from (a).

Figure 6.15 Illustration of the downstream area and comparison to the D_α photon emission for the poloidal cross section at $\varphi = 154.7°$.

of the observed Balmer photon emission at the tangential line of sight (see figures 5.9(a) and 5.8). Figure 6.15(b) shows the poloidal cross section of the D_α photon flux density overlaid with contour lines of the laminar plot in (a). The black line shows the boundary of the downstream area at this toroidal location. Using the D_α photon flux as a measure of the plasma source distribution, a ratio of downstream sources to the total sources in the observation volume can be calculated. This ratio however is only representative as long as the photon emission reflects the plasma source and the radial extent of the observation volume is much larger than the penetration depth. Especially the second condition is not fulfilled with the setup used, as the diagnostic has to cover a large angle of view. Only in the area around the equatorial plane it is guaranteed, that the observation area is large enough. At the top and bottom, part of the photon emission is vignetted in the radial as well as in the poloidal direction. For an integration region of $r = 0.4\,\mathrm{m}$ to $0.477\,\mathrm{m}$ (target surface) and $\theta = 138°$ to $223°$, the ratio was estimated to $Q_{\mathrm{down}}/Q_{\mathrm{tot}} \approx 0.45$. If this experimentally derived ratio between upstream and downstream sources holds true can be judged by a comparison to the results of the three-dimensional modelling. Here not only the calculated plasma sources can be summed up in the downstream area and in the whole simulated volume but also the estimation from the integrated photon emission can be evaluated. According to this analysis (see section 7.4), the estimation of the downstream sources from the line integrated Balmer α emission is slightly higher than the experimental value (0.49) and underestimates the source distribution by about

8 %. Roughly 50 % of the sources therefore lie outside the downstream area. This is typical of limiter configurations and of the low recycling regime in a poloidal divertor where the ionisation mainly takes place either outside the SOL or to some extent further upstream inside the SOL. Only when the major fraction of the ionisation takes place in the downstream area, flow along the SOL is reduced, heat is transported by conduction and a temperature gradient develops, finally leading to the high recycling regime. The variation of the ratio of downstream to total sources with rising plasma density is discussed in the next chapter and analysed using an extended two-point model with convection (see section 7.4).

6.5 Neutral hydrogen source distribution

Inferring the poloidal and toroidal distribution of the neutral hydrogen sources at the target plates from photon flux measurements is not straightforward, especially in the complex three-dimensional plasma structure of the helical divertor several things have to be taken into account:

Source effects

- the mixing of the particles from different sources leads to a smearing of the detailed source distribution (depending on the penetration depths of the particles and the distances of the sources).
- the strong modulation of the plasma parameters in front of the target (see section 6.1)
- the toroidal asymmetry of the magnetic field structure
- the inhomogeneity of the flux across the whole target due to the inaccuracies in the target tile alignment

Integration effects

- the smearing of the local photon emission due to the integration at incidence angles other than identical to the target normal in conjunction with the helical inclination of the strike points
- the photon flux from the low field side in the tangential line of sight

The effect of the mixing of particles from different sources was already discussed in section 4.1.4. The sources here are the adjacent strike points or strike lines of presumably different recycling flux. If the penetration depth of the particles is larger than the separation of the lines, intermixing of the particles can lead to an under- or overestimation of the particle fluxes. As the penetration depth of molecular hydrogen is considerably smaller than of atomic hydrogen, the Fulcher

band emission from molecular hydrogen is able to show a more detailed neutral source distribution.

As a first estimate of the poloidal modulation of the neutral particle fluxes from the target, the photon emission in a very thin region in front of the target plates is analysed. Therefore in images 6.4 and 6.9 (showing the tangential line of sight) the photon flux density and the Fulcher band emission, respectively, are averaged for $0.475\,\mathrm{m} \leq r \leq 0.477\,\mathrm{m}$ resembling the photon emission directly at the target but including integration effects as discussed above. Figure 6.16 shows the poloidal modulation of the photon emission from molecular hydrogen (a) and atomic hydrogen (b). The corresponding location and distances of the neutral particle sources can be estimated as a first approximation by the calculated magnetic field structure using the ATLAS code. Hence, additional to the photon emission the characteristic lengths of the magnetic field lines intersecting the target is shown in figures 6.16(a) and (b). Figure 6.16 shows, that for molecular as well as atomic deuterium, larger photon emission corresponds to longer connection lengths as well as a deeper penetration of the field lines into the plasma.

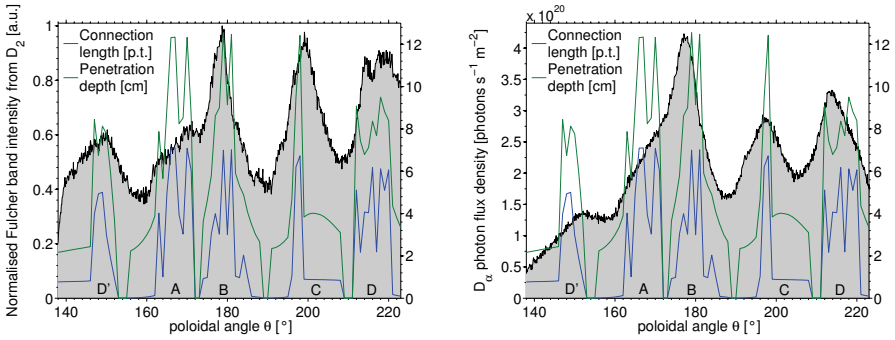

(a) Fulcher band emission from molecular deuterium

(b) D_α emission from atomic deuterium

Figure 6.16 Poloidal profile of the line integrated photon emission in front of the divertor target averaged for a minor radius of $0.475\,\mathrm{m} \leq r \leq 0.477\,\mathrm{m}$ at the tangential line of sight at $\varphi = 154.7°$ (black line), as well as the connection lengths and penetration depths of the magnetic field lines intersecting the target at this toroidal location (blue and green lines). The strike point labelled D' according to the 3D magnetic field topology belongs to strike point D (see section 3.3.2).

The widths of the strike points and the private flux regions according to the calculated connection lengths of the magnetic field lines is summarised in table 6.2. In section 6.3 the radial penetration depth of atomic hydrogen at the strike points was estimated to between 3 and 4 cm. Due to the lower electron density and

temperature in the private flux region, however, particles moving sideways from a strike point in the direction of a PFR will have a larger penetration depth in this direction. Thus, a neutral particle starting from the target e.g. at the edge of strike point B in the direction of the upper private flux region has a good chance of crossing the private flux region and reaching the lower edge of strike point C. Strong mixing is expected and the ratio of 50 of the particle flux at the strike points to that in the private flux region measured by target Langmuir probes (see section 3.3.3) is expected to show up less pronounced in the measured photon fluxes. In the light of molecular hydrogen (figure 6.16(a)), due to its smaller penetration depth, strike point A is distinguishable from strike point B and a substructure can be discerned at strike point D. Although the penetration depths of the atomic hydrogen particles is considerably larger than that of the molecules, the measured factor between the photon flux at the private flux region and the peak emission at strike point B is not larger for the Fulcher band emission. According to the profiles shown, in both cases the emission in the private flux region is about 2.5 times lower than the peak emission at strike point B. This is probably mainly due to the integration effects mentioned above, in particular the contribution from the low field side.

Strike point	width [°]	width [cm]
A	10	8.3
B	12	10.0
C	12	10.0
D	10	8.3
lower PFR	10	8.3
upper PFR	9	7.5

Table 6.2 Widths of the strike points and private flux regions (PFR) according to the field line connection lengths as shown in figure 6.16.

The integration effects are reduced for lines of sight closer to the target normal, which furthermore provide the possibility to estimate absolute neutral particle fluxes from the target plates from the measured line integrated Balmer line emission (see section 4.1.4). Figure 6.17 shows the D_α photon emission integrated along oblique lines of sight onto the divertor target at two different toroidal locations (P1 and P2, see figures 5.9(a) and 5.8). The abscissa shows the distance from the equatorial plane along the target.

Due to the toroidal asymmetry of the magnetic structure and the target tile alignment inaccuracies, the recycling flux and hence the photon emission strongly varies not only poloidally but also toroidally. The two toroidal positions were chosen because at P1 local measurements of the target ion flux, electron density and temperature by a Langmuir probe are available (about 5 cm below the equatorial plane, see figure 6.17(a)) and P2 lies closer to the perpendicular line of sight while still showing a fairly equal distribution of the photon emission among strike points B, C and D. It should be noted, that these toroidal locations are otherwise not

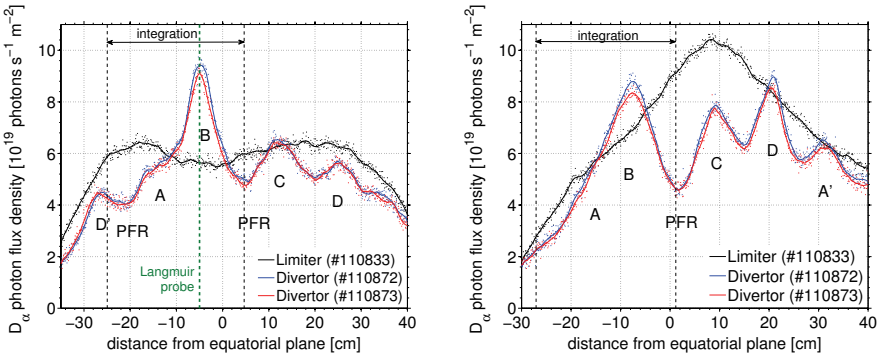

(a) Profile P1 at $\varphi = 176.5°$ ($\approx 47°$ versus the target normal)

(b) Profile P2 at $\varphi = 195°$ ($\approx 19°$ versus the target normal)

Figure 6.17 Poloidal profiles of the D_α photon emission integrated along oblique incidence angles for the reference discharge (black line) and two similar discharges with divertor operation (blue and red lines).

preferable in any way to other toroidal locations, they are not particularly more or less representative. The photon flux densities were averaged in the toroidal direction over an angle of 0.3° corresponding to about 7 mm along the target surface.

In the divertor discharge in profile P1 (figure 6.17(a)) the photon flux density is maximum at the location of the Langmuir probe, whereas in the limiter discharge (black line) a reduction in the photon emission is seen around this location caused by the target tile alignment inaccuracies already discussed before. The good agreement of the profiles from the different divertor discharges shows that the poloidal modulation of the photon flux is very reproducible. In profile P2 (figure 6.17(b)) during limiter operation the photon flux is strongest about 8 cm above the equatorial plane with about $1 \cdot 10^{20}\,\mathrm{m^{-2}s^{-1}}$ and quickly decreases towards top and bottom of the target. During divertor operation the strike point structure is more pronounced than for profile P1, the strongest photon flux is observed at strike points B and D with about $9 \cdot 10^{19}\,\mathrm{m^{-2}s^{-1}}$. At the upper private flux region the photon flux density is two times lower than at strike point B. A similar factor of 2.5 between the line integrated photon emission at these two locations is calculated by the EMC3-EIRENE code. The corresponding poloidal profile of the line integrated H_α emission calculated by the code is shown in figure 6.18 (blue line). Also shown in this figure are the local H_α emission averaged over a region of 1 cm width in front of the target plates (green line) as well as the calculated ion flux density at the target (red line). The peak ion flux density at strike point B calculated by the EMC3-EIRENE code is $\Gamma_{\mathrm{target}} \approx 1.7\,\mathrm{kAm^2} \approx 1 \cdot 10^{22}\,\mathrm{ions\,s^{-1}m^{-2}}$, it is 800 times larger than the minimum flux density in the private flux region.

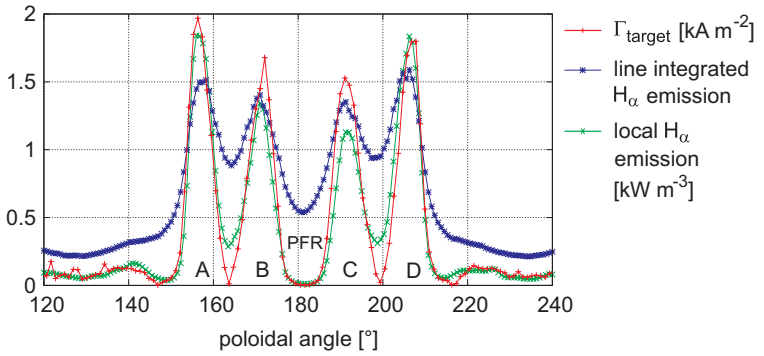

Figure 6.18 Poloidal profiles calculated by the EMC3-EIRENE code at the position of profile P2 ($\varphi = 195°$) for $n_{e,sep} = 2 \cdot 10^{19}\,m^{-3}$ [Frerichs 2010b]. The line integrated H_α emission is compared to the local H_α emission to demonstrate the influence of the line-of-sight integration.

The strike point structure in the calculated, line averaged photon emission is more pronounced than in the experimentally observed photon emission, where especially strike point A cannot be distinguished from strike point B. The experimental observations on the other hand (fig. 6.17(b)) show photon emission from a different part of strike point A (called A') which is not seen in the calculated photon emission. A possible reason for this is a small vertical shift of the whole plasma column towards the top of the vessel probably in conjunction with a shaded target tile at the location of strike point A. The peaks in the target ion flux density are slightly shifted versus the position of the peaks in the photon emission - the local as well as the line integrated. This shift is therefore inherent to the helical divertor and mainly does not result from the line-of-sight integration.

The modelled peak ion flux density can be compared to the ion flux density measured by the Langmuir probe at the position of profile P1 in the divertor discharge. As shown in figure 6.17(a) the peak photon flux density at strike point B is measured at the location of the probe. Hence, the ion flux density measured by the probe can be assumed to be close to the peak target ion flux density in this strike point and can be compared to the calculated peak ion flux density given above. The measured ion flux density can be read from figure 7.23 at the corresponding edge density of $n_e(2.15\,m) = 1.4 \cdot 10^{19}\,m^{-3}$ in the divertor discharge giving $\Gamma_{\parallel,LP} = 7 \cdot 10^{23}\,ions\,s^{-1}m^{-2}$. For comparison, in the limiter discharge the measured ion flux density is about half as large reading $\Gamma_{\parallel,LP} = 3 \cdot 10^{23}\,ions\,s^{-1}m^{-2}$ at the corresponding edge density of $n_e(2.15\,m) = 1.8 \cdot 10^{19}\,m^{-3}$ (corresponding to the same electron content in the plasma). This ion flux density however refers to a different area than the modelled flux density, as the Langmuir probe measures the ion flux parallel to the magnetic field. To be able to compare the flux densities, the incidence angle of the magnetic field lines at the location of Langmuir probe

has to be taken into account:

$$\Gamma_{\parallel} = \Gamma_{\text{target}} / \sin\alpha$$

with α defined as the angle between the target surface and the magnetic field line. Figure 6.19 shows α as calculated by the field line tracing code GOURDON. At the location of the Langmuir Probe the angle of incidence is $\alpha_{\text{LP}} \approx -0.8°$. Thus, the calculated parallel ion flux density is $\Gamma_{\parallel} \approx 7 \cdot 10^{23}\,\text{ions}\,\text{s}^{-1}\text{m}^{-2}$. In earlier experiments, toroidal profiles of the target ion flux have been measured with the help of several target Langmuir probes and the application of strike point sweeping (see sections 4.2 and 3.3.3). A factor of 60 between the parallel ion flux at the strike point and in the private flux region was measured which agrees well with the modelled modulation of the target particle flux (factor 800) taking into account the different incidence angles of the field lines in the private flux region (< 0.1) and at the strike point ($\approx 0.8°$).

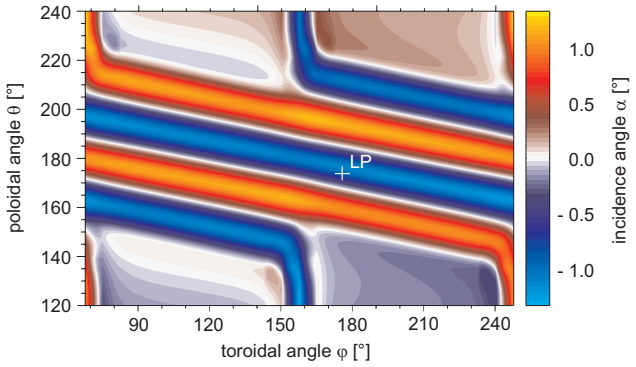

Figure 6.19
Incidence angle of the magnetic field lines on the divertor target calculated by the GOURDON code [Frerichs 2010b].

Secondly, the calculated ion flux to the target can be compared to the estimation of the neutral particle flux from the Balmer line emission. For graphite surfaces it is assumed that the incident ion flux is equal to the flux of released neutral hydrogen. For the strike point structure of the helical divertor, due to the mixing of the neutral particles from the different adjacent sources, the particle flux per unit length (in the toroidal direction), i.e. the poloidally integrated particle flux density, from strike points A and B is estimated and compared to the calculated ion flux. Therefore, several assumptions have to be made about the relation between particle flux and observation volume:

- In the *toroidal* direction the variation of the particle flux is small and the helical inclination of the strike points can be neglected if the particle flux density is averaged over a toroidal angle $\Delta\varphi$ small compared to the inclination angle of the strike points. In this direction, the particle fluxes from and into the observation volume are assumed to be balanced, the number of particles lost to the sides has to be equal to the number gained from the surrounding sources.

- In the *poloidal* direction strike points A and B are bound by the lower and the upper private flux region. The border of the integration region in this direction is chosen as the location of the minimum ion flux density calculated by the EMC3-EIRENE code within these private flux regions.
- To be able to use the inverse photon efficiencies for ionising plasmas calculated by a collisional radiative model provided for example by ADAS [Summers 2004], the population densities of exited states have to be determined mainly by electron impact excitation from the ground state. Furthermore, the inverse photon efficiency has to have only a weak dependence on electron density and temperature, so that the modulation of those along the line of sight and across the target can be neglected.

The integration of the calculated ion flux density from $\theta_1 = 146.9°$ to $\theta_2 = 181.6°$ yields an ion flux per unit length of

$$\int_{s(\theta_1)}^{s(\theta_2)} \Gamma_{\text{target}} \, \mathrm{d}s = 1.2 \cdot 10^{21} \, \text{ions}\, \text{s}^{-1}\text{m}^{-1}$$

at strike points A and B. The local electron density and temperature for the divertor discharge at the location of the photon emission can be approximated from figure 6.8 in accordance with the target parameters measured by the Langmuir probe (see section 6.1) yielding $n_\text{e} \approx 1 \cdot 10^{19}\,\text{m}^{-3}$ and $T_\text{e} \approx 30\,\text{eV}$. For these parameters, the inverse photon efficiency for D_α is $S/XB \approx 18$. The poloidally integrated photon flux density at profiles P1 and P2 is approximately

$$\int_{s(\theta_1)}^{s(\theta_2)} \Phi \, \mathrm{d}s = 1.7 \cdot 10^{19} \, \text{photons}\, \text{s}^{-1}\text{m}^{-1}$$

leading to an estimated neutral particle flux of $\Gamma_\text{n} \approx 3.1 \cdot 10^{20}\,\text{s}^{-1}\text{m}^{-1}$ for the two selected toroidal locations P1 and P2.

By using this inverse photon efficiency the assumption is made, that the hydrogen particles are dominantly released as atoms from the target surface. As pointed out earlier and seen from the observation of the D_2 Fulcher band emission, this is not the case here, but the particles are dominantly released as molecules from the graphite surface at surface temperatures below 1100 K. Therefore the S/XB value has to be replaced by an effective inverse photon efficiency. In accordance with earlier measurements [Brezinsek 2001], local injection experiments with molecular deuterium showed that the effective inverse photon efficiency for the plasma parameters considered here is about 2.5 times larger than the S/XB value given by the collisional radiative model for atoms. This leads to an estimation of the atomic deuterium flux of $\Gamma_\text{n} \approx 7.7 \cdot 10^{20}\,\text{s}^{-1}\text{m}^{-1}$. The chosen boundary for the integration of the photon flux density leads to an underestimation of the neutral particle flux from the two strike points.

6.6 Global recycling flux

In the previous section, the recycling flux in the divertor configuration integrated over two of the four strike points and the peak ion flux at strike point B were compared to the modelled target particle flux and were found to be in good agreement. In this section, the difference in the global recycling flux between the limiter configuration and the divertor configuration is discussed.

The strength of the recycling flux at the divertor target plates at the location monitored by the diagnostic is reflected on the one hand in the poloidally integrated D_α photon flux densities (see figure 6.20(a)) and in the poloidally integrated Fulcher band emission from molecular deuterium D_2 (see figure 6.20(b)). Both figures show, that at the same line averaged density at $R = 1.75\,\mathrm{m}$ the recycling flux on the divertor target plates at the monitored location is the same with and without divertor operation with good approximation.

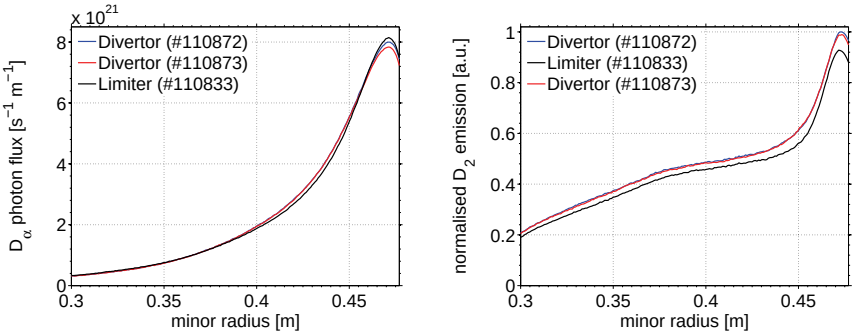

(a) D_α photon flux **(b)** D_2 Fulcher band emission

Figure 6.20 Radial profiles of the D_α photon flux integrated at the tangential line of sight from $\theta = 130°$ to $230°$ with and without divertor operation at $\varphi = 154.7°$. (a) is calculated from 6.4(a) and 6.4(b).

To conclude now on the variation in the global recycling flux between limiter and divertor configuration, the recycling flux on the other limiting objects in TEXTOR has to be considered. In section 3.2 it was pointed out, that in the limiter configuration, in particular at low plasma densities, the DED protection limiter constitutes the main limiting object for the plasma. The same observation is made in the divertor configuration, also here $\sim 92\,\%$ of the recycling takes place at the DED protection limiter, while $\sim 4\,\%$ takes place at the two poloidal limiters and the ALT-II limiter, respectively. This leads to the conclusion, that the recycling flux on the divertor target plates is not different between limiter and divertor operation and that the magnetic structure of the helical divertor only leads to a redistribution of the particle fluxes across the target. With the

assumptions of complete recycling at graphite surfaces, the overall particle *outflow* in the two configurations will be the same as well and as the total electron content in the plasma is also approximately equal, the particle confinement time cannot be significantly different between the limiter and the divertor case.

7 Characterisation of the high density regimes

In the previous chapter the hydrogen recycling at the divertor target plates was discussed at low plasma edge and core density. In this chapter the recycling at higher plasma densities up to the density limit is discussed. In order to study the low as well as the high density regime in the helical divertor in TEXTOR, discharges were performed in which the density at the plasma centre was increased continuously (so-called *density ramps*) leading to a corresponding increase of the density at the plasma edge. Aiming at studying the recycling in a fixed helical divertor structure, the current in the divertor coils was kept constant throughout the density ramp. Changes of the topology due to the rising density and hence a change in the poloidal beta β_{p} (ratio of the mean plasma pressure to the poloidal magnetic field pressure) are expected to be negligible as the divertor legs are fairly wide in the configuration studied and magnetic field calculations at various reasonable poloidal beta values showed no significant alteration of the topology.

This chapter gives an overview of the edge and divertor plasma phenomenology in the helical divertor in TEXTOR and, as far as presently understood, of the underlying physics. A comparison with modelling results from the EMC3-EIRENE code is done mainly by checking the consistency in general trends. Additionally an extended two-point model is used to assess possible leading-order effects for the observations made.

For the characterisation of the divertor regimes with the aid of the two-point model, the *downstream* parameters and fluxes in the divertor have to be related to the parameters at the *upstream* position at the stagnation point of the plasma flow in the scrape-off layer. In the helical divertor in TEXTOR the upstream position is difficult to define due to the complex three-dimensional geometry (see section 7.1.1). For further discussions and interpretations, the line averaged density at major radius $R = 2.15\,\mathrm{m}$, a location inside the stochastic region at the low field side, is used to analyse the global functionality.

7.1 Plasma parameters

7.1.1 Upstream plasma parameters

Density regimes in a divertor are usually characterised with the aid of the two-point model, comparing plasma parameters and fluxes at the target to the electron density and temperature at the stagnation point of the flux tube, the so-called upstream position, from where a continuous parallel flow to the target is built up. In the helical divertor in TEXTOR such a single upstream position common to all flux tubes does not exist, upstream can be at different radial and poloidal positions for different field lines. The stochastic edge exhibits a complex flow pattern where on short magnetic field lines ($L_c = 29\,\mathrm{m} \approx 1$p.t.) a single stagnation point can be identified, while on longer field lines (e.g. $L_c = 128\,\mathrm{m} \approx 4$p.t.) several stagnation points can exist [Frerichs 2010a]. Furthermore, changes in the plasma source distribution and consequently in the flow pattern might change the location of the upstream position throughout the density ramp. This makes the determination of upstream and downstream plasma parameters for the same flux tube extremely difficult, such measurements could not be carried out within the framework of this thesis. Instead, the line averaged density at a location inside the stochastic region at the low field side $n_{e,\mathrm{l.a.}}(2.15\,\mathrm{m})$ is used for the analysis of the general functionality. It could still be connected nonlinearly to the 'true' upstream density for a given downstream location.

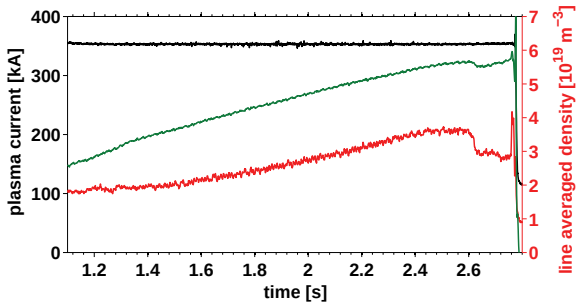

Figure 7.1 Time traces of plasma current and line averaged densities at $R = 1.75\,\mathrm{m}$ (green) and $R = 2.15\,\mathrm{m}$ (red) for divertor discharge #110872.

The density $n_{e,\mathrm{l.a.}}(2.15\,\mathrm{m})$ is measured in TEXTOR by an HCN interferometer-polarimeter [Koslowski and Soltwisch 1997] and is shown in figure 7.1 (red line) for the divertor discharge mainly studied in this chapter. The current in the DED coils was ramped up from 1.1 s to 1.4 s and then kept constant to the end of the discharge which ended in a disruption due to the formation of a MARFE close to the density limit. Also shown is the line averaged density in the core $n_{e,\mathrm{l.a.}}(1.75\,\mathrm{m})$ (green line)

which is observed to be nonlinearly related to $n_{\mathrm{e,l.a.}}(2.15\,\mathrm{m})$, as changes in the particle transport from the core lead to changes in the radial density profiles.

For comparisons of the experimentally observed plasma parameters and fluxes to those calculated by the three-dimensional modelling code, the line averaged density calculated by the code at the location of the interferometer channel at $R = 2.15\,\mathrm{m}$ was determined. It was then compared to the density used for analysing the modelling results, the separatrix density n_{sepx}, which is the prescribed density at the inner simulation boundary and hence an input parameter of the simulation. The relation of these two densities was found to be fairly linear between $n_{\mathrm{sepx}} = 0.7\,\mathrm{m}^{-3}$ and $4.8\,\mathrm{m}^{-3}$ with n_{sepx} (see figure 7.2). The figure also demonstrates the slightly nonlinear relation between the density at the stagnation point of a field line in one of the two short magnetic flux tubes (F1 in [Frerichs 2010a]), i.e. the upstream location of this flux tube, and the separatrix density.

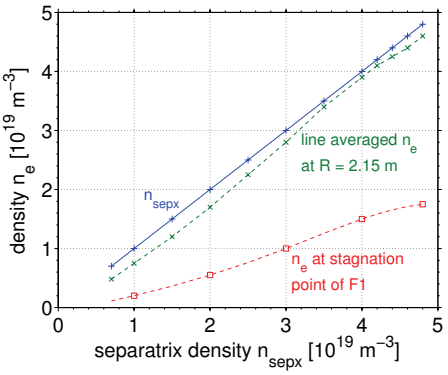

Figure 7.2
Calculated density at the location of the HCN interferometer channel at $R = 2.15\,\mathrm{m}$ (green line) and density at the stagnation point of one of the short magnetic flux tubes versus (red line) the separatrix density used in the transport analysis of the EMC3-EIRENE modelling results.

7.1.2 Downstream plasma parameters

The plasma parameters at the target, namely electron density and temperature, have been measured by a single Langmuir probe embedded in a target tile at poloidal angle $\theta = 173.8°$ and toroidal angle $\varphi = 176.5°$ (see figure 5.8 for the location). As the topology is expected to stay unaltered during the density ramp, the Langmuir probe measurement provides information of target plasma parameters and ion fluxes inside strike point B throughout the density ramp. The variation of the downstream electron density and temperature during the density ramp is shown in figure 7.3 for a limiter (black) and a divertor discharge (blue). In both graphs the ordinate shows the line averaged density at major radius $R = 2.15\,\mathrm{m}$. The large difference in the electron temperature (see fig. 7.3(a)) at the measurement position between limiter and divertor discharge at low densities (of about 40 eV) was already discussed in section 6.1. It is due to the fact that the target tile the Langmuir probe is installed in, is shadowed by the edges of

surrounding tiles. Therefore in the limiter configuration this location is subject to a lower particle flux from the plasma compared to other toroidal positions. This shadowing has a smaller effect in the divertor configuration, where the field lines are drawn onto the target by the magnetic perturbation field.

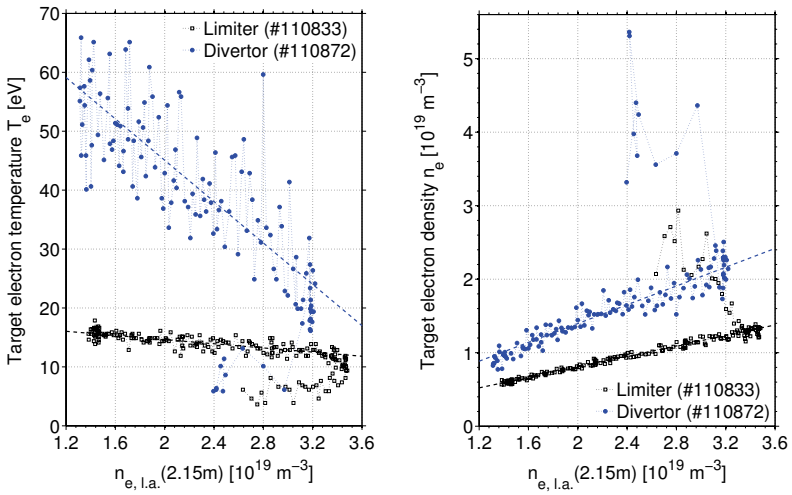

(a) Target electron temperature **(b)** Target electron density

Figure 7.3 Plasma parameters measured at the divertor target by the Langmuir probe at P1 in a limiter (black squares) and a divertor discharge (blue dots). For each discharge the dashed line shows a linear fit to the data between $n_{\mathrm{e,l.a.}}(2.15\,\mathrm{m}) \approx 1.4 \cdot 10^{19}\,\mathrm{m}^{-3}$ and $3.2 \cdot 10^{19}\,\mathrm{m}^{-3}$.

In the limiter discharge the electron *temperature* T_e at the target (see fig. 7.3(a)) is well described by a linear fit up to a threshold density of $n_\mathrm{thresh} \approx 3.2 \cdot 10^{19}\,\mathrm{m}^{-3}$. The temperature drops from $T_\mathrm{e} = 16\,\mathrm{eV}$ to 13 eV while the 'upstream' density rises from $n_{\mathrm{e,l.a.}}(2.15\,\mathrm{m}) \approx 1.4 \cdot 10^{19}\,\mathrm{m}^{-3}$ to n_thresh, the slope is therefore about $-1.7\,\mathrm{eV}$ per $10^{19}\mathrm{m}^{-3}$. Beyond n_thresh the temperature drops below 10 eV while the 'upstream' density first increases slightly up to $n_{\mathrm{e,l.a.}}(2.15\,\mathrm{m}) = 3.5 \cdot 10^{19}\,\mathrm{m}^{-3}$ and then drops to $n_{\mathrm{e,l.a.}}(2.15\,\mathrm{m}) = 2.7 \cdot 10^{19}\,\mathrm{m}^{-3}$. The drop in temperature is connected to the formation of a radiation instability (MARFE). In the divertor discharge the target electron temperature can also be described by a linear fit up to the same threshold density of $n_\mathrm{thresh} \approx 3.2 \cdot 10^{19}\,\mathrm{m}^{-3}$. Here the temperature drops from $T_\mathrm{e} \approx 57\,\mathrm{eV}$ to 25 eV while the 'upstream' density rises from $n_{\mathrm{e,l.a.}}(2.15\,\mathrm{m}) \approx 1.3 \cdot 10^{19}\,\mathrm{m}^{-3}$ to n_thresh, the slope is therefore ten times larger than in the limiter case with about $-17\,\mathrm{eV}$ per $10^{19}\mathrm{m}^{-3}$. In the divertor discharge the 'upstream' density also reaches a maximum value similar to the limiter discharge, beyond this point the 'upstream' density drops again and the downstream temperature decreases to around 10 eV. It cannot be ruled out, however, that the probe data

overestimate the downstream temperatures at these conditions. In particular, for scenarios with steep temperature gradients along field lines, probe characteristics tend to be affected by high-energy tail electrons from upstream positions with higher temperature. At high densities, these temperatures should therefore be seen as an upper limit of the local temperature.

The electron *density* n_e at the target (see fig. 7.3(b)) in the limiter case also increases linearly with the 'upstream' density throughout most of the density ramp with a slope of 0.35. From $n_{e,\,l.a.}(2.15\,\mathrm{m}) = 3.5 \cdot 10^{19}\,\mathrm{m}^{-3}$ it first drops with the same slope and then more than doubles while the 'upstream' density drops. This linear increase of the downstream (target) temperature with the 'upstream' temperature is characteristic of the sheath-limited regime and fulfilled in the limiter discharge up to the formation of the MARFE. In the divertor discharge the electron density at the target also increases linearly with the 'upstream' density, the slope being 0.6 and therefore larger than in the limiter case. The divertor seems to stay in the sheath-limited regime over almost the whole density ramp. Only at the 'upstream' density where the temperature drop is observed in figure 7.3(a), the target density rises strongly by a factor of two, but here the 'upstream' density also changes, dropping finally to $n_{e,\,l.a.}(2.15\,\mathrm{m}) = 2.4 \cdot 10^{19}\,\mathrm{m}^{-3}$.

Comparison to analytical model and 3D modelling

In the sheath-limited regime the target temperature is related to the upstream density $n(0)$ by $T_{\mathrm{target}} \sim n(0)^{-2/3}$ when the power flux into the scrape-off layer is constant (see equation 2.8). In the conduction limited regime, an exponent of -2 is predicted according to the two-point model. The three-dimensional modelling with the EMC3-EIRENE code showed, that also in the helical divertor in TEXTOR $T_{e,\mathrm{target}}$ can be described by a power law

$$T_{e,\mathrm{target}} = T_0 \left(\frac{n_0}{n_{\mathrm{sepx}}} \right)^{\alpha}$$

with two significantly different coefficients α_1 and α_2 for low and high densities (see [Frerichs 2010a]). The coefficients at strike point D were estimated to be

$$\begin{aligned} \alpha_1 &= 0.78 \pm 0.03 \quad \text{for low densities } (n_{\mathrm{sepx}} < 2.4 \cdot 10^{19}\,\mathrm{m}^{-3}) \\ \alpha_2 &= 3.40 \pm 0.12 \quad \text{for high densities } (n_{\mathrm{sepx}} > 2.4 \cdot 10^{19}\,\mathrm{m}^{-3}). \end{aligned}$$

At the other three strike points these coefficients are a bit smaller.

The measured target electron temperatures can also be described by such a power law up to a density of $n_{e,\,l.a.}(2.15\,\mathrm{m}) \approx 3.2 \cdot 10^{19}\,\mathrm{m}^{-3}$ (see the logarithmic plot in figure 7.4). In the limiter discharge the exponent is determined to be

$$\alpha_{\mathrm{Lim}} = 0.27 \pm 0.02$$

Compared to the expected scaling in the sheath-limited regime this leads to the conclusion that the power flux into the scrape-off layer cannot be constant here but increases approximately with $n_{\mathrm{e,l.a.}}(2.15\,\mathrm{m})^{1/2}$. This is consistent with the fact that the power flux into the SOL typically increases with rising core density.

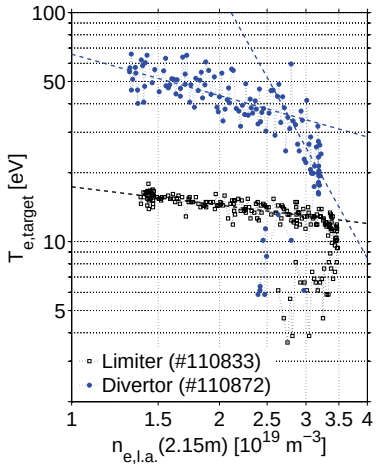

Figure 7.4
Logarithmic plot of the target electron temperature measured by the Langmuir probe with the dashed lines showing power law fits to the data.

In the divertor discharge also two different coefficients can be determined for low and high densities with a threshold density of $n_{\mathrm{thresh}} \approx 2.6 \cdot 10^{19}\,\mathrm{m}^{-3}$. At $n_{\mathrm{e,l.a.}}(2.15\,\mathrm{m}) < n_{\mathrm{thresh}}$ the target electron temperature can be described by a power law with exponent

$$\alpha_1 = 0.60 \pm 0.08.$$

For $n_{\mathrm{e,l.a.}}(2.15\,\mathrm{m}) > n_{\mathrm{thresh}}$ the exponent increases to

$$\alpha_2 = 3.9 \pm 0.5.$$

The scaling at low densities is in fair agreement with the modelling results in particular considering that the Langmuir probe measures the target parameters at strike point B. At medium and high densities however the behaviour is different in several ways:

- the threshold density is higher ($n_{\mathrm{e,l.a.}}(2.15\,\mathrm{m}) = 2.6 \cdot 10^{19}\,\mathrm{m}^{-3}$ corresponds to $n_{\mathrm{sepx}} \approx 2.9 \cdot 10^{19}\,\mathrm{m}^{-3}$)
- the measured temperature at the threshold density is higher ($T_{\mathrm{e}} \approx 35\,\mathrm{eV}$ compared to 20 eV)
- the second coefficient is larger, i.e. the temperature drops faster

This could be due to the fact that the power flux into the scrape-off layer was kept constant in the simulations and that these simulations did not include impurities which were present in the experiment mainly in the form of carbon. The

EMC3-EIRENE modelling results showed, that the strong change in the power law coefficient, i.e. the strong drop in temperature, corresponds to an increased power loss due to plasma-neutral interactions such as charge exchange processes and also corresponds to a drop in the target heat flux. At the experimentally observed target temperatures this explanation is however questionable, pointing towards the importance of impurity radiation for lowering the target temperature. A discrepancy between measurement and simulation is also seen in the target electron density scaling. While the measured target density shows a linear scaling with $n_{\mathrm{e,\,l.a.}}(2.15\,\mathrm{m})$ up to the formation of the MARFE, the simulated density shows a more than linear increase at medium densities followed by a beginning saturation at high densities (see figure 7.5). At the start of the density ramp though (corresponding to $n_{\mathrm{sepx}} \approx 1.7 \cdot 10^{19}\,\mathrm{m}^{-3}$) the absolute values of the target electron density are in good agreement.

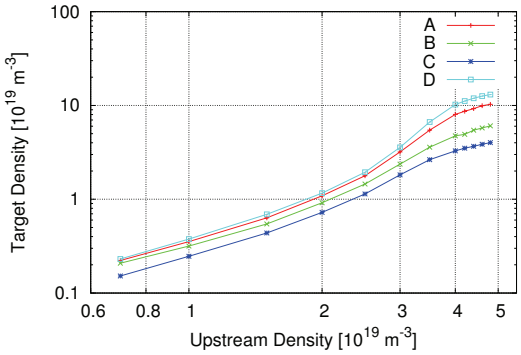

Figure 7.5
Electron density at the target modelled with the EMC3-EIRENE code at the four strike points [Frerichs 2010b]. The upstream density is estimated here as the separatrix density n_{sepx} which is an input parameter of the simulation.

The scaling of target temperature and density with $n_{\mathrm{e,\,l.a.}}(2.15\,\mathrm{m})$ raises doubts regarding the usage of the latter as a general measure of the upstream density for an analysis of the high density behaviour using the two-point model. According to the temperature scaling, the divertor leg connecting to strike point B of the helical divertor is in the sheath-limited regime at $n_{\mathrm{e,\,l.a.}}(2.15\,\mathrm{m}) < 2.6 \cdot 10^{19}\,\mathrm{m}^{-3}$ and shows a stronger drop in the target temperature than expected for the high recycling regime for $n_{\mathrm{e,\,l.a.}}(2.15\,\mathrm{m}) > 2.6 \cdot 10^{19}\,\mathrm{m}^{-3}$. At the same time, the target density shows only a linear scaling with $n_{\mathrm{e,\,l.a.}}(2.15\,\mathrm{m})$ which is in contradiction to the two-point model, where the localisation of the ionisation close to the divertor target in the high recycling regime is connected to a strong - nonlinear - increase in the local recycling and correspondingly in the target electron density.

7.2 Balmer photon emission

In the previous section it was shown that the plasma parameters at the target plates change significantly when the plasma core and edge density is increased

by gas puffing. Apart from the changes of electron density and temperature at the target, pronounced changes in these parameters in front of the target are visible in the modelling throughout the density ramp (see [Frerichs 2010a]). This is closely linked to changes in the neutral hydrogen density and the Balmer photon emission in front of the target. When the plasma density increases, the ion flux to the target increases likewise if no volumetric momentum losses or particle sinks exist in front of the target. As a consequence, the recycling flux from the target (saturated graphite surface, recycling coefficient $R \approx 1$) will also increase and the electron temperature in front of the target decreases, provided the power entering the scrape-off layer stays constant. Correspondingly, the photon emission will grow (see equation 4.10), not only due to the increasing neutral hydrogen flux from the target but also because of a decrease in the number of ionisations per photon in the observed temperature range (see figure 4.3).

In this section, the changes of the photon emission in front of the target plates with rising 'upstream' density observed by the spectroscopic camera observation system SPEW (see chapter 5) are presented and analysed. It is shown how the observations correspond to the spatially resolved and line integrated photon emission calculated with the three-dimensional modelling code EMC3-EIRENE and how the variations in the photon emission can be interpreted.

7.2.1 Poloidal and radial distribution

The changes in the radial and poloidal distribution of the D_α photon emission in the divertor discharge are observed at the tangential line of sight of the observation angle (see figures 5.8 and 5.9(a)). Figure 7.6 shows the poloidal cross section at various densities during the density ramp with the line averaged density at $R = 2.15\,\mathrm{m}$ given in the caption below each image. The target is located at the right hand side of the images at a geometrical minor radius of $r_{\mathrm{DED}} = 0.477\,\mathrm{m}$. The chronological order of the images during the discharge is identical to the alphabetical order from (a) to (h). The last five images are a sequence of consecutive frames at the highest plasma densities reached, separated by about 0.03 s. As already discussed in chapter 6, when interpreting this poloidal cross section it has to be taken into account that the distribution does not show an exact cut at the respective toroidal location but that the photon emission is integrated along the line of sight of the observation system. As the strike lines helically run around the torus, the integration leads to smearing compared to the cross sectional photon emission. This difference was visualised at low densities in figure 6.12 using the photon emission calculated by the three-dimensional modelling code.

The images recorded by the diagnostic show that the D_α photon emission at the strike points varies. At first the photon flux density at strike point D seems to increase stronger than at the other strike points. From frame (d) on the photon flux density at strike point C increases while it decreases at the other strike points.

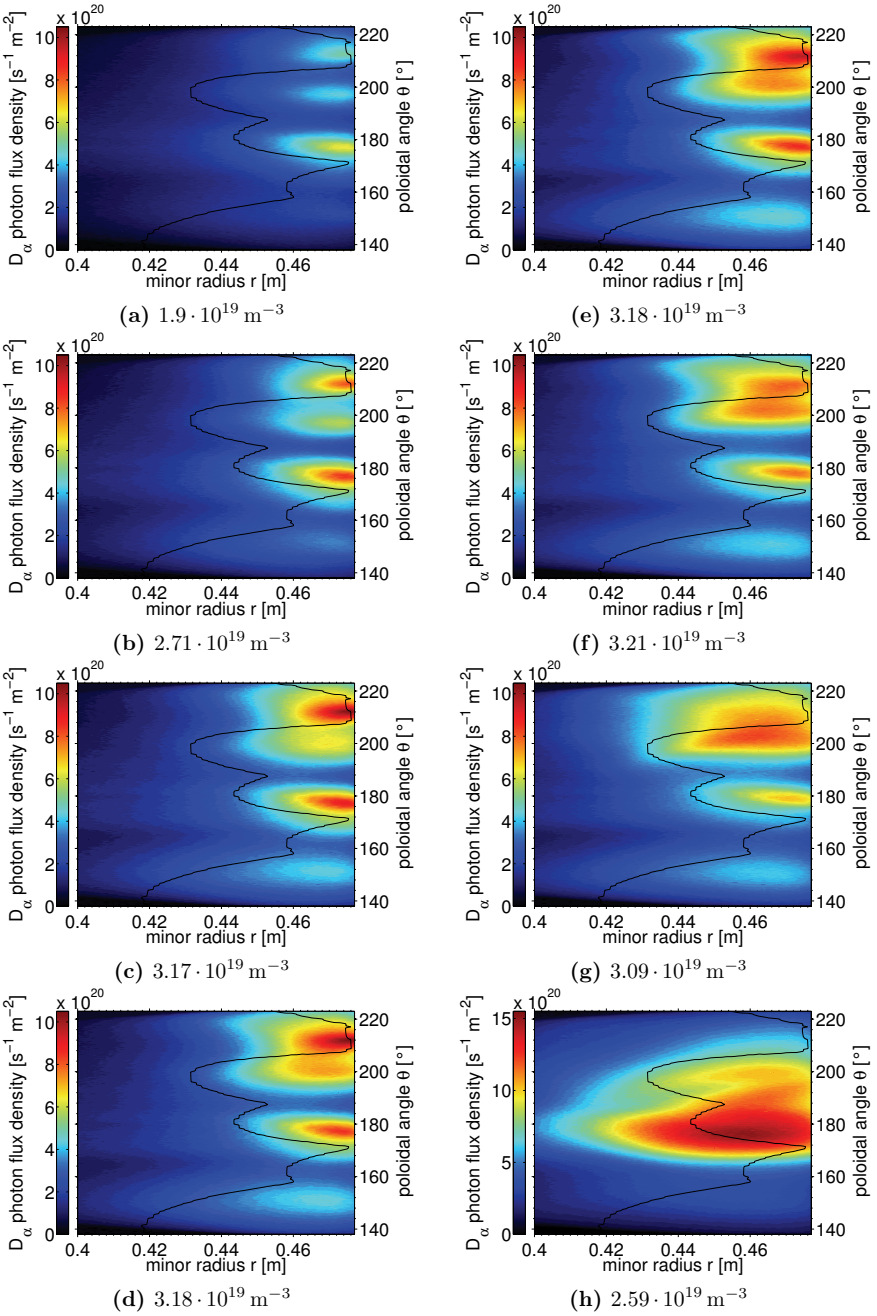

(a) $1.9 \cdot 10^{19}\,\mathrm{m}^{-3}$ **(e)** $3.18 \cdot 10^{19}\,\mathrm{m}^{-3}$

(b) $2.71 \cdot 10^{19}\,\mathrm{m}^{-3}$ **(f)** $3.21 \cdot 10^{19}\,\mathrm{m}^{-3}$

(c) $3.17 \cdot 10^{19}\,\mathrm{m}^{-3}$ **(g)** $3.09 \cdot 10^{19}\,\mathrm{m}^{-3}$

(d) $3.18 \cdot 10^{19}\,\mathrm{m}^{-3}$ **(h)** $2.59 \cdot 10^{19}\,\mathrm{m}^{-3}$

Figure 7.6 Radial cross sections of the D_α photon flux density at $\varphi = 154.7°$ with $n_{\mathrm{e,l.a.}}(2.15\,\mathrm{m})$. The black line indicates the scrape-off layer.

In the last time step from (g) to (h) a drastic increase in the photon emission occurs and the center of emission moves to strike points B and C. These images will be analysed further in section 7.3 as the poloidal cross section of the photon emission gives insight into the penetration depths of the neutral particles and therefore into the distribution of the plasma sources in front of the target (see section 7.4).

7.2.2 Radially integrated photon emission

The D_α photon emission integrated along oblique lines of sight onto the divertor target was analysed in chapter 6 at low plasma density (see for example the poloidal profile in figure 6.17(b)). According to the changes in the photon emission with rising plasma core density visualised above in the poloidal cross section, changes in the photon flux density can also be observed in the photon emission integrated along these oblique lines of sight. Figure 7.7 shows the variation in the line integrated photon flux density for profile P2.

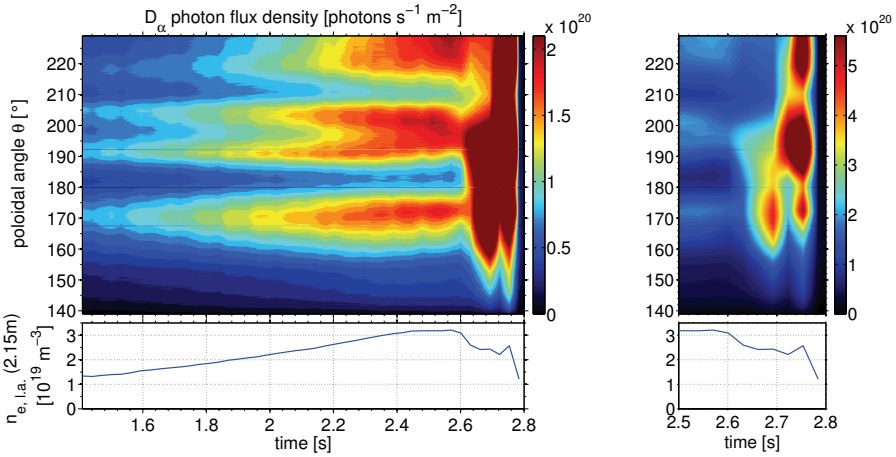

(a) Phase of constant divertor coil current until the density limit disruption.

(b) High density phase with different color axis.

Figure 7.7 Evolution of the D_α photon flux density at $\varphi \approx 195°$ with rising plasma core density. Below, the evolution of the line averaged electron density at $R = 2.15\,\mathrm{m}$ is depicted. In (b) the colour axis was chosen in order to visualise the saturated part in (a) at the location and time of the MARFE formation.

The photon flux density given in the figure was averaged toroidally over $\Delta\varphi = 0.5°$ equivalent to $\Delta s = 11\,\mathrm{mm}$ along the target tile. The poloidal angle can be

transferred to a poloidal coordinate along the target tiles in metres using the minor radius in toroidal coordinates of the target surface of $r_{\mathrm{DED}} = 0.477\,\mathrm{m}$. It can be seen that the photon flux density increases at each strike point regarding peak value and poloidal width of the emission. At intermediate to high densities strike points C and D start to combine, with the stronger emission still located at strike point D. The emission observed above strike point D at about 220° according to the magnetic footprint belongs to strike point A. Between 2.5 s and 2.6 s the photon emission first seems to shortly drop and shrink in poloidal extent before it strongly increases exceeding the colour axis maximum in figure 7.7(a). This part of the time trace is therefore shown again with a different colour scale in figure 7.7(b). It can be seen here that the emission is first located mainly at strike point A/B and then seems to jump to strike point C before the discharge ends in a density limit disruption.

Poloidal average of the photon emission

The global behaviour of the photon flux in front of the target plates, i.e. the average photon flux density between $\theta = 139°$ and 229° is shown in figure 7.8 and compared to the global behaviour in the limiter discharge. The selected toroidal angle is the same as above (profile P2, $\varphi \approx 195°$).

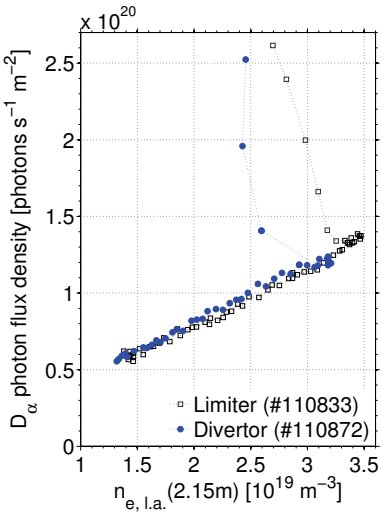

Figure 7.8
D_α photon flux density at profile P2 ($\varphi \approx 195°$) averaged between $\theta = 139°$ and 229° versus the line averaged electron density at $R = 2.15\,\mathrm{m}$. The dashed line shows the chronological order of the measured values.

In the limiter discharge the photon flux density linearly increases with rising line averaged electron density at $R = 2.15\,\mathrm{m}$ up to $n_{\mathrm{e,l.a.}}(2.15\,\mathrm{m}) = 3.5 \cdot 10^{19}\,\mathrm{m}^{-3}$ with a slope of $2.25 \cdot 10^{16}$ photons/s per $10^{19}\mathrm{m}^{-3}$. Beyond this point the 'upstream' density decreases again and the photon flux density at first decreases as well with the same slope as before but then it strongly increases at a density of

$n_{e,\,l.a.}(2.15\,m) \approx 3.2 \cdot 10^{19}\,m^{-3}$, roughly doubling its value. This strong increase in the Balmer photon emission can be attributed to the formation of a MARFE.

In the divertor discharge the photon flux density also increases approximately linearly with the 'upstream' density up to a threshold density of $n_{e,\,l.a.}(2.15\,m) = 3.1 \cdot 10^{19}\,m^{-3}$ where it seems to saturate shortly. The 'upstream' density reaches a maximum value of $n_{e,\,l.a.}(2.15\,m) \approx 3.3 \cdot 10^{19}\,m^{-3}$ and then decreases along with the photon flux density. When the density has dropped to $n_{e,\,l.a.}(2.15\,m) \approx 3.0 \cdot 10^{19}\,m^{-3}$ the photon emission starts to increase again finally rising to twice its value. This rise occurs also due to the formation of a MARFE which still shows a structure imposed by the magnetic field of the divertor coils. The edge density measured at $R = 2.15\,m$ at the onset of the MARFE formation is therefore slightly smaller than in the limiter case. The line averaged density in the plasma centre however is larger in the divertor case at the onset of the MARFE.

Photon emission averaged at selected strike points

When analysing and comparing the photon emission at the strike points of the helical divertor it has to be taken into account, that due to the spreading of the recycling particles no clear separation between the photon emission "belonging" to a particular strike point exists. When using the strike line pattern at the target plates as a separation criterion according to the connection lengths of the magnetic field lines calculated by the ATLAS code, the spreading of the recycling particles and the connected photon emission is not accounted for. However, this separation according to the magnetic field structure is done in this analysis bearing in mind that due to the intermixing the absolute values are not necessarily representative.

Overall the behaviour of the photon emission with rising 'upstream' density at the four selected strike points shown in figure 7.9 is quite similar to the poloidally averaged photon emission. Nevertheless, pronounced differences can be observed. The saturation in the photon flux density is generally more pronounced in all four strike points compared to the poloidally averaged signal. At strike point A the emission is not only considerably lower but also clearly saturates and even decreases at the highest 'upstream' densities reached. Such a reduction is also seen less pronounced at strike point B. During this photon flux reduction, according to the Langmuir probe measurement at strike point B, the target temperature drops from $T_e \sim 25\,eV$ to $< 10\,eV$ while the target density rises from $n_e \sim 2 \cdot 10^{19}\,m^{-3}$ to $> 4 \cdot 10^{19}\,m^{-3}$. In this temperature range, small uncertainties especially in the temperature lead to large differences in the corresponding inverse photon efficiencies (see figure 4.3) and hence in the interpretation of the photon flux. At a temperature drop to $T_e \sim 10\,eV$ and a density rise to $n_e \sim 4 \cdot 10^{19}\,m^{-3}$, the S/XB value would increase and the photon flux decrease would result from a saturation in the recycling flux. A slightly lower temperature would mean a constant or decreasing S/XB and hence the decreasing photon flux would be connected to a

drop in the recycling flux. As pointed out in section 7.1.2, the Langmuir probe measurements of the temperature should be seen as an upper limit of the local temperature at these conditions. This points towards a decreasing recycling flux at strike points A and B and thereby to a transient partial detachment prior to the MARFE formation.

The rise in the photon emission at the formation of the radiation instability is also significantly different at the four strike points. In strike points A, B and D, the photon flux at first increases only slightly while the 'upstream' density strongly drops to $n_e \sim 2.4 \cdot 10^{19}\,\mathrm{m}^{-3}$. At the same time the photon emission at strike point C already increases more pronounced.

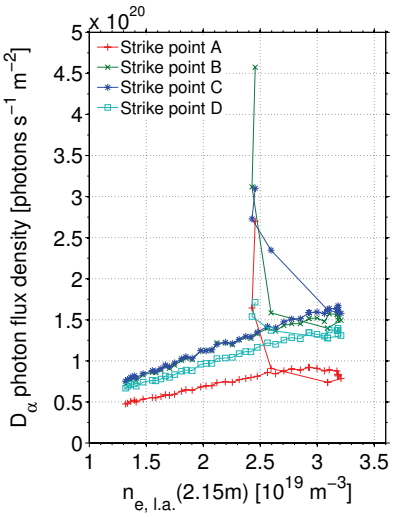

Figure 7.9
D_α photon flux density at $\varphi \approx 195°$ averaged at four selected strike point locations versus the line averaged electron density at $R = 2.15\,\mathrm{m}$. In the toroidal direction the photon flux density was averaged over $\Delta\varphi = 0.5°$. The solid line shows the chronological order of the measured values.

The three-dimensional modelling with the EMC3-EIRENE code shows a corresponding code instability at high separatrix density, i.e. the simulations turn unstable at $n_{\mathrm{sepx}} = 5.0 \cdot 10^{19}\,\mathrm{m}^{-3}$. When comparing the observations to the modelling results this part of the discharge is therefore left out here. Figure 7.10(a) shows again the photon emission measured at the strike points at $\varphi \approx 195°$, this time cut before the strong increase in the radiation due to the MARFE formation. Figure 7.10(b) shows the photon emission at a different toroidal location where the angle between target normal and line of sight is 50° and therefore larger than at the other toroidal location. It can be seen that the photon emission measured at strike point A does not differ between the two toroidal locations. At strike point B a deviation is seen in the higher density range from the linear increase seen in figure (a). At strike points C and D the photon emission is generally lower and does not increase as much as at the other toroidal location.

The calculations by the three-dimensional modelling code provide the opportunity to not only look at the line integrated photon emission as observed by the camera

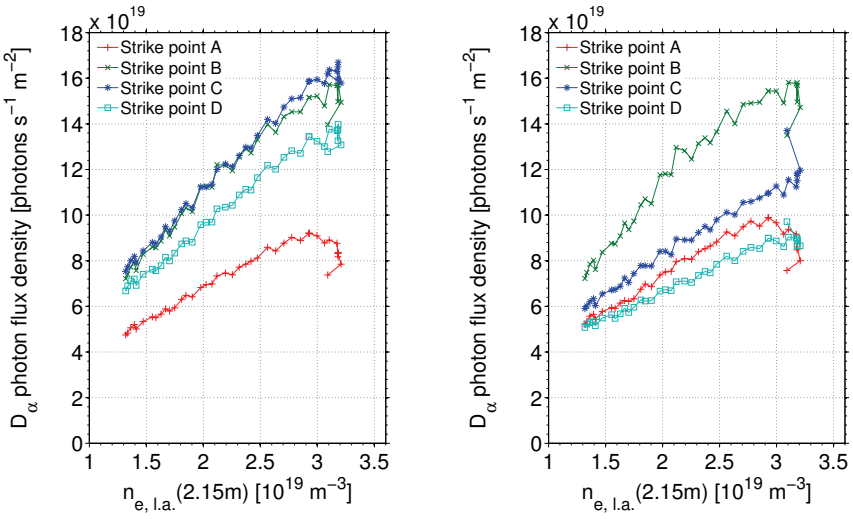

(a) At profile P2 ($\varphi = 195°$). **(b)** At profile P1 ($\varphi = 176.5°$).

Figure 7.10 D_α photon flux density averaged at the four selected strike point locations at profiles P1 and P2 versus the line averaged electron density at $R = 2.15\,\mathrm{m}$. Figure (a) shows the same as figure 7.9 except for the measurement points during the MARFE phase. The solid line shows the chronological order of the measured values.

diagnostic but also at very local changes in the photon emission, e.g. directly at the target. Furthermore a distinction can be made between Balmer line radiation from excitation processes and recombination processes. Figure 7.11(b) shows the calculated D_α emission from a radial width of 1 cm in front of the target separated into the contribution from excitation (solid lines) and from recombination (dashed lines, almost zero) at the same toroidal location as discussed above (profile P2). The contribution from recombination processes to the H_α line emission is still very small as plasma temperatures are still fairly high and recombination processes dominantly populate the higher excitation levels.

Figure 7.11(a) shows the calculated photon emission integrated along a line determined according to the line of sight of the camera diagnostic. It can be seen that - as expected - the integration along the line of sight has a largely influence on the observed evolution of the photon emission. Directly at the target a more than linear increase especially at strike points A and D can be observed at medium densities followed by a drop for separatrix densities larger than $n_{\mathrm{sepx}} = 3.5 \cdot 10^{19}\,\mathrm{m}^{-3}$. This behaviour is smoothed out to a large extent in the line integrated signal, instead of a drop a saturation is observed at large

'upstream' densities. This saturation is observed at larger 'upstream' densities than experimentally observed (inspite of the offset between n_{sepx} and $n_{\mathrm{e,l.a.}}(2.15\,\mathrm{m})$) and also the increase in the photon emission observed experimentally is smaller than according to the calculations. From figure 7.10(b) it can be seen that the measured photon emission at strike point D increases by a factor of 1.6 when the 'upstream' density is doubled, whereas the calculated photon emission increases by a factor of 3.2 in the same density range. The drop in the H_α emission directly in front of the target plates could also be observed experimentally at the tangential line of sight. This is shown in section 7.16(b), where radial profiles of the photon emission at various densities are analysed.

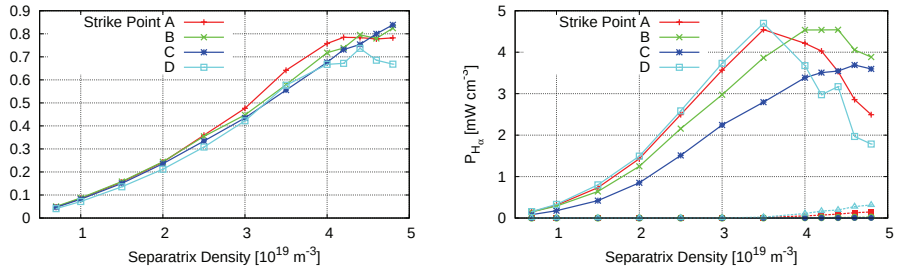

(a) Photon emission in arbitrary units integrated along a line of sight onto the divertor target. The sum of the contributions from excitation and recombination is shown [Frerichs 2010b].

(b) Photon emission averaged in 1 cm region in front of the divertor target. Contributions from electron impact excitation (solid) and recombination processes (dashed). Taken from [Frerichs 2010a].

Figure 7.11 H_α photon emission at profile P1 (toroidal angle $\varphi = 176.5°$) calculated by the three-dimensional modelling code EMC3-EIRENE.

7.2.3 Balmer line ratios

The different contributions to the observed Balmer line radiation from the excitation and recombination population processes of the upper levels of the hydrogen neutrals (see figure4.1) also shows in the measured signals. Here however it is not possible to distinguish between the two contributions a priori, but by calculating the ratios of different Balmer lines, such as the D_α and the D_γ line for example, it is possible to draw conclusions on the relative importance of the radiation from recombination processes. Therefore the D_α/D_γ line ratio is analysed and discussed in the following. This is done on the one hand averaged poloidally across the target and on the other hand at the four selected strike points at the two toroidal positions already discussed in the previous section on the D_α photon emission.

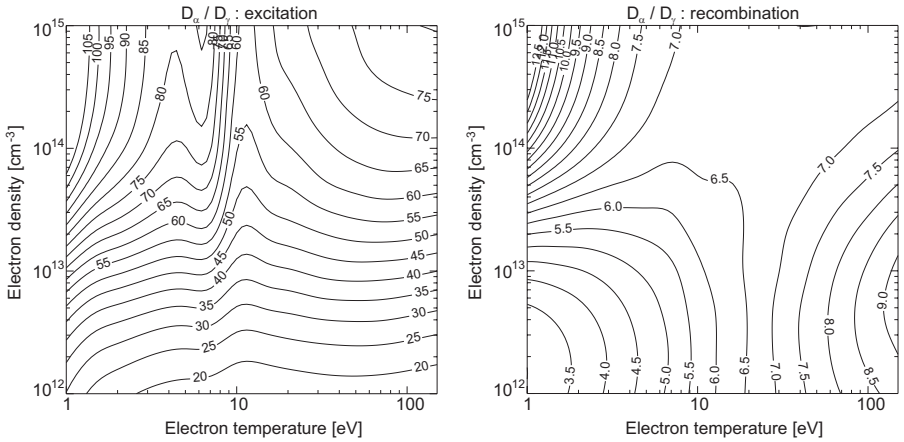

(a) Ionising plasma. **(b)** Recombining plasma.

Figure 7.12 Ratio of D_α and D_γ line emission due to excitation and recombination from the ADAS database [Summers 2004; McCracken et al. 1998].

Line ratio averaged across the target

Up to a threshold density, the averaged Balmer line ratio D_α/D_γ grows with rising 'upstream' density in the limiter as well as in the divertor discharge (see figure 7.13). In the limiter discharge the ratio grows linearly from about 39 to 49 and then drops strongly after reaching the maximum upstream density when the radiation instability forms. The radiation instability is characterised by a very cold and dense plasma in front of the target plates which is dominated by recombination processes. Therefore the D_γ line radiation increases much more strongly than the D_α line radiation leading to such a strong drop in the ratio of the two. The line ratio however does not drop as low as expected from a recombining plasma which can partly be attributed to the fact, that the MARFE has a restricted extent in the poloidal direction and the line ratio has been averaged over a larger poloidal range. Generally the D_α/D_γ line ratio is slightly higher in the limiter discharge compared to the divertor discharge. From the line ratios taken from the ADAS database (figure 7.12(a)) this points towards a higher averaged electron density in front of the target plates in the limiter discharge as the ratio is fairly insensitive to changes in the electron temperature between $T_\mathrm{e} \approx 15\,\mathrm{eV}$ and $100\,\mathrm{eV}$.

In the divertor discharge the ratio also grows linearly from 35 to 45 up to an 'upstream' density of $n_{\mathrm{e,l.a.}}(2.15\,\mathrm{m}) \approx 2.9 \cdot 10^{19}\,\mathrm{m}^{-3}$. Between 2.9 and $3.3 \cdot 10^{19}\,\mathrm{m}^{-3}$ the ratio drops again to about 39 while the D_α photon flux alone keeps increasing (see figure 7.9). According to the predicted line ratio from the ADAS database (figure 7.12(a)) this could be explained either by a drop in density or by a drop

both in temperature and density. The spectroscopically observed line ratio hence supports the interpretation of the decrease in the photon flux density in section 7.2.2 as resulting from a decrease in the recycling flux and the assumption, that the target temperature is overestimated by the Langmuir probe measurement. A stronger drop in the line ratio to ≈ 27 is observed during the MARFE. At this point, the 'upstream' density has already dropped to $n_{\mathrm{e,\,l.a.}}(2.15\,\mathrm{m}) \approx 2.5 \cdot 10^{19}\,\mathrm{m}^{-3}$. This line ratio however is still larger than expected for a plasma dominated by recombination (see figure 7.12(b)). As in the limiter case, this can be due to the averaging across the target, strong drops in the ratio can be equalled out by higher values at different poloidal locations. Hence, a spatially resolved analysis is done in the following, showing differences in the Balmer line ratio between the strike points.

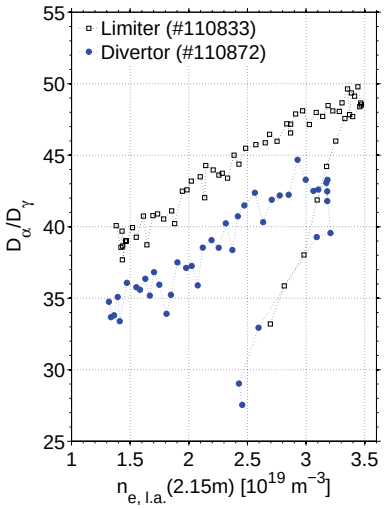

Figure 7.13
Poloidally averaged ratio of the D_α and D_γ line emission at profile P2 ($\varphi = 195°$) versus the line averaged electron density at $R = 2.15\,\mathrm{m}$. The dashed line shows the chronological order of the measured values.

Line ratio at selected strike points

For the spatially resolved analysis of the D_α/D_γ line ratio the average of the ratio is calculated across each of the four strike points and shown in figures 7.14(a) at profile P2 and (b) at profile P1. The ratio does not vary much between the different strike points but is generally a bit higher at profile P1, where the target is viewed under a larger angle versus the target normal.

In the discussion of the target plasma parameters in section 7.1 a threshold density of $n_{\mathrm{thresh}} \approx 2.6 \cdot 10^{19}\,\mathrm{m}^{-3}$ was identified beyond which the drop in the target electron temperature was larger, finally reaching $T_\mathrm{e} \approx 20\,\mathrm{eV}$. The Balmer line ratio exhibits a corresponding saturation followed by a slight drop for $n_{\mathrm{e,\,l.a.}}(2.15\,\mathrm{m}) > n_{\mathrm{thresh}}$. The behaviour of the line ratio at the MARFE formation strongly differs

between the strike points. At the upper two strike points C and D the ratio only drops to the value at the start of the density ramp whereas at the lower two strike points it strongly drops to a value of around 15. The ratio at these two strike points is still higher than expected for a recombination dominated plasma but leads to the conclusion that recombination processes contribute a major fraction to the line radiation locally across the target and the plasma temperature must have dropped below $T_e \approx 1.5\,\mathrm{eV}$ (see figure 4.1).

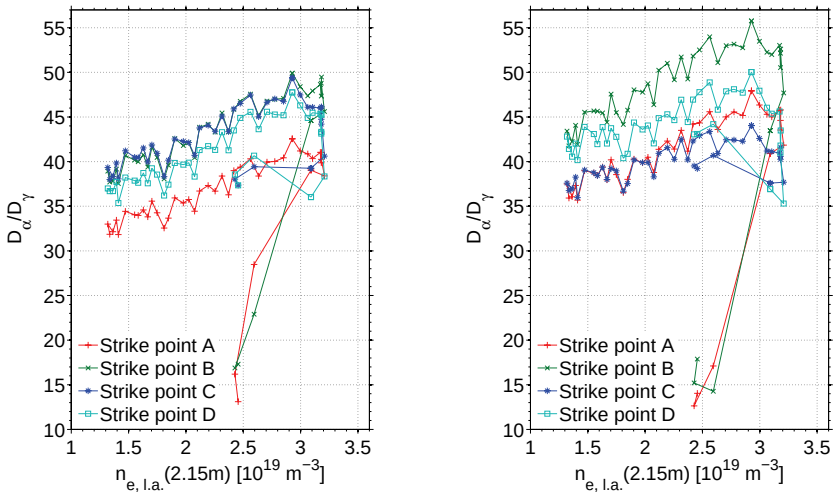

(a) For profile P2 ($\varphi = 195°$). **(b)** For profile P1 ($\varphi = 176.5°$).

Figure 7.14 Ratio of the H_α and H_γ line emission averaged at the four selected strike points at the two profiles P1 and P2 versus the line averaged electron density at $R = 2.15\,\mathrm{m}$. The solid line shows the chronological order of the measured values.

The measured line ratio is in fair agreement with the line ratio calculated from the EMC3-EIRENE modelling results (see figure 7.14) although the calculated line ratio is generally slightly lower than the experimentally derived. At the separatrix density $n_{\mathrm{sepx}} \approx 2.9 \cdot 10^{19}\,\mathrm{m}^{-3}$ corresponding to the experimental threshold density, the line ratio shows a short stronger increase before leveling off as also seen in figures 7.14(a) and (b). The behaviour at the different strike points differs from the experimental observation, where all of the four strike points show a drop in the line ratio before the strong drop at strike points A and B occurs due to the formation of the MARFE.

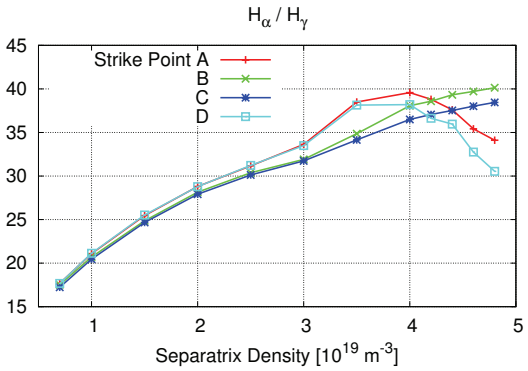

Figure 7.15
Ratio of the H_α and H_γ line emission from the neutral densities and plasma parameters modelled with the EMC3-EIRENE code [Frerichs 2010b].

7.3 Penetration depth of atomic hydrogen

As shown in the previous sections, the photon emission distribution in front of the target plates changes significantly with rising plasma core density in the limiter discharge as well as in the divertor discharge. This corresponds to a change in the penetration depths of the neutral particles. Radial emission profiles at strike point D ($\theta = 210°$) from the images in 7.6 are shown in figure 7.16(b). Their chronological order is visualised by the color coding of the profiles (starting from blue going via green and yellow to red). Radial profiles from the limiter discharge at the same poloidal location are shown in figure 7.16(a) for various densities. Here the photon flux density constantly increases with rising plasma density and still increases when the edge density drops again. A drastic increase in the emission is seen in the last time step together with a deformation of the radial profile. In the divertor discharge the photon flux density first increases with rising density, then the edge density stays roughly constant while the photon flux density keeps increasing and then drops and radially moves away from the target.

Figure 7.17 shows a closer analysis of the movement of the peak emission and of the e-folding length at strike point D for both - limiter and divertor discharge. In the limiter discharge the distance of the peak emission from the target surface stays approximately constant throughout the whole density range. The distance of the e-folding length from the target surface at first decreases linearly starting from low densities up to the maximum edge density reached and then linearly increases again with a different slope. In the divertor discharge, the peak emission is closer to the target compared to the limiter case and the distance from the target first decreases slightly by about 0.5 cm. At $n_{\mathrm{e,l.a.}}(2.15\,\mathrm{m}) \approx 3.3 \cdot 10^{19}\,\mathrm{m}^{-3}$ the distance suddenly increases by about 1 cm and stays at this location while the edge density drops to $2.4 \cdot 10^{19}\,\mathrm{m}^{-3}$. The distance of the e-folding length from the target surface behaves similarly: At low densities it is smaller by about 1.5 cm compared to the limiter case. From there it decreases at first, reaching minimum

proximity at $r \approx 0.447\,\mathrm{m}$ at an edge density of $n_{\mathrm{e\ l.a.}}(2.15\,\mathrm{m}) \approx 3 \cdot 10^{19}\,\mathrm{m}^{-3}$. At $n_{\mathrm{e\ l.a.}}(2.15\,\mathrm{m}) \approx 3.3 \cdot 10^{19}\,\mathrm{m}^{-3}$ the distance suddenly increases strongly, thereby showing a sudden increase in the penetration depth of the neutral particles at this poloidal location.

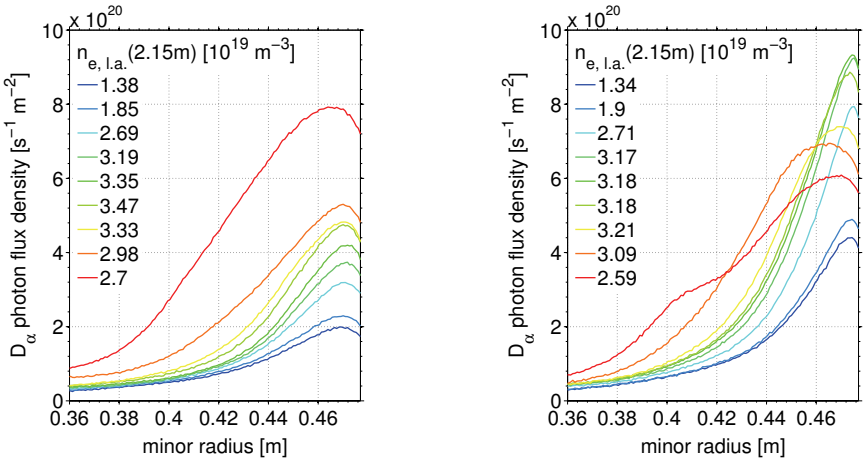

(a) Limiter operation. **(b)** Divertor operation.

Figure 7.16 Radial profiles of the D_α photon flux density at $\varphi = 154.7°$ for several 'upstream' densities. The photon flux density was averaged poloidally at $\theta = 213.5°$ over $\Delta\theta = 2°$. In radial direction the spatial resolution is $\approx 0.8\,\mathrm{mm}$.

The modelled Balmer line emission shows a very similar behaviour. The left graph in figure 7.18 shows radial emission profiles at strike point D at various densities from the EMC3-EIRENE modelling. The black circles are the locations of the peak emission also shown at additional intermediate density steps. As can be seen, the distance of the peak emission first decreases to $r = 0.473\,\mathrm{m}$ at a separatrix density of $n_{\mathrm{sepx}} = 2 - 3 \cdot 10^{19}\,\mathrm{m}^{-3}$. Then the distance increases first slightly and then strongly at a threshold density of $n_{\mathrm{sepx}} = 3 - 4 \cdot 10^{19}\,\mathrm{m}^{-3}$ to 2.5 cm. The right graph in figure 7.18 shows the radial profiles of the ionisation source which looks very similar at first glance. It shows, however, that the maximum ionisation source is located closer to the target than the peak Balmer line emission, especially at low separatrix densities. Already from a density of $n_{\mathrm{sepx}} = 2 \cdot 10^{19}\,\mathrm{m}^{-3}$ the peak ionisation source slightly moves away from the target and the distance strongly increases above $n_{\mathrm{sepx}} = 3 \cdot 10^{19}\,\mathrm{m}^{-3}$.

The decrease of the penetration depth can be attributed to the rising electron density in the divertor region. It is already known from the transition from the low recycling to the high recycling regime in poloidal divertors. For establishing

high recycling like in a poloidal divertor, however, a major fraction of the neutral particles has to be ionised not only inside the scrape-off layer but furthermore close to the target. This distribution of the plasma sources in the helical divertor is discussed in the following section.

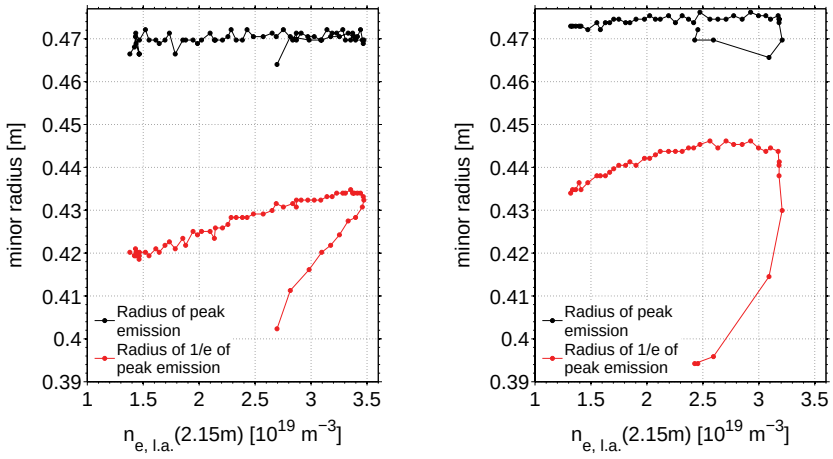

(a) Limiter operation. **(b)** Divertor operation.

Figure 7.17 Radius of peak D_α emission and e-folding length at strike point D ($\theta = 210°$) versus line averaged electron density at $R = 2.15\,\mathrm{m}$.

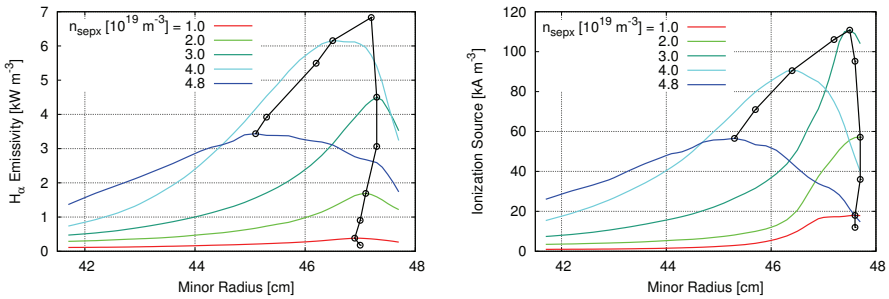

(a) H_α emission. **(b)** Ionisation source.

Figure 7.18 Radial profiles of H_α emissivity and ionisation source [Frerichs 2010a].

7.4 Plasma source distribution

In section 6.4 in the analysis of the low density regime it has already been pointed out that the location of the ionisation source with respect to the scrape-off layer and with respect to the target has a large impact on the plasma flow and the possibility of creating large temperature gradients between the LCFS and the target. A *downstream area* was defined, approximately comprising the region with shortest connection lengths to the target of up to 0.3 poloidal turns. In this section, the variation in the ratio between the ionisation sources in the downstream area and the total ionisation sources with rising plasma density is investigated. Experimentally, the plasma source distribution is approximated as the integral of the observed Balmer photon emission at the tangential line of sight.

The variation in the ratio of the downstream sources to the total sources changes only slightly with rising 'upstream' density (see figure 7.19(a)). It increases from about $Q_{\mathrm{down}}/Q_{\mathrm{tot}} \approx 0.45$ to 0.5 up to an 'upstream' density of $n_{\mathrm{e\ l.a.}}(2.15\,\mathrm{m}) \approx 2.5 \cdot 10^{19}\,\mathrm{m}^{-3}$. Then it stays roughly constant and finally drops towards the creation of the MARFE.

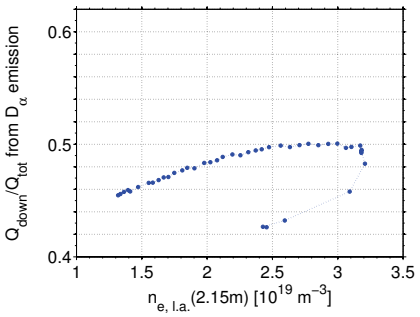

(a) Ratio derived from the measured D_α emission at the tangential line of sight. The line indicates the chronological order.

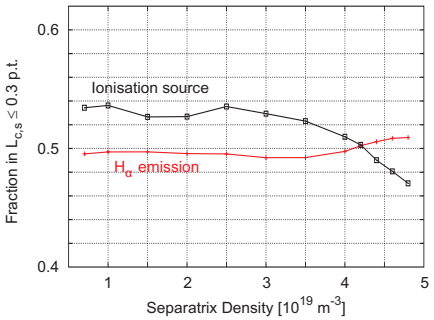

(b) Ratio derived from modelled H_α emission and ionisation sources (for three different perpendicular diffusion coefficients D) [Frerichs 2010b].

Figure 7.19 Ratio of downstream ionisation sources to total sources from experiments and three-dimensional modelling with the EMC3-EIRENE code.

The ratio estimated from the modelling results with the EMC3-EIRENE code shows a different behaviour (see figure 7.19(b)). According to the simulations, the integrated H_α emission at the tangential line of sight of the camera diagnostic stays approximately constant at about 0.5 throughout the density ramp and does not reflect the ratio of the ionisation sources. The volume integrated ionisation sources also stay approximately constant at low densities but start to decrease

slowly at the threshold density identified in the analysis of the target electron temperature, finally reaching a fraction of 0.47.

Throughout the density ramp, a considerable amount of the ionisation takes place outside the downstream area which means, in case of the studied helical divertor configuration, that it also takes place outside of the scrape-off layer. The standard two-point model for poloidal divertors does not take into account ionisation outside the scrape-off layer. This is a further possible explanation why the scaling of the measured target electron temperature and density with the 'upstream' density did not obey the scaling predicted by the standard two-point model. Extensions of the standard two-point model have been developed which take into account convective heat flux and have been applied e.g. to limiter configurations [Tokar et al. 2004] and also the helical divertor configuration in TEXTOR [Lehnen et al. 2008]. Such a model is now used in the following to assess the accessibility of a high recycling regime in the studied configuration.

Two-point model with convection

The simplified geometry used for this model is depicted in figure 7.20. It shows a flux tube of length L that is split up into a downstream or *recycle region* of length L_{rec} where ionisation takes place inside the flux tube and a region of length $L_{\mathrm{cond}} = L - L_{\mathrm{rec}}$ called *conduction region* in the standard two-point model, where heat transport can be dominated by conduction. The heat flux along this conduction region is now described including not only heat conduction but also heat convection along the magnetic field driven by the fraction f_{conv} of particles coming from the target which is ionised outside the scrape-off layer:

$$q_{\parallel} = q_{\parallel,\mathrm{cond}} + q_{\parallel,\mathrm{conv}} = -\kappa_0 T^{5/2} \frac{\partial T}{\partial x} + \left(\frac{1}{2} m v_{\parallel}^2 + 5 k_{\mathrm{B}} T \right) \Gamma_{\parallel} \tag{7.1}$$

The equation is based on the following assumptions:

- the coupling of electrons and ions is high and the electron temperature is hence equal to the ion temperature $T = T_{\mathrm{i}} = T_{\mathrm{e}}$
- the heat conduction is dominated by the electrons with the electron heat conductivity $\kappa_0 \approx 2000$ (for T [eV]) according to the theory of heat conduction by [Spitzer and Härm 1953]
- the plasma is quasineutral $n_{\mathrm{e}} = n_{\mathrm{i}}$ (hydrogen) and the plasma flow is ambipolar $v_{\mathrm{e}} = v_{\mathrm{i}}$

The kinetic term in equation 7.1 is neglected in the following, knowing that the maximum parallel velocity $v_{\parallel}$ is the sound speed $c_{\mathrm{s}} = \sqrt{2 k_{\mathrm{B}} T / m}$ and the heat flux is thus underestimated at maximum by 20 %.

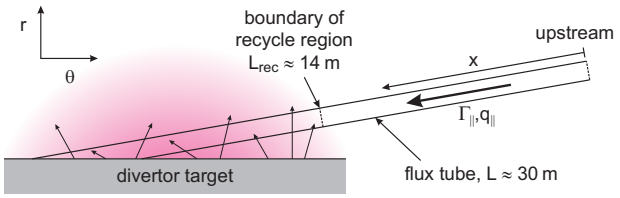

Figure 7.20
Simplified picture of a flux tube in the helical divertor configuration.

The convective heat flux density $q_{\parallel,\mathrm{conv}}$ is driven by the particle source inside the confined plasma, in a stationary state this is a fraction of the recycling flux, i.e. the neutral particle flux from the target $f_{\mathrm{conv}}\Gamma_0 A_\perp$. Assuming complete recycling, the ion flux to the target is equal to the recycling flux $\Gamma_{\parallel,\mathrm{t}} A_\parallel = \Gamma_0 A_\perp$, with the cross section of the flux tube $A_\parallel$ and its projection onto the target surface, i.e. the wetted target surface $A_\perp$. With the particles uniformly entering the flux tube all along the length of the conduction region L_{cond}, the particle transport is described by:

$$\frac{\partial \Gamma_\parallel}{\partial x} = \frac{f_{\mathrm{conv}}\Gamma_0 A_\perp}{A_\parallel L_{\mathrm{cond}}} = f_{\mathrm{conv}}\frac{\Gamma_{\parallel,\mathrm{t}}}{L_{\mathrm{cond}}}.$$

The power coming into the flux tube from the confined volume P_{SOL} is finally lost through two channels, it is transferred to the target with the kinetic energy of the charged particles and lost on ionisation and excitation of neutrals recycling from the limiter:

$$\frac{P_{\mathrm{SOL}}}{A_\parallel} = q_{\parallel,\mathrm{t}} + (1 - f_{\mathrm{conv}})\frac{\Gamma_0 A_\perp}{A_\parallel} E_{\mathrm{i}}$$

with the parallel target heat flux density

$$q_{\parallel,\mathrm{t}} = \gamma \Gamma_{\parallel,\mathrm{t}} k_{\mathrm{B}} T_{\mathrm{t}}, \tag{7.2}$$

the parallel target particle flux density

$$\Gamma_{\parallel,\mathrm{t}} = n_{\mathrm{t}} c_{\mathrm{s}} = n_{\mathrm{t}}\sqrt{\frac{2k_{\mathrm{B}}T_{\mathrm{t}}}{m}}, \tag{7.3}$$

the sheath transmission coefficient $\gamma \approx 7.5$, target temperature T_{t}, density n_{t} and the effective energy loss by ionisation and excitation $E_{\mathrm{i}} \approx 30\,\mathrm{eV}$ [Tokar et al. 2004]. Assuming that the heat influx into the flux tube is distributed over the whole length of the conduction region L_{cond}, the heat transport is described by

$$\frac{\partial q_\parallel}{\partial x} = \frac{P_{\mathrm{SOL}}}{A_\parallel L_{\mathrm{cond}}} = \frac{q_{\parallel,\mathrm{t}}}{L_{\mathrm{cond}}} + (1 - f_{\mathrm{conv}})\frac{\Gamma_{\parallel,\mathrm{t}}}{L_{\mathrm{cond}}} E_{\mathrm{i}}.$$

This two order differential equation in T can be transformed into a system of two first order differential equations and solved numerically with boundary conditions:

$$\left.\frac{\partial T}{\partial x}\right|_{x=0} = 0 \quad \text{and} \quad T|_{x=L_{\mathrm{cond}}} = T_{\mathrm{t}}.$$

Input parameters are the target heat and particle flux densities $q_{\parallel,\mathrm{t}}$ and $\Gamma_{\parallel,\mathrm{t}}$. The target temperature and density are defined via equations 7.2 and 7.3. Finally, the upstream density is derived from the assumption that the loss of particle momentum can be neglected (condition for attachment in the standard two-point model, see section 2.3.3). In this case the sum of static and dynamic pressure is constant along the flux tube, giving:

$$n_\mathrm{u} T_\mathrm{u} = 2 n_\mathrm{t} T_\mathrm{t}.$$

Figure 7.21 shows the result of the calculation for $q_{\parallel,\mathrm{t}} = 47\,\mathrm{MW}$ and $L_\mathrm{cond} = 16\,\mathrm{m}$ (the recycle region is at maximum $L_\mathrm{rec} = 1/3\,\mathrm{p.t.} \approx 14\,\mathrm{m}$).

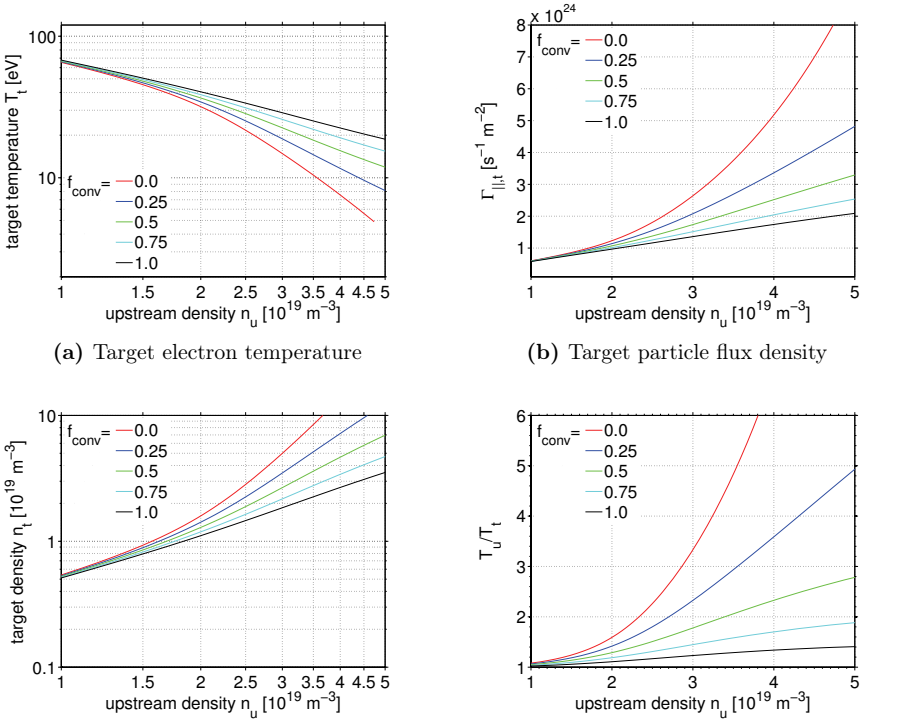

(a) Target electron temperature

(b) Target particle flux density

(c) Target electron density

(d) Ratio of upstream and target electron temperature

Figure 7.21 Relation between upstream and downstream plasma parameters calculated using the extended two-point model with convection. The fraction of convective heat flux was used as a parameter.

For the measured ratio of convective transport of $f_\mathrm{conv} = 0.5$ no strong increase in the target particle flux in the experimentally achievable density range is seen

and the temperature ratio between upstream and downstream location is small. This is consistent with the experimentally observed target plasma parameters (see section 7.1.2) and particle fluxes (see section 7.5) except for the saturation seen at the highest densities. A high recycling like regime is only seen, when the convective transport is strongly reduced, i.e. when the model merges into the standard two-point model (including the hydrogen recycle loss energy) for $f_{\mathrm{conv}} \to 0$. The observed absence of a high recycling regime can therefore be explained by the localisation of a large fraction of the ionisation source outside the scrape-off layer of the helical divertor driving convective heat flux to the target. The model does not explain the saturation in the particle flux observed experimentally as well as in the simulations.

7.5 Recycling flux

The method of estimating neutral particle fluxes from line integrated photon flux densities was already discussed and applied at low plasma density in section 6.5. In this section the variation in the integrated particle flux density from strike points A and B (in particles per unit time and length) with rising plasma density is discussed. The particle flux is not only derived from the D_α line emission but also from two other Balmer lines (D_β, D_γ) using the appropriate inverse photon efficiencies. To account for the variation in the inverse photon efficiencies due to the changes in the plasma parameters during the density ramp, the derivation of the inverse photon efficiencies is based on the measured target electron density and temperature. The comparison of the particle flux density deduced from the different Balmer line measurements at low and medium plasma densities showed, that the D_β emission has to be scaled by a factor of 1.6 in order to give the same particle flux as deduced from the D_α and D_γ emission. The reason for this systematic error, however, is currently unknown.

Figure 7.22 shows the integrated particle flux density from strike points A and B in the divertor configuration and from the same poloidal location in the limiter configuration. In figure 7.22(a) the particle flux density evolution prior to the MARFE is shown. In the limiter configuration it rises linearly up to $\Gamma_{\mathrm{n}} \approx 1 \cdot 10^{21}\,\mathrm{s^{-1}m^{-1}}$ at $n_{\mathrm{e,l.a.}}(2.15\,\mathrm{m}) = 3.2 \cdot 10^{19}\,\mathrm{m^{-3}}$ and then drops to $\Gamma_{\mathrm{n}} \approx 0.6 \cdot 10^{21}\,\mathrm{s^{-1}m^{-1}}$. In the divertor configuration the particle flux density is generally larger than in the limiter configuration and grows more strongly with rising density. It also rises linearly, though only up to $n_{\mathrm{e,l.a.}}(2.15\,\mathrm{m}) = 2.4 \cdot 10^{19}\,\mathrm{m^{-3}}$ and then starts to saturate. Although a decrease in the photon flux density at strike points A and B could be observed at the highest densities, the inverse photon efficiency determined from the interpolated target electron density and temperature measured by the Langmuir probe increases and thereby counteracts the photon flux drop. The uncertainty in the determination of the recycling flux based on this method at

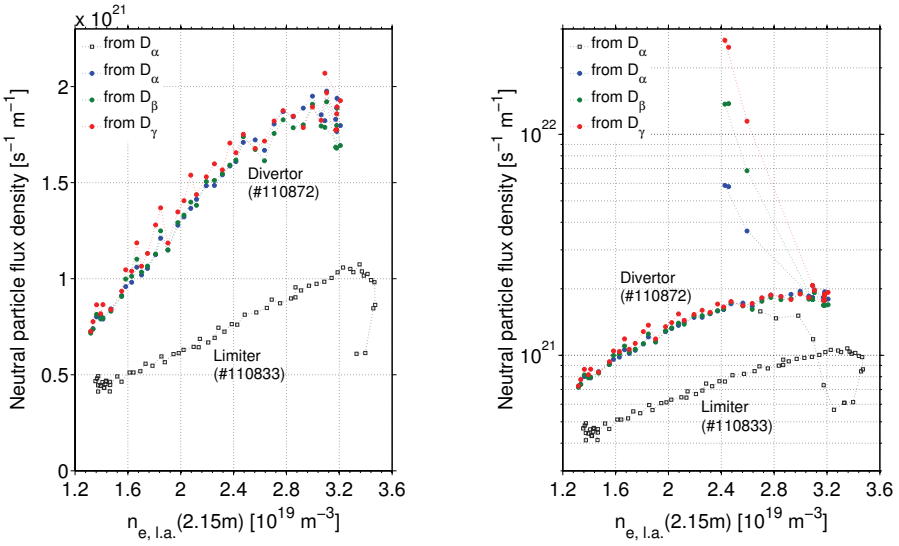

(a) Density ramp prior to MARFE. **(b)** Density ramp including MARFE phase.

Figure 7.22 Integrated neutral particle flux density from strike points A and B at profile P1 ($\varphi = 176.5°$) estimated from the measured photon flux.

this point of the density ramp is too large to draw a definit conclusion on the behaviour of the recycling flux from this analysis. However, in section 7.2.2 and 7.2.3 it was already pointed out, that the decrease in the photon flux density at strike points A and B just before the MARFE formation most likely results from a decrease in the recycling flux.

The particle flux evolution including the MARFE phase is shown in (b), showing that here the flux strongly increases to a level above the maximum flux reached at the end of the density ramp in the limiter as well as the divertor configuration. The fluxes derived from the different Balmer lines strongly deviate. This is the consequence of the observation of the drop in the Balmer line ratio discussed in section 7.2.3, which indicates recombination processes becoming important. These processes on the one hand contribute to the Balmer line emission, especially for the D_β and D_γ emission, and on the other hand the condition is not fulfilled anymore that every recycled atom is ionised only once on its way into the plasma. Hence the particle flux is overestimated when this contribution is not accounted for in the inverse photon efficiency. An effect of the drop in the D_α/D_γ line ratio observed *before* the MARFE formation is not detected. This could be either due to measurement uncertainties or because this drop cannot be attributed to recombination processes but occurs purely due to changes in local plasma parameters.

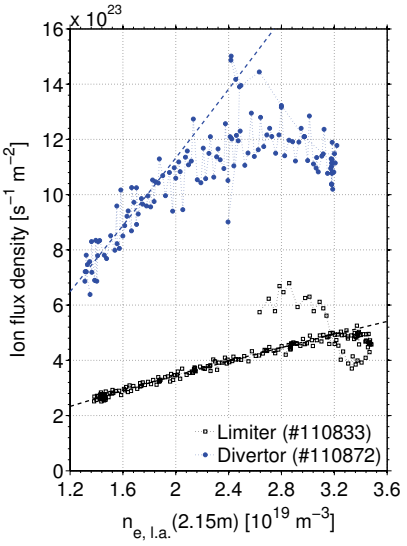

(a) Peak parallel ion flux density $\hat{\Gamma}_{\parallel,\mathrm{B}}$ in strike point B.

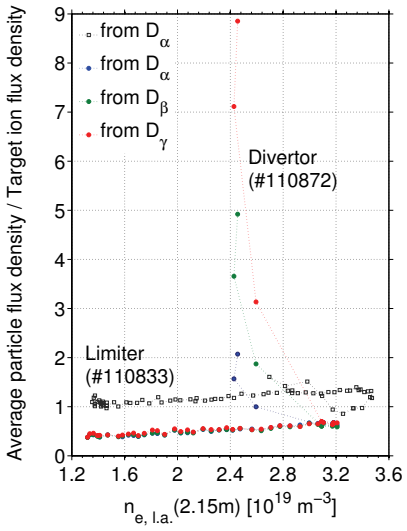

(b) Ratio between average parallel particle flux at strike points A and B and peak ion flux density shown in (a).

Figure 7.23 Peak parallel ion flux density $\hat{\Gamma}_{\parallel,\mathrm{B}}$ measured in strike point B by the Langmuir probe and comparison to the average parallel particle flux $\langle \Gamma_{\parallel,\mathrm{AB}} \rangle$ at strike points A and B deduced from spectroscopic measurements for the limiter and the divertor configuration.

In order to compare this neutral particle flux density integrated over two strike points to the parallel target ion flux measured by the Langmuir probe (see figure 7.23(a)) and calculated with the help of the extended two-point model in the previous section, the average flux density per unit area has to be calculated and the incidence angle of the magnetic field needs to be taken into account as discussed in section 6.5. Therefore, the neutral particle flux is divided by the estimated strike point width of $\Delta s_{\mathrm{A,B}} \approx 0.183\,\mathrm{m}$ (see table 6.2) and transformed into a parallel particle flux using an average incidence angle of $\alpha \approx 0.5°$ for the limiter configuration and $\alpha \approx 0.8°$ for the divertor configuration. Figure 7.23(b) shows the ratio of this average parallel particle flux density $\langle \Gamma_{\parallel,\mathrm{AB}} \rangle$ at strike points A and B and the peak parallel ion flux density $\hat{\Gamma}_{\parallel,\mathrm{B}}$ in strike point B measured by the Langmuir probe. In the limiter configuration, the local ion flux measured by the Langmuir probe shows a very similar behaviour compared to the neutral particle flux deduced from the Balmer line emission. It rises linearly up to $n_{\mathrm{e,l.a.}}(2.15\,\mathrm{m}) \approx 3.2 \cdot 10^{19}\,\mathrm{m}^{-3}$ and then drops shortly before rising to $\hat{\Gamma}_{\parallel,\mathrm{B}} \approx 6 \cdot 10^{23}\,\mathrm{s}^{-1}\mathrm{m}^{-2}$ during the MARFE. The ratio shown in figure 7.23(b)

is consequently approximately equal to one during the whole density ramp and even during the MARFE. In the divertor configuration the peak ion flux also rises linearly at low densities but levels off at $n_{\mathrm{e,l.a.}}(2.15\,\mathrm{m}) \approx 2.0 \cdot 10^{19}\,\mathrm{m}^{-3}$ and also drops slightly before increasing to $\hat{\Gamma}_{\parallel,\mathrm{B}} \approx 1.5 \cdot 10^{24}\,\mathrm{s}^{-1}\mathrm{m}^{-2}$ due to the MARFE formation. Its absolute value at low densities is about twice as high as $\langle \Gamma_{\parallel,\mathrm{AB}} \rangle$ deduced from the spectroscopic measurements, showing a good correspondence between the measurements, having in mind the poloidal modulation of the particle flux in the divertor configuration. The ratio between average and peak flux also increases only slightly during the density ramp prior to the MARFE. In the MARFE phase, the overestimation of the neutral particle flux from the measured Balmer photon fluxes leads to a strong deviation from the peak target ion flux.

Finally, the behaviour of the measured recycling flux density can be compared to the behaviour of the target particle flux density at the selected strike points calculated by the EMC3-EIRENE code (see figure 7.24). Calculations using a cross-field transport coefficient of $D_\perp = 1\,\mathrm{m}^2\mathrm{s}^{-1}$ (a free model parameter) showed a similar behaviour of the target particle flux with an almost linear rise at low and intermediate densities followed by a saturation at high densities. The particle flux density is lowest at the strike point consisting almost completely of one of the short magnetic flux tubes with a target-to-target connection length of about one poloidal turn. Strike point B comprises the other end of this flux tube, but also flux tubes of longer target-to-target connection length and deeper penetration.

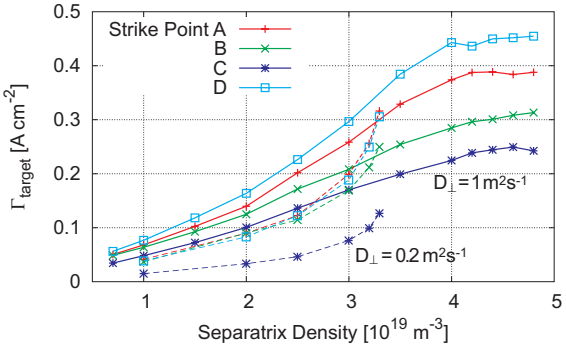

Figure 7.24
Target particle flux density at the selected strike points calculated by the EMC3-EIRENE code [Frerichs 2010b] for two different levels of cross-field transport $D_\perp$ and $\chi_\perp = 3D_\perp$.

For a five times lower cross-field transport coefficient of $D_\perp = 0.2\,\mathrm{m}^2\mathrm{s}^{-1}$, the behaviour of the calculated target particle flux density with respect to the separatrix density (input parameter) is considerably different. A linear increase at low densities is followed by a strongly nonlinear increase at intermediate densities at all four strike points. If this behaviour can be interpreted as a high recycling behaviour is not clear yet, as the separatrix density in this case could be related nonlinearly to the density at an upstream reference point for the flux tubes connecting to the strike points. The simulations finally turn unstable at much lower separatrix densities compared to the simulations with $D_\perp = 1\,\mathrm{m}^2\mathrm{s}^{-1}$. Due

to the larger separatrix densities reached in the simulations with higher cross-field transport, the target particle flux densities reached there are still higher than for $D_\perp = 0.2\,\mathrm{m^2 s^{-1}}$.

7.6 Heat flux

One aim of the high density divertor operation is the reduction of the heat flux on the divertor target at still high upstream temperatures of $> 100\,\mathrm{eV}$. In the helical divertor configuration, the redistribution of the particle flux on the divertor target also leads to a concentration of the heat flux at the strike points [Jakubowski et al. 2007].

The local heat flux density at one of the strike points can be estimated from the target ion flux density and target electron temperature measured by the Langmuir probe using equation 4.11. Using the same heat transmission coefficient ($\gamma = 7.5$) as previously used in the extended two-point model, gives the heat flux density shown in figure 7.25.

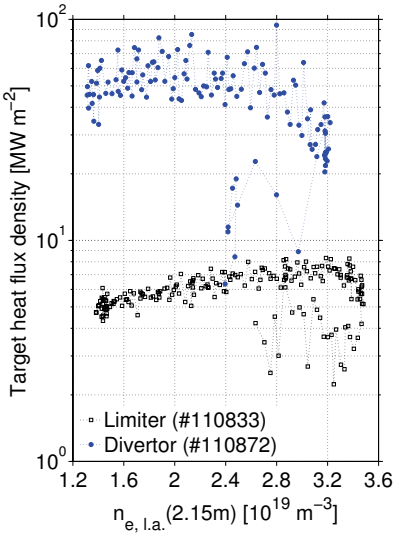

Figure 7.25
Target heat flux density at strike point B derived from the Langmuir probe measurement of target ion flux density and electron temperature.

The measurements show that indeed in the divertor configuration the heat flux density drops at high densities below the level at the start of the density ramp, while in the limiter configuration, the heat flux density rises continuously up to $n_{\mathrm{e,l.a.}}(3.2\,\mathrm{m}) \approx 2.0 \cdot 10^{19}\,\mathrm{m^{-3}}$. Due to the shading of the location of the Langmuir probe in the limiter configuration and the concentration of the recycling at the strike points in the divertor configuration, the heat flux density in the first case is

considerably smaller than in the latter. In the MARFE phase, the heat flux drops in both configurations but strongly oscillates due to a small signal to noise ratio in the temperature determination. This local measurement is consistent with the density evolution of the calculated total heat flux at the divertor target from the EMC3-EIRENE modelling published in [Frerichs 2010a] using a cross-field transport coefficient of $D_\perp = 1\,\mathrm{m^2 s^{-1}}$. The calculated heat flux also shows a slight rise at low densities followed by a gradual decrease beginning at $n_{\mathrm{sepx}} = 2.5 \cdot 10^{19}\,\mathrm{m^{-3}}$ [Frerichs 2010a].

8 Discussion and Conclusion

8.1 Magnetic field calculations and plasma structures

In a magnetised plasma, the behaviour of the plasma particles is strongly determined by the magnetic field topology and knowledge about this topology is the basis for the interpretation of experimental observations as well as the modelling of the plasma in such a system. In particular, this knowledge is essential for the investigation of stochastic boundaries, as here the magnetic field poses a complex three-dimensional system where layered closed magnetic flux surfaces only exist in the unperturbed volume. Calculations of the magnetic field for stochastic boundaries are often based on numerical field line tracing methods without plasma response, the so-called *vacuum approximation*. In this approach the vacuum perturbation field is superimposed to an axisymmetric equilibrium field, while the modification of the magnetic perturbation field due to a plasma response is neglected. Such an approach was also taken in this thesis for the calculation of the magnetic field topology of the helical divertor in TEXTOR.

The correlation between the observed plasma structures at the divertor target plates and the calculated magnetic field topology within the uncertainties of measurements and calculations support the assumption, that the vacuum approximation poses a reasonable prediction of the magnetic field structures in the near field of the divertor coils. The observation of the plasma structures is mainly based on spectroscopic measurements of photon emission from hydrogen atoms and molecules complemented by local measurements at the divertor target with a Langmuir probe. They showed, that the deposition of particles and heat on the divertor target is concentrated in areas of field lines with deep penetration correlated with long connection lengths. Considerably less particle and heat flux is observed in areas of field lines with little penetration and extremely short connection lengths (private flux regions). This is in agreement with the prediction, that strike point widths and locations on the divertor target correlate with the penetration depth of the field lines intersecting the target on characteristic transport scale length. Field lines penetrating into hotter and more dense regions closer to the core on these transport scale length are the main transport channels between core and target and lead to peak particle and heat fluxes there. According to the magnetic field calculations, two helical strike point pairs are created at the divertor target plates,

each of these four strike points having a poloidal width of about 8 - 10 cm. The possibility of observing the separate strike points at the divertor target plates depends on the measurement method and the spatial resolution of the respective diagnostic system compared to the strike point separation. The separation between the strike points in each pair is only a few mm while the pairs are separated by the private flux regions with a width of about 8 cm.

The spectroscopic camera system which was designed, developed and built as part of this thesis provides two major advantages: Firstly, it facilitates the simultaneous measurement of the poloidal and toroidal pattern of the recycling flux at the divertor target, no strike point sweeping is needed by the diagnostic in contrast to the measurements done so far with the target Langmuir probes. Secondly, the simultaneous observation of different spectral lines also from different species reduces the uncertainty in the measurements as the contribution from uncertainties in the reproducibility of plasma parameters in different discharges are eliminated and only the uncertainty of the measurement method limits the accuracy. The spatial resolution of the system is about $0.8\,\mathrm{mm} \pm 0.01\,\mathrm{mm}$ in poloidal and toroidal direction and is therefore small compared to the strike point width and separation. On the other hand, the line-of-sight integration and the penetration depth of the light emitting species, has been found to limit the capability of the measurement method to resolve small scale structures. A comparison of the measured line integrated photon emission with spatially resolved as well as line integrated emissivities calculated by a three-dimensional plasma transport code (EMC3-EIRENE) was found to be important for the interpretation of spectroscopic data in this complex three-dimensional topology. The plasma transport modelling with this code is also based on the magnetic field topology calculated using the vacuum approximation. The code is a coupling of the 3D fluid Monte-Carlo code EMC3 and the neutral transport code EIRENE. It provides plasma transport modelling by self-consistently treating plasma and neutral particles in a realistic geometry taking into account the complex three-dimensional magnetic field structure and divertor plate geometry, with the possibility of including impurities. The Balmer photon emission calculated using the modelling results shows a good agreement with the experimentally observed photon emission in front of the target plates and thereby supports the use of the vacuum approximation for predicting the magnetic topology. The three-dimensional modelling showed, that a modulation with a factor of 50 in the parallel target ion flux between one of the divertor strike points and one of the private flux regions, partly due to cross-talk between adjacent strike points but mainly due to line of sight integration, leads to a factor of only about 2.5 in the modulation of the photon flux density. This factor in the photon flux density was indeed observed with the spectroscopic camera system while the modulation in the parallel target ion flux between divertor strike point and private flux region measured by target Langmuir probes proved to be in agreement with the calculated particle flux. With the help of the magnetic field calculations delivering the angle of incidence of the magnetic field lines at the target plates, a

comparison between the measured peak target ion flux in one of the strike points and the hydrogen recycling flux averaged over two strike points derived from the spectroscopic measurements was possible. Hence, good agreement has been found between two independent measurements of the target particle flux (spectroscopic and probe measurements) and the flux modelled with the 3D code.

8.2 High density operation

The operation of a divertor at high plasma densities is a means of achieving several beneficial effects with respect to heat and particle exhaust. The divertor functionality sought includes high neutral densities in the divertor for efficient pumping and improved density control, heat dissipation through increased radiation in the divertor volume, large temperature gradients for high core and low divertor temperature resulting in reduced physical sputtering of the divertor target and possibly a state of strongly reduced particle and heat load (detachment regime) for increasing target lifetime and reduced impurity production. In the framework of this thesis it was investigated in how far this functionality is provided by the helical (ergodic) divertor configuration in TEXTOR.

In an open divertor configuration such as the one investigated here, where no baffles keep the recycling neutrals from penetrating into the confined volume, the neutral compression has to be provided purely by the divertor plasma. Increased neutral densities in high plasma density operation, as observed in the high recycling regime in poloidal divertors, would be connected to a strong increase in the neutral particle flux from the divertor target. In poloidal divertors in the high recycling regime, the neutral density in the divertor volume was observed to increase at least quadratically with the density at the stagnation point of the scrape-off layer (upstream density) leading to an increased pumping efficiency. High recycling, i.e. a more than linear increase in the neutral particle flux from the divertor target was not observed experimentally in the helical divertor configuration in TEXTOR and hence no increase in the neutral density in the divertor volume is inferred. The behaviour of the target particle flux and the target temperature with rising core and edge density does not correspond to the behaviour typically known from poloidal divertors. It can, however, be separated into several phases specific to this particular divertor configuration. In the first phase at low densities, the particle flux rises linearly with the edge density at a target temperature of about $T_e \sim 50\,\mathrm{eV}$ measured by the target Langmuir probe. With rising plasma density this phase more or less gradually evolves into a second phase, where a saturation in the particle flux is observed in conjunction with a reduction in the peak target temperature to $T_e \approx 20\,\mathrm{eV}$. This is followed by a third very transient phase of a strong increase in the penetration depth of the neutral particles from 3.3 cm to 6.3 cm measured by the D_α emission and a drop in the target temperature to $T_e < 10\,\mathrm{eV}$, progressing

into the fourth phase, the development of a radiation instability which leads to the formation of a poloidally and helically structured radiation belt at the high field side of TEXTOR characterised by a cold, recombining plasma at $T_e \sim 1.5\,\mathrm{eV}$, a so-called MARFE (multifacetted asymmetric radiation from the edge). In divertors with similar structures at Tore Supra, W7-AS and LHD different observations regarding a high recycling regime have been made: In the helical divertor in LHD and the island divertor in W7-AS also no particle flux enhancement in high density divertor operation was observed while a flux amplification could be observed with the ergodic divertor in Tore Supra.

In the stochastic boundary of these divertor configurations, different transport domains regarding energy and momentum transport can be identified: Due to the intersection of the stochastic boundary with the target plates, part of the boundary has short connection to the divertor target and is hence dominated by *parallel* transport, the ratio of parallel to cross-field transport time scales $\tau_\parallel/\tau_\perp$ is smaller than one. In analogy to the limiter and poloidal divertor configuration it can be regarded as the scrape-off layer of the divertor configuration. In ergodic divertors this domain is termed the laminar region, its extent is given by parallel transport scale lengths, stemming from the correlation of neighbouring field lines in conjunction with cross-field diffusion. In the divertor configuration in TEXTOR studied within this thesis the laminar region exhibits a varying radial extent Δr between a few mm and 6 cm. In the helical divertor in LHD the divertor legs (without analogy in TEXTOR) and part of the edge surface layers constitute the 'laminar region', while in the island divertor in W7-AS the last part of the island fans in front of the target will be dominated by parallel transport.
In the domain characterised by longer connection lengths to the target plates, *cross-field* transport time scales become comparable to the parallel transport time scales $\tau_\parallel/\tau_\perp \approx 1$ providing the possibility of friction between adjacent counter streaming plasma flows. In the ergodic divertors in TEXTOR and Tore Supra this domain consists of the ergodic region with connection lengths to the target large compared to the field line correlation length and a region with intermediate connection lengths which, strictly speaking, belongs neither to the laminar nor the ergodic region. Such a transport domain can also be found in LHD, its width and connection lengths are comparable to the ones found in TEXTOR. The relation between parallel and cross-field momentum and energy transport in the different divertor topologies can be characterised by the field line pitch Θ, which defines the relative perpendicular displacement of a field line towards the targets per field line length. In TEXTOR as well as LHD, the field line pitch is $\Theta \sim 10^{-4}$ resulting from an ergodic layer thickness of 10 cm divided by several 100 m connection length. In the island divertor in W7-AS and also in W7-X, the major parts of the island fans are considered to belong to the transport domain with $\tau_\parallel/\tau_\perp \approx 1$. Here, the field line pitch can be estimated from the parallel and perpendicular X-point-to-target distances giving $\Theta \sim 10^{-3}$. In comparison, the field line pitch in the scrape-off layer of a poloidal divertor is larger by two orders of magnitude.

The different transport domains have a different impact on the establishment of temperature and density gradients across the stochastic boundary and the capability of creating a high recycling regime:
Gradients across the laminar region are reduced considerably by convective heat transport driven by large fractions of neutrals escaping the laminar region and preventing temperature gradients along the flux tubes. This was shown to be a possible explanation for the absence of a high recycling regime in the helical divertor in TEXTOR in this thesis by the application of an extended two point model including convective heat transport. The model showed that the observed absence of a strong particle flux enhancement in the helical divertor in TEXTOR can be explained by the large fraction of convective transport dominating the heat transport to the target and decreasing parallel temperature gradients. Although a decreasing penetration depth λ_n of atomic as well as molecular hydrogen with rising edge density was observed, the strong variation of the radial extent Δr of the laminar region across the divertor target plates results in $\lambda_\mathrm{n}/\Delta r > 1$ and hence a considerable fraction (about 50 %) of the plasma sources located outside the laminar region. This generates strong plasma flows throughout the scrape-off layer and leads to convective heat transport dominating over conductive heat transport parallel to the magnetic field. A reduction of the convective contribution in the extended two-point model leads to a strong increase in downstream particle fluxes and the ratio of upstream and downstream temperature. In poloidal divertors, where convective heat transport in the scrape-off layer can be neglected at high densities due to $\lambda_\mathrm{n}/\Delta r \ll 1$, upstream temperatures of $\sim$ 100 eV and target temperatures down to $\sim$ 10 eV in the high recycling regime have been observed. The high recycling observed in Tore Supra is therefore probably due to a reduction in the convective heat transport because of better neutral screening, observed experimentally in Tore Supra for hydrogen as well as impurities. This is supposedly achieved in Tore Supra by a larger radial extent of the laminar region caused by the coils of the ergodic divertor being located at the low field side and the weak baffling due to the retreated position of the divertor plates. Increasing the radial extent of the scrape-off layer of the helical divertor in TEXTOR especially in front of the divertor strike points could hence lead to an improvement in this respect and provide access to a high recycling regime. The different base modes of the DED provide a different potential for such an improvement, with the 6/2 base mode, the base mode investigated within this thesis, having the largest potential. The 12/4 base mode with its thin stochastic boundary presumably does not have the capability for creating a scrape-off layer of sufficient width. This is the opposite for the 3/1 base mode which exhibits a large stochastic boundary, but this base mode suffers from tearing mode excitation and already an increased impact on the plasma core. However, the identification and analysis of different density regimes in a divertor based on a two-point model depends on the relation of plasma parameters at the divertor target (downstream) to those at the stagnation point of the scrape-off layer (upstream). While an upstream location can be identified quite straightforward in poloidal divertors, in the helical divertor in TEXTOR

such a single upstream position common to all flux tubes does not exist, multiple stagnation points along field lines and flux tubes of various connection length located in close vicinity lead to a complication of this matter. It remains to be clarified, if the density used within this thesis (a line integrated density in the ergodic region of the stochastic boundary) and in the analysis of the modelling results is connected linearly to the density at the stagnation point of every flux tube connecting to the divertor target and therefore resembles a general upstream density.
In W7-AS as well as LHD, high recycling is assumed to be suppressed in the ergodic region (or islands, respectively) by momentum losses due to friction between counter streaming plasma flows which lead to pressure drops along the field lines already at low density and high temperature conditions and no temperature gradient across this region. Due to the very similar topology to the helical divertor in LHD, this can also be assumed to hold for the ergodic region in the helical divertor in TEXTOR, although this could not be confirmed as yet and lay beyond the scope of this thesis. On the other hand, convective heat transport across the region dominated by parallel transport as discussed before is also a possible explanation for the absence of a high recycling regime in W7-AS and LHD. In this laminar region, friction caused by cross-field transport does not play a role by definition. In poloidal divertors, a pressure drop is only observed when ion-neutral friction becomes important at target temperatures below 10 eV.

Indications for a state of reduced particle and heat flux, i.e. detachment from the divertor target, have been found in the helical divertor in TEXTOR, the phase however is very transient and tends to MARFE formation. Due to the short time constant of this phase compared to the response time of a feedback system acting on the gas supply, a stabilisation of the transient detachment phase was not achieved. In the second phase described above at high edge densities, a saturation in the integrated particle flux from two of the strike points estimated from photon flux density measurements was observed while a local drop by $\sim 8\,\%$ in the peak ion flux and by $\sim 50\,\%$ in the peak heat flux in one of these strike points could be seen. The reduction in the particle flux, however, is negligible compared to the particle flux reduction of a factor of three observed during complete detachment in poloidal divertors and should hence be regarded rather as the onset of detachment. The measured target temperature in this saturation phase of $T_\mathrm{e} \approx 20\,\mathrm{eV}$ is still too high to explain the saturation by increased momentum losses due to charge exchange processes which only become dominant at $T_\mathrm{e} < 10\,\mathrm{eV}$ as observed in poloidal divertors at the onset of detachment. It cannot be ruled out, however, that the probe data overestimate the downstream temperatures at these conditions. The onset of detachment is followed by the third phase described above with a sudden increase in the penetration depth of atomic as well as molecular hydrogen across the whole target which is typical of detachment also in other devices. It is accompanied by a decrease of the target temperature to $T_\mathrm{e} < 10\,\mathrm{eV}$ according to the Langmuir probe measurement, while the spectroscopic observations of

the Balmer line ratio D_α/D_γ supports the assumption of an overestimation of the target temperature by the probe. Hence, in this third phase the observed decrease in the Balmer α emission is interpreted as resulting from a decrease in the recycling flux locally across the target. As no further drop in the peak target particle flux could be observed at the same time by the Langmuir probe, the transient detachment is assumed to be partial. Different kinds of detachment phenomena have also been observed in the helical divertor in LHD, exhibiting both, transient and stable detachment regimes characterised by a reduction in the target ion flux at high core and edge densities. In the island divertor in W7-AS, stable partial detachment in the high-density H-mode regime was achieved, partial meaning that the plasma detaches from most of the divertor target surface except of a small region. This is somewhat similar to the partial detachment scenario achieved in poloidal divertors in the H-mode regime which is the envisaged divertor regime for ITER, where only the inner divertor leg is detached completely while the outer leg remains partially attached. Similar to observations of carbon radiation in the visible spectral range during detachment in LHD and W7-AS, a strong increase in the emission from doubly ionised carbon (CIII at 465 nm) during the second, saturation phase from the observation volume by 50 % was observed in TEXTOR. In poloidal divertors as well as in the island divertor, stable partial detachment is followed by full detachment and the formation of a MARFE when the density is further increased. In the helical divertor in TEXTOR, the transient detachment phase is also typically followed by the formation of a MARFE at the high field side in the vicinity of the equatorial plane.

The experimental observations in the different density regimes are in good agreement with the results from the three-dimensional simulations with the EMC3-EIRENE code, which also do not show high recycling at intermediate and high plasma densities. Common trends and partly agreement in absolute values are observed in

- the Balmer line emission directly in front of the target including a saturation followed by a drop at high plasma densities
- the target temperature including a strong drop at high plasma densities
- the line integrated Balmer photon flux at the individual strike points
- the line ratio of the Balmer α and γ lines
- the target heat flux
- the target particle flux, globally and at the individual strike points. The simulations with carbon impurities included even showed not only a saturation but also the experimentally observed drop at high plasma densities

Simulations were performed using two different cross-field transport coefficients which are free model parameters of the EMC3-EIRENE code. The simulations with a particle diffusion coefficient of $D_\perp = 1\,\mathrm{m^2 s^{-1}}$ and a cross-field heat transport

coefficient of $\chi_\perp = 3D_\perp$ proved to be in good agreement with the experimental observations while simulations using $D_\perp = 0.2\,\mathrm{m^2 s^{-1}}$ did not agree with the experimental findings, showing a strong nonlinear relation between target ion flux and 'upstream' density.

The ionisation sources inside the downstream area were derived with the simulations to be about 50 % of the total ionisation sources inside the plasma and were seen to deviate only little from this value throughout the density ramp. When using the D_α emission at the tangential location observed by the camera diagnostic as a measure of the relation between the ionisation sources inside and outside of the downstream area, only a small error is made according to the modelling results. At low and intermediate densities, the downstream source fraction estimated from the D_α emission deviates from the fraction based on the calculated ionisation sources by about 6 %. The slight decrease in the ionisation source fraction at high densities is not reflected in the photon emission, the variation in the source distribution is however small and does not change the general interpretation using the extended two-point model. A discrepancy between measurements and modelling results which has an influence on the interpretation of the observations with respect to the underlying physics, is seen in the target temperature. The temperature measured locally at the target by the Langmuir probes is generally higher than the calculated temperature. According to the modelling results, the saturation in the target particle flux can be attributed to an increase in ion-neutral friction by charge exchange at temperatures below about 15 eV and the drop in the Balmer line emission directly in front of the divertor target plates to a temperature drop to 5 eV and below. Knowledge about the uncertainties in the Langmuir probe measurements and the spectroscopic observations point towards an overestimation of the target temperatures under the present conditions. In this case the explanation derived from the three-dimensional modelling for the onset of detachment as resulting from an increase in ion-neutral friction when reaching a threshold temperature, appears a reasonable assumption.

8.3 Operational limit

The operational limit without as well as with divertor operation is determined by the formation of a MARFE at the high field side of TEXTOR. Further gas injection typically leads to an accumulation of density at the location of the MARFE which finally leads to a density limit disruption. The measurements indicate, that the helical divertor operation slightly raises the operational density limit by 4% compared to the limiter configuration, where the DED protection limiter is the main limiting object. In the limiter configuration the MARFE forms approximately when the line averaged density at $R = 1.75\,\mathrm{m}$ reaches the Greenwald density, an empirical density limit derived for tokamaks, of $n_\mathrm{e} \approx 5.5 \cdot 10^{19}\,\mathrm{m^{-3}}$.

However, the line averaged density at the edge ($R = 2.15\,\mathrm{m}$) in the divertor discharge is lower compared to the limiter discharge due to the change in the density profile. This result however is not significant as this limiter configuration is not the standard and optimal limiter configuration in TEXTOR (where the ALT-II pump limiter is the main limiter).

The MARFE that develops in the helical divertor configuration shows some specific features and could provide some of the requested divertor functionalities discussed above. The strong increase in the Balmer γ emission and the strong drop in the ratio of the Balmer lines indicates recombination processes becoming important - one of the characteristics of a MARFE - and hence a local drop of the electron temperature below 1.5 eV. This temperature drop is beneficial for the reduction of physical and also chemical sputtering of the target material and the recombination furthermore leads to an increased neutral density which could be beneficial for pumping neutrals at the target. A special feature of the helical divertor MARFE is the structure imposed on the MARFE by the magnetic topology, it is modulated poloidally and helically inclined.

The emission from doubly ionised carbon shows a similar behaviour as the Balmer line emission, increasing by a factor of five during the MARFE compared to the low density regime. This increase in the photon emission results not from an increase in the carbon source at the target but from the decrease in the electron temperature in front of the target reducing the ionisation rate. The strongly localised carbon radiation during the MARFE in the helical divertor in TEXTOR, however, is neither located in the scrape-off layer of the helical divertor nor in the confined volume but resides within the stochastic edge layer in the ergodic zone at a remnant island. This is very similar to observations during detachment and MARFEs in stellarator divertors, where the carbon radiation is also seen to strongly increase and concentrate at magnetic islands or remnant islands but could be stabilised outside the confinement region in W7-AS. The strong enhancement of the edge radiation in the helical ergodic in TEXTOR does not only help in spreading the heat load on the divertor target plates and the vessel wall, it can furthermore be used to stabilise the helical divertor MARFE using a feedback control system based on the observation of the radiation from singly ionised carbon (CII at 426.7 nm) in the MARFE. Thus, feedback control is a potential tool for stabilising MARFEs in other machines to operate at high density if the detachment operational window is too narrow.

9 Summary

Divertors with chaotic magnetic field structures are a field of major interest in todays fusion research not only for stellarators with their inherent complex magnetic field structures but also in tokamaks due to the application of resonant magnetic perturbations. This method is also used in the limiter tokamak TEXTOR for creating a helical divertor structure with a complex, three-dimensional magnetic field topology that guides the particle and heat fluxes to the divertor target plates forming a helical target pattern. The functionality of such divertors regarding control and efficient exhaust of particles and energy is still under investigation. Increasing the understanding in this respect has been the major motivation for this thesis.

The accessibility of favourable divertor regimes with large temperature gradients between plasma core and divertor target, high neutral density in the divertor volume for efficient pumping and strong radiation for heat dissipation (high recycling regime) or additionally with reduced target particle and heat loads (detachment), is largely determined by the recycling of the hydrogen plasma at the divertor target. The aim of this thesis was therefore to investigate the hydrogen recycling at the target plates of the helical divertor in TEXTOR and by this the capability of this divertor configuration to access such favourable operational regimes. Typically, these regimes are reached by increasing the plasma density in the divertor volume. In TEXTOR the density in the divertor volume is increased by increasing the total plasma density through increased gas injection. In order to study the low as well as the high density regime, discharges were performed in which the total plasma density was increased continuously up to the density limit. The recycling was investigated in a fixed helical divertor structure where two strike point (or strike line) pairs are created at the divertor target plates, each of these four strike points having a poloidal width of about 8 - 10 cm. The possibility of observing these separate strike points depends on the measurement method used and the spatial resolution of the respective diagnostic system compared to the strike point separation. The separation between the strike points in each pair is only a few mm while the pairs are separated by regions of very short connection length - the private flux regions - with a width of about 8 cm. The helical divertor configuration is furthermore characterised by different transport domains, with the region dominated by parallel transport (laminar region) exhibiting a varying radial extent Δr between a few mm and 6 cm.

The experimental investigation of the hydrogen recycling was carried out using mainly spectroscopic methods supplemented by Langmuir probe, interferometric and atomic beam measurements. In the framework of this thesis a spectroscopic multi camera system has been designed and built that facilitates the simultaneous observation of four different spectral lines, recording two dimensional images of the divertor target plates and the plasma volume close to the target. The system has been absolutely calibrated for the Balmer α, β and γ line and thereby enables the measurement of the line integrated photon emission with an uncertainty of about 10%. The system provides two major advantages: It facilitates the simultaneous measurement of the poloidal and toroidal pattern of the recycling flux at the divertor target without the need for sweeping the plasma structure, in contrast to the measurements done so far with the target Langmuir probes. Secondly, the simultaneous observation of different spectral lines reduces the uncertainty in the analysis based on several lines, as the contribution from uncertainties in the reproducibility of plasma parameters in different discharges are eliminated and only the uncertainty of the measurement method limits the accuracy. The spatial resolution of the system is about $0.8\,\mathrm{mm} \pm 0.01\,\mathrm{mm}$ in poloidal and toroidal direction and is therefore small compared to the strike point separation. The line-of-sight integration and the penetration depth of the light emitting species, though, has been found to limit the capability of the measurement method to resolve small scale structures. This should be taken into account in the design of future diagnostic systems for the investigation of recycling in similar divertor configurations.

The measurements with the spectroscopic camera system and a Langmuir probe embedded in a divertor target plate showed, that the recycling flux increases linearly with increasing plasma density with a tendency towards the formation of a radiation instability at the highest plasma densities reached. A high recycling regime, as it is known from poloidal divertor tokamaks, is not observed. Its absence can be explained using a simple, extended two point model including heat convection applied to the region dominated by parallel transport (laminar region). The radial penetration depth of the neutral hydrogen particles ($\lambda_\mathrm{n} \approx 3 - 4\,\mathrm{cm}$) estimated from the spectroscopic measurements was found to be often larger than the radial extent of this laminar region $\lambda_\mathrm{n}/\Delta r > 1$. This leads to a considerable fraction of ionisation sources outside the laminar region and thereby to strong plasma flows throughout this region. In this case, energy transport between core and target is dominated by convective heat transport which reduces temperature gradients and prevents the development of a flux amplification. In poloidal divertors the condition $\lambda_\mathrm{n}/\Delta r \ll 1$ is much more readily fulfilled due to the larger distance between divertor target plates and X-point. Increasing the radial extent Δr of the region dominated by parallel transport especially in front of the divertor strike points by appropriately modifying the helical divertor configuration in TEXTOR could lead to an improvement in this respect and provide access to a high recycling regime. The large penetration depth of neutrals compared to the radial extent of

the scrape-off-layer is also a possible explanation for the absence of a high recycling regime in the divertors of the stellarators W7-AS and LHD. The closing of the open divertor geometry of the helical divertor at LHD through the installation of baffles (which is currently under way) is therefore expected to provide access to a high recycling regime there. Accordingly, the larger island size in the island divertor of the stellarator W7-X compared to its predecessor W7-AS could also lead to the accessibility of a high recycling regime.

The radiation instability developing at high plasma densities in the helical divertor in TEXTOR is preceded by a transient partial detachment of the plasma from the divertor target plates and leads to the formation of a poloidally structured and helically inclined radiating belt, a helical divertor MARFE. While typically leading to a density limit disruption, the helical divertor MARFE has been stabilised using a feedback system and could provide some divertor functionality such as low target temperature, increased neutral density and increased radiation within the stochastic boundary.

A detailed comparison of the experimental observations to results from three-dimensional modelling with the EMC3-EIRENE code showed reasonable agreement in the high density behaviour (in particular absence of a high recycling regime) as well as in the absolute values of the calculated target particle flux and the two independent measurements of the target particle flux using the Langmuir probe and optical emission spectroscopy on hydrogen. Simulations using two different cross-field transport coefficients showed, that this agreement is only found at a certain level of cross-field transport ($D_\perp = 1\,\mathrm{m^2 s^{-1}}$), while a five times reduced cross-field transport leads to strong nonlinear relation between target ion flux and the density at the last closed flux surface. Furthermore the inclusion of carbon impurities in the simulations was found to have a significant impact on the plasma edge eventually resulting in the experimentally observed reduction of the recycling flux. These findings support the use of the EMC3-EIRENE code for predictive modelling for other divertors with similar stochastic magnetic field structures. For the island divertor in W7-X calculations with the EMC3-EIRENE code predict the development of a high recycling regime, fitting well to the speculation made above based on the observations and interpretations within this thesis.

References

Abdullaev, S. On mapping models of field lines in a stochastic magnetic field. *Nuclear Fusion*, **44** (2004), 6, S12. doi:10.1088/0029-5515/44/6/S02.

Abdullaev, S. S. et al. Overview of magnetic structure induced by the TEXTOR-DED and the related transport. *Nuclear Fusion*, **43** (2003), 5, 299–313. doi:10.1088/0029-5515/43/5/302.

Alejaldre, C. et al. TJ-II Project - A Flexible Heliac Stellarator. *Fusion Technology*, **17** (1990), 1, 131–139.

Becoulet, M. et al. Numerical study of the resonant magnetic perturbations for Type I edge localized modes control in ITER. *Nuclear Fusion*, **48** (2008), 2, 024003. doi:10.1088/0029-5515/48/2/024003.

Braginskii, S. Transport processes in a plasma. In Leontovich, M. A., editor, Reviews of Plasma Physics, volume 1, pages 205–311. Consultants Bureau, New York (1965). Authorized translation from the Russian by Herbert Lashinsky, University of Maryland, USA.

Brezinsek, S. Untersuchung von atomarem und molekularem Wasserstoff vor einer Graphitoberfläche in einem Hochtemperatur-Randschichtplasma. Ph.D. thesis, Heinrich-Heine-Universität Düsseldorf (2001).

Brezinsek, S. et al. The impact of divertor detachment on carbon sources in JET L-mode discharges. *Journal of Nuclear Materials*, **390-391** (2009), 267–273. doi:10.1016/j.jnucmat.2009.01.100.

Chirikov, B. V. Resonance processes in magnetic traps. *Journal of Nuclear Energy. Part C, Plasma Physics, Accelerators, Thermonuclear Research*, **1** (1960), 4, 253. doi:10.1088/0368-3281/1/4/311.

EIRENE. EIRENE - A Monte Carlo linear transport solver (2010). URL `http://www.eirene.de`

Engelhardt, W. and Feneberg, W. Influence of an ergodic magnetic limiter on the impurity content in a tokamak. *Journal of Nuclear Materials*, **76-77** (1978), 518–520. doi:10.1016/0022-3115(78)90198-8.

Evans, T. E. et al. Suppression of Large Edge-Localized Modes in High-Confinement DIII-D Plasmas with a Stochastic Magnetic Boundary. *Physical Review Letters*, **92** (2004), 23, 235003. doi:10.1103/PhysRevLett.92.235003.

Evans, T. E. et al. Edge stability and transport control with resonant magnetic perturbations in collisionless tokamak plasmas. *Nat Phys*, **2** (2006), 6, 419–423. doi:10.1038/nphys312.

Faulconer, D. W. Current Drive. *Transactions of Fusion Science and Technology*, **53** (2008), 2T, 210–219.
URL http://epubs.ans.org/?a=1707

Federici, G. et al. Key ITER plasma edge and plasma-material interaction issues. *Journal of Nuclear Materials*, **313-316** (2003), 11–22. doi:10.1016/S0022-3115(02)01327-2. Plasma-Surface Interactions in Controlled Fusion Devices 15.

Feneberg, W. and Wolf, G. A Helical Magnetic Limiter For Boundary-layer Control In Large Tokamaks. *Nuclear Fusion*, **21** (1981), 6, 669–676.

Feng, Y. et al. 3D Edge Modeling and Island Divertor Physics. *Contributions to Plasma Physics*, **44** (2004), 1-3, 57–69. doi:10.1002/ctpp.200410009.

Feng, Y. et al. Physics of island divertors as highlighted by the example of W7-AS. *Nuclear Fusion*, **46** (2006), 8, 807–819. doi:10.1088/0029-5515/46/8/006.

Feng, Y. et al. Fluid features of the stochastic layer transport in LHD. *Nuclear Fusion*, **48** (2008), 2, 024012. doi:10.1088/0029-5515/48/2/024012.

Feng, Y. et al. Comparative divertor-transport study for helical devices. *Nuclear Fusion*, **49** (2009), 9, 095002 (11pp). doi:10.1088/0029-5515/49/9/095002.

Fenstermacher, M. E. et al. Pedestal, SOL and divertor plasma properties in DIII-D RMP ELM-suppressed discharges at ITER relevant edge collisionality. *Journal of Nuclear Materials*, **363** (2007), 476–483. doi:10.1016/j.jnucmat.2007.01.270.

Finken, K. et al. Operating space of the Dynamic Ergodic Divertor for TEXTOR-94. *Nuclear Fusion*, **39** (1999), 5, 637. doi:10.1088/0029-5515/39/5/306.

Finken, K. et al. The structure of magnetic field in the TEXTOR-DED, volume 45 of *Schriften des Forschungszentrums Jülich. Reihe Energietechnik/Energy Technology*. Forschungszentrum Jülich, Zentralbibliothek, Verlag (2005).
URL http://nbn-resolving.de/urn/resolver.pl?urn=urn:nbn:de:0001-00312

Frerichs, H. 3D plasma transport in open chaotic magnetic fields: A computational assessment for tokamak edge layers. Ph.D. thesis, RWTH Aachen University (2010a).

Frerichs, H. private communication (2010b).

Ghendrih, P.; Grosman, A. and Capes, H. Theoretical and experimental investigations of stochastic boundaries in tokamaks. *Plasma Physics and Controlled Fusion*, **38** (1996), 10, 1653. doi:10.1088/0741-3335/38/10/002.

Ghendrih, P. et al. Control of the Edge Transport with the Ergodic Divertor. *Contributions to Plasma Physics*, **32** (1992), 3-4, 179–191. doi:10.1002/ctpp.2150320303.

Ghendrih, P. et al. Progress in ergodic divertor operation on Tore Supra. *Nuclear Fusion*, **42** (2002), 10, 1221–1250. doi:10.1088/0029-5515/42/10/308.

Goebel, D. et al. ALT-II toroidal belt pump limiter performance in TEXTOR. *Journal of Nuclear Materials*, **162-164** (1989), 115 – 127. doi:10.1016/0022-3115(89)90262-6.

Grieger, G.; Renner, H. and Wobig, H. Wendelstein Stellarators. *Nuclear Fusion*, **25** (1985), 9, 1231–1242.

Grigull, P. et al. First island divertor experiments on the W7-AS stellarator. *Plasma Physics and Controlled Fusion*, **43** (2001), A175–A193. doi:10.1088/0741-3335/43/12A/313.

Groebner, R. J. An emerging understanding of H-mode discharges in tokamaks. *Physics of Fluids B: Plasma Physics*, **5** (1993), 7, 2343–2354. doi:10.1063/1.860770.

Gunn, J. P. et al. Particle recirculation in the ergodic divertor of Tore Supra. *Plasma Physics And Controlled Fusion*, **41** (1999), B243–B257. doi:10.1088/0741-3335/41/12B/318.

Hartmann, D. A. Stellarators. *Transactions of Fusion Science and Technology*, **53** (2008), 2T, 44–55.
URL http://epubs.ans.org/?a=1690

Heinloth, K. Die Energiefrage. Vieweg Verlag, 2nd edition (2003).

Hey, J.; Chu, C. and Hintz, E. Spectroscopic studies of cold atomic hydrogen and deuterium produced in a tokamak edge plasma. *Contributions To Plasma Physics*, **40** (2000), 1-2, 9–22. doi:10.1002/(SICI)1521-3986(200004)40:1/2<9::AID-CTPP9>3.0.CO;2-F.

Hirsch, M. et al. Major results from the stellarator Wendelstein 7-AS. *Plasma Physics and Controlled Fusion*, **50** (2008), 5, 053001. doi:10.1088/0741-3335/50/5/053001.

Hutchinson, I. H. Principles of Plasma Diagnostics. Cambridge University Press (1988).

Huysmans, G. T. A. ELMs: MHD instabilities at the transport barrier. *Plasma Physics and Controlled Fusion*, **47** (2005), 12B, B165. doi:10.1088/0741-3335/47/12B/S13.

Iiyoshi, A. et al. Overview of the Large Helical Device project. *Nuclear Fusion*, **39** (1999), 9Y, 1245. doi:10.1088/0029-5515/39/9Y/313.

ITER Physics Basis Editors et al. Chapter 1: Overview and summary. *Nuclear Fusion*, **39** (1999), 12, 2137–2174. doi:10.1088/0029-5515/39/12/301.

Jakubowski, M. W. Predicted structures and measured heat fluxes for the Dynamic Ergodic Divertor in TEXTOR. Ph.D. thesis, Ruhr-Universität Bochum (2004).

Jakubowski, M. W. et al. Change of the magnetic-field topology by an ergodic divertor and the effect on the plasma structure and transport. *Physical Review Letters*, **96** (2006), 3, 035004. doi:10.1103/PhysRevLett.96.035004.

Jakubowski, M. W. et al. Influence of the Dynamic Ergodic Divertor on the heat deposition pattern in TEXTOR at different collisionalities. *Plasma Physics And Controlled Fusion*, **49** (2007), 7, S109–S121. doi:10.1088/0741-3335/49/7/S08.

Kalupin, D. et al. On the difference of H-mode power threshold in divertor and limiter tokamaks. *Plasma Physics and Controlled Fusion*, **48** (2006), 5A, A309–A317. doi:10.1088/0741-3335/48/5A/S30.

Keilhacker, M. H-mode confinement in tokamaks. *Plasma Physics and Controlled Fusion*, **29** (1987), 10A, 1401–1413. doi:10.1088/0741-3335/29/10A/320.

Kobayashi, M. et al. Frequency dependence of tokamak plasma response to the externally applied rotating helical field. *Physics of Plasmas*, **7** (2000), 8, 3288–3300. doi:10.1063/1.874194.

Kobayashi, M. et al. 3D numerical transport study of the edge ergodized plasma in TEXTOR-DED. *Nuclear Fusion*, **44** (2004), 6, S64. doi:10.1088/0029-5515/44/6/S07.

Koch, R. Fast Particle Heating. *Transactions of Fusion Science and Technology*, **53** (2008a), 2T, 173–183.
URL http://epubs.ans.org/?a=1703

Koch, R. The Ion Cyclotron, Lower Hybrid and Alfven Wave Heating Methods. *Transactions of Fusion Science and Technology*, **53** (2008b), 2T, 194–201.
URL http://epubs.ans.org/?a=1705

Koch, R. et al. Ion cyclotron resonance heating on TEXTOR. *Fusion Science and Technology*, **47** (2005), 2, 97–107.

Konig, R. et al. The divertor program in stellarators. *Plasma Physics And Controlled Fusion*, **44** (2002), 11, 2365–2422. doi:10.1088/0741-3335/44/11/306.

Konig, R. et al. Divertors for helical devices: Concepts, plans, results, and problems. *Fusion Science and Technology*, **46** (2004), 1, 152–166.

Koslowski, H. R. and Soltwisch, H. Electron density and q profile measurements with the far-IR interferometer-polarimeter on the TEXTOR tokamak. *Fusion Engineering and Design*, **34-35** (1997), 143 – 150. doi:10.1016/S0920-3796(96)00683-7. Fusion Plasma Diagnostics.

Kruezi, U. Entwicklung einer Heliumstrahldiagnostik zur Messung der Elektronendichte und -temperatur mit hoher räumlicher und zeitlicher Auflösung. Ph.D. thesis, Heinrich-Heine-Universität Düsseldorf (2007).
URL http://hdl.handle.net/2128/2506

Lehnen, M. et al. First results from the dynamic ergodic divertor at TEXTOR. *Journal of Nuclear Materials*, **337-39** (2005a), 1-3, 171–175. doi:10.1016/j.jnucmat.2004.10.100.

Lehnen, M. et al. Transport and divertor properties of the dynamic ergodic divertor. *Plasma Physics And Controlled Fusion*, **47** (2005b), B237–B248. doi:10.1088/0741-3335/47/12B/S18.

Lehnen, M. et al. The effect of the magnetic topology on particle recycling in the ergodic divertor of TEXTOR. *Journal of Nuclear Materials*, **363** (2007), 377–381. doi:10.1016/j.jnucmat.2007.01.125.

Lehnen, M. et al. The DED at TEXTOR: transport and topological properties of a helical divertor. *Plasma and Fusion Research*, **3** (2008), S1039. doi:10.1585/pfr.3.S1039.

Liang, Y. et al. Active Control of Type-I Edge-Localized Modes with $n = 1$ Perturbation Fields in the JET Tokamak. *Physical Review Letters*, **98** (2007), 26, 265004. doi:10.1103/PhysRevLett.98.265004.

Loarte, A. et al. Plasma detachment in JET Mark I divertor experiments. *Nuclear Fusion*, **38** (1998), 3, 331–371. doi:10.1088/0029-5515/38/3/303.

Masuzaki, S. et al. The divertor plasma characteristics in the Large Helical Device. *Nuclear Fusion*, **42** (2002), 6, 750–758. doi:10.1088/0029-5515/42/6/313.

McCool, S. et al. The effect of magnetic perturbations on edge transport in TEXT. *Journal of Nuclear Materials*, **176-177** (1990), 716 – 720. doi:10.1016/0022-3115(90)90132-7.

McCormick, K. et al. New Advanced Operational Regime on the W7-AS Stellarator. *Physical Review Letters*, **89** (2002), 1, 015001. doi:10.1103/PhysRevLett.89.015001.

McCracken, G. M. et al. Evidence for volume recombination in jet detached divertor plasmas. *Nuclear Fusion*, **38** (1998), 4, 619–629. doi:10.1088/0029-5515/38/4/311.

Meslin, B. et al. Plasma edge characterisation and control in ergodic divertor experiments on Tore Supra. *Journal of Nuclear Materials*, **266** (1999), 318–323. doi:10.1016/S0022-3115(98)00875-7.

Miyazawa, J. et al. Detachment phenomena in LHD compared to W-AS. *Fusion Science and Technology*, **50** (2006a), 2, 192–200.

Miyazawa, J. et al. Self-sustained detachment in the Large Helical Device. *Nuclear Fusion*, **46** (2006b), 5, 532–540. doi:10.1088/0029-5515/46/5/005.

Murakami, M. et al. Progress toward fully noninductive, high beta conditions in DIII-D. *Physics of Plasmas*, **13** (2006), 5, 056106. doi:10.1063/1.2173627.

Neubauer, O. et al. Design features of the Tokamak TEXTOR. *Fusion Science and Technology*, **47** (2005), 2, 76–86.

Nguyen, F.; Chendrih, P. and Grosman, A. Interaction of stochastic boundary layer with plasma facing components. *Nuclear Fusion*, **37** (1997), 6, 743. doi:10.1088/0029-5515/37/6/I03.

Ohyabu, N. et al. Observation of Stable Superdense Core Plasmas in the Large Helical Device. *Physical Review Letters*, **97** (2006), 5, 055002. doi:10.1103/PhysRevLett.97.055002.

Pitcher, C. S. and Stangeby, P. C. Experimental divertor physics. *Plasma Physics And Controlled Fusion*, **39** (1997), 6, 779–930. doi:10.1088/0741-3335/39/6/001.

(prepared by C. Gormezano), J. T. High performance with modified magnetic shear in JET DD and DT plasmas. *Nuclear Fusion*, **39** (1999), 11Y, 1875. doi:10.1088/0029-5515/39/11Y/329.

Proxitronic. Proxitronic Detector Systems GmbH (2010).
URL http://www.proxitronic.de

Rechester, A. B. and Rosenbluth, M. N. Electron Heat Transport in a Tokamak with Destroyed Magnetic Surfaces. *Physical Review Letters*, **40** (1978), 1, 38–41. doi:10.1103/PhysRevLett.40.38.

Reiser, D. and Chandra, D. Plasma currents induced by resonant magnetic field perturbations in tokamaks. *Physics of Plasmas*, **16** (2009), 4, 042317. doi:10.1063/1.3126548.

Reiter, D.; Baelmans, M. and Borner, P. The EIRENE and B2-EIRENE codes. *Fusion Science and Technology*, **47** (2005), 2, 172–186.
URL http://epubs.ans.org/?a=698

Reiter, D. et al. Helium removal from tokamaks. *Plasma Physics and Controlled Fusion*, **33** (1991), 13, 1579. doi:10.1088/0741-3335/33/13/008.

Renner, H. et al. Divertor concept for the W7-X stellarator and mode of operation. *Plasma Physics and Controlled Fusion*, **44** (2002), 6, 1005. doi:10.1088/0741-3335/44/6/325.

Runov, A. M. et al. Monte Carlo study of heat conductivity in stochastic boundaries: Application to the TEXTOR ergodic divertor. *Physics of Plasmas*, **8** (2001), 3, 916–930. doi:10.1063/1.1344921.

Sardei, F. et al. Island divertor studies on W7-AS. *Journal of Nuclear Materials*, **241-243** (1997), 135 – 148. doi:10.1016/S0022-3115(97)80036-0.

Schaffer, M. et al. Study of in-vessel nonaxisymmetric ELM suppression coil concepts for ITER. *Nuclear Fusion*, **48** (2008), 2, 024004. doi:10.1088/0029-5515/48/2/024004.

Schmitz, O. Experimentelle Untersuchung der Plasmastruktur und Charakterisierung des Transportverhaltens in der laminaren Zone einer stochastisierten Plasmarandschicht. Ph.D. thesis, Heinrich-Heine-Universität Düsseldorf (2006). URL http://hdl.handle.net/2128/2503

Schmitz, O. et al. Application of advanced edge diagnostics for transport studies in the stochastic boundary of TEXTOR-DED. *AIP Conference Proceedings*, **993** (2008a), 1, 135–142.

Schmitz, O. et al. Identification and analysis of transport domains in the stochastic boundary of TEXTOR-DED for different mode spectra. *Nuclear Fusion*, **48** (2008b), 2, 024009. doi:10.1088/0029-5515/48/2/024009.

Self, S. A. and Ewald, H. N. Static Theory of a Discharge Column at Intermediate Pressures. *Physics of Fluids*, **9** (1966), 12, 2486–2492. doi:10.1063/1.1761642.

Smirnov, V. Tokamak foundation in USSR/Russia 1950-1990. *Nuclear Fusion*, **50** (2010), 1, 014003. doi:10.1088/0029-5515/50/1/014003.

Spitzer, L. and Härm, R. Transport Phenomena in a Completely Ionized Gas. *Physical Review*, **89** (1953), 5, 977–981. doi:10.1103/PhysRev.89.977.

Spitzer, L., Jr. The Stellarator Concept. *Physics of Fluids*, **1** (1958), 4, 253–264. doi:10.1063/1.1705883.

Stangeby, P. C. The Plasma Boundary of Magnetic Fusion Devices, volume 43. Taylor & Francis Group (2001).
URL http://stacks.iop.org/0741-3335/43/i=2/a=702

Summers, H. P. The ADAS User Manual 2.6 - Introduction (2004).
URL http://adas.phys.strath.ac.uk

Tokar, M. Z.; Kobayashi, M. and Feng, Y. Improved two-point model for limiter scrape-off layer. *Physics of Plasmas*, **11** (2004), 10, 4610–4615. doi:10.1063/1.1791232.

Uhlemann, R. and Ongena, J. Variation of injected neutral beam power at constant particle energy by changing the beam target aperture of the textor neutral beam injectors. *Fusion Technology*, **35** (1999), 1, 42–53.

Van Rompuy, T. Study of Ergodic Divertor Edge Density Regimes on the Tokamaks Tore Supra and TEXTOR and Sensitivity of Tunnel Probe Electron Temperature Measurements to a Suprathermal Electron Component. Ph.D. thesis, Universiteit Gent (2009).

Voitsekhovitch, I. et al. Non-inductive current drive and transport in high β_N plasmas in JET. *Nuclear Fusion*, **49** (2009), 5, 055026. doi:10.1088/0029-5515/49/5/055026.

Wagner, F. et al. Regime Of Improved Confinement And High-Beta In Neutral-Beam-Heated Divertor Discharges Of The Asdex Tokamak. *Physical Review Letters*, **49** (1982), 19, 1408–1412. doi:10.1103/PhysRevLett.49.1408.

Wesson, J. A. Hydromagnetic-stability of Tokamaks. *Nuclear Fusion*, **18** (1978), 1, 87–132.

Wesson, J. A. Tokamaks. Clarendon Press, Oxford [u.a.] (2004).

Westerhof, E. Electron Cyclotron Waves. *Transactions of Fusion Science and Technology*, **53** (2008), 2T, 202–209.
URL http://epubs.ans.org/?a=1705

Westerhof, E. et al. Electron cyclotron resonance heating on TEXTOR. *Fusion Science and Technology*, **47** (2005), 2, 108–118.

Danksagung

An dieser Stelle möchte ich mich herzlich bei allen bedanken, die zum Gelingen dieser Arbeit beigetragen haben, insbesondere:

Herrn Prof. Dr. Ulrich Samm, dass er mir die Möglichkeit gegeben hat, an dieser interessanten Fragestellung zu arbeiten, und für die Unterstützung bei der Einordnung der Ergebnisse. Herrn Prof. Dr. Georg Pretzler danke ich für die bereitwillige Übernahme des Koreferats.

Herrn Dr. Sebastijan Brezinsek dafür, dass er nie müde wurde mich davon zu überzeugen, dass das Glas halb voll ist und nur noch die Zutaten für eine gute Limo fehlen: ein wenig Wasser, etwas Zucker und ein paar Spritzer Zitrone. Herrn Dr. Michael Lehnen für die kollegiale Zusammenarbeit und die vielen hilfreichen Diskussionen über die Einordnung der gewonnenen Daten. Herrn Dr. Oliver Schmitz für die Unterstützung bei der Durchführung der Experimente an TEXTOR.

Den Kollegen aus dem technischen Sektor danke ich für die konstante Unterstützung bei Bau, Justage und Kalibrierung der Diagnostik sowie ihre Einsatzbereitschaft wenn es um das Gelingen der Messungen ging, ganz besonders den Herren Klaus Klören und Kalle von Bovert. Herrn Jon Krom danke ich für die geduldige Unterstützung eines Physikers bei Programmierung und Softwareentwicklung.

Allen weiteren Kollegen, die mich ebenfalls in den alltäglichen Herausforderungen beim Aufbau der Diagnostik, der Durchführung der Experimente an TEXTOR und der Interpretation der Messergebnisse unterstützt haben: Herrn Dr. Bernd Schweer für die Hilfe bei allen technischen Fragen, Herrn Dr. Albrecht Pospieszczyk, dass er einen Teil seiner Rentenzeit für meine Messungen geopfert hat, Herrn Dr. Heinke Frerichs für Analyse, Diskussion und Bereitstellung seiner EMC3-EIRENE Modellierungen und Herrn Prof. Dr. Detlev Reiter, dass er sich immer Zeit für meine Fragen genommen hat.

Herrn Dr. Jan Willem Coenen danke ich für mehr als zwei Jahre tolle Bürogemeinschaft, Herrn Dipl.-Phys. Henning Stoschus für seine Freundschaft und viele angeregte Diskussionen, Frau Dipl.-Phys. Ruth Laengner, dass sie meine Diagnostik adoptiert hat und mit Frau Nadine Baumgarten und M.Sc. Maria Matveeva die Frauenquote unter den Doktoranden im IEF-4 weiter hochhält, sowie insgesamt allen Mitgliedern der Arbeitsgruppe für Plasma-Wand-Wechselwirkung für die sehr freundliche und kollegiale Arbeitsatmosphäre.

Bei Frau Dr.Katharina Brands bedanke ich mich dafür, dass unsere Freundschaft meine Zeit in Düsseldorf überdauert hat und ich mich auch in schwierigen Zeiten immer auf unsere Freundschaft verlassen konnte.

Meinen Eltern danke ich dafür, dass sie mich immer bei allem unterstützt haben, was ich mir vorgenommen habe.

Björn danke ich, dass er uns nie aufgegeben hat und mir insbesondere in der letzten Phase der Arbeit in jeder Hinsicht den Rücken frei gehalten hat.

1. **Einsatz von multispektralen Satellitenbilddaten in der Wasserhaushalts- und Stoffstrommodellierung – dargestellt am Beispiel des Rureinzugsgebietes**
   von C. Montzka (2008), XX, 238 Seiten
   ISBN: 978-3-89336-508-1

2. **Ozone Production in the Atmosphere Simulation Chamber SAPHIR**
   by C. A. Richter (2008), XIV, 147 pages
   ISBN: 978-3-89336-513-5

3. **Entwicklung neuer Schutz- und Kontaktierungsschichten für Hochtemperatur-Brennstoffzellen**
   von T. Kiefer (2008), 138 Seiten
   ISBN: 978-3-89336-514-2

4. **Optimierung der Reflektivität keramischer Wärmedämmschichten aus Yttrium-teilstabilisiertem Zirkoniumdioxid für den Einsatz auf metallischen Komponenten in Gasturbinen**
   von A. Stuke (2008), X, 201 Seiten
   ISBN: 978-3-89336-515-9

5. **Lichtstreuende Oberflächen, Schichten und Schichtsysteme zur Verbesserung der Lichteinkopplung in Silizium-Dünnschichtsolarzellen**
   von M. Berginski (2008), XV, 171 Seiten
   ISBN: 978-3-89336-516-6

6. **Politikszenarien für den Klimaschutz IV – Szenarien bis 2030**
   hrsg.von P. Markewitz, F. Chr. Matthes (2008), 376 Seiten
   ISBN 978-3-89336-518-0

7. **Untersuchungen zum Verschmutzungsverhalten rheinischer Braunkohlen in Kohledampferzeugern**
   von A. Schlüter (2008), 164 Seiten
   ISBN 978-3-89336-524-1

8. **Inorganic Microporous Membranes for Gas Separation in Fossil Fuel Power Plants**
   by G. van der Donk (2008), VI, 120 pages
   ISBN: 978-3-89336-525-8

9. **Sinterung von Zirkoniumdioxid-Elektrolyten im Mehrlagenverbund der oxidkeramischen Brennstoffzelle (SOFC)**
   von R. Mücke (2008), VI, 165 Seiten
   ISBN: 978-3-89336-529-6

10. **Safety Considerations on Liquid Hydrogen**
    by K. Verfondern (2008), VIII, 167 pages
    ISBN: 978-3-89336-530-2

11. **Kerosinreformierung für Luftfahrtanwendungen**
von R. C. Samsun (2008), VII, 218 Seiten
ISBN: 978-3-89336-531-9

12. **Der 4. Deutsche Wasserstoff Congress 2008 – Tagungsband**
hrsg. von D. Stolten, B. Emonts, Th. Grube (2008), 269 Seiten
ISBN: 978-3-89336-533-3

13. **Organic matter in Late Devonian sediments as an indicator for environmental changes**
by M. Kloppisch (2008), XII, 188 pages
ISBN: 978-3-89336-534-0

14. **Entschwefelung von Mitteldestillaten für die Anwendung in mobilen Brennstoffzellen-Systemen**
von J. Latz (2008), XII, 215 Seiten
ISBN: 978-3-89336-535-7

15. **RED-IMPACT**
Impact of Partitioning, Transmutation and Waste Reduction Technologies on the Final Nuclear Waste Disposal
SYNTHESIS REPORT
ed. by W. von Lensa, R. Nabbi, M. Rossbach (2008), 178 pages
ISBN 978-3-89336-538-8

16. **Ferritic Steel Interconnectors and their Interactions with Ni Base Anodes in Solid Oxide Fuel Cells (SOFC)**
by J. H. Froitzheim (2008), 169 pages
ISBN: 978-3-89336-540-1

17. **Integrated Modelling of Nutrients in Selected River Basins of Turkey**
Results of a bilateral German-Turkish Research Project
project coord. M. Karpuzcu, F. Wendland (2008), XVI, 183 pages
ISBN: 978-3-89336-541-8

18. **Isotopengeochemische Studien zur klimatischen Ausprägung der Jüngeren Dryas in terrestrischen Archiven Eurasiens**
von J. Parplies (2008), XI, 155 Seiten, Anh.
ISBN: 978-3-89336-542-5

19. **Untersuchungen zur Klimavariabilität auf dem Tibetischen Plateau - Ein Beitrag auf der Basis stabiler Kohlenstoff- und Sauerstoffisotope in Jahrringen von Bäumen waldgrenznaher Standorte**
von J. Griessinger (2008), XIII, 172 Seiten
ISBN: 978-3-89336-544-9

20. **Neutron-Irradiation + Helium Hardening & Embrittlement Modeling of 9%Cr-Steels in an Engineering Perspective (HELENA)**
by R. Chaouadi (2008), VIII, 139 pages
ISBN: 978-3-89336-545-6

21. **in Bearbeitung**

22. **Verbundvorhaben APAWAGS (AOEV und Wassergenerierung) – Teilprojekt: Brennstoffreformierung – Schlussbericht**
von R. Peters, R. C. Samsun, J. Pasel, Z. Porš, D. Stolten (2008), VI, 106 Seiten
ISBN: 978-3-89336-547-0

23. **FREEVAL**
Evaluation of a Fire Radiative Power Product derived from Meteosat 8/9 and Identification of Operational User Needs
Final Report
project coord. M. Schultz, M. Wooster (2008), 139 pages
ISBN: 978-3-89336-549-4

24. **Untersuchungen zum Alkaliverhalten unter Oxycoal-Bedingungen**
von C. Weber (2008), VII, 143, XII Seiten
ISBN: 978-3-89336-551-7

25. **Grundlegende Untersuchungen zur Freisetzung von Spurstoffen, Heißgaschemie, Korrosionsbeständigkeit keramischer Werkstoffe und Alkalirückhaltung in der Druckkohlenstaubfeuerung**
von M. Müller (2008), 207 Seiten
ISBN: 978-3-89336-552-4

26. **Analytik von ozoninduzierten phenolischen Sekundärmetaboliten in *Nicotiana tabacum* L. cv Bel W3 mittels LC-MS**
von I. Koch (2008), III, V, 153 Seiten
ISBN 978-3-89336-553-1

27. **IEF-3 Report 2009. Grundlagenforschung für die Anwendung**
(2009), ca. 230 Seiten
ISBN: 978-3-89336-554-8

28. **Influence of Composition and Processing in the Oxidation Behavior of MCrAlY-Coatings for TBC Applications**
by J. Toscano (2009), 168 pages
ISBN: 978-3-89336-556-2

29. **Modellgestützte Analyse signifikanter Phosphorbelastungen in hessischen Oberflächengewässern aus diffusen und punktuellen Quellen**
von B. Tetzlaff (2009), 149 Seiten
ISBN: 978-3-89336-557-9

30. **Nickelreaktivlot / Oxidkeramik – Fügungen als elektrisch isolierende Dichtungskonzepte für Hochtemperatur-Brennstoffzellen-Stacks**
von S. Zügner (2009), 136 Seiten
ISBN: 978-3-89336-558-6

31. **Langzeitbeobachtung der Dosisbelastung der Bevölkerung in radioaktiv kontaminierten Gebieten Weißrusslands – Korma-Studie**
von H. Dederichs, J. Pillath, B. Heuel-Fabianek, P. Hill, R. Lennartz (2009), Getr. Pag.
ISBN: 978-3-89336-532-3

32. **Herstellung von Hochtemperatur-Brennstoffzellen über physikalische Gasphasenabscheidung**
von N. Jordán Escalona (2009), 148 Seiten
ISBN: 978-3-89336-532-3

33. **Real-time Digital Control of Plasma Position and Shape on the TEXTOR Tokamak**
by M. Mitri (2009), IV, 128 pages
ISBN: 978-3-89336-567-8

34. **Freisetzung und Einbindung von Alkalimetallverbindungen in kohlebefeuerten Kombikraftwerken**
von M. Müller (2009), 155 Seiten
ISBN: 978-3-89336-568-5

35. **Kosten von Brennstoffzellensystemen auf Massenbasis in Abhängigkeit von der Absatzmenge**
von J. Werhahn (2009), 242 Seiten
ISBN: 978-3-89336-569-2

36. **Einfluss von Reoxidationszyklen auf die Betriebsfestigkeit von anodengestützten Festoxid-Brennstoffzellen**
von M. Ettler (2009), 138 Seiten
ISBN: 978-3-89336-570-8

37. **Großflächige Plasmaabscheidung von mikrokristallinem Silizium für mikromorphe Dünnschichtsolarmodule**
von T. Kilper (2009), XVII, 154 Seiten
ISBN: 978-3-89336-572-2

38. **Generalized detailed balance theory of solar cells**
by T. Kirchartz (2009), IV, 198 pages
ISBN: 978-3-89336-573-9

39. **The Influence of the Dynamic Ergodic Divertor on the Radial Electric Field at the Tokamak TEXTOR**
von J. W. Coenen (2009), xii, 122, XXVI pages
ISBN: 978-3-89336-574-6

40. **Sicherheitstechnik im Wandel Nuklearer Systeme**
von K. Nünighoff (2009), viii, 215 Seiten
ISBN: 978-3-89336-578-4

41. **Pulvermetallurgie hochporöser NiTi-Legierungen für Implanat- und Dämpfungsanwendungen**
von M. Köhl (2009), XVII, 199 Seiten
ISBN: 978-3-89336-580-7

42. **Einfluss der Bondcoatzusammensetzung und Herstellungsparameter auf die Lebensdauer von Wärmedämmschichten bei zyklischer Temperaturbelastung**
von M. Subanovic (2009), 188, VI Seiten
ISBN: 978-3-89336-582-1

43. **Oxygen Permeation and Thermo-Chemical Stability of Oxygen Permeation Membrane Materials for the Oxyfuel Process**
by A. J. Ellett (2009), 176 pages
ISBN: 978-3-89336-581-4

44. **Korrosion von polykristallinem Aluminiumoxid (PCA) durch Metalljodidschmelzen sowie deren Benetzungseigenschaften**
von S. C. Fischer (2009), 148 Seiten
ISBN: 978-3-89336-584-5

45. **IEF-3 Report 2009. Basic Research for Applications**
(2009), 217 Seiten
ISBN: 978-3-89336-585-2

46. **Verbundvorhaben ELBASYS (Elektrische Basissysteme in einem CFK-Rumpf) - Teilprojekt: Brennstoffzellenabgase zur Tankinertisierung - Schlussbericht**
von R. Peters, J. Latz, J. Pasel, R. C. Samsun, D. Stolten
(2009), xi, 202 Seiten
ISBN: 978-3-89336-587-6

47. **Aging of ^{14}C-labeled Atrazine Residues in Soil: Location, Characterization and Biological Accessibility**
by N. D. Jablonowski (2009), IX, 104 pages
ISBN: 978-3-89336-588-3

48. **Entwicklung eines energetischen Sanierungsmodells für den europäischen Wohngebäudesektor unter dem Aspekt der Erstellung von Szenarien für Energie- und CO_2 - Einsparpotenziale bis 2030**
von P. Hansen (2009), XXII, 281 Seiten
ISBN: 978-3-89336-590-6

49. **Reduktion der Chromfreisetzung aus metallischen Interkonnektoren für Hochtemperaturbrennstofzellen durch Schutzschichtsysteme**
von R. Trebbels (2009), iii, 135 Seiten
ISBN: 978-3-89336-591-3

50. **Bruchmechanische Untersuchung von Metall / Keramik-Verbundsystemen für die Anwendung in der Hochtemperaturbrennstoffzelle**
von B. Kuhn (2009), 118 Seiten
ISBN: 978-3-89336-592-0

51. **Wasserstoff-Emissionen und ihre Auswirkungen auf den arktischen Ozonverlust**
Risikoanalyse einer globalen Wasserstoffwirtschaft
von T. Feck (2009), 180 Seiten
ISBN: 978-3-89336-593-7

52. **Development of a new Online Method for Compound Specific Measurements of Organic Aerosols**
by T. Hohaus (2009), 156 pages
ISBN: 978-3-89336-596-8

53. **Entwicklung einer FPGA basierten Ansteuerungselektronik für Justageeinheiten im Michelson Interferometer**
von H. Nöldgen (2009), 121 Seiten
ISBN: 978-3-89336-599-9

54. **Observation – and model – based study of the extratropical UT/LS**
by A. Kunz (2010), xii, 120, xii pages
ISBN: 978-3-89336-603-3

55. **Herstellung polykristalliner Szintillatoren für die Positronen-Emissions-Tomographie (PET)**
von S. K. Karim (2010), VIII, 154 Seiten
ISBN: 978-3-89336-610-1

56. **Kombination eines Gebäudekondensators mit H2-Rekombinatorelementen in Leichwasserreaktoren**
von S. Kelm (2010), vii, 119 Seiten
ISBN: 978-3-89336-611-8

57. **Plant Leaf Motion Estimation Using A 5D Affine Optical Flow Model**
by T. Schuchert (2010), X, 143 pages
ISBN: 978-3-89336-613-2

58. **Tracer-tracer relations as a tool for research on polar ozone loss**
by R. Müller (2010), 116 pages
ISBN: 978-3-89336-614-9

59. **Sorption of polycyclic aromatic hydrocarbon (PAH) to Yangtze River sediments and their components**
by J. Zhang (2010), X, 109 pages
ISBN: 978-3-89336-616-3

60. **Weltweite Innovationen bei der Entwicklung von CCS-Technologien und Möglichkeiten der Nutzung und des Recyclings von CO_2**
Studie im Auftrag des BMWi
von W. Kuckshinrichs et al. (2010), X, 139 Seiten
ISBN: 978-3-89336-617-0

61. **Herstellung und Charakterisierung von sauerstoffionenleitenden Dünnschichtmembranstrukturen**
von M. Betz (2010), XII, 112 Seiten
ISBN: 978-3-89336-618-7

62. **Politikszenarien für den Klimaschutz V – auf dem Weg zum Strukturwandel, Treibhausgas-Emissionsszenarien bis zum Jahr 2030**
hrsg. von P. Hansen, F. Chr. Matthes (2010), 276 Seiten
ISBN: 978-3-89336-619-4

63. **Charakterisierung Biogener Sekundärer Organischer Aerosole mit Statistischen Methoden**
von C. Spindler (2010), iv, 163 Seiten
ISBN: 978-3-89336-622-4

64. **Stabile Algorithmen für die Magnetotomographie an Brennstoffzellen**
von M. Wannert (2010), ix, 119 Seiten
ISBN: 978-3-89336-623-1

65. **Sauerstofftransport und Degradationsverhalten von Hochtemperatur-membranen für CO2-freie Kraftwerke**
von D. Schlehuber (2010), VII, 139 Seiten
ISBN: 978-3-89336-630-9

66. **Entwicklung und Herstellung von foliengegossenen, anodengestützten Festoxidbrennstoffzellen**
von W. Schafbauer (2010), VI, 164 Seiten
ISBN: 978-3-89336-631-6

67. **Disposal strategy of proton irradiated mercury from high power spallation sources**
by S. Chiriki (2010), xiv, 124 pages
ISBN: 978-3-89336-632-3

68. **Oxides with polyatomic anions considered as new electrolyte materials for solid oxide fuel cells (SOFCs)**
by O. H. Bin Hassan (2010), vii, 121 pages
ISBN: 978-3-89336-633-0

69. **Von der Komponente zum Stack: Entwicklung und Auslegung von HT-PEFC-Stacks der 5 kW-Klasse**
von A. Bendzulla (2010), IX, 203 Seiten
ISBN: 978-3-89336-634-7

70. **Satellitengestützte Schwerewellenmessungen in der Atmosphäre und Perspektiven einer zukünftigen ESA Mission (PREMIER)**
von S. Höfer (2010), 81 Seiten
ISBN: 978-3-89336-637-8

71. **Untersuchungen der Verhältnisse stabiler Kohlenstoffisotope in atmosphärisch relevanten VOC in Simulations- und Feldexperimenten**
von H. Spahn (2010), IV, 210 Seiten
ISBN: 978-3-89336-638-5

72. **Entwicklung und Charakterisierung eines metallischen Substrats für nanostrukturierte keramische Gastrennmembranen**
von K. Brands (2010), vii, 137 Seiten
ISBN: 978-3-89336-640-8

73. **Hybridisierung und Regelung eines mobilen Direktmethanol-Brennstoff-zellen-Systems**
von J. Chr. Wilhelm (2010), 220 Seiten
ISBN: 978-3-89336-642-2

74. **Charakterisierung perowskitischer Hochtemperaturmembranen zur Sauerstoffbereitstellung für fossil gefeuerte Kraftwerksprozesse**
von S.A. Möbius (2010) III, 208 Seiten
ISBN: 978-3-89336-643-9

75. **Characterization of natural porous media by NMR and MRI techniques: High and low magnetic field studies for estimation of hydraulic properties**
by L.-R. Stingaciu (2010), 96 pages
ISBN: 978-3-89336-645-3

76. **Hydrological Characterization of a Forest Soil Using Electrical Resistivity Tomography**
by Chr. Oberdörster (2010), XXI, 151 pages
ISBN: 978-3-89336-647-7

77. **Ableitung von atomarem Sauerstoff und Wasserstoff aus Satellitendaten und deren Abhängigkeit vom solaren Zyklus**
von C. Lehmann (2010), 127 Seiten
ISBN: 978-3-89336-649-1

78. **18th World Hydrogen Energy Conference 2010 – WHEC2010 Proceedings**
Speeches and Plenary Talks
ed. by D. Stolten, B. Emonts (2010)
ISBN: 978-3-89336-658-3

78-1. **18th World Hydrogen Energy Conference 2010 – WHEC2010 Proceedings**
Parallel Sessions Book 1:
Fuel Cell Basics / Fuel Infrastructures
ed. by D. Stolten, T. Grube (2010), ca. 460 pages
ISBN: 978-3-89336-651-4

78-2. **18th World Hydrogen Energy Conference 2010 – WHEC2010 Proceedings**
Parallel Sessions Book 2:
Hydrogen Production Technologies – Part 1
ed. by D. Stolten, T. Grube (2010), ca. 400 pages
ISBN: 978-3-89336-652-1

78-3. **18th World Hydrogen Energy Conference 2010 – WHEC2010 Proceedings**
Parallel Sessions Book 3:
Hydrogen Production Technologies – Part 2
ed. by D. Stolten, T. Grube (2010), ca. 640 pages
ISBN: 978-3-89336-653-8

78-4. **18th World Hydrogen Energy Conference 2010 – WHEC2010 Proceedings**
Parallel Sessions Book 4:
Storage Systems / Policy Perspectives, Initiatives and Cooperations
ed. by D. Stolten, T. Grube (2010), ca. 500 pages
ISBN: 978-3-89336-654-5

78-5. **18th World Hydrogen Energy Conference 2010 – WHEC2010 Proceedings**
Parallel Sessions Book 5:
Stategic Analysis / Safety Issues / Existing and Emerging Markets
ed. by D. Stolten, T. Grube (2010), ca. 530 pages
ISBN: 978-3-89336-655-2

78-6. **18th World Hydrogen Energy Conference 2010 – WHEC2010 Proceedings**
Parallel Sessions Book 6:
Stationary Applications / Transportation Applications
ed. by D. Stolten, T. Grube (2010), ca. 330 pages
ISBN: 978-3-89336-656-9

78 Set (complete book series)

18th World Hydrogen Energy Conference 2010 – WHEC2010 Proceedings
eb. by D. Stolten, T. Grube, B. Emonts (2010)
ISBN: 978-3-89336-657-6

79. **Ultrafast voltex core dynamics investigated by finite-element micromagnetic simulations**
by S. Gliga (2010), vi, 144 pages
ISBN: 978-3-89336-660-6

80. **Herstellung und Charakterisierung von keramik- und metallgestützten Membranschichten für die CO_2-Abtrennung in fossilen Kraftwerken**
von F. Hauler (2010), XVIII, 178 Seiten
ISBN: 978-3-89336-662-0

81. **Experiments and numerical studies on transport of sulfadiazine in soil columns**
by M. Unold (2010), xvi, 115 pages
ISBN: 978-3-89336-663-7

82. **Prompt-Gamma-Neutronen-Aktivierungs-Analyse zur zerstörungsfreien Charakterisierung radioaktiver Abfälle**
von J.P.H. Kettler (2010), iv, 205 Seiten
ISBN: 978-3-89336-665-1

83. **Transportparameter dünner geträgerter Kathodenschichten der oxidkeramischen Brennstoffzelle**
von C. Wedershoven (2010), vi, 137 Seiten
ISBN: 978-3-89336-666-8

84. **Charakterisierung der Quellverteilung von Feinstaub und Stickoxiden in ländlichem und städtischem Gebiet**
von S. Urban (2010), vi, 211 Seiten
ISBN: 978-3-89336-669-9

85. **Optics of Nanostructured Thin-Film Silicon Solar Cells**
by C. Haase (2010), 150 pages
ISBN: 978-3-89336-671-2

86. **Entwicklung einer Isolationsschicht für einen Leichtbau-SOFC-Stack**
von R. Berhane (2010), X, 162 Seiten
ISBN: 978-3-89336-672-9

87. **Hydrogen recycling and transport in the helical divertor of TEXTOR**
by M. Clever (2010), x, 172 pages
ISBN: 978-3-89336-673-6

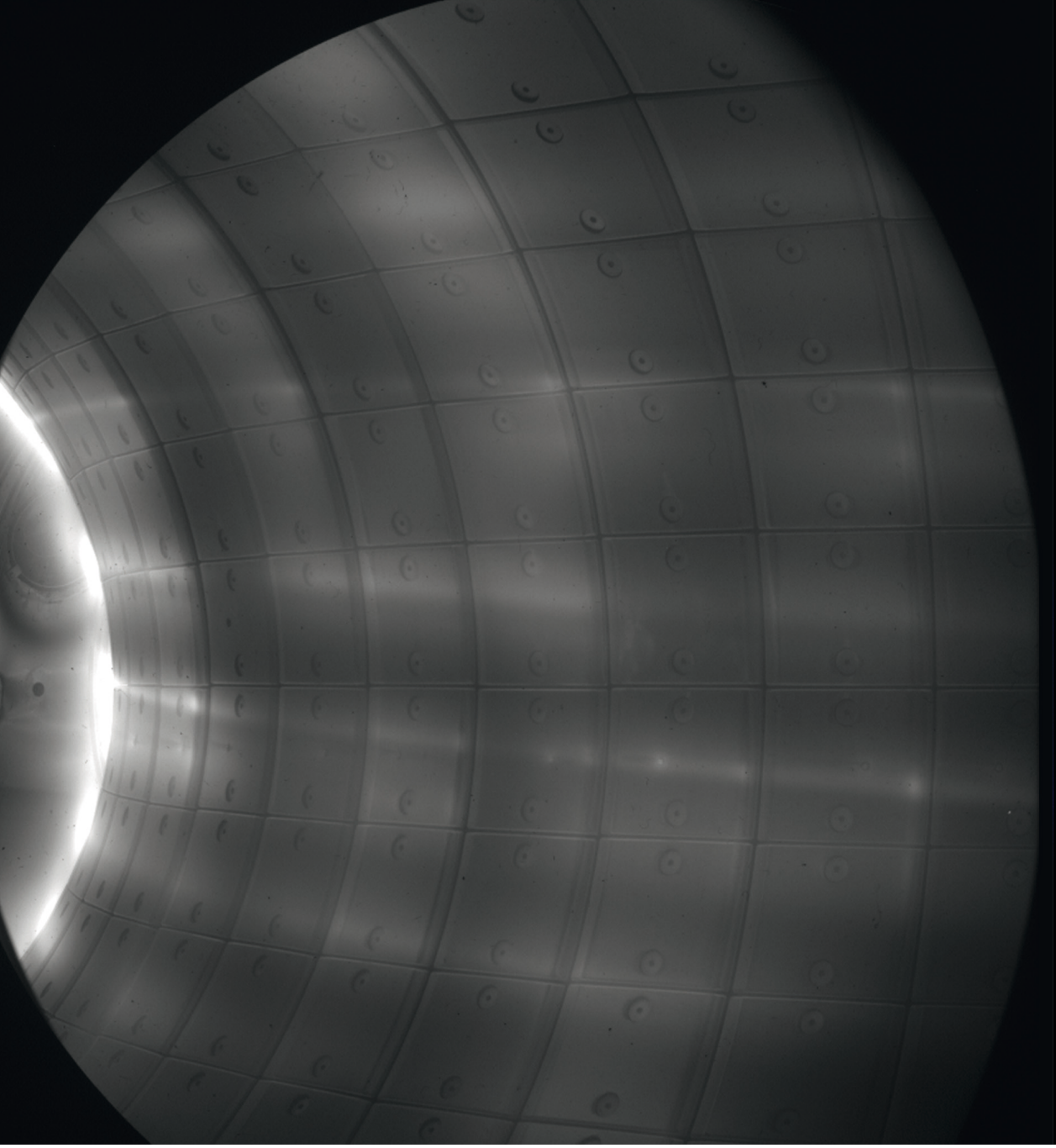

Energie & Umwelt / Energy & Environment
Band / Volume 87
ISBN 978-3-89336-673-6

JÜLICH
FORSCHUNGSZENTRUM